Leonard Koch

Search for Resonant X(3872) Formation in Electron Positron Annihilations and the Development of a Prototype Data Acquisition for the Crystal Zero Degree Detector at BESIII

Dissertation
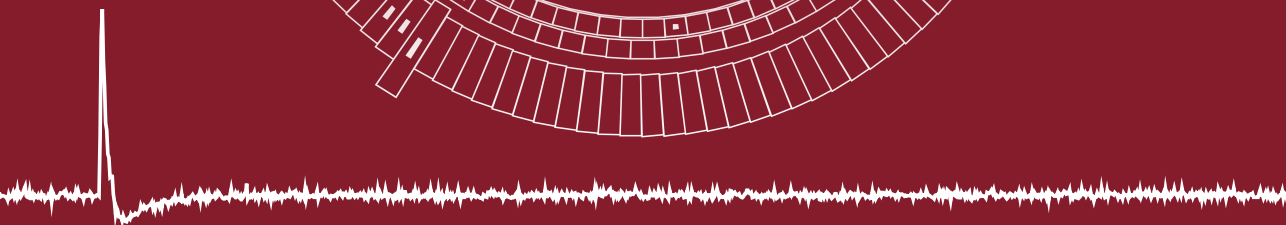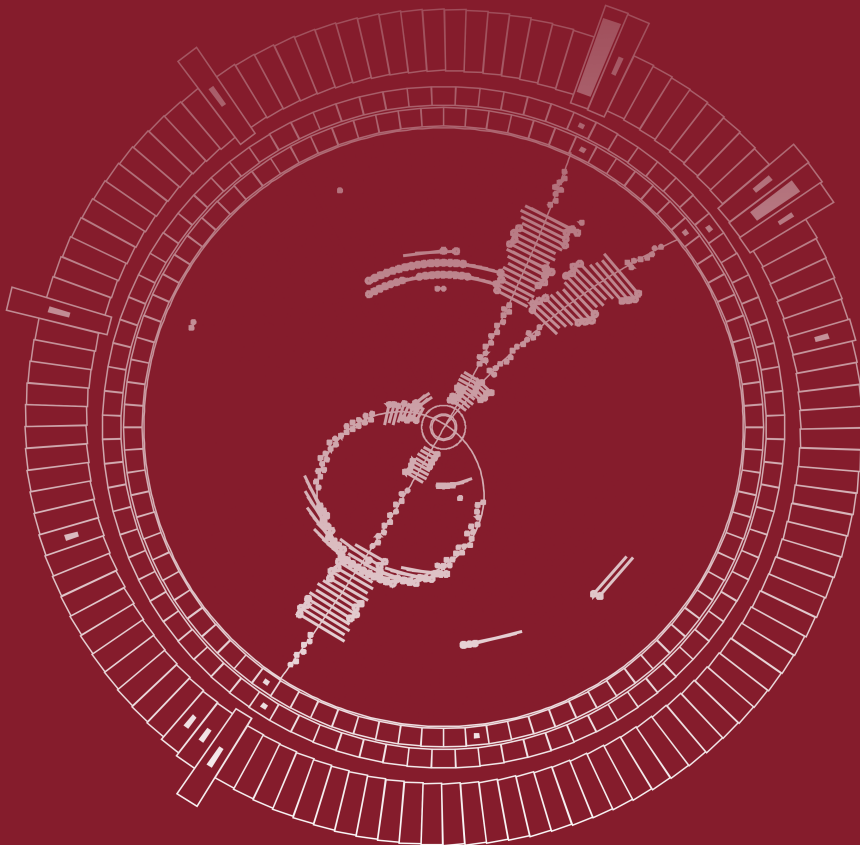
Search for Resonant X(3872) Formation in Electron Positron Annihilations and the Development of a Prototype Data Acquisition for the Crystal Zero Degree Detector at BESIII

Search for Resonant $X(3872)$ Formation in Electron Positron Annihilations and the Development of a Prototype Data Acquisition for the Crystal Zero Degree Detector at BESIII

Inauguraldissertation

zur Erlangung des Doktorgrades am

Fachbereich Mathematik und Informatik, Physik, Geographie

der

Justus-Liebig-Universität Gießen

vorgelegt von

Leonard Koch

aus Gießen

Gießen (2019)

Aus dem II. Physikalischen Institut

Dekan:	Prof. Dr. Kai-Thomas Brinkmann
Gutachter:	Prof. Dr. Wolfgang Kühn
Gutachterin:	Prof. Dr. Claudia Höhne

Danksagung

Die Erarbeitung dieser Dissertation erschien mir nur möglich, da ich mich auf den Rückhalt zahlloser Menschen in meinem Umfeld verlassen konnte, denen Ich zu tiefstem Dank verpflichtet bin.

Zu allererst möchte ich mich bei meinem Betreuer Prof. Dr. Wolfgang Kühn bedanken. Du hattest immer ein offenes Ohr und gabst mir durch deine Erfahrung und enormes Fachwissen immer den richtigen Impulsübertrag, um meine Arbeit voranzutreiben.

I would like to thank the whole BESIII collaboration which made it possible for me to take part in such a big international experiment at the cutting edge of today's understanding of nature.

Desweiteren möchte ich mich bei jedem einzelnen Mitglied der Arbeitsgruppe Kühn/Höhne für die angenehme Arbeitsatmosphäre bedanken. Die zahlreichen Diskussion — auch über nichtphysikalische Themen — machten mir die Arbeit deutlich leichter.

PD Dr. Sören Lange gebührt besonderer Dank. Du warst es, der mich für die Erforschung der XYZ Zustände begeisterte und mich überzeugte, der Arbeitsgruppe Kühn beizutreten. Ohne dich hätte ich diese Arbeit nie geschrieben.

A big thank you goes to Dr. Yutie Liang. You supplied an infinite amount of practical help on the BOSS framework and anything related to IHEP. Furthermore, I would like to thank you for your enormous assistance with the X(3872) analysis and the DAQ development as well as for your guidance during my first visits to China. I am very sorry that my Chinese skills are still extremely poor, but I know the following and I truly mean it: 谢谢!

Bei Klemens Lautenbach möchte ich mich nicht nur für die ausgezeichnete Büroatmosphäre und für die Hilfe bei der Strahlzeit bedanken, sondern auch für all die gemeinsamen Abenteuer in Novosibirsk, Liechtenstein, Mainz, etc.

Ich möchte mich bei Thomas Geßler für das bereitwillige Teilen seiner umfangreichen Fachkenntnisse bezüglich FPGA Programmierung und den manchmal doch sehr abschweifenden Austausch über LaTeX/TikZ bedanken.

Für all die administrative, bürokratische und technische Hilfestellungen bedanke ich mich bei Christa Momberger, Gundi Bernhardt, Anita Rühl und Thomas Köster.

Erklärung der Urheberschaft

Ich erkläre: Ich habe die vorgelegte Dissertation selbstständig und ohne unerlaubte fremde Hilfe und nur mit den Hilfen angefertigt, die ich in der Dissertation angegeben habe. Alle Textstellen, die wörtlich oder sinngemäß aus veröffentlichten Schriften entnommen sind, und alle Angaben, die auf mündlichen Auskünften beruhen, sind als solche kenntlich gemacht. Ich stimme einer evtl. Überprüfung meiner Dissertation durch eine Antiplagiat-Software zu. Bei den von mir durchgeführten und in der Dissertation erwähnten Untersuchungen habe ich die Grundsätze guter wissenschaftlicher Praxis, wie sie in der „Satzung der Justus-Liebig-Universität Gießen zur Sicherung guter wissenschaftlicher Praxis" niedergelegt sind, eingehalten.

_____   _____

Datum   Unterschrift

Kurzdarstellung

Die X(3872) Resonanz ist das berühmteste Beispiel der exotischen charmoniumähnlichen XYZ Zustände. Diese Klasse von Hadronen liegt in der Charmonium-Massenregion, hat aber Eigenschaften, die ihre Interpretation als konventionelle Charmonium Zusände erschweren. Viele Alternativen wie kompakte Tetraquarks oder Meson Moleküle werden diskutiert, aber die innere Struktur dieser Zustände bleibt ungeklärt. Eine Eigenschaft, die helfen könnte, die Situation zu vereinfachen, ist die elektronische Breite Γ_{ee} des X(3872) Zustands. Diese Größe kann durch die Messung der bis jetzt unbeobachteten $e^+e^- \to$ X(3872) Reaktion bestimmt werden.

Im Rahmen dieser Thesis wurde nach dieser Reaktion gesucht, indem Daten von Elektron Positron Kollisionen in der Nähe der X(3872) Masse analysiert wurden. Die Daten mit einer über vier Kollisionsenergien verteilten integrierten Luminosität von $(322.3 \pm 1.7)\,\mathrm{pb}^{-1}$ wurden vom BESIII Detektor am BEPCII Beschleuniger in Peking (China) aufgezeichnet. Es wurde nach dem X(3872) Zustand im Zerfall X(3872) $\to \pi^+\pi^- J/\psi$ gefolgt von $J/\psi \to \ell^+\ell^-$ gesucht, wobei ℓ für e oder μ steht.

Mithilfe von Maximum Likelihood Fits an das J/ψ Signal in den Verteilungen der invarianten Dilepton Masse wurde der Wirkungsquerschnitt von $e^+e^- \to \pi^+\pi^- J/\psi$ bestimmt. Es gibt kein Anzeichen für ein X(3872) Signal. Eine obere Grenze für das Produkt aus der elektronischen Breite und dem Verzweigungsverhältnis wurde mithilfe einer Bayesischen Likelihood Analyse bestimmt: $7 \times 10^{-3}\,\mathrm{eV}$ bei einem Konfidenzniveau von 90 %. Dies ist eine Verbesserung um den Faktor von ungefähr 20 im Vergleich zu bestehenden oberen Grenzen.

Das zweite Thema dieser Arbeit ist die Entwicklung einer FPGA-basierten Prototypdatenauslese für einen kleinen Detektor, welcher sehr dicht an der Strahlachse im Vorwärts- und Rückwärtsbereich von BESIII plaziert

werden soll. Dieser Detektor hat die Aufgabe, abgestrahlte Photonen aus dem Anfangszustand zu messen, was von großem Vorteil für die präzise Messungen von Wirkungsquerschnitten diverser Hadronenproduktionen in e^+e^- Vernichtungen sein wird. Das aktive Detektormaterial wird LYSO sein, ein schneller und dichter anorganischer Szintillator, dessen Licht von Silizium Photomultipliern gesammelt wird.

An der vorgesehenen Position wird der Detektor einer extrem hohen Untergrundrate im MHz Bereich ausgesetzt sein. Die implizierten Anforderungen an das Design der Datenauslese sind die Fähigkeiten, zeitliche Ereignisüberlagerungen in Echtzeit zu erkennen und die Zuordnung der Ereignisse zum BESIII Trigger.

Im Zusammenhang dieser Thesis wurde der Prototyp einer Datenauslese auf Grundlage eines bereits existierenden Sampling ADCs mit FPGA Untestützung und einer Samplingrate von 125 MHz entwickelt. Eine zusätzliche FPGA-Platine (ebenfalls bereits existierend) dient als Puffer zwischen dem ADC und einem PC, welcher die aufgezeichneten Daten auf Festplatte schreibt. Verfügbare Lösungen sowohl für die serielle Hochgeschwindigkeitskommunikation zwischen den FPGAs als auch für die Gigabit Ethernet Verbindung zum PC für Monitor- und Kontrollzwecke und den Transfer der Daten wurden durch selbsterstellte Design ergänzt. Die Prototypdatenauslese führt derzeit noch keine Zuordnung der Ereignisse zu einem Trigger Signal oder eine Erkennung der Ereignisüberlagerung aus, bietet dafür aber die Möglichkeit, kontinuierlich digitalisierte Signalformen aufzuzeichnen, welche dann offline analysiert werden können.

Die Prototypdatenauslese wurde zusammen mit einem Prototyp Detektormodul im Elektronenstrahl des MAMI Beschleunigers in Mainz getestet. Der Strahl hatte eine feste Energie von 855 MeV und variierende Raten zwischen 2.7 kHz und 13.9 MHz. Auf Grundlage der aufgezeichneten Daten wurden Algorithmen für die Extraktion von Pulscharakeristika und das Erkennen von Ereignisüberlagerungen zur späteren Implementierung

auf den FPGAs entwickelt. Es wurde gezeigt, dass ungefähr 90 % aller Ereignisüberlagerungen für Raten bis zu 6 MHz erkannt werden können.

Abstract

T HE X(3872) resonance is the most famous member of the family of exotic charmonium-like XYZ states. This class of hadrons lies in the charmonium mass region, but exhibits properties disfavoring their interpretation as conventional charmonium states. Many alternatives like compact tetraquarks or meson molecules are discussed while the inner structure of these states remain unclear. A property that might help to clarify the situation is the electronic width Γ_{ee} of the X(3872) state. This quantity is accessible in the measurement of the so far unobserved $e^+e^- \to X(3872)$ reaction.

Within the framework of this thesis, the search for this reaction has been performed by analyzing electron positron collision data in the vicinity of the X(3872) mass. The data with an integrated luminosity of $(322.3 \pm 1.7)\,\mathrm{pb}^{-1}$ spreading over four different collision energies was recorded by the BESIII detector at the BEPCII accelerator in Beijing (China). The X(3872) state has been searched for via the decay of $X(3872) \to \pi^+\pi^- J/\psi$ and the subsequent $J/\psi \to \ell^+\ell^-$ decay, where ℓ stands for e or μ.

The cross section of $e^+e^- \to \pi^+\pi^- J/\psi$ has been extracted from maximum likelihood fits to the J/ψ peak in the distributions of the invariant dilepton mass. There is no evidence for a X(3872) signal. An upper limit on the product of the electronic width times the branching fraction $\Gamma_{ee} \times \mathcal{B}(X(3872) \to \pi^+\pi^- J/\psi)$ has been determined by a Bayesian likelihood analysis to be $7 \times 10^{-3}\,\mathrm{eV}$ at 90 % confidence level. This is an improvement of a factor of about 20 upon existing limits.

The second topic of this thesis is the development of an FPGA based prototype data acquisition for a small detector to be placed very closely to the beam line in the forward and backward direction of BESIII. This detector is designed to measure photons from initial state radiation which will be of great benefit for precise measurements

of various hadron production cross sections in e^+e^- annihilations. The active material will be LYSO, a fast and dense inorganic scintillator, with silicon photomultipliers to collect the scintillation light.

At the designated position, the detector will be exposed to an extremely high background rate in the MHz region. The implied design requirements on the data acquisition are realtime capabilities to detect pile-up and to correlate the events with the BESIII trigger.

In the context of this thesis, a prototype data acquisition based on an already existing sampling ADC with FPGA support and a sampling frequency of 125 MHz has been developed. An additional FPGA board (already existing, too) acts as a buffer between the ADC and a PC which in turn writes the sampled data to disk. Available solutions for the high speed serial communication between the FPGAs as well as for monitoring/controlling and data transfer to the PC via Gigabit Ethernet have been complemented by custom designs. The prototype data acquisition has not performed event correlation or pile-up detection yet, but it provides means to record continuously sampled waveforms that can be analyzed offline.

The prototype data acquisition was tested together with a prototype detector module in an electron beam at the MAMI accelerator in Mainz. The beam had a fixed energy of 855 MeV and a varying rate between 2.7 kHz and 13.9 MHz. Based on the recorded data, feature extraction and pile-up detection algorithms have been developed for the later implementation on the available FPGAs. It has been shown that about 90 % of pile-up events can be detected for rates of up to 6 MHz.

CONTENTS

INTRODUCTION

Q UANTUM CHROMO DYNAMICS (QCD) is one of the pillars of the standard model of particle physics. Already since the 70s, it is the established theory of the strong interaction, yet far from fully understood. Due to the color structure and the self-interaction of gluons, the strong coupling constant becomes very large for small momentum transfers. The consequence is the failure of perturbation theory in this regime. It is the scale at which quarks form hadrons.

The observation that hadrons can be arranged in multiplets according to their quantum numbers gave birth to the quark model in the first place [1–3]. The field of hadron spectroscopy deals with the masses, decay widths, and quantum numbers of hadrons. The experimental measurement of these observables are important tests of different theoretical techniques and models.

Approaches like lattice QCD [4–7] or functional methods [8–16] make predictions from the first principles of QCD. However, they are not yet mature enough to compete with the accuracy of experimental measurements. A different approach from the theoretical side is to use models and effective field theories like chiral perturbation theory [17, 18] or potential non-relativistic QCD [19, 20].

In recent years, the situation became more complex with the discovery of the XYZ states in the charmonium region [21–29]. They are hadrons with properties incompatible with so far very successful models. It is believed that they are not conventional hadrons like baryons or mesons. They are dubbed QCD exotica and many different interpretations like tetraquarks or mesons with gluonic excitations are discussed, but without a definite conclusion. The inner structure of these exotic hadrons remains unclear.

A prime example of the XYZ states is the X(3872) resonance, being the first XYZ state to be discovered [21]. It was observed in the decay to $\pi^+\pi^- J/\psi$ in 2003. With a mass of $(3871.69 \pm 0.17)\,\text{MeV}$ it is in the region of the charmonium system [30].[1] Moreover, all

---

[1]This thesis follows the convention of natural units, i.e. $c = \hbar = 1$. By doing so, masses and momenta can be written in energy units. Lengths are expressed in inverse units of the energy.

of the observed decay channels involve charmonia or D mesons. With the current resolution, the mass cannot be distinguished from the threshold of the $D^0\bar{D}^{*0}$ system. This observation favors the interpretation as a $D^0\bar{D}^{*0}$ molecule. Another eye-catching feature is the remarkably narrow width of the $X(3872)$, untypical for a state above the open-charm threshold. The current upper limit reads $\Gamma < 1.2\,\text{MeV}$ at 90 % confidence level [30, 31].

One more important property of the $X(3872)$ resonance is the electronic width Γ_{ee}. It is directly proportional to the cross section of $e^+e^- \to X(3872)$ and may help to reveal the $X(3872)$'s inner structure. However, the quantum numbers $J^{PC} = 1^{++}$ of the $X(3872)$ state require an additional virtual photon in the Feynman diagram leading to a strong suppression of Γ_{ee}. So far, only an upper limit on the product of Γ_{ee} and the decay branching fraction $\mathcal{B}(X(3872) \to \pi^+\pi^- J/\psi)$ of 0.13 eV at 90 % confidence level has been determined [32].

BESIII is one of the most successful experiments recording data of e^+e^- annihilations in the energy region of the charmonium system [33]. It is located at the BEPCII storage ring of the Institute of High Energy Physics in Beijing. The accelerator provides the worlds highest e^+e^- luminosity at these center-of-mass energies enabling BESIII to collect the worlds largest data sets in the τ-charm region [34, 35]. Hence, BESIII is the ideal laboratory to perform the search for $e^+e^- \to X(3872)$. For that reason, collision data was collected directly at and slightly below the $X(3872)$ mass during a period of ten days in June 2017.

Higher order electron positron annihilation does not necessarily include two virtual photons like the resonant $X(3872)$ formation. Instead, it can also involve one virtual photon in association with the emission of one real photon from the initial state. This initial state radiation (ISR) reduces the effective center-of-mass energy carried by the virtual photon [36, 37]. The effect of ISR can be exploited to simultaneously perform a gapless cross section scan of $e^+e^- \to$ hadrons covering all effective center-of-mass energies below the actual energy provided by the beams.

The precise measurement of these cross sections is vital for solving another puzzle of non-perturbative QCD: the theoretical prediction for the anomalous magnetic moment of the muon differs by $3.5\,\sigma$ from the experimental measurement [30, 38–40]. The theoretical uncertainty is dominated by the estimation of the hadronic

contribution. Important inputs for the accurate prediction of this contribution are the experimental results of the aforementioned $e^+e^- \to$ hadrons cross sections, in particular for low energies.

Unfortunately, the major part of ISR photons is emitted inside a cone very close to the beam axis, which is not covered by the detectors acceptance [36, 37]. They escape without being detected. There are two options for analyzing ISR events. Either the events are only partially reconstructed without the missing photon or only the small fraction of events with the photon inside the acceptance are analyzed. In order to add a third option, a small detector, specifically designed to detect ISR photons, is planned to be installed very close to the beam axis at BESIII. Limited space and extremely high background rates impose stringent requirements like a very compact design and capabilities to identify pile-up events.

The first topic of this thesis describes the development of such a detector with the main attention drawn to an FPGA based prototype data acquisition. In November 2017, a full prototype module was tested in a high rate beam test at MAMI in Mainz. Based on the recorded data, pile-up detection algorithms have been developed and optimized.

The second part of this thesis is dedicated to the analysis of the newly recorded BESIII data in the vicinity of the X(3872) mass. The best way to access the X(3872) state is the decay channel X(3872) $\to$ $\pi^+\pi^- J/\psi$. As a first step, the cross section of $e^+e^- \to \pi^+\pi^- J/\psi$ is extracted around the X(3872) mass. The second step is a Bayesian likelihood analysis of this cross section providing information on the electronic X(3872) width.

This thesis is organized as follows: the next Chapter gives an overview of the theoretical background. It starts with an introduction to the standard model of particle physics. Afterwards, the focus is set on the puzzles of the muon anomalous magnetic moment and of hadron spectroscopy in the charmonium system. A discussion follows on how they can be approached experimentally by electron positron collisions. Chapter 3 details the BESIII experiment and its physics program. Chapter 4 addresses the detector design for ISR photons to be placed at BESIII. The prototype beam test is described and results are presented. In Chapter 5, the analysis of $e^+e^- \to \pi^+\pi^- J/\psi$ at center-of-mass energies close to the X(3872) mass is detailed. The measured cross sections are used to search for

the resonant $X(3872)$ formation in electron positron annihilations. Chapter 6 concludes this thesis.

————

PHYSICS BACKGROUND
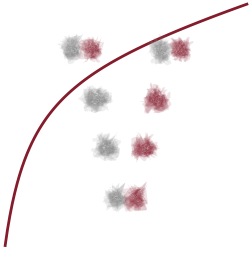
This Chapter lays the theoretical groundwork of this thesis. First, the great theoretical framework of the standard model of particle physics is introduced. Afterwards, the focus is set on two selected challenges in the non-perturbative regime of the strong interaction, namely the spectroscopy of charmonium (-like) states and the anomalous magnetic moment of the muon. The Chapter closes with experimental methods to approach those challenges using electron positron collisions.

2.1 *The Standard Model of Particle Physics*

THE theoretical basis of high energy physics is the standard model of particle physics (SM). It combines three of the four known fundamental forces (the electromagnetic, the weak, and the strong interaction) into one relativistic quantum field theory (QFT) acting at the most elementary level.[1] The whole theory is encoded in a Lagrangian density, from which the relevant equations of motions are derived. The SM Lagrangian exhibits a local gauge invariance corresponding to the symmetry group

$$SU(3)_C \times SU(2)_L \times U(1)_Y \quad , \tag{2.1}$$

reflecting the three incorporated interactions (cf. e.g. references [30, 42, 43]). The strong interaction has the $SU(3)$ color symmetry and the $SU(2)_L \times U(1)_Y$ is the symmetry group of the electroweak sector. It unifies weak and electromagnetic interactions.

The elementary particles are divided into fermions and bosons. Fermions have a spin of 1/2 and are the building blocks of matter. The gauge bosons (spin 1) mediate the interactions between

_____

[1]The fourth fundamental interaction, gravitation, is described by the classical field theory of general relativity [41]. So far, any attempt to quantize gravitation was unsuccessful.

Table 2.1: The twelve elementary fermions together with the interaction in which they take part.

	Generation			Takes part in interaction		
	I	II	III	Strong	Electromagnetic	Weak
Quarks	u	c	t	✓	✓	✓
	d	s	b	✓	✓	✓
Leptons	e^-	μ^-	τ^-		✓	✓
	ν_e	ν_μ	ν_τ			✓

Table 2.2: The gauge bosons with the interaction that they mediate. The spin J, parity P, and charge conjugation C quantum numbers are given as well as the interactions in which they take part. The weak gauge bosons are neither an eigenstate of the parity, nor of the charge conjugation operator. So, no P and C can be assigned. This also applies to the charge conjugation of the gluon g. The masses of the $W^\pm$ and the Z^0 bosons are experimental measurements taken from reference [30]

Boson	Mediates	J^{PC}	Takes part in	Mass / GeV
γ	EM	1^{--}		0
g	Strong	1^-	Strong	0
$W^\pm$	Weak	1	EM & Weak	80.379 ± 0.012
Z^0	Weak	1	Weak	91.1876 ± 0.0021

them. Additionally, there is the scalar (spin 0) Higgs boson. The twelve elementary fermions are further categorized into six quarks and six leptons (cf. Table 2.1). Three generations of fermions exist. A quark generation contains one up-type quark with an electric charge of $+2/3\,e$ and one down-type quark with $-1/3\,e$. The up-type quarks are the up, charm, and top quarks (abbreviated as u, c, and t) and the down type quarks are down, strange, and bottom (d, s, and b). The lepton generations (also called lepton families) are made from an electrically charged ($-1\,e$) and a neutral lepton called neutrino. The three charged leptons are e^-, μ^-, and τ^-. The neutrinos are labeled correspondingly ν_e, ν_μ, ν_τ. The gauge bosons (cf. Table 2.2) can be unambiguously assigned to one of the three interactions, which are described in the following.

2.1.1 Electromagnetic Interaction

The electromagnetic interaction is described by quantum electrodynamics (QED) obeying a $U(1)$ symmetry [30, 42–51]. It is mediated by the photon (γ), which couples to electric charge. Consequently, electrically neutral particles do not take part in the electromagnetic interaction. The photon itself carries no charge and is massless, which results in an infinite range of the interaction. At small momentum transfer, the coupling constant α is approximately 1/137.

2.1.2 Weak Interaction

In the weak interaction, there are charged current and neutral current interactions. They are mediated by the massive $W^\pm$ and Z^0 bosons, respectively [30, 42, 43].

The charged current interaction is maximally parity and charge conjugation violating: the $W^\pm$ boson couples only to left handed chiral particles and right handed chiral anti-particles. $W^\pm$ exchange is the only flavor changing process in the SM coupling a charged lepton to the corresponding neutrino or an up-type quark to a down-type quark. In the lepton sector, only transitions within a lepton family are possible, but with a universal coupling strength. Neutrino oscillations constitute an exception to this (cf. last paragraph). In the quark sector, all up-type quarks can convert into all down-type quarks with a non-universal coupling strength. This flavor-dependence is encoded in the Cabibbo-Kobayashi-Maskawa (CKM) matrix [52, 53]. It is a unitary 3×3 matrix with a total of four physical parameters. The CKM matrix can be viewed as a rotation in flavor space. It converts the down-type mass eigenstates d, s, and b into the weak flavor eigenstates d', s', and b'. The coupling of the weak eigenstates to the $W^\pm$ boson has now a uniform strength and is only allowed within one quark generation (e.g. ud' but not us'). One of the CKM matrix parameters is an imaginary phase, which introduces CP violation.

The neutral current interaction is very similar to the electromagnetic interaction, but the coupling depends on the electric charge and the chirality. The neutral current also violates parity and charge conjugation.

The strength of weak couplings are comparable to the electromagnetic, but the massive gauge bosons render the interaction weak (hence the name) at momentum transfers much smaller than the

masses $m_{W^\pm}$, m_{Z^0}. In other words, the weak interaction is very short ranged.

Similar to the down-type quarks, the neutrino flavor eigenstates are not equal to the mass eigenstates. Analogously to the CKM matrix, the Pontecorvo–Maki–Nakagawa–Sakata (PMNS) matrix describes the transformation between the two bases [54–56]. An effect is the neutrino flavor oscillation: a neutrino is produced with a defined flavor, travels a certain distance, and is detected having a different flavor. For a long time neutrinos have been thought to be massless. However, the experimental observation of neutrino oscillation implies a non-zero mass for at least two of the three neutrinos.[2]

2.1.3　Electroweak Unification

A great success on the way to a grand unifying theory is the unification of the electromagnetic and the weak interaction by Glashow, Salam, and Weinberg [57–60]. It introduces the concept of weak isospin I_w and weak hypercharge Y. All left handed chiral fermions are grouped into $I_w = 1/2$ doublets according to the lepton families and quark generations. The right handed chiral particles build $I_w = 0$ singlets. The weak hypercharge is constructed from the third component of I_w and the electric charge: $Y = 2Q - I_w^3$. The symmetry groups are $SU(2)_L$ and $U(1)_Y$, where L denotes the required left handed chirality. The massless gauge bosons are arranged in a weak isotriplet W^k ($k = 1, 2, 3$) and a singlet B^0.

The W^3 and the B^0 bosons mix and result in the Z^0 boson and the photon γ. After spontaneous symmetry breaking by the scalar Higgs field, the Z^0 boson acquires mass, while the photon remains massless [61–65]. The W^1 and W^2 bosons recombine into the $W^\pm$ bosons, which also acquire mass. They are related to ladder operators of the weak isospin. The non-zero vacuum expectation value of the Higgs field manifests in the scalar Higgs boson H^0. It also provides a way to give mass to the initially massless fermions via a Yukawa coupling.

Thanks to the Glashow-Salam-Weinberg unification, the couplings to the photon and the $W^\pm$ and Z^0 bosons can be related to each other.

---

[2]Some physicists do not regard massive neutrinos and neutrino oscillations as part of the SM. In some sense, these phenomena can be viewed already as physics beyond the SM.

2.1.4   *Strong Interaction*

The strong interaction is described by quantum chromodynamics (QCD) with the $SU(3)$ symmetry [30, 42, 43, 66]. The charge of QCD is called color, which can attain red, green, and blue (r, g, and b) with the corresponding anti-colors anti-red, anti-green, and anti-blue (r̄, ḡ, and b̄). From the group of fundamental fermions, only quarks carry color, anti-quarks have anti-color. The gauge bosons mediating the strong interaction are gluons coupling to (anti-) color. The fact that $SU(3)$ is non-abelian, leads to the self-interaction of gluons: they simultaniously carry a color and an anti-color, of which eight different combinations are allowed.

No free quarks have been observed. They are bound in colorless hadrons, where the three colors rgb together result in "white" = colorless, or color-neutral. Such a configuration needs to be made from three quarks. They are called baryons and the proton and the neutron are the most prominent representatives as they are the constituents of atomic nuclei. Another possibility to obtain a color-neutral state is the combination of a color with its anti-color (rr̄, gḡ, or bb̄). Accordingly, these states contain a quark and an antiquark and are called mesons. Pions, Kaons, etc. belong to this species.

As gluons are colored, they are not allowed to travel freely either. In principle, two or more gluons could form a colorless object being referred to as a glueball. Similarly, the combinations of two quarks with two anti-quarks or four quarks with one anti-quark could be colorless. These tetraquarks and pentaquarks as well as the glueballs are labeled exotic. There is some evidence for the existence of exotic hadrons, but they have not been identified unambiguously. The phenomenon of quarks being always bound in colorless objects is called confinement [30, 42, 43]. It is believed to be closely linked to the self-interaction of gluons. However a definite proof of this hypothesis is still pending.

Other than that, it is clear that the self-interaction defines the behavior of the running coupling constant α_s shown in Figure 2.1 as a function of the momentum transfer. For large momentum transfers (small distances), α_s is sufficiently small to allow perturbative calculations. In the limit of infinite momentum transfer (zero distance), α_s vanishes and the quarks move freely [67–69]. This is termed asymptotic freedom. On the contrary, the coupling constant becomes large at small momentum transfers [30, 70], too large for a perturbative
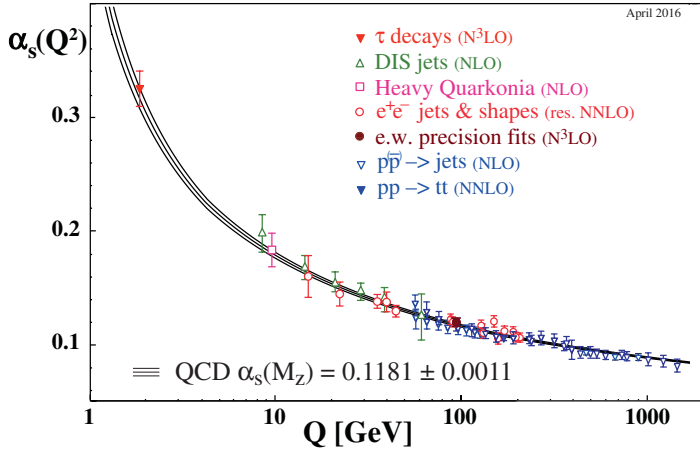
Figure 2.1: Running of the strong coupling constant, taken from reference [30].

series to converge. Non-perturbative methods have to be developed to make reliable predictions in the low energy region of QCD.

2.2   Low Energy QCD

2.2.1   The Need for non-perturbative Methods

The equations of motion of interacting QFTs (such as the SM interactions) are highly non-linear and the search for analytical closed-form solutions is a lost cause. A very powerful tool is perturbation theory, where the solution is expanded into a series with increasing orders of the coupling constant. When the coupling constant is small, the series converges quickly and higher orders can be neglected. A beautiful demonstration is the prediction of the magnetic moment of the electron. The theoretical calculation yields a value with a relative deviation to the experimental measurement of only 10^{-11} [71–73]. It is considered as the most stringent test of QED.

Perturbation theory can be applied to QCD only at large momentum transfers, where the coupling constant is small [74]. Predictions agree well with experimental measurements of inclusive observables like multiplicities and angular distributions of multi-jet events in

high energy collisions, e.g. at the LHC.[3] A fully inclusive observable is the so-called R-value, the cross section ratio of hadron and di-muon production in e^+e^- collisions:

$$R = \frac{\sigma(e^+e^- \to \text{hadrons})}{\sigma(e^+e^- \to \mu^+\mu^-)} \quad , \tag{2.2}$$

where the dimuon cross section is not the experimental value, but the lowest order QED calculation. It is given by $4\pi\alpha^2/3s$ with s being the squared center-of-mass energy. The comparison between the experimental measurements and the predictions of perturbative QCD are shown in Figure 2.2. While the theoretical prediction sufficiently describes the data at large center-of-mass energy $\sqrt{s}$, it only reproduces the order of magnitude at low $\sqrt{s}$. It completely fails to describe the hadronic resonances as can be seen in the charmonium region and below.

In order to predict the observables of low-q^2 QCD, in particular confinement and the hadron spectrum, non-perturbative methods are developed and applied. A very successful one is lattice QCD [4, 30]. It discretizes space time into a finite, four dimensional Euclidean grid (lattice). This approximation has the benefit that the number of possible field configurations becomes finite and the path integrals can be calculated numerically.[4] Continuum QCD is recovered in the limit of zero lattice spacing and infinite lattice volume. As this limit approaches, the required computing power increases to the point, where only supercomputer farms can produce accurate results. Despite the arising difficulties, such as the explicit breaking of Lorentz invariance due to the discrete space time, lattice QCD predictions become better and better. The mass spectrum of the light hadron ground states is reproduced at the few percent level [5–7].

Lattice QCD is complemented by a different approach to non-perturbative QCD that has evolved in parallel. Dyson-Schwinger

---

[3]In spite of the low-q^2 hadronization following all hard scattering processes in QCD, the non-perturbative corrections to inclusive observables are small.

[4]The expression that comes closest to a "solution" of a QFT, is the corresponding partition function or generating functional [45, 75]. All Green's functions of the theory can be obtained as derivatives of the partition function. It contains path integrals, which are integrals over all possible (uncountable infinite) paths connecting two points. In a discretized, finite volume, however the number of paths (also called configurations) is finite.
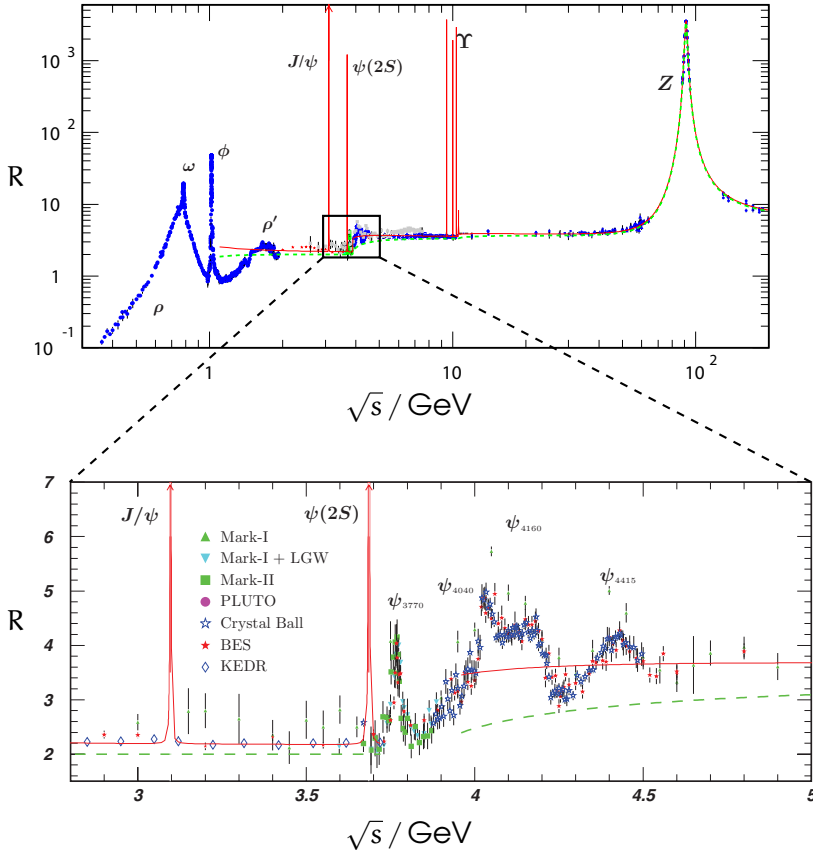
Figure 2.2: R-value as a function of the center-of-mass energy $\sqrt{s}$. The lower panel shows a zoomed in view of the τ-charm region. The points with error bars are measurements by several experiments and the red lines are the three-loop perturbative QCD predictions with the addition of the narrow charmonium (ψ) and bottomonium (Υ) resonances. The dashed green line is the naive quark model prediction only considering the three different colors as well as the charges of the quarks that are available at a certain $\sqrt{s}$. The different hadronic resonances are clearly noticeable in the charmonium region and below, adapted from reference [30].

and Bethe-Salpeter equations represent functional differential equations for the Green's functions of the relevant fields [8–12]. In principle, there are infinite many such equations, but after a truncation, only a finite number is taken into account. The contributions beyond this truncation needs to be modeled or extracted from lattice QCD. Functional methods are able to reproduce the experimentally observed mass spectrum of light hadrons even for excited states which is one of the weak spots of lattice QCD [13–16].

2.2.2 *Charmonium Spectroscopy*

Charmonia are mesons composed of a charm and an anti-charm quark. Similarly to the positronium system (e^+e^- bound state), different combinations of spin and orbital angular momentum result in different masses of the state (fine and hyperfine structure). Therefore, charmonium is also referred to as positronium of QCD. Due to the heavy mass of the charm quark ($\approx 1.3\,\text{GeV}$ [30]), the mass splittings in the charmonium system are much larger and the different states are labeled with individual names. The charmonium mass range is roughly between $3\,\text{GeV}$ and $4.5\,\text{GeV}$. Figure 2.3 depicts the level scheme of charmonium. The individual columns indicate the quantum numbers J^{PC}.

The charmonium system is well suited to test QCD because it meets both the perturbative and the non-perturbative regime of QCD. The hard scale is at the order of the quark mass m_c, which itself is large in comparison to Λ_{QCD} and hence in the perturbative region. The soft and ultra soft scale are given by the relatively low momenta and kinetic energies of the quarks, which live in the non-perturbative region [20]. In addition, the relatively high mass of the charm quark compared to the charmonium mass enables the use of non-relativistic effective field theories.

The simplest model of charmonium is the positronium-inspired movement of two non-relativistic quarks in a potential. Solving the Schrödinger equation yields the charmonium spectrum. Different parameterizations of the potential have been considered. The so-called Cornell potential [77, 78] has proven to be very successful. It has the semi-empirical form

$$V^{(c\bar{c})}(r) = -\frac{4}{3}\frac{\alpha_s}{r} + b\,r \quad , \tag{2.3}$$
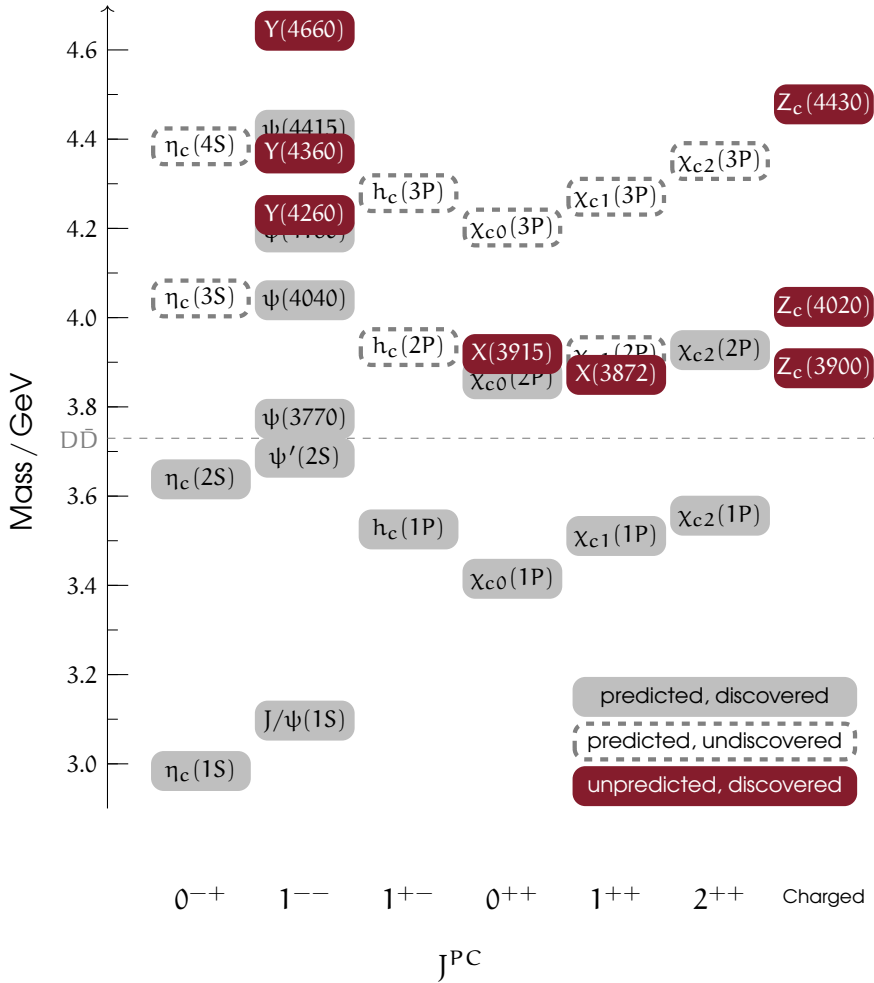
Figure 2.3: Charmonium level scheme ordered by the quantum numbers J^{PC}. The dashed horizontal line marks the open-charm threshold. The gray boxes correspond to established charmonium states. States that have been predicted, but not yet observed, are indicated by the dashed bound boxes. Exotic charmonium-like states are represented by red boxes. They have been observed unexpectedly. The $Z_c(3900)$ and $Z_c(4020)$ states in the last column exist not only in the charged, but also in a neutral state as part of an isospin triplet. The observed masses are taken from reference [30] and the predicted but unobserved masses are taken from reference [76].

with the Coulomb-like term proportional to α_s and a linear term proprtional to the "string constant" b. The potential is constantly growing with increasing radius r ensuring confinement. In this model, α_s, b, and also the charm quark mass m_c are parameters that need to be fitted to experimental data. Nevertheless, after taking additional terms responsible for the spin-spin, spin-orbit, and tensor interactions into account, very accurate results are obtained for the whole charmonium spectrum [76].

In the framework of potential non-relativistic QCD (pNRQCD), a potential for the charmonium system can be derived rigorously from first principles [19, 20]. The Lagrangian is expressed as a series in powers of $1/m_c$ and the hard scale is integrated out perturbatively. With increasing orders of $1/m_c$, the resulting potential shows strong similarities with the phenomenological Cornell potential. Even the static quark anti-quark potential as extracted from lattice QCD agrees with the Cornell model [79, 80].

Apart from the potential, lattice QCD can predict the charmonium spectrum directly [81, 82]. Similarly, functional methods are implemented to predict the spectrum [83, 84]. These two fully non-perturbative approaches are able to reproduce the general structure of the spectrum, but are surprisingly outperformed by the simple Cornell model when it comes to precision, in particular for higher lying states.

Replacing the (anti-) charm quark by an (anti-) bottom quark, one arrives in the bottomonium system at masses in the range of 9.4 to 11 GeV. Here, all the above mentioned techniques can be applied as well. The heavier bottom quark ($\approx 4.2\,\text{GeV}/^2$ [30]) makes it even easier to justify the non-relativistic approximations. The bottomonium level scheme is very similar to the one of charmonium. A toponium system does not exist because the extremely heavy top quark decays before it can form hadrons ($m_t \approx 173\,\text{GeV}$ [30]).

2.2.3 *Exotic Charmonia*

In 2003, the Belle Collaboration reported the discovery of a narrow resonance with a mass of 3872 MeV in the $\pi^+\pi^- J/\psi$ subsystem of the $B^\pm \rightarrow K^\pm \pi^+ \pi^- J/\psi$ decay [21]. Because this state does not match the expectation for a conventional charmonium state above the open-charm threshold, it was just called X(3872) and labeled charmonium-like. Over the years, other unexpected particles have

been discovered in the charmonium mass region being named Y and Z states giving birth to the field of XYZ physics. Some of which carry electric charge being inherently incompatible with a pure $c\bar{c}$ picture. Selected reviews can be found in references [27–29]. By now, a commonly accepted nomenclature assigns the name X followed by its parenthesized mass in MeV to all neutral states with non-vector quantum numbers. The ones with vector quantum numbers ($J^{PC} = 1^{--}$) are called Y states and the charged states[5] are called Z states, sometimes with the subscript c indicating the charmonium-likeliness: Z_c. The established exotic charmonium-like XYZ states are shown in Figure 2.3 as red boxes. However, the Particle Data Group (PDG) follows a different naming convention.[6]

Why are they considered incompatible with the quark model predictions for a $c\bar{c}$ meson? For the charged Z_c states, the answer is trivial: because a pure $c\bar{c}$ compound must be electrically neutral. The X and Y resonances simply have no corresponding charmonium predictions. Furthermore, they are relatively narrow and decay much more often to charmonia than expected from $c\bar{c}$ states above the open-charm threshold. They would decay almost entirely to open-charm final states like the $\psi(3770)$ resonance with $\mathcal{B}(\psi(3770) \to D\bar{D}) = 93\%$ [30]. Moreover, an overpopulation of the 1^{--} spectrum is observed (cf. Figure 2.3). The predicted vector charmonia have been discovered, leaving no unassigned $c\bar{c}$ state for the newly discovered ones. An interesting relation among the X, Y, and Z states is that there is evidence for the decay $Y(4260) \to \pi^\pm Z_c(3900)^\mp$ as well as for $Y(4260) \to \gamma X(3872)$ [25, 86].

In order to form a narrow charged state in the charmonium mass region, the Z_c states need to contain at least four constituent quarks. The true nature of the XYZ states is unclear and subject of dispute in the theorist community. The following pictures are being discussed, of which all (but the last one) go beyond the simple quark model. Although there has not been any unambiguous assignment to experimentally observed resonances, there is no plausible reason why they should not be allowed in QCD.

---

[5]Or neutral states that are isospin partners of charged states.

[6]The current Review of Particle Physics (2018) assigns the names of conventional charmonia when possible [30]. The Y states are called $\psi(\dots)$ and the X(3872) state is referred to as $\chi_{c1}(3872)$. In the previous review (2016), all XYZ states were called $X(\dots)$ [85].

Meson molecules are conventional (colorless) mesons bound by residual QCD interactions via meson exchange, just like the deuteron is a bound state of two baryons [87–90]. Due to their relative low binding energy, they are expected to have a mass closely below the corresponding two-meson threshold.

Compact tetraquarks can be thought of as a tightly bound four-quark state. Often, it is assumed to be formed from a diquark anti-diquark pair $(cq)(\bar{c}\bar{q})$, where q stands for any light quark flavor [91–93]. The diquarks itself are colored and a color neutral state is only obtained in the combination with the anti-diquark. Most models use an effective Hamiltonian for the (anti-) diquarks, but also the employment of Bethe-Salpeter equations predicts bound four-quark states. In the latter case however, the meson-meson interactions dominates over the diquark-anti-diquark interaction [94–96].

Hadro-charmonium can be viewed as a central conventional charmonium state embedded in a cloud of light hadrons [97]. The dissociation of the core and the cloud would result in the decay to a lower lying charmonium state and additional light hadrons, as has been observed for many XYZ states. However, the observed open-charm decays impose difficulties for this model.

Hybrids are mesons with an additional (excited) valence gluon [98, 99]. Lattice QCD predicts the lightest charmonium hybrid multiplet in the mass region of $\approx 4.2\,\text{GeV}$, of which one member has 1^{--} quantum numbers making the Y(4260) state a candidate [100].

Glueballs are hadrons formed just by gluons caused by their self-interaction. Glueballs are not considered as candidates for the charmonium-like exotics because of their expected flavor-blind decays. Carrying no (hidden) flavor, glueballs should decay to different flavored final states with comparable probabilities. In contrast, the XYZ states show a strong affinity to the charm quark. So far, no XYZ decay has been observed to a final state without a charm quark. Glueballs are mostly searched for in the light hadron sector. They emerge naturally in non-perturbative QCD via lattice QCD [101, 102] as well as via functional methods [103].

Threshold effects could mimic a resonance without the necessity for a pole in the S-matrix [104–106]. The $Z_c(3900)$ and $Z_c(4020)$ states have a mass just above the $\bar{D}^*$ and $D^*\bar{D}^*$ threshold incompatible with the molecule interpretation. Instead of any of the above bound state hypotheses, a rescattering process is a purely kinematic effect that could produce a cusp close to (and also above) threshold [107, 108].

Bottomonium-like exotics have also been observed [109]. The XYZ nomenclature and the discussed models can be applied by just exchanging the charm quark (D meson) with the bottom quark (B meson). Furthermore, a pentaquark candidate has been discovered at LHCb [110]. The above discussed pictures can be easily extended to the baryon sector (baryon-meson molecule, compact pentaquark, hybrid baryon, etc.).

The field of XYZ studies illustrates nicely that the naive quark model is insufficient for describing the rich spectrum of hadrons. QCD is the well established theory of the strong interaction, yet far from understood in its full glory.

2.2.4 *The* X(3872) *Resonance*

The observation of the X(3872) resonance by the Belle Collaboration in 2003 [21] and its quick confirmation by other experiments [22, 86, 111–114] mark the beginning of XYZ spectroscopy. The X(3872) state is probably the most famous and also the best studied representative of charmonium-like exotics. It has been observed in B decays [21, 22, 113], very likely in radiative transitions of the Y(4260) resonance [86], as well as in inclusive pp [113, 114] and p$\bar{\text{p}}$ collisions [111, 112]. In addition to the discovery channel of X(3872) $\rightarrow \pi^+\pi^- J/\psi$, where the pion pair forms a ρ^0, it has been seen in five other decay channels. They are X(3872) $\rightarrow \gamma J/\psi$ [115, 116], X(3872) $\rightarrow \gamma\psi'$ [116, 117], X(3872) $\rightarrow \omega J/\psi$ [118], X(3872) $\rightarrow D^0\bar{D}^{*0}$ + c.c. [119–121] and X(3872) $\rightarrow \pi^0\chi_{c1}$ [122]. The quantum numbers of the X(3872) state have been determined to be 1^{++} [123, 124].

Both its mass and width are remarkable. The mass ($(3871.69 \pm 0, 17)$ MeV) is right at the $D^0\bar{D}^{*0}$ threshold ((3871.68 ± 0.07) MeV), the main decay channel with a branching ratio above 30 % [30]. Therefore, it is a prime candidate for a $D^0\bar{D}^{*0}$ molecule. There are

many models that predict a loosely bound $D^0\bar{D}^{*0}$ molecule with the correct quantum numbers 1^{++} [125–127]. Such a molecule is an extended object with a radius of several fm (comparable to atomic nuclei). The same models do not allow a bound $D\bar{D}$ state, which is in accordance with the non-observation of a resonance at the $D\bar{D}$ threshold. Furthermore, the threshold of the charged $D^{\pm}\bar{D}^{*\mp}$ is about 7 MeV higher than the $X(3872)$ mass, so the molecule only has a subleading $D^{\pm}\bar{D}^{*\mp}$ component. The arising isospin breaking is reflected in the observed decay channels ($\rho^0 J/\psi$ vs. $\omega J/\psi$).

The main counterargument against the molecule hypothesis is the abundant prompt $X(3872)$ production at high transverse momenta in hadronic collisions [128, 129]. The production cross section is several orders of magnitude larger than that of other molecule-like objects like deuterons [29]. If the $X(3872)$ is a molecule, its constituents have to be produced very closely in phase space first in order to deexcite into a bound molecule. Therefore, its production cross section would be significantly lower than observed [130]. However, the study of XYZ states is a very active field and this counterargument is questioned in return [131]. In the end, the nature of the $X(3872)$ state is still a mystery and various pictures are discussed. Even the prosaic interpretation as the conventional χ'_{c1} state is up to debate [132]. One should not forget the possibility of a superposition of different models. A mixture of the conventional χ'_{c1} state with a $D^0\bar{D}^{*0}$ molecule may account for the aforementioned properties [133–135].

A key parameter of the $X(3872)$ state is its width, which is extraordinarily narrow. Currently, only an upper limit of 1.2 MeV at 90 % confidence level is known [31]. Its precise measurement is crucial for the clarification of the $X(3872)$'s inner structure. Another important quantity is the electronic width. It is directly proportional to the formation cross section of the $X(3872)$ resonance in e^+e^- annihilations. The $J^{PC} = 1^{++}$ quantum numbers require at least two virtual photons in the Feynman diagram for $e^+e^- \rightarrow X(3872)$ leading to a strong suppression of this reaction. From this point of view, it is clear that the size of the electronic width is very small. The exact value, however, might provide insight into the inner structure of the $X(3872)$ state. The interplay between the non-hadronic initial state (e^+e^-) with the exotic $X(3872)$ hadron surely is different for an extended object like a molecule than for the conventional $c\bar{c}$ state χ'_{c1}.

2.2.5 *Hadronic Contribution to the Anomalous Magnetic Moment of the Muon*

At first glance, the magnetic moment of the muon is a purely electromagnetic property that has nothing to do with the strong interaction. A closer look reveals, however, that QCD indeed contributes to the magnetic moment via quantum loop corrections, in particular in the non-perturbative regime.

Any electrically charged particle with spin has a magnetic moment. For the muon, it is given by

$$\vec{M} = g_\mu \frac{e}{2m_\mu} \vec{S} \quad , \tag{2.4}$$

with the elementary charge e, the muon mass m_μ, and the spin $\vec{S}$. Neglecting quantum corrections (as in Dirac theory), the gyromagnetic ratio g_μ is exactly 2 [136, 137]. The deviation is parameterized as the anomalous magnetic moment

$$a_\mu = \frac{g_\mu - 2}{2} \quad . \tag{2.5}$$

It is an interesting body of research because both experiment [40] and theory [138] obtain very precise values. The comparison of the two is a precision test of the SM. The accuracy has reached a level at which contributions from the weak and the strong interactions play a role as well. Figures 2.4(a) - (c) show the corresponding QED Feynman diagrams in leading order (LO), nexto-to-LO (NLO), and next-to-NLO (NNLO), respectively. For the NNLO level, there are actually seven different diagrams, of which only one is shown. The current QED prediction is calculated at the N^5LO level. The weak contribution is calculated at two-loop order. Two different contributions of QCD are depicted in the Feynman diagrams in Figure 2.4(d) and (e). The first one is the hadronic vacuum polarization (HPV) and the second one is the hadronic light-by-light scattering (HLbL). Both contributions are dominated by the non-perturbative regime of QCD. They can be obtained via lattice QCD [139–141] and Dyson-Schwinger equations [142], both of which have significant uncertainties. While those methods are maturing, other approaches are applied using experimental inputs.

The $(\gamma^* \rightarrow \text{hadrons} \rightarrow \gamma^*)$ process in the HVP diagram can be linked to the $(\gamma^* \rightarrow \text{hadrons})$ reaction using the optical theorem.
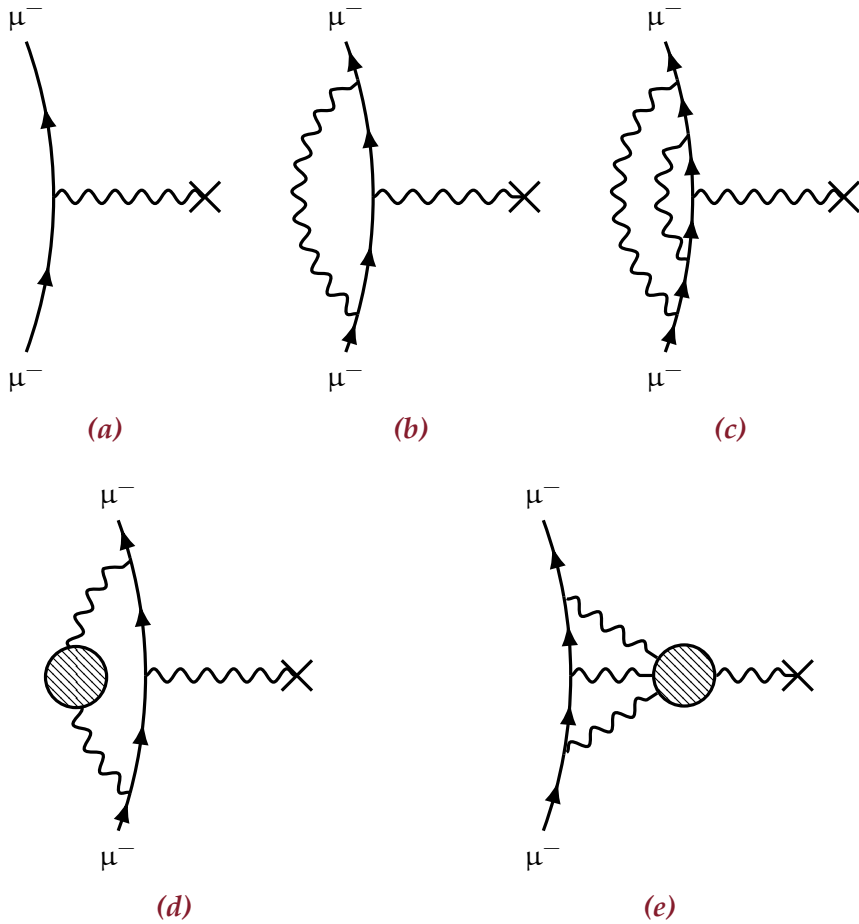
Figure 2.4: Feynman diagrams contributing to the magnetic moment of the muon. The cross represents the external magnetic field to which the muon couples. *(a)* LO QED diagram. *(b)* NLO QED diagram. *(c)* One exemplary NNLO QED diagram. *(d)* HVP diagram. *(e)* HLbL diagram. The blob stands for hadronic interaction, see text for description.

Table 2.3: Comparison between theoretical and experimental values of a_μ [30, 38–40]. The individual contributions to the SM prediction are listed as well.

Contribution	Value $\times 10^{11}$	Uncertainty $\times 10^{11}$
a_μ^{QED}	116 584 718.95	0.08
a_μ^{EW}	153.6	1.0
a_μ^{HVP}	6 845	34
a_μ^{HLbL}	105	26
a_μ^{SM}	116 591 823	43
a_μ^{exp}	116 592 091	63

Consequently, the HVP contribution can be obtained from the earlier mentioned R-value (cf. Section 2.2.1 and Figure 2.2) via a dispersion integral. It turns out that the low-$\sqrt{s}$ region dominates. The ρ^0 resonance alone makes up about 75 % [38]. In a similar fashion, the HLbL contribution can be related to the so-called hadronic transition form-factors encoding the coupling of $(\gamma^*\gamma^* \to \text{hadrons})$ [143].

Table 2.3 lists the different contributions to the SM prediction and compares it with the experimental value. The difference is

$$a_\mu^{\text{exp}} - a_\mu^{\text{SM}} = 268 \pm 76 \quad , \tag{2.6}$$

a deviation of 3.5 σ. The theoretical uncertainty is clearly dominated by the uncertainty of the hadronic contribution, which itself can be traced back to the input from experiment. Still, the uncertainty of a_μ^{exp} is about 50 % larger than that of the theoretical value, but a new experiment is currently running, which is expected to bring the uncertainty down by a factor of four [144–146].

2.3 Probing Non-Perturbative QCD in Electron Positron Collisions

In contrast to pp or p$\bar{\text{p}}$ collisions like at $\overline{\text{P}}$ANDA [147], electron positron collisions have the advantage of providing a very clean environment for the study of non-perturbative QCD.[7] Electrons and

---

[7]Of course, hadron colliders have advantages as well. First and foremost, the hadron production cross sections are much larger. Furthermore, (anti-) proton beams can be cooled resulting in a very small momentum spread. In particular, $\overline{\text{P}}$ANDA will benefit from a cooled $\bar{\text{p}}$ beam [147].
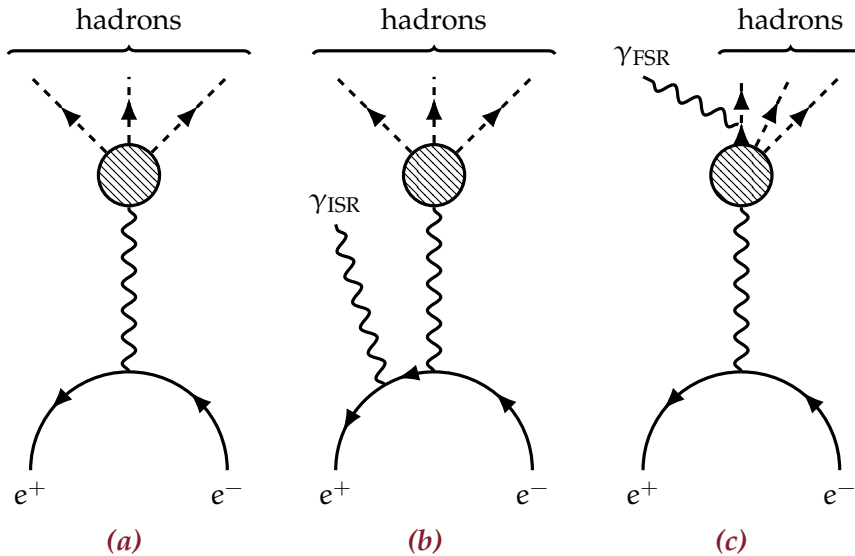
Figure 2.5: Feynman diagrams with one virtual photon for hadron production in e^+e^- collisions with. The blob represents hadronic interaction. *(a)* Lowest order diagram. *(b)* Radiative correction in the form of initial state radiation (ISR) and *(c)* final state radiation.

positrons have no substructure, so the initial state taking part in the hard scattering process is well defined, as opposed to proton (anti-) proton collisions. The leading Feynman diagram describing hadron production in e^+e^- collisions is shown in Figure 2.5(a). For center-of-mass energies much smaller than the Z^0 mass (91 GeV), the weak contribution is negligible.

2.3.1 *Charmonium Production*

In leading order, the Feynman diagram contains a single virtual photon. Because the electromagnetic and the strong interaction conserve parity and charge conjugation, and thanks to the always present conservation of angular momentum, the final state has to carry the vector quantum numbers of the virtual photon, which are 1^{--}. As a consequence, only vector resonances can be produced in formation via a single virtual photon. In the charmonium system, they correspond to the second column of Figure 2.3. As one can see in

Figure 2.2, the R-value has massive spikes at the J/ψ and ψ' masses, indicating a very large cross section for their formation. Consequently, large amounts of J/ψ and ψ' events can be recorded in e^+e^- annihilations. Charmonia with other quantum numbers can be produced either in association with other particles, e.g. in the reactions $e^+e^- \to \pi^+\pi^- h_c$ [148] and $e^+e^- \to \omega\chi_{cJ}$ ($J = 0, 1, 2$) [149], or they can be produced in decays of other vector charmonia, e.g. $\psi' \to \pi^0 h_c$ [150], $\psi' \to \gamma\chi_{cJ}$ ($J = 0, 1, 2$) [151], $\psi' \to \gamma\eta_c'$ [152], or $J/\psi \to \gamma\eta_c$ [153].

Exotic charmonium-like XYZ states can be studied very well at e^+e^- colliders. The Y states already carry the necessary 1^{--} quantum numbers. Furthermore, many Z_c states are produced in the $e^+e^- \to \pi Z_c$ reaction [25, 154–157] and the $e^+e^- \to \gamma X(3872)$ production mechanism has been observed [86, 122].

2.3.2 Initial State Radiation

Of course, there are higher order processes happening in e^+e^- collisions. The two diagrams in Figures 2.5(b) and (c) depict reactions with the emission of a real photon. The additional vertex introduces a suppression in the order of $\alpha \approx 1/137$ compared to the leading order diagram. The first process is called initial state radiation (ISR) because the photon is emitted from a lepton before the annihilation. Analogously, the second process is termed final state radiation (FSR). The probability for those processes is of the order $\ln(s/m^2)$, with m being the mass of the radiating particle. Due to the relatively large masses of hadrons compared to electrons, FSR only plays a subordinate role [36].

The emission of an ISR photon with the energy $E_{\gamma\text{ISR}}$ lowers $\sqrt{s}$ to an effective center-of-mass energy $\sqrt{s'}$ at the annihilation vertex:

$$\sqrt{s'} = \sqrt{s - 2\sqrt{s}E_{\gamma\text{ISR}}} \quad . \tag{2.7}$$

In other words, the hadronic system is not produced at $\sqrt{s}$, but a lower $\sqrt{s'}$, which lies in the interval between the threshold of the specific final state and the original $\sqrt{s}$. Additionally, the hadronic system experiences a boost in the opposite direction of the emitted photon. Considering a final state X_i, QED is able to give a simple relation between the non-radiative cross section ($e^+e^- \to X_i$) and

the $\sqrt{s'}$-differential radiative cross section ($e^+e^- \to \gamma_{ISR}X_i$):

$$\frac{d\sigma_{rad}(\sqrt{s})}{d\sqrt{s'}} = \frac{2\sqrt{s'}}{s}W(x,s)\sigma_{nonrad}(\sqrt{s'}) \quad , \qquad (2.8)$$

where $W(x,s)$ is the angular integrated radiator function with the substitution $x = 2E_{\gamma_{ISR}}/\sqrt{s} = 1 - s'/s$ [36]:

$$W(x,s) = \frac{\alpha}{\pi x}\left(\ln\frac{s}{m_e^2} - 1\right)(2 - 2x + x^2) \quad . \qquad (2.9)$$

Since $x < 1$, the x-dependence is dominated by the $1/x \propto 1/E_{\gamma_{ISR}}$ term, as expected. For the sake of completeness, the full angular-dependent radiator function is given as well [36, 37]:

$$w(\theta,x) = \frac{\alpha}{\pi x}\left[\frac{\left(1 - x + \frac{x^2}{2}\right)\sin^2\theta - \frac{x^2}{2}\sin^4\theta}{\left(\sin^2\theta + \frac{4m_e^2}{s}\cos^2\theta\right)^2}\right.$$
$$\left. - \frac{4m_e^2}{s}\frac{(1 - 2x)\sin^2\theta - x^2\cos^4\theta}{\left(\sin^2\theta + \frac{4m_e^2}{s}\cos^2\theta\right)^2}\right] \quad , \qquad (2.10)$$

with θ being the polar angle measured with respect to the beam axis. The most important features are the extreme maxima at $\theta = 0°$ and $\theta = 180°$, outside the typical detector acceptance. For $\sqrt{s} = 3.770\,\text{GeV}$ and an angular acceptance of $|\cos\theta| < 0.93$ (conditions at the BESIII experiment, see next Chapter), the probability of an ISR photon to be detected varies from 15 to 20 %, depending on the energy of the ISR photon.

When one wants to measure a certain cross section of $e^+e^- \to X_i$, there is always a small irreducible background from $e^+e^- \to \gamma_{ISR}X_i$, in particular, if the energy of the radiated photon is comparable to the detectors energy resolution (i.e. small). Then, the ISR process looks like the non-radiative reaction, even after requiring energy and momentum balance of the initial e^+e^- state and the final state X_i. Thanks to the above relation in equation (2.8), a correction factor $(1 + \delta)$ can be defined, which in combination with the reconstruction efficiency ϵ converts the visible cross section into the true non-radiative cross section [36]:

$$\sigma_{nonrad} = \frac{\sigma_{vis}}{\epsilon(1 + \delta)} \quad . \qquad (2.11)$$

It is important to note that the efficiency itself depends on the energy distribution of the ISR photons.

The idea to make use of ISR is rather old [37], but only modern high-luminosity experiments are able to compensate for the suppression compared to the non-radiative process. The idea behind the ISR technique is to measure $e^+e^- \rightarrow \gamma_{ISR}X_i$ and to use equation (2.8) to infer the cross section of $e^+e^- \rightarrow X_i$ for each $\sqrt{s'} \in (E_{theshold}, \sqrt{s})$ simultaneously. The obvious drawback of the aforementioned suppression stands against a whole series of advantages. In order to scan a certain range of center-of-mass energies without using ISR, the accelerator settings need to be changed between each scan point. At different points, the accelerator performance changes and systematic uncertainties vary, e.g. the luminosity needs to be determined at each point individually. In ISR operation, the accelerator can run at a fixed setting that does not need to be changed, increasing the efficiency of data taking. Furthermore, the ISR technique gives access to a continuous spectrum of $\sqrt{s'}$, resolving narrow structures that might be hidden between two scan points.[8] Additionally, with the ISR technique, effective center-of-mass energies far below the accelerators specification are available that cannot be reached by a scan. Another advantage of the ISR technique is the measurement directly at the production threshold for a certain reaction. In a direct scan at threshold, the produced hadrons are basically at rest and cannot reach the detector. In an ISR event, the hadronic system is boosted opposite to the photon and hence can be detected even with $\sqrt{s'}$ directly at threshold. The most important advantage of the ISR technique is that it comes for free. Data sets recorded at 3.770 GeV with the intention to produce abundantly D mesons can be analyzed with the ISR technique as well. Hence, the number of different analysis targets associated with a data sample is increased, and so is the physics outcome.

Due to the high probability of the ISR photons to be emitted at small angles with respect to the e^+e^- beam line, there are two different event topologies, cf. Figure 2.6. In the tagged topology, the photon is detected by the electromagnetic calorimeter. In the untagged topology, the photon escapes outside the detectors acceptance and its energy and direction needs to be inferred from the momentum

---

[8]The detector performance still needs to be good enough to resolve the narrow structures.
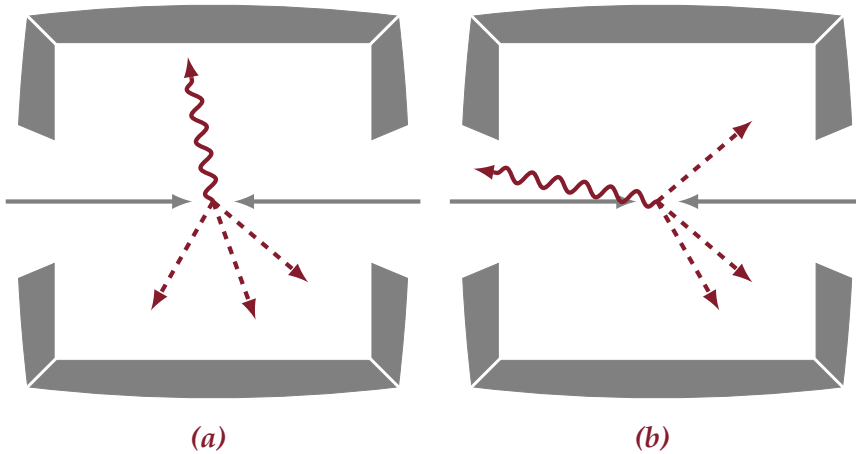
Figure 2.6: Topologies of ISR events. The horizontal gray arrows indicate the incident e^+e^- pair and the gray area represents the cross sectional geometry of a typical electromagnetic calorimeter. The wiggly arrow stands for the ISR photon and the dashed arrows are hadrons. *(a)* The photon is detected by the calorimeter. This is termed a tagged ISR event. *(b)* Untagged topology, i.e. the ISR photon is outside the detectors acceptance and cannot be detected. In $\geqslant 80\,\%$ of the times, the photon is emmited in an untagged topology.

balance of the initial and partly reconstructed final state. As already mentioned, the probability of an untagged topology is $\geqslant 80\,\%$ [36].

The applications of the ISR technique is based on the previously discussed advantages. The high precision measurements of $e^+e^- \to$ hadrons cross sections as a function of center-of-mass energy leads to an improved knowledge of the R-value and ultimately to a better understanding of the hadronic contribution to the anomalous magnetic moment of the muon. Furthermore, timelike nucleon form factors can be measured, which are important nucleon structure observables [158–161]. In particular, the measurement of the $e^+e^- \to n\bar{n}$ is quite challenging because of the difficult detection of the neutron [162].[9] The tagged ISR photon with its accurately measured four momentum brings an additional constraint into the equation, simplifying the whole measurement. Moreover, with the

---

[9]The anti-neutron, however, has the clear signature of the annihilation with a neutron of the detector material.
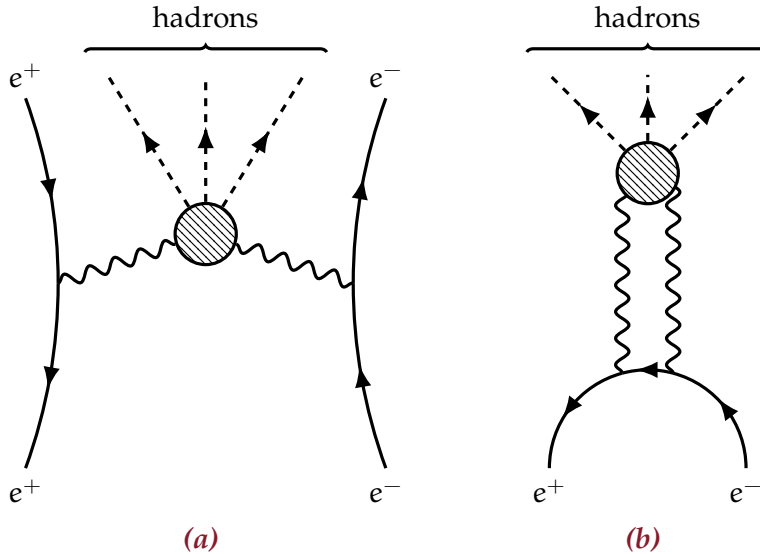
Figure 2.7: Feynman diagrams with two virtual photons for hadron production in e^+e^- collisions. The blob represents hadronic interaction. *(a)* Two photon collision with surviving leptons and *(b)* e^+e^- annihilation into two photons.

help of the ISR technique, unexpected vector states were found. In the charmonium region, the $Y(4260)$, $Y(4360)$, as well as the $Y(4660)$ state (cf. Section 2.2.3) were discovered in ISR events [23, 24, 163–165].

One part of this thesis contributes to the improvement of the ISR capabilities at the BESIII experiment. Chapter 4 deals with the development of the data acquisition for a small calorimeter specifically designed for the detection of ISR photons at almost zero degree polar angle.

2.3.3 *Two Photon Processes*

Figure 2.7 shows two Feynman diagrams of electron positron collisions with two virtual photons. The additional vertex entails an even stronger suppression than the ISR process. In the first diagram, the two leptons survive the reaction. This process is also referred to as photon fusion. Similar to ISR, the leptons dominantly

travel along the beam axis and there are three different event topologies: untagged, single-tagged, and double-tagged corresponding to the detection of none, one, or both leptons [143]. The q^2 carried by the photons is related to the scattering angle of the corresponding lepton. As a result, in the untagged topology, both photons are quasi-real. In the single-tagged topology, it is one photon and in the double-tagged, both photons are off-shell. Due to the two photons, the hadronic system carries quantum numbers that can be formed from $(1^{--}) \times (1^{--}) \times L$ with $L =$ orbital angular momentum, e.g. 0^{-+}, 0^{++}, 1^{++}, 2^{++}, etc. Photon fusion reactions can be used to determine various meson TFF's [143, 166–168].[10]

In the second diagram (Figure 2.7(b)), the e^+e^- pair annihilates and the full energy is transferred to the hadronic system. Following the previous discussion, other non-vector quantum numbers are produced. The BaBar experiment observed the reactions $e^+e^- \to \rho^0\rho^0$ and $e^+e^- \to \phi\rho^0$ at $\sqrt{s} = 10.58\,\text{GeV}$ [169]. The vector quantum numbers of the ρ^0 and the ϕ imply at least two virtual photons in the process. However, the diagram of Figure 2.7(b) is not necessarily involved. Instead, the reaction likely proceeds via a tree diagram of $e^+e^- \to \gamma^*\gamma^*$ and the subsequent coupling of each photon to one of the ρ^0 or ϕ mesons without any loop [170].

A process to which the loop diagram must contribute is the resonant formation. Here, the whole energy of the initial e^+e^- pair is completely transferred into the mass of a single resonance. Albeit allowed from the theoretical point of view, no such reaction has been observed experimentally so far. Within the context of this thesis, the search for the resonant formation of the X(3872) state with 1^{++} quantum numbers in e^+e^- annihilations is performed (see Chapter 5).

---

[10]In the spacelike region. The timelike region can be probed in Dalitz decays like $\pi^0 \to \gamma e^+e^-$ or in $e^+e^- \to P\gamma$ reactions, where P stands for a pseudo-scalar meson [143].

Chapter 3

THE BESIII EXPERIMENT
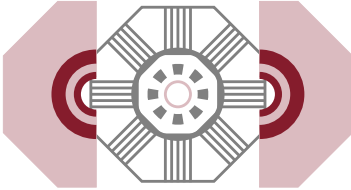
This thesis circles around the BESIII experiment, which is described in this Chapter. Both the experimental facilities of the accelerator complex and the detector are outlined as well as the BESIII physics program.

A FTER 15 years of successfull operation, China's first high energy physics particle accelerator, the Beijing Electron Positron Collider (BEPC) [171, 172], was shut down in 2004 to give way to its successor, the new BEPCII [173]. Along with the new accelerator, which provides an approximately 100 times increased luminosity, the new BESIII detector [33, 174, 175] was installed, being the third version of the Beijing Spectrometer (BES) [176] and the upgraded BESII [177]. BESIII started physics operation in 2009 and is one of the most successful experiments in the world recording data of e^+e^- collisions in the τ-charm energy region. It is hosted by the Institute of High Energy Physics (IHEP) of the Chinese Academy of Sciences in Beijing.

Like all large scale high energy physics experiments, BESIII can only be handled by a large scale international collaboration. The BESIII collaboration counts approximately 450 members from 67 institutions in 14 countries. Up to now, more than 230 papers have been published in international scientific journals, including highlights such as the discovery of the exotic $Z_c^\pm(3900)$ state [25].

The next Section gives an overview of BEPCII, followed by a description of the BESIII detector and its components. Afterwards, the system for a high precision determination of the beam energies is presented. The last Section of this Chapter outlines the available data sets and the physics program of BESIII.

3.1   BEPCII

The BEPCII provides symmetric e^+e^- collisions in the center-of-mass energy region of $(2.0 - 4.6)\,\text{GeV}$. The luminosity is optimized for beam energies of $1.89\,\text{GeV}$ corresponding to a center-of-mass energy of the $\psi(3770)$ mass. In spring 2016, the design luminosity of $10^{33}\,\text{cm}^{-2}\text{s}^{-1}$ was achieved [34, 173].

BEPCII is installed in the existing tunnel and partly reuses the old dipole magnets of BEPC. All other components are rebuilt. The accelerator consists of two Sections. First, the electrons (positrons) are accelerated in the 202 m long linear accelerator to the final beam energy. Then, they are injected into the storage ring. In contrast to the old collider, which only had a single ring structure, the electron and positron beams circulate in two separate rings. They cross each other at two points (one in the north and one in the south area of the ring). The beams collide only at the south crossing point (the interaction point), where the BESIII detector is located. The luminosity increase of a factor of about 100 compared to the predecessor collider is achieved in a twofold way. Firstly, focusing magnets compress the beam profile at the interaction point. Secondly, the double-ring allows the number of bunches per beam to be increased from one to 93 [33, 173]. The key design parameters of both BEPC and BEPCII are listed in Table 3.1.

In the near future, BEPCII is going to be upgraded. The maximum center-of-mass energy will be raised from 4.6 to $4.7\,\text{GeV}$ in 2019 and in a later stage to $4.9\,\text{GeV}$ [178]. Furthermore, a new injection scheme will be implemented, which will allow continuous injection during a physics run. As a result, the average luminosity will increase by up to 30 % [179].

Like its predecessor, BEPCII also serves as a high flux synchrotron radiation source for the Beijing Synchrotron Radiation Facility (BSRF). In the dedicated synchrotron radiation mode, the storage ring holds an electron beam of 250 mA at $2.5\,\text{GeV}$ [33].

3.2   The BESIII Detector

The BESIII detector is built to reconstruct hadronic events emerging in e^+e^- collisions of BEPCII. Therefore, the design is based on the requirements imposed by the event rate and the typical event topology. The average multiplicity of both charged particles and photons

Table 3.1: BEPCII key design parameters in comparison with those of BEPC, taken from reference [33].

Parameter	BEPC	BEPCII
$\sqrt{s}$ / GeV	$2.0 - 5.0$	$2.0 - 4.6$
Ring circumference / m	240.4	237.5
Number of rings	1	2
RF frequency / MHz	199.5	499.8
Peak luminosity / $\mathrm{cm^{-2}s^{-1}}$	$\approx 10^{31}$	10^{33}
Number of bunches	2×1	2×93
Beam current / mA	2×35	2×910
Bunch spacing / m (ns)	$-$	$2.4\,(8)$
Bunch length σ_z / cm	≈ 5	1.5
Bunch width σ_x / μm	≈ 840	≈ 380
Bunch height σ_y / μm	≈ 37	≈ 5.7
Relative energy spread	5×10^{-4}	5×10^{-4}
Crossing angle / mrad	0	2×11

in final states is four. The most probable momentum of charged particles is about 300 MeV, while the most probable photon energy is approximately 100 MeV when running at $\sqrt{s} = 3.77$ GeV [33].

Like many other high energy physics detectors, the BESIII detector is composed of many subdetectors arranged in an onion-shell layout, cf. Figure 3.1. The cylindrical core has an acceptance covering 93 % of the full solid angle. From the inside to the outside, BESIII consists of a multilayer drift chamber (MDC), a time-of-flight system (TOF) and a CsI(Tl) electromagnetic calorimeter (EMC) embedded in a uniform 1 T magnetic field provided by a superconducting solenoid magnet (SSM). The octagonal return yoke for the magnetic flux is instrumented as an absorber for the muon chamber (MUC). The individual components of BESIII are described below. A detailed description of the detector can be found in reference [33].

3.2.1 Beam Pipe

Before the particles from the collision can be detected by BESIII, they have to leave the vacuum chamber of the accelerator. In order to minimize the risk of secondary interactions, the central beam pipe must introduce as little material as possible within the detectors acceptance. At the same time, the beam pipe must be rugged enough
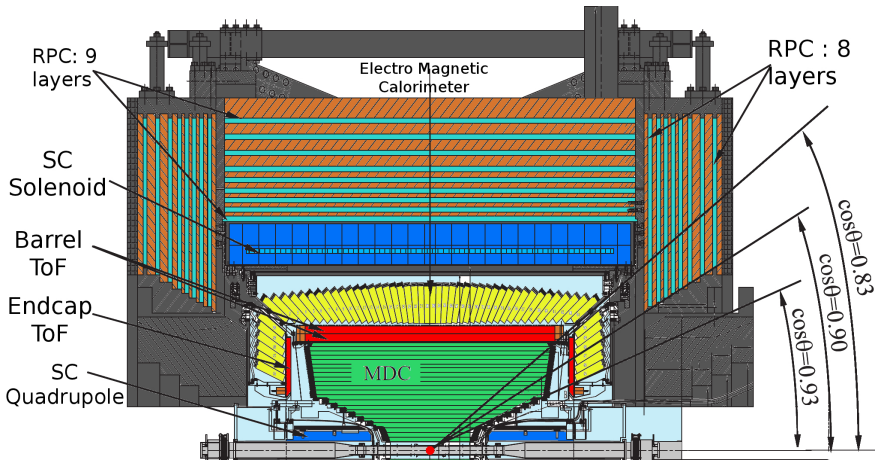
Figure 3.1: Schematic depiction of the BESIII detector. The top half is shown in a $z - y$ cross sectional view. The red dot indicates the interaction point. From inside to outside, the components are the drift chamber (MDC, green), the time-of-flight system (TOF, red), the electromagnetic calorimeter (yellow), the superconducting solenoid (large blue structure), and the muon chamber (orange $\widehat{=}$ passive absorber, cyan $\widehat{=}$ active RPC detector). Additionally, the superconducting quadrupole magnets for the final focus of the beams are shown (blue structures close to the interaction point). The figure is taken from reference [180].

to sustain the vacuum (5×10^{-10} Torr) and to resist the heat load resulting from the image current of the beam (≈ 700 W) [33, 181].

The central part of the beam pipe is a 29.6 cm long double walled beryllium tube with an inner diameter of 63 mm. The inner wall has a thickness of 0.8 mm and the outer wall has a thickness of 0.6 mm. They are separated by a 0.8 mm gap acting as a channel for a cooling fluid made from mineral oil. Due to its low atomic number ($Z = 4$), the probability of Coulomb scattering in beryllium is minimal, making it the ideal material. A 14.6 μm gold plating on the inner surface of the beam pipe reduces the intensity of synchrotron radiation entering the detector. The mineral oil flows with a velocity of 0.8 m/s ensuring an outer wall temperature of (20 ± 1) °C, which prevents wire breakage in the adjacent drift chamber [33, 181].

The central beam pipe is extended on both sides (outside the angular coverage of BESIII) by copper tubes until ±50 cm from the

interaction point to shield the detector against beam-related background. These extensions also have a double-wall structure, which is filled by cooling water [33, 181].

3.2.2 *Multilayer Drift Chamber*

Being the most important subdetector of BESIII, the MDC has to fulfill several tasks: the reconstruction of charged particles tracks does not only enable precise momentum determination, but also provides relevant vertex information. Furthermore, the MDC generates a trigger signal and the dE/dx measurement is used for particle identification (PID) [33, 182–184].

The MDC occupies a volume of approximately $4\,m^3$ between the radii of 59 to 810 mm over a maximum length of 2582 mm, resulting in an acceptance of $|\cos\theta| < 0.93$. The 6796 sense and 21 844 field wires are arranged into 43 layers of quadratic drift cells with a width of 12 mm (inner eight layers) or 16 mm (others). In each cell, one central sense wire is surrounded by eight field wires. Four layers are combined into one superlayer, except for the outer one which contains only three. Superlayers $3-5$ and $10-11$ have wires parallel to the z-axis while the wires of superlayers $1-2$ and $6-9$ are slightly tilted with respect to the z-axis by a stereo angle in the range of $\pm(2.4-3.6)\,^\circ$. The combination of these axial and stereo wires allows the reconstruction of the z-component of a charged particles track [33, 182–184].

The MDC is filled with a $3:2$ mixture of helium and propane at 3 mbar above ambient pressure. With a radiation length of 550 m, the multiple Coulomb scattering rate is minimized. The 110 μm thick field wires are made from gold coated aluminum, whereas the sense wires have a diameter of 25 μm and consist of gold coated tungsten. A voltage of $+2200\,V$ is applied to the sense wires, while the field wires are on ground potential [33, 182–184].

The signals from the sense wires are amplified in transimpedance preamplifiers located $50\,cm - 100\,cm$ from the MDC end plates. Afterwards, they are sent via 18 m long twisted pair cables to a set of VME crates hosting the readout electronics. Here, the signals are shaped and digitized by flash analog-to-digital converters (flash ADCs, FADCs). The digitized pulses are further processed and buffered in field programmable gate arrays (FPGAs). In parallel, the input signals are discriminated against a programmable

threshold and precise time stamps are generated by time-to-digital converters (TDCs). Upon receipt of a level 1 (L1) trigger, the charge and time information is sent to the event builder. Furthermore, the input signals to the TDCs are directly sent to the L1 trigger [33, 182–184].

A single wire resolution of 135 µm leads to a transverse momentum determination with an uncertainty of 0.5 % at 1 GeV. The trajectories can be measured in z-direction with an accuracy of 2 mm at the interaction point. The dE/dx resolution is 6 % allowing a pion/kaon separation at a 3σ level in the momentum range below 770 MeV [33, 182–184].

In the near future, a cylindrical gas electron multiplier (GEM) detector will replace the inner chamber, i.e. the first two superlayers, which exhibit a performance loss due to aging effects. It will cover the angular region of $|\cos\theta| < 0.93$ with three layers of triple GEM foils. The upgrade will maintain the momentum resolution of the current setup, while the spatial resolution in z-direction will improve by a factor of 2 [185–190].

3.2.3 *Time-of-Flight System*

The main PID device is the TOF also providing a fast trigger signal and a precise event start time. It is located between the MDC and the EMC and is divided into a barrel part ($|\cos\theta| < 0.82$) and two end caps ($0.85 < |\cos\theta| < 0.95$). The gap in between is taken up by support structures of the MDC and service lines [33].

The barrel part consists of two layers of each 88 trapezoidal plastic scintillator bars at radii between 81 and 93 cm. Each bar has a length of 230 cm and a thickness of 5 cm. They are made of the organic BC-408 scintillator by Saint-Gobain, which has a high light output (64 % relative to Anthracene), fast rise and decay time (0.9 and 2.1 ns), and a long attenuation length (380 cm) [191]. A wrapping in aluminum foil enhances the effective light yield at the end faces of the bars, where photomultiplier tubes (PMTs) collect the scintillation light. The R5924-70 PMTs from Hamamatsu with fine-mesh dynodes are well suited to operate in high magnetic fields [192, 193]. Supplied with a high voltage of 2000 V, the PMTs have a gain of approximately 2×10^5 in the magnetic field configuration of BESIII. They have a diameter of 51 mm and the cathode covers $37\% - 39\%$ of the end face of the scintillator bar [33, 194–198].

The two TOF end caps are placed directly behind the MDC end plates. They were made from plastic scintillators similar to the barrel TOF and eventually replaced in 2015 by multigap resistive plate chambers (MRPCs) [33, 197, 199–206].

In the plastic scintillator layout, the end caps consist of a single disc-shaped layer composed from 48 trapezoidal segments. Each segment has a thickness of 50 mm, a width of 62 and 109 mm at the inner and and outer edge, which are 480 mm apart. At the inner edge, a 45° cut reflects the scintillation light into PMTs which are aligned perpendicular to the scintillators and hence parallel to the magnetic field. The same type of PMTs as in the barrel part is used. The end cap segments have a smaller size than the bars in the barrel, so a long attenuation length is not as important as in the barrel part. The BC-404 scintillator by Saint-Gobain is used, which has a shorter attenuation length than the barrel material (160 cm), but a slightly higher light yield (68 % relative to Anthracene) and faster response (0.7 ns rise and 1.8 ns decay time) [191]. The end cap scintillator is wrapped in a 3M Vikuiti™ ESR (Enhanced Specular Reflector) film [33, 194–197, 199].

In the MRPC layout, each end cap consists of 36 trapezoidal modules arranged in a circular double layer. Each module is double stack MRPC with thickness of 25 mm, a height of 397 mm, and a width of 134 and 201 mm at the inner and outer edge. There are 12 gas layers of 0.22 mm thickness separated by glass sheets with a thickness of 0.4 and 0.55 mm. A high voltage of approximately 14 kV is applied between two graphite layers coated onto the outermost glass sheets. The working gas is a $90 : 5 : 5$ mixture of $C_2F_4H_2$, SF_6, and C_4H_{10}. The signal is picked up by 12 strips oriented in ϕ direction, which are read out on both sides [200–206].

The readout for the PMT signals is very similar to the MDC readout: first, the signals are preamplified directly after the PMTs and transferred by 18 m twisted pair cables to the readout electronics in VME crates. Then, they are split and fed into ADC circuits and discriminators followed by TDCs for charge and time measurements. The digitized data is sent to the event builder, after an L1 trigger is received. For each scintillator, a fast trigger signal is generated from the mean timing information [33].

In the upgraded version of the end cap, the signals from the strips are amplified and converted by a time-over-threshold discriminator directly next to the MRPC elements. The charge is now en-

coded in the length of the resulting pulse, which is sent off-detector
to VME based TDC modules. The TDCs extract the charge and
time information, which is sent to the event builder upon L1 trigger
receipt. The TDC inputs corresponding to each three neighboring
strips are combined into a trigger signal [204–207].

In the barrel part, the time resolution for electrons from Bhabha
events is 78 ps [198]. The plastic end caps achieved a resolution
of 110 ps [33, 197], while the replacement by MRPCs significantly
improves the resolution to 60 ps superseding the expectations from
simulation [205, 206, 208].

3.2.4 *Electromagnetic Calorimeter*

The main task of the EMC is the precise measurement of photons
in energy (~ 20 MeV to ~ 2 GeV) and position, the identification of
electrons, and the creation of a trigger signal. The EMC features 6240
thalium doped CsI crystals grouped in 56 rings (44 in the barrel
and 2×6 in the end caps). The crystals have a length of 28 cm
corresponding to 15.1 radiation lengths. They point towards the
interaction point with a small tilt of $1.5° - 3.0°$ to avoid photons
escaping through slits between crystals [33, 209, 210].

The barrel part covers the angular region of $|\cos θ| < 0.82$ and has
an inner radius of 94 cm. The crystals in the barrel have a surface
area of 5.2×5.2 cm^2 at the front and 6.4×6.4 cm^2 at the rear. Each
of the 44 barrel rings is made from 120 crystals. The end caps are
placed at $z = \pm 138$ cm and cover the region $0.83 < |\cos θ| < 0.93$.
They contain $64 - 96$ crystals per ring. All crystals are wrapped in
layers of 260 µ Tyvek$^®$ fleece, 25 µm aluminum, and 25 µm polyester
film. At the rear of the crystals, two PIN photodiodes with the size
1×2 cm^2 (Hamamatsu S2744-08 [211]) collect the scintillation light.
For calibration, LEDs can inject light pulses via optical fibers into
the crystals [33, 209, 210, 212].

Each photodiode has its own preamplifier mounted on the crys-
tal, whose outputs are sent via twisted pair cables off-detector to
NIM modules with shaping amplifiers. Here, the two signals from
one crystal are added and sent to VME based FADCs boards featur-
ing FPGAs. When an L1 trigger arrives, the digitized waveforms are
scanned for a peak exceeding a given threshold and its samples are
sent together with a timestamp to the event builder. Additionally,
the NIM modules send the signal sums from each 4×4 crystals (15
in the end cap) to the L1 trigger system [33, 209, 210, 213].

The photon energy resolution is 2.5 % (5.0 %) in the barrel (end cap) at 1 GeV matching the design specifications [33, 209, 212].

3.2.5 *Superconducting Solenoid Magnet*

The SSM encloses the detector core (MDC, TOF, and EMC) and provides a uniform magnetic field of 1 T parallel to the beam axis. The superconducting coil is made from NbTi/Cu wires embedded in a high purity aluminum stabilizer. It has 848 turns and a nominal current of 3369 A. The stored field energy is 9.8 MJ. A cryostat with liquid helium cooling keeps the coil temperature at 4.5 K to ensure superconductivity. Its shape is a hollow cylinder with an inner (outer) radius of 137.5 cm (170 cm) and a length of 391 cm. The flux return yoke of the solenoid is used as an absorber for the MUC [33, 214–217].

3.2.6 *Muon Chamber*

The MUC is the outermost subdetector used to discriminate muons from hadrons which are mainly charged pions. It is located outside the magnet coil and consists of alternating layers of steel plates and resistive plate chambers (RPCs). The steel plates serve as an absorber for hadrons as well as the flux return yoke of the solenoid [33, 218–221].

In the octagonal barrel part ($|\cos\theta| < 0.75$), there are 9 RPC layers and the steel thickness is increasing from the inner layer with 3 cm to the outer layer with 15 cm. The end caps ($0.75 < |\cos\theta| < 0.89$) are constructed as pairs of movable doors providing access to the inner detectors. They only have 8 RPC layers and the thickness of the steel plates ranges from 3 to 8 cm [33, 219–221].

The active detector elements are double stack RPCs filling the 4 cm gaps between the steel plates. Each RPC module is made from two 2 mm Bakelite®-like phenolic paper laminate plates with a gas filled gap of 2 mm inbetween. The working gas is a mixture of Ar, $C_2F_4H_2$, and C_4H_{10} in a 50 : 42 : 8 ratio. The RPCs operate at a voltage of 8 kV in streamer mode. The readout strips are placed between the two modules in a double stack. Their orientation is rotated by 90° in every other layer allowing the reconstruction of three dimensional coordinates. In total, the MUC has 9152 strips covering an area of approximately 700 m² [33, 218–221].

The average pulse height of the signals from the RPC strips is in the order of 500 mV, so there is no need for preamplifiers. Instead, the signals are directly discriminated and buffered in FPGAs at the detector site. When an L1 trigger is received, the data is sent to VME modules off-detector, which combines the data from all strips and sends it to the event builder [33, 219–221].

3.2.7 *Level 1 Trigger and Event Filter*

The selection of physics events to be written to mass storage is divided into the two stages: L1 trigger and event filter. The first one is a pipelined hardware trigger based on FPGAs and the second one is realized on a CPU farm. The physics event rate is $\leqslant 2$ kHz, while the mainly beam related background rate is ≈ 20 MHz. In order to reduce the amount of data to be processed in software, the L1 trigger needs to suppress the background rate by four orders of magnitude [33, 222–224].

Subtriggers for the MDC, TOF, and EMC check for 33 different trigger conditions such as a certain number of clusters in the EMC or back-to-back hits in the TOF. A global trigger logic combines them into 13 channels to form an L1 trigger decision. The maximum trigger rate is 4 kHz with a latency of 6.4 μs before the MRPC upgrade of the end cap TOF and 8.6 μs afterwards [33, 222, 225–227].

The event builder receives event fragments from the VME crates of the subdetector readouts and assembles them into full events. The average data size of one event is 14.2 kB. The event is partially reconstructed and categorized based on the total energy deposited in the EMC, shower acoplanarity, track multiplicity and acollinearity, and so on. The background contamination is further reduced by ≈ 50 %. Finally, the surviving events are written to tape with a data rate of ≈ 42 MB/s [33, 223, 224].

The selection efficiency for hadronic events is larger than 99.9 % [228].

3.2.8 *Beam Luminosity Monitor*

The determination of the integrated luminosity with highest precision can only be done offline. Typically, the QED reactions $e^+e^- \rightarrow e^+e^-$ (Bhabha scattering) and $e^+e^- \rightarrow \gamma\gamma$ are analyzed because their very high cross sections can be predicted accurately by theory [33, 229–231].

In order to have an instant estimate of the luminosity, two beam luminosity monitors (BLMs) are installed $\approx$ 3.4 m up- and downstream of the interaction point. They determine the luminosity by counting photons from the radiative Bhabha process ($e^+e^- \to \gamma e^+e^-$). A very high fraction of the photons are emitted in within 1 mrad of the outgoing beam. A dipole magnet bends the beam and the photons travel further on a straight line until they exit the vacuum chamber and hit the BLM. Due to spatial limitations between the two beam pipes, the BLM needs to be very compact. They are made from a 12 mm thick tungsten absorber ($3.5 X_0$) followed by a $40 \times 45 \times 66$ mm^3 block of fused silica equipped with two PMTs (Hamamatsu R7400U). In the absorber, the photons convert and the resulting electrons (positrons) radiate Cherenkov light in the silica which is registered by the PMTs [33, 229–231].

In 2011 the BLM on the east side of BESIII was replaced by a zero degree detector (ZDD) made from scintillating plastic fibers embedded in a lead matrix. The differences to the BLM is a better energy resolution as well as the L1 triggered readout. As a result, the ISR photons corresponding to hadronic events in BESIII can be detected [232]. However, the ZDD does not work properly and the replacement by a redesigned detector is planned (cf. Chapter 4). The ZDD is described in more detail in Section 4.1.

3.3 The Beam Energy Measurement System

For most physics analyses, a measurement uncertainty of the collision energy in the order of 1 MeV is sufficient. This can be achieved by the offline analysis of dimuon events ($e^+e^- \to \mu^+\mu^-$). For some analyses[1] however, the center-of-mass energy needs to be known with highest possible accuracy and already while data taking. For this reason, the beam energy measurement system (BEMS) has been installed at the north crossing point of BEPCII (opposite side of BESIII). It is an ensemble of devices to measure the energy of Compton back scattered photons from the electron/positron beams and hence infers the corresponding beam energy in real time [233–239]. The layout is sketched in Figure 3.2.

A CO_2 laser with 50 W creates photons with the energy $\omega_0 = 0.117$ eV ($\lambda_0 = 10.59$ μm). The spectral density has a relative width

---

[1]Including the one presented in Chapter 5 of this thesis.
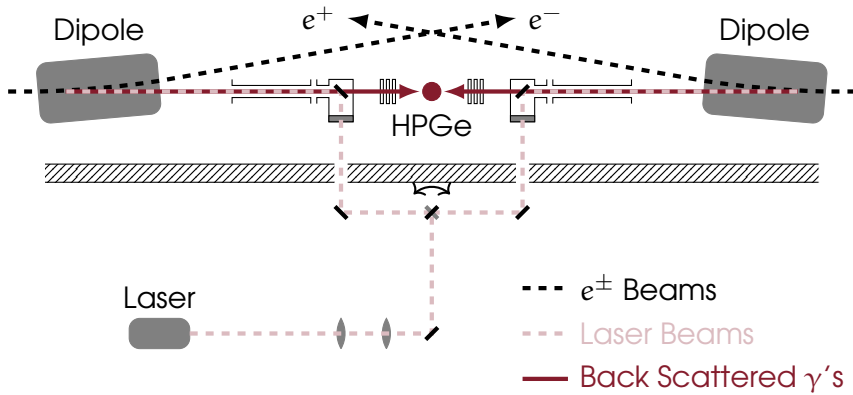
Figure 3.2: Sketch of the BEMS layout. The laser beam is guided into the vacuum chamber of the accelerator and directed to collide with the electrons (positrons). The rotatable mirror selects the e^+ or the e^- beam. The back scattered γ rays have an energy in the 2 to 10 MeV range and are detected by a HPGe detector. Figure based on reference [234].

of 3 ppm. The photons are guided by lenses and mirrors into the vacuum chamber. A rotatable mirror selects whether the photons enter the electron or positron ring. The lenses and the entrance windows at the vacuum boundaries are made from ZnSe which is transparent to infrared light [233–239].

In the vaccum, the photons are reflected once more in order to collide head on with the $e^\pm$ beam. The corresponding mirrors are made from copper. As they are positioned directly at the tangent of the $e^\pm$ trajectories in the bending dipole field, they are hit by synchrotron radiation and have to endure a heat load of 200 W. Therefore, they are equipped with water cooling [233–239].

Depending on the BEPCII beam energy, the 180° back scattered photons are in the range of 2 to 10 MeV. They return to the copper mirror and pass through it. After leaving the vacuum chamber, they hit a high purity germanium (HPGe) detector. They are known to have an excellent resolution for photons of that energy. The P-type coaxial HPGe detector GEM25P4-70 from ORTEC is used. An electric cooler maintains a detector temperature below 100 K. Due to severe beam related background contamination, the detector is sur-

rounded by several layers of iron, lead, and paraffin. The detector is read out by a multi channel analyzer with 14 bits resolution [233–239].

The recorded spectrum of the HPGe contains the photon energies after back scattering at $180\,^\circ$ and less. Hence, the Compton edge is visible. It is fitted with a function taking into account the asymmetric response function of the detector, the (theoretical) shape of the Compton edge, the beam energy spread, and a background term. After the fit and calibration, the maximum energy ω_{max} of the back scattered photons (corresponding to a scattering angle of exactly $180\,^\circ$) and the beam energy spread are available. The beam energy ε is obtained by

$$\varepsilon = \frac{\omega_{max}}{2} \left(1 + \sqrt{1 + \frac{m_e^2}{\omega_0 \omega_{max}}} \right) \quad . \tag{3.1}$$

The outstanding energy resolution of the HPGe detector (1.74 keV FWHM at the energy of 1.33 MeV) and the negligible uncertainties of the electron mass m_e and the initial photon energy of the laser ω_0 lead to a relative uncertainty of the beam energy at the 10^{-5} level, much better than via the usual dimuon method [233–239].

In 2011, the BEMS was operated successfully during a scan around the $e^+e^- \to \tau^+\tau^-$ threshold [240]. The cross section of this process was measured as a function of $\sqrt{s}$ and the tau mass was extracted from a fit. Thanks to the BEMS, this result is still the most precise tau mass measurement in the world [30].

3.4 *Software*

The BESIII offline software system (BOSS) is built upon the GAUDI [241] architecture using C++ and runs on scientific linux SLC5 and SLC6. The whole chain of data simulation, reconstruction, and analysis is performed within BOSS [33, 242]. Each of the above steps is described in the following.

Simulation. Monte Carlo (MC) simulations are absolutely essential for the analysis of high energy physics data. The simulation step provides MC data mimicking real data from collisions. Within BOSS, the simulation is further divided into the event

generation and the subsequent particle propagation through the BESIII detector. There is a wide range of MC generators for various processes available in BOSS. They are responsible for the creation of (simulated) events containing particles with the correct kinematics and topology. Afterwards, the GEANT4 package [243] propagates them through the magnetic field simulating the interaction and the response of the detector elements. The read out electronics including noise and dead channels is simulated as well. In the end, the events are stored in the same data format as the raw events recorded by BESIII [33, 242].

Reconstruction. The reconstruction part includes all general procedures that are applied to the data sets. During this step, the digitized signals from the individual detector channels are converted into more abstract objects: the MDC hits are joined into tracks, which are fitted by a Kalman filter [244]. The TOF and EMC hits are clustered and matched with the MDC tracks. They are extrapolated and combined with tracks found in the MUC. Furthermore, the individual dE/dx measurements are associated with their tracks and the precise timing information from the TOF is obtained. The reconstruction is performed on the raw data from collisions and MC data [33, 242].

Analysis. In the last step, higher level procedures are applied to the output files from the reconstruction. Here, tools such as kinematic fits and global PID algorithms using the information of all subdetectors are available. The usage of them heavily depends on the specific physics channel being studied [33, 242].

While the reconstruction step is universal, the simulation and analysis procedures need to be changed, when different physics channels are investigated.

3.5   *Data Sets and Physics at BESIII*

BESIII has the unique capability to collect e^+e^- collision data in the τ-charm energy region with unprecedented statistics. This enables a rich physics program that is detailed in reference [245] and can be categorized in the following way:

Light hadron physics deals with the spectroscopy of hadrons containing u, d, and s quarks, as well as the search for light hybrids, glueballs, and multiquark configurations. Most of those (candidate) particles are rather broad and interfere with other states. In order to disentangle the different states, partial wave analyses are indispensable, which itself require almost background free data samples with very large statistics. At BESIII, the J/ψ resonance is easily formed and serves as an excellent source because it decays to all different kinds of light mesons. So far, BESIII recorded data of about 10^{10} J/ψ decays, the worlds largest data set [35].

Charmonium physics can be subdivided in the categories of conventional charmonium physics and the physics of exotic charmonium-like XYZ states (see Section 2.2.3). For the studies of conventional charmonia, mostly a data set containing roughly 450×10^6 ψ' decays is used. All charmonia below the open-charm threshold appear as ψ' decay products [246].

For XYZ physics, data sets between 4 and 4.6 GeV are used. Up to now, about $12 \, \text{fb}^{-1}$ of data has been collected in this region, being spread over various data points. At few center-of-mass energies, the integrated luminosity reaches up to $3 \, \text{fb}^{-1}$. There are 81 tightly spaced data points with only 5 to $10 \, \text{pb}^{-1}$ per point and a high statistics scan is currently in progress with $500 \, \text{pb}^{-1}$ data points and a step size of 10 MeV above 4.2 GeV [246]. All those data samples enable valuable cross section line shape measurements for the study of Y states [148, 149, 247–250]. The X(3872) and the charged Z_c states can be studied with the same data sets as they are produced in $e^+e^- \to \gamma X(3872)$ and $e^+e^- \to \pi Z_c$ reactions [25, 86, 122, 154–157]. With the future upgrade of the BEPCII accelerator and the increase of the maximum collision energy to 4.9 GeV, the Y(4660) will also be studied at BESIII.

Recently, two additional data points in the vicinity of the X(3872) mass were taken specifically for the search of the resonant X(3872) formation via two virtual photons [246], as discussed in Chapter 5 of this thesis.

Tau and QCD physics at BESIII deals with the determination of hadronic form factors and the R-value as well as measurements

of tau lepton properties. It is for a reason that the energy range covered by BESIII is called tau-charm region. Both timelike form factors and spacelike TFFs are determined at BESIII in order to improve the understanding of the hadronic contribution to the muon anomalous magnetic moment (cf. Section 2.2.5). Often, the ISR technique (cf. Section 2.3.2) is employed, for which all data sets at BESIII can be used, except for the ones at the J/ψ and the ψ' mass (background from radiative decays).

With the use of the precise beam energy measured by the BEMS (cf. Section 3.3), a scan around the $\tau^+\tau^-$ threshold yields the currently most precise value of the tau mass [30, 240].

Charm physics involves open-charm hadrons like $D_{(s)}$ mesons and the Λ_c^+ baryon. BESIII has recorded a data set of $2.9\,\mathrm{fb}^{-1}$ at the $\psi(3770)$ resonance, which almost entirely decays to D mesons, enabling measurements of the D^0-$\bar{D}^0$ mixing parameters [251, 252]. With the additional data sets above $4\,\mathrm{GeV}$, $D_s\bar{D}_s$ pairs are created. The measurement of the product of the decay constant and the CKM matrix element $f_{D_{(s)}^+} \times |V_{cu(cs)}|$ is an important test of lattice QCD and the unitarity of the CKM matrix [253–255].

With the data sample of $500\,\mathrm{pb}^{-1}$ at $4.6\,\mathrm{GeV}$, BESIII is able to investigate the Λ_c^+ baryon. The world's first absolute determination of various branching fractions of Λ_c^+ decay channels was performed at BESIII [256]. Those are only few of the many charmed hadron studies at BESIII.

New physics refers to physics beyond the SM. The search for physics beyond the SM is pushed forward simultaneously at the high energy frontier and the precision frontier. The first is the domain of experiments like ATLAS and CMS at the LHC searching for very heavy particles. On the precision frontier however, processes at moderate energies are investigated with the help of high statistics and the resulting precision. Arbitrarily heavy particles can contribute to loop diagrams and alter the SM prediction of certain processes. In particular, reactions that are forbidden or very rare in the SM, are sensitive to new physics, like lepton flavor violating processes or flavor changing neutral currents, e.g. $D^0 \rightarrow \pi^0 \ell^+ \ell^-$. There are numerous

starting points for the search of physics beyond the SM at the precision frontier, ranging from tests of lepton universality in various (semi-) leptonic decays to the search for a dark photon, a hypothetical dark matter candidate [257].

———

PROTOTYPE DATA ACQUISITION FOR THE CRYSTAL ZERO DEGREE DETECTOR
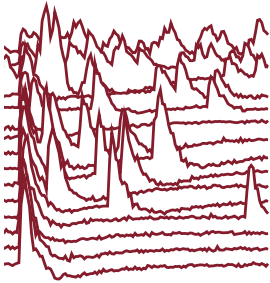
This Chapter presents the design of a small detector for the tagging of ISR photons at very small angles at BESIII. This thesis contributes to the project of this crystal zero degree detector by developing and testing a prototype data acquisition in a test beam environment. Additionally, a method to identify pile-up was developed and the important geometry of the accelerator structure around the detector was implemented into a simulation.

THE puzzle of the anomalous magnetic moment of the muon is about to experience a boost as a new experiment is currently running [144–146]. A new experimental value of a_μ with an uncertainty quartered compared to the current world average is expected to be released shortly. In order to obtain theoretical predictions at a competitive level, new measurements of the R-value are required. The ISR technique is an ideal tool for such measurements at BESIII (cf. Section 2.3.2). However, only about 15 to 20 % of all ISR events are of the tagged type, and in all other cases, the ISR photon is emitted outside BESIII's acceptance along the beam line. The capabilities of BESIII to employ the (tagged) ISR technique will be greatly enhanced by a zero degree detector (ZDD). It is a detector placed at very small forward/backward angles specifically for the detection of ISR photons.

The idea of a ZDD at BESIII is not new: a ZDD was installed in 2012 but with little success [232]. It suffered serious problems that could not be solved. This Chapter contributes to the development of a redesigned ZDD, in particular with respect to data acquisition. The next Section briefly describes the current ZDD. In Section 4.2, the design of the new ZDD is outlined. Both the detector itself and the DAQ scheme are presented. Section 4.3 focuses on the material budget in front of the detector. Its effect is studied with the help of

simulations. In the Section afterwards, the development and evaluation of a prototype detector module and the corresponding DAQ in a high rate beam test is described. The Chapter closes in Section 4.5 with the development of waveform analysis algorithms to detect pile-up events.

4.1   *The Present Zero Degree Detector*

In 2012, a ZDD was installed at the east side of BESIII [232]. It replaced the BLM (cf. Section 3.2.8) located approximately 3.4 m in z-direction from the interaction point. The design constraints are given by the limited available space and the high background coming from processes like $e^+e^- \rightarrow \gamma e^+e^-$, the primary source for luminosity measurement by the BLM.

In order to capture as much as possible of the electromagnetic shower and to resolve the timing of individual events, the detector needs to be made from a material with short radiation length (i.e. high density) and a fast response. The INFN group decided to go with scintillating plastic fibers glued into a lead matrix. The fiber : lead : glue volume ratio of 42 : 48 : 10 results in a radiation length of 1.6 cm and a density of $5\,g/cm^3$. The scintillating fibers are of the SCSF-81 type from Kuraray with a diameter of 1 mm and a decay time of 2.4 ns [232, 258].

The major background are photons from radiative Bhabha events ($e^+e^- \rightarrow \gamma e^+e^-$). Here, the photon angular distribution is even stronger peaked at $\theta = 0\,°$ and $180\,°$ than for ISR photons. In order to reduce the contamination from this background, the ZDD is divided into two blocks of each $(4 \times 6 \times 14)\,cm^3$ separated by a small gap, through which the radiative Bhabha photons escape. The two blocks are mounted on a vertically movable support allowing the size of the gap to be adjusted [232] (cf. Figure 4.1(a)).

The limited space and the presence of magnetic fields do not allow a direct placement of PMTs onto the detector blocks. Instead, optical fibers guide the scintillation light to PMTs about 2 m from the ZDD. Additionally, this minimizes the effect of magnetic fringe fields from one of the close by magnets on the PMTs. Each detector block is further divided into eight segments, of which each segment is connected to one PMT [259].

The ZDD faced serious problems concerning the identification of the "correct" ZDD events compared to BESIII events. Eventually, the ZDD was never used for physics analysis.

4.2 Redesign of the Zero Degree Detector

4.2.1 The Crystal Zero Degree Detector

A redesign of the ZDD was proposed and evaluated in a previous work by Marcel Werner [260]. The main feature of the new detector is a superior DAQ by means of an FPGA based realtime event correlation between the ZDD and the BESIII L1 trigger. The sensitive detector is made from crystals of a dense inorganic scintillator with a longer decay time than the plastic fibers, but shorter radiation length and much better radiation hardness. The current design foresees the material LYSO ($Lu_{1.8}Y_{0.2}SiO_5 : Ce$), although the initial concept of Werner considered lead tungstate ($PbWO_4$). To emphasize that the detector is made from crystals, the new detector is called crystal zero degree detector (cZDD). The design of two blocks separated by a gap is kept from the old ZDD for the same reason of background reduction. Each block consists of a 4×3 array of $(1 \times 1 \times 14)\,cm^3$ crystals. The geometry is sketched in Figure 4.1(b). The scintillation light is collected by silicon photomultipliers (SiPMs). Their preamplified outputs are digitized by sampling ADCs (sADCs) performing feature extraction and subevent building. The subevents are sent to an FPGA based platform, which buffers the data and correlates it with the L1 trigger. Afterwards, the data is sent to the BESIII event builder and written to mass storage.

Furthermore, Werner implemented modules for the whole simulation-reconstruction-analysis chain of the cZDD in the BOSS framework (cf. Section 3.4).

Based on this work [260], a new cZDD working group in BESIII was formed as a collaboration between Mainz and Gießen. The basic design is adopted from Werner. However, the choices of the explicit hardware components are completely new, such as the decision to use LYSO instead of $PbWO_4$, other SiPMs, newer and more advanced FPGAs, etc. These individual components are described in the following.

(a)   *(b)*
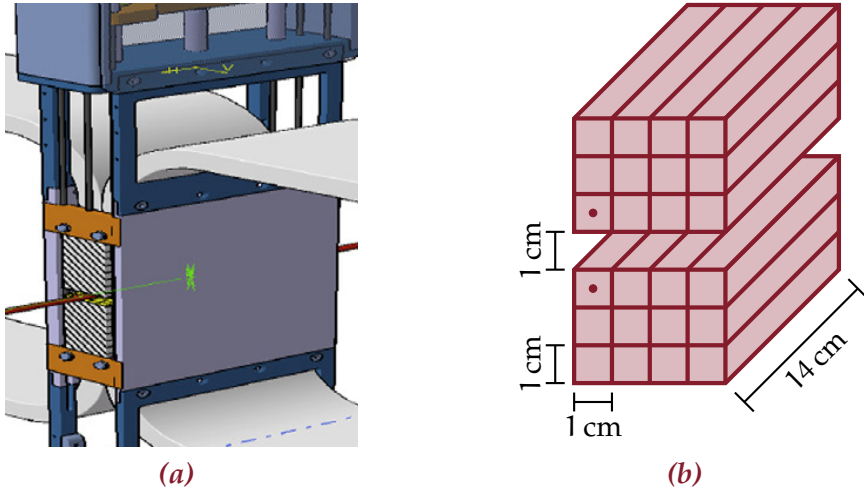
Figure 4.1: Geometry of the zero degree detector. *(a)* The two ZDD
blocks with the vertically movable support [232]. The gray bands
above and below are the light guides transferring the scintillation
light to the PMTs. *(b)* Layout of the new cZDD (based on refer-
ence [260]). The two crystals marked by the dots experience the
highest rate and have the least material budget in front.

Table 4.1: Scintillation properties of PbWO$_4$, LYSO, and NaI(Tl) [30,
261]. Lead tungstate has two components with different decay time
constants. Both are listed. The light yield in number of photons per
MeV energy deposition is given at room temperature. The properties
of NaI are just given for comparison, as it is a common benchmark
scintillator.

	PbWO$_4$	LYSO	NaI(Tl)
Density / (g/cm^3)	8.28	7.10	3.67
Radiation length / cm	0.89	1.15	2.59
Molière radius / cm	2.00	2.07	4.13
Decay time constant / ns	10, 30	40	245
Light yield / (ph/MeV)	31	32 000	37 700
Relative light yield - temperature coefficient / (%/°C)	−2.5	−0.2	−0.2

LYSO Crystals

LYSO ($Lu_{1.8}Y_{0.2}SiO_5$: Ce) is an inorganic scintillator with properties compared to lead tungstate in Table 4.1. It is slightly less dense than lead tungstate and as a consequence has a somewhat larger radiation length and Molière radius. Other than that, the scintillation decay time is in the same order of magnitude as the one of $PbWO_4$, however a bit longer. The most striking difference is the light yield. At room temperature, the scintillation light output of LYSO is roughly a thousandfold larger. Additionally, the light yield is much more stable with respect to temperature changes. The strong temperature dependence of $PbWO_4$ can be exploited to increase the amount of scintillation light by cooling it down. The $\overline{P}ANDA$ experiment will have a $PbWO_4$ electromagnetic calorimeter being held at $-25\,°C$ [262]. By doing so, the light yield is enhanced by a factor of four compared to room temperature. However, a well calibrated signal requires a precisely controlled temperature environment. The narrow available space for the cZDD forbids the use of a cryostat and the direct neighborhood to the beam pipes create an ambient temperature significantly above room temperature.

The previously described geometry enters the current design unaltered. The manufacturing of $(1 \times 1 \times 14)\,cm^3$ $PbWO_4$ crystals imposes difficulties because lead tungstate is rather fragile and the crystals tend to break during the cutting process into such a small $(1 \times 1)\,cm^2$ cross section [260]. Considering the mechanical stability and the temperature behavior, it was decided to use LYSO instead of lead tungstate. In the cZDD, the individual crystals will be wrapped in reflective material ensuring an optical decoupling of the crystals.

Silicon Photomultipliers

Apart from the missing space for PMTs, the already mentioned fringe fields of the close by beam magnets do not allow the instrumentation of PMTs. Instead, SiPMs will be used to collect the scintillation light. They are very compact, operate in magnetic fields, and stand high rates.

The SiPMs of the SensL series C [263] will be used. They offer several features beneficial for the cZDD. Such are the photon peak sensitivity at $420\,nm$ matching the emission spectrum of LYSO [30, 261]. Furthermore, these SiPMs operate with a supply voltage of around $29.5\,V$ eliminating the need for high voltage power supplies.

The most handy aspect is that the SensL SiPMs have an additional output terminal with pulse widths below 1 ns.[1] Because of the high rate and the risk of pile-up, the fast output will be used for the cZDD.

4.2.2 *Data Acquisition of the Full cZDD*

Sampling ADCs

Despite the fast output of the SiPMs, the cZDD signals are still susceptible to pile-up and an analog pulse integration is not feasible. Instead, the signals will be digitized by sampling ADCs allowing pulse shape analysis and pile-up detection.

Since the cZDD is a relatively small detector with a limited channel count, the development of dedicated ADC circuits is not viable. As an alternative, the ADC boards for the $\overline{\text{P}}$ANDA EMC will be used. They are developed by Pawel Marciniewski (Uppsala University, Sweden) and can digitize up to 64 differential inputs within $\pm$1V and a resolution of 14 bits. For the application at $\overline{\text{P}}$ANDA, the sampling rate is 80 MHz, but for the cZDD it will be increased to 125 MHz corresponding to a sampling interval of 8 ns [264, 265].

A photograph of such a board is shown in Figure 4.2. It features two Xilinx® Kintex®-7 FPGAs [266] receiving the data from eight ADC chips, which each digitize eight input channels simultaneously. The FPGAs can be programmed to perform waveform processing such as feature extraction and pile-up detection. The ADC board is equipped with two SFP+ cages, each connected to one FPGA. They provide the interface to serial data transfer with rates of several Gbit/s, e.g. via optical fibers.

In order to keep the analog signal lines as short as possible, two ADC boards will be required, one for each cZDD at the east and west side of BESIII.

Event Correlator

The real time event correlation of the cZDD with the L1 trigger takes place on the so-called event correlator. It receives, buffers, and correlates the ADC data with the L1 trigger and sends out subevents to the BESIII event builder. The requirements of having sufficient

---

[1]The actual pulse width in the cZDD setup is larger due to the intrinsic scintillation decay time of LYSO ($\tau = 40$ ns).
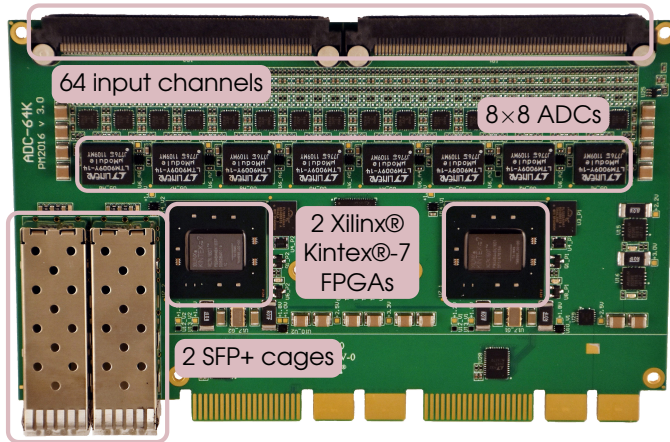
Figure 4.2: Photograph of the ADC board with courtesy of Pawel Marciniewski.

memory and high bandwidth connectivity as well as a powerful FPGA are met by the commercially available FPGA demonstrator board AES-KU040-DB-G from Avnet [267, 268], cf. Figure 4.3. Its core is a Xilinx® Kintex® UltraScale™ FPGA [269], which has access to 1 GB of DDR4 SDRAM. Two RJ45 connectors enable Gigabit Ethernet networking and two SFP+ cages provide high-speed serial interfaces with data rates of each up to 12.5 Gbit/s. This can be greatly enhanced by an add-on card plugged into the FMC HPC connector with eight additional serial lanes, each of which is capable of 10 Gbit/s.

Data Flow

The digital data flow starts at the ADC boards. The waveform of each input channel is continuously sampled, buffered, and searched for pulses. When a pulse is found, features including pulse integral, pulse height, etc. are extracted and forwarded to a pile-up detection unit. Based on these features, the decision is made whether the pulse is a pile-up candidate or not. The data is formed into a packet and is sent to the event correlator via optical fibers. If considered as pile-up, the packet contains a time stamp and the channel number together with the whole sample train of the pulse. If no pile-up is detected, the packet contains just the features instead of the full sample train.
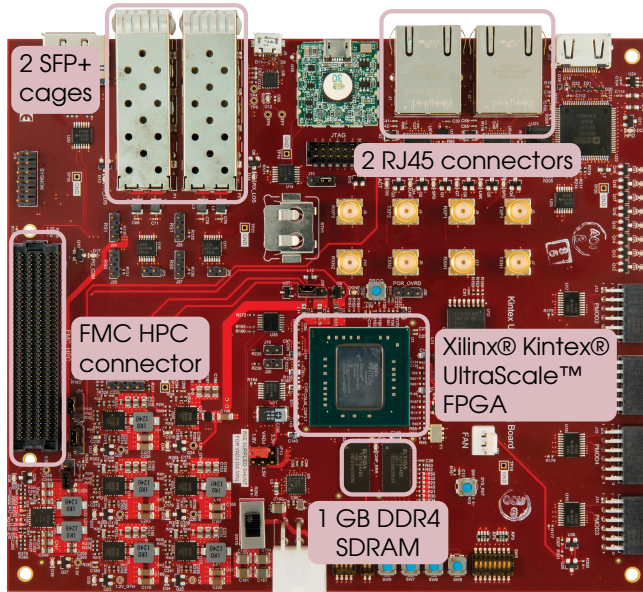
Figure 4.3: The event correlator board with main features high-
lighted. Adapted from reference [268].

Since there are two cZDDs and also two ADC boards (east and
west side of BESIII), the event correlator receives two data streams.
If multiple pulses are observed in different channels but within a
close timing window, they are combined into a cZDD subevent. Af-
terwards, the subevent is written to memory. Upon receipt of an L1
trigger, the memory is searched for the corresponding subevent. If
the search is successful, the subevent will be sent to the BESIII event
builder via Gigabit Ethernet.

Slow control proceeds via Gigabit Ethernet too. Since the only
external connection to the ADC boards are the optical fibers to the
event correlator, the latter one needs to bridge the control and mon-
itor signals to the ADC boards via said fibers. The full DAQ is
sketched in Figure 4.4.

4.3   *Material in Front of the Detector*

The cZDD will be located outside the vacuum chamber. Hence,
the ISR photons coming from the interaction point (IP) will need
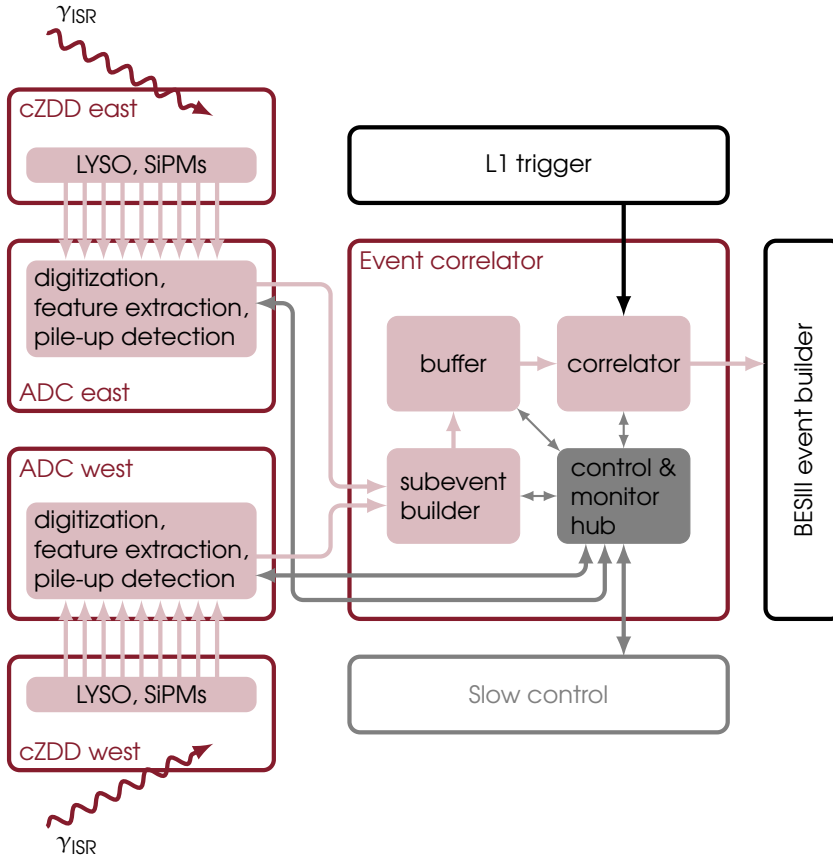
Figure 4.4: Data acquisition scheme of the cZDD. Boxes with a solid border stand for separated hardware components. The general data flow is from left to right. Light red arrows indicate the data stream holding physical information about an cZDD event. Gray arrows represent control and monitor signals. The L1 trigger signal is the black arrow.

to traverse the corresponding material in order to reach the cZDD. The path of the ISR photons through the accelerator structures is sketched in Figures 4.5 and 4.6(a). The statement that the highest ISR photon flux is at 0° (and 180°), holds only true in the center-of-mass frame. Due to the non-zero crossing angle between the two beams, the center-of-mass frame is slightly boosted in x direction with respect to the laboratory frame. In the latter reference frame, the ISR photons follow the outgoing beam at an angle of 11 mrad to the z-axis. The outgoing beam is bent by the so-called ISPB magnet for a quicker separation of the two beam pipes. The ISR photons continue to travel on a straight line and exit the vacuum chamber. The beam pipe wall in this region is slightly tilted, such that the effective path length in the material is reduced. Although this window was designed with the radiative Bhabha photons for the BLM in mind, it serves the same purpose for the cZDD.

Unfortunately, the tilt angle is rather small and the effective length still varies between 2.4 and 7 cm, depending on which of the cZDD crystals is aimed for. Like most part of the beam pipe, the window is made from copper and the ISR photons have to pass 1.6 to 5 radiation lengths. The smallest material budget is reached for the corner crystal of each cZDD block directly at the separating gap and closest to the outgoing beam pipe. Those crystals are marked by a dot in Figure 4.1(b). Figure 4.6 shows a close-up of the region around the cZDD. As one can see, only the outer edge of the cZDD can be directly hit by photons originating at the IP. Photons at a different angle would either miss the cZDD, or get absorbed by the ISPB magnet yoke or the bellows at the incoming beam pipe.

In order to investigate the effect of the material in front of the cZDD, parts of the accelerator structure were implemented in the Geant4 simulation (cf. Figure 4.7). The summed energy depositions in the material and in the cZDD for typical events is shown in Figure 4.8. Even when the photon momentum points directly to the aforementioned corner crystal with the least material in front, there is a significant energy deposition outside the cZDD, in particular in the beam pipe window and due to shower leakage caused by the compact size of the detector. On an event by event basis, the energy information is almost completely lost. It turns out that the cZDD cannot be used as a calorimeter but only as a tagger. A tagger measures only if an event occurs but not the corresponding energy. This is still valuable for the analysis of ISR events because it can be
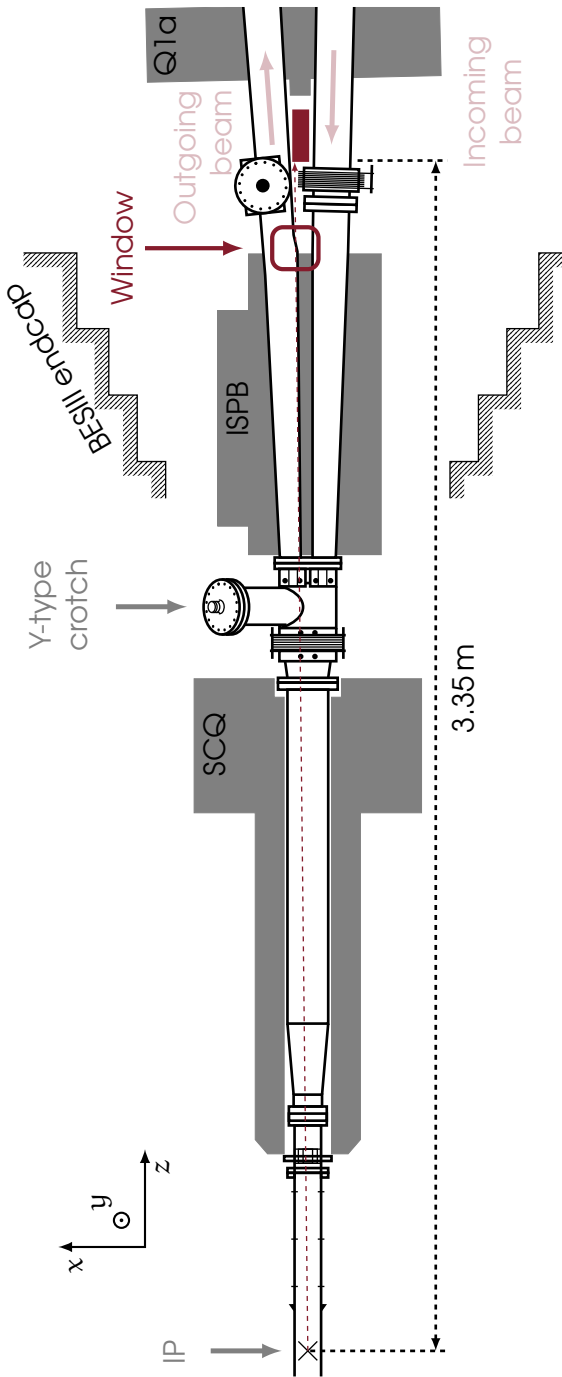
Figure 4.5: Top view of the accelerator structures between the interaction point (IP, bottom) and the cZDD (red, right hand side). The incoming and outgoing beams share a common beam pipe until they split at the Y-type crotch. The gray areas indicate magnets. The superconducting quadrupole magnet (SCQ) is for the final focus of the beams. The ISPB magnet deflects only the outgoing beam and the Q1a magnet is a quadrupole. The path of the ISR photons is indicated by the dashed red line. They leave the vacuum chamber through the window, a slightly tilted part of the beam pipe wall. A magnified view of the region around the cZDD is shown in Figure 4.6(a). Figure based on reference [270].

(a)   *(b)*
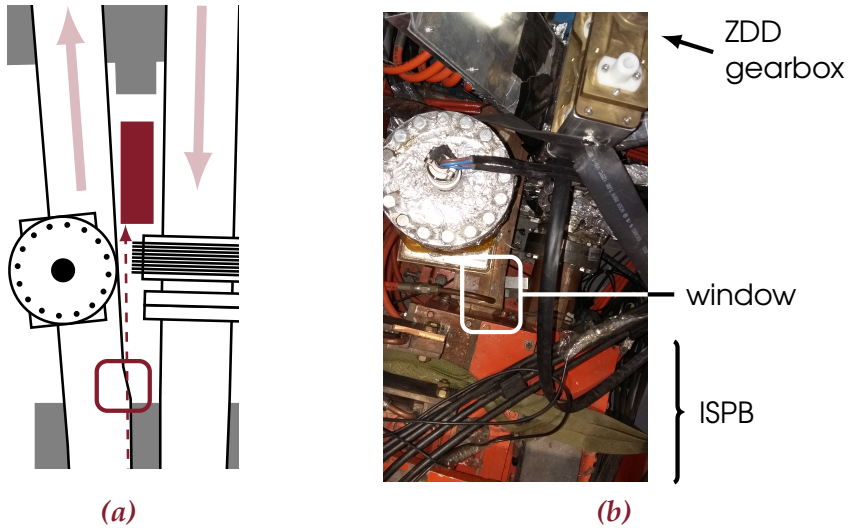
Figure 4.6: Close-up view of the cZDD region and the beam pipe window. *(a)* Schematic drawing. The path of the ISR photons is indicated by the red dashed arrow. The red area indicates the cZDD between the two beam pipes and the red rectangle marks the beam pipe window. Figure based on reference [271]. *(b)* Photograph of the same region. The window is indicated by the white rectangle. The orange structure at the bottom is the ISPB magnet. The gearbox for the vertical movement of the present ZDD is visible in the top right corner. The ZDD is directly below the gearbox.

used to suppress background in an untagged analysis, where the ISR photon's four momentum is inferred from the total four momentum balance. When the photons are aligned with the direction of highest ISR and radiative Bhabha photon flux of $\theta = 11$ mrad, the photons would escape through the gap between the two cZDD blocks. The interaction with the window starts a shower partly hitting in the detector.

Brice Garillon from Mainz took over the simulation studies. In order to investigate the background rate, he simulated radiative Bhabha events with the event generator BBBREM [272] and found out that the event rate in the cZDD is in the MHz region [273]. It is mostly dominated by low energetic cZDD events. When a minimum energy deposition of 100 MeV is required, the rate drops well
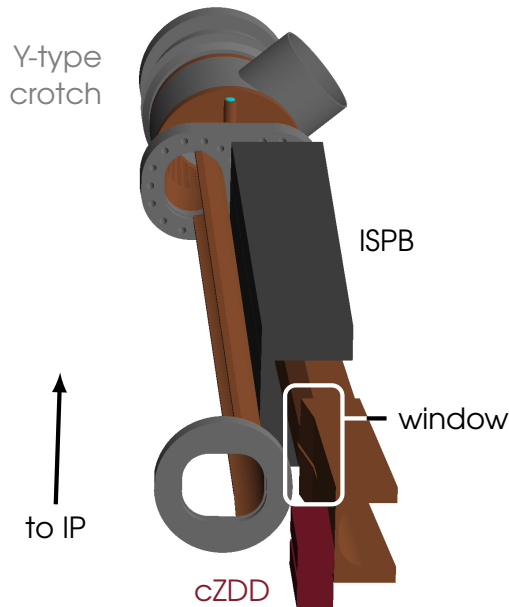
Figure 4.7: Geometry of the Material in front of the cZDD as imple-
mented in Geant4. Most parts of the vacuum chamber are made
from copper (brown). Few parts are made from stainless steel (gray)
and the ISPB magnet yoke (dark gray) is made from iron. Only the
sides of the incoming and outgoing beam pipes facing the cZDD are
implemented because the other sides will not affect the cZDD.

below the 1 MHz mark. The high rate is mostly concentrated on the
corners closest to the $\theta = 11$ mrad axis (the aforementioned crystals
marked by a dot in Figure 4.1). The crystals far from this corner
are not directly hit by incident photons (or electrons/positrons from
showers), due to the screening by the accelerator structures. Never-
theless, they register an important energy fraction of the shower that
started in the cZDD. A simulation of ISR events with the Phokhara
event generator [274–276] showed that the corner crystals together
with the neighboring crystals above/below detect about 5 % of all
ISR photons, although they cover only 0.4 % of the solid angle.[2]

---

[2]Comparison: the EMC covers 93 % solid angle and detects $15 - 20$ % of the ISR
photons.

(a)

(b)
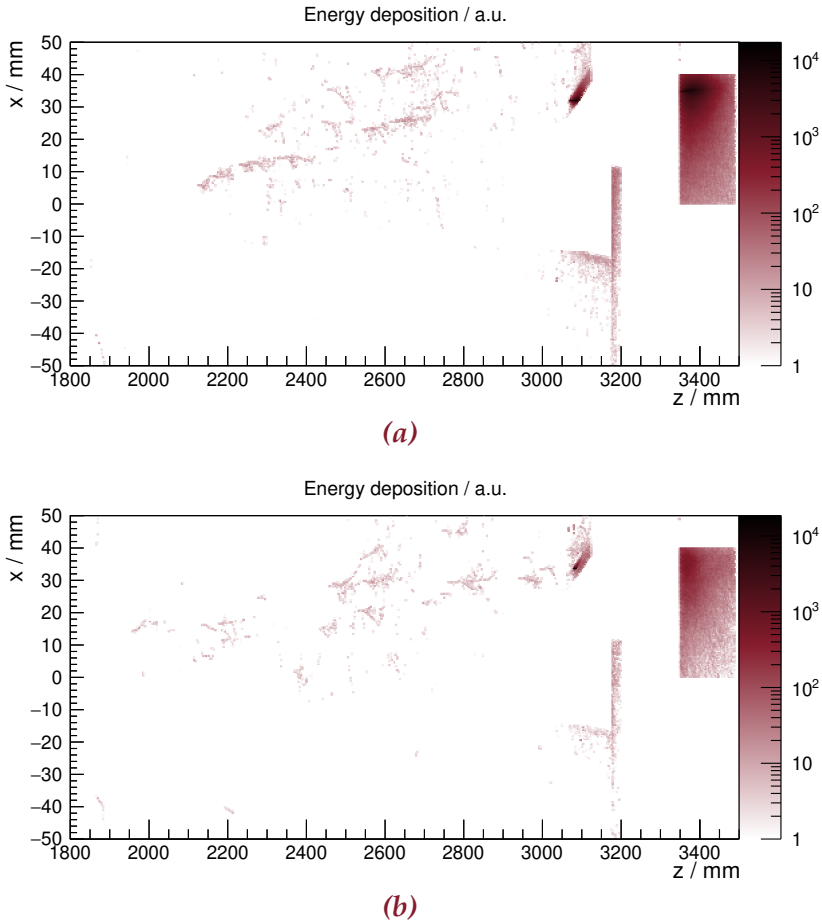
Figure 4.8: Simulated energy deposition as function of the z and x positions. The sum of 10 000 single photon events with 1 GeV is shown. *(a)* The photons aim at the corner crystal with least material budget in front. *(b)* The photons follow the 11 mrad trajectory of maximum ISR (and radiative Bhabha) photon flux. In both cases, two hot spots at the beam pipe window and the rectangular cZDD are visible. In the second scenario, the cZDD registers an energy deposition only because the photons already start to shower in the window. Without any material, the photons would escape through the gap between the cZDD halves without any interaction.
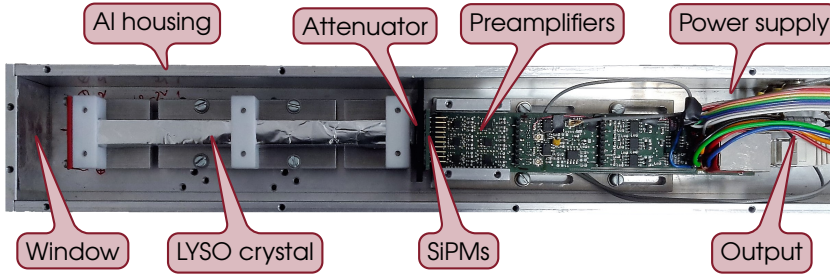
Figure 4.9: Prototype module of the cZDD. The top of the aluminum housing is removed to give insight into the detector.

4.4 Prototype Beam Test

The cZDD will experience a background rate in the MHz region. It is worth noting that the vast majority of those events include a hit in the aforementioned corner crystals. For that reason, it is very important to know the detector's response to such a high rate beforehand. In order to study the behavior of the crystals, the SiPMs, and the ADCs with the DAQ in a high rate environment, a prototype cZDD module was built and tested in a test beam. The prototype module was build by the Mainz group and the prototype DAQ was developed as part of this thesis.

4.4.1 The cZDD Prototype Module

Figure 4.9 shows a photograph of the cZDD prototype module. The sensitive material is a single LYSO crystal with the $1 \times 1 \times 14 \, \text{cm}^3$ dimensions like the full cZDD design. All sides but the back are wrapped in aluminum foil. The used SiPMs are of the 60035 type from the SensL C series [263] with the fast output terminal. They have an active area of $6 \times 6 \, \text{mm}^2$ with 18980 pixels of each $35 \, \mu\text{m}$. They are arranged in a 3×3 array. During the beam test, the SiPM plane was shifted with respect to the crystal. Only one of the SiPMs was completely behind the $1 \times 1 \, \text{cm}^2$ crystal end face. Three others were partly covered by the crystal. In order to avoid saturation of the SiPMs, an optical attenuator was placed between the crystal and the SiPMs. All the above components are held in position within a light tight aluminum housing. A small entrance window made of aluminum foil at the front reduces the material budget in front of the crystal.

4.4.2 The Prototype Data Acquisition

The DAQ for the beam test already uses the designated hardware for the final cZDD setup, i.e. the ADC and event correlator boards (cf. Section 4.2.2). The difference to the full design is basically a reduced firmware on the respective FPGAs. First of all, the FPGA on the ADC board performs no pulse detection, but directly pipelines the stream of digitized samples to the event correlator board.

The reason for not implementing a pulse detection algorithm is that it requires the full knowledge of the pulse shapes under the high rate conditions. Before the beam test, however, this information is unknown and only acquired by recording the complete waveform during the test. In a later stage, the pulse shapes are analyzed and a suitable detection algorithm is developed offline without the tight time constraints of a beam test (cf. Section 4.5.1).

Despite its name, the event correlator does not perform the cZDD subevent correlation with a trigger, simply because of the absence of a trigger signal in the beam test. In addition, there is no subevent building because it would require time stamps of detected pulses. They are not available in the streaming mode. The event correlator is basically just a bridge between the ADC board and a PC substituting the BESIII event builder in the prototype test beam setup. The PC receives the data and writes it to disk.

The following pages detail the parts of the firmware, that have been developed in the context of this thesis.

Firmware Development

Firmware running on an FPGA is usually written in a hardware description language (HDL) like VHDL.[3] A software maps the described hardware onto the available FPGA resources and produces a configuration file which is to be loaded to the FPGA. As the FPGAs in the cZDD (prototype) DAQ are produced by Xilinx, the corresponding software from Xilinx has to be used which is the Vivado® Design Suite [277].

In large projects, a firmware is often structured in a modular fashion into independent units called IP cores.[4] These building

---

[3]VHDL stands for VHSIC hardware description language and VHSIC in turn stands for very high speed integrated circuit.

[4]IP stands for intellectual property.

blocks can have arbitrary complexity ranging from a simple first-in-first-out buffer (FIFO) to a DDR4 memory controller. Many IP cores are provided by the FPGA manufacturer and are ready to use, while others need to be licensed. Most IP cores have customizable parameters in order to be adaptable to a wide range of applications.

Proper data transfer between IP cores is guaranteed by complying with standardized protocols. Many IP cores running on FPGAs from Xilinx have interfaces conforming to the AXI4 specification of AMBA® [278]. There is the distinction between three different AXI4 protocols: AXI4-Stream, AXI4-Lite, and (full) AXI4. AXI4-Stream is, as the name suggests, a protocol for streaming data from one master interface to one slave interface. AXI4-Stream is well suited for pipelined designs, where data is transferred through a chain of IP cores. The other two, AXI4-Lite and full AXI4, are memory mapped bus protocols. A master interface issues write and/or read requests to memory addresses in a slave IP core. A bus-like structure enables the connection between multiple master IP cores and multiple slave IP cores. The full AXI4 bus handles data transfer with high throughput, e.g. writing or reading to/from a DDR memory controller. AXI4-Lite is a reduced version of the full protocol with limited throughput, but the implementation utilizes far fewer resources. Typical applications are the management of control and monitor registers in other IP cores.

Any entity described by HDL source code can be packed into an IP core. Furthermore, the Xilinx software Vivado High Level Synthesis (HLS), offers the user friendly possibility to automatically generate HDL code from source code written in C or C++ [279]. The advantage is that the complex interfaces for the memory mapped AXI4 protocols are immediately realized with the correct switching behavior.

IP cores and the corresponding interconnections can be directly instantiated in HDL source code. As an alternative, the IP cores can be placed on a block diagram, a purely graphic representation provided by the Xilinx IP Integrator as part of Vivado. IP cores are represented by blocks and the connections between them are represented as lines. In the IP Integrator, the required bus structure between memory mapped AXI4 interfaces is automatically generated. An address table defines the memory space of the slave interfaces and guarantees unique addresses of the slave registers.

A simplified version of the block diagram for the firmware running on the event corelator FPGA is shown in Figure 4.10. The individual IP cores are described in the following: first the ones in the path of the ADC data (rose blocks), then the ones for slow control (gray blocks). The full block diagram from the IP Integrator is shown in Appendix A.

Firmware for the ADC Data Path on the Correlator

The path of the ADC data on the correlator starts at the Aurora IP core and ends at the SiTCP IP core. The data is passed through a sequence of IP cores via the AXI4-Stream protocol. In the following, the IP cores of that sequence are described. The IP cores marked with a red frame have been developed within the context of this thesis.

Aurora   The connection between the ADC board and the event correlator board is realized by optical fibers plugged into the SFP+ modules. The data transfer proceeds via the Xilinx® Aurora 8b/10b protocol [280]. It is open-source and easily implementable on FPGAs, in particular on FPGAs from Xilinx. It is designed for (bidirectional) high speed serial data transfer between two end-points. High data rates are achieved by the so-called 8b/10b encoding. Each eight bit data word is transmitted as a ten bit character. The data rate between the two boards is configured to 5 Gb/s. The implied bandwidth for the payload is 4 Gb/s or alternatively 32 bits per 8 ns, the sampling interval of the ADC. Consequently, two of the 14-bit channels can be streamed continuously to the event correlator.

Gate   In order for the processing algorithm to be able to ignore any incoming ADC data, this very simple IP core is inserted directly after the Aurora core. Its sole purpose is to start and stop a data taking run.
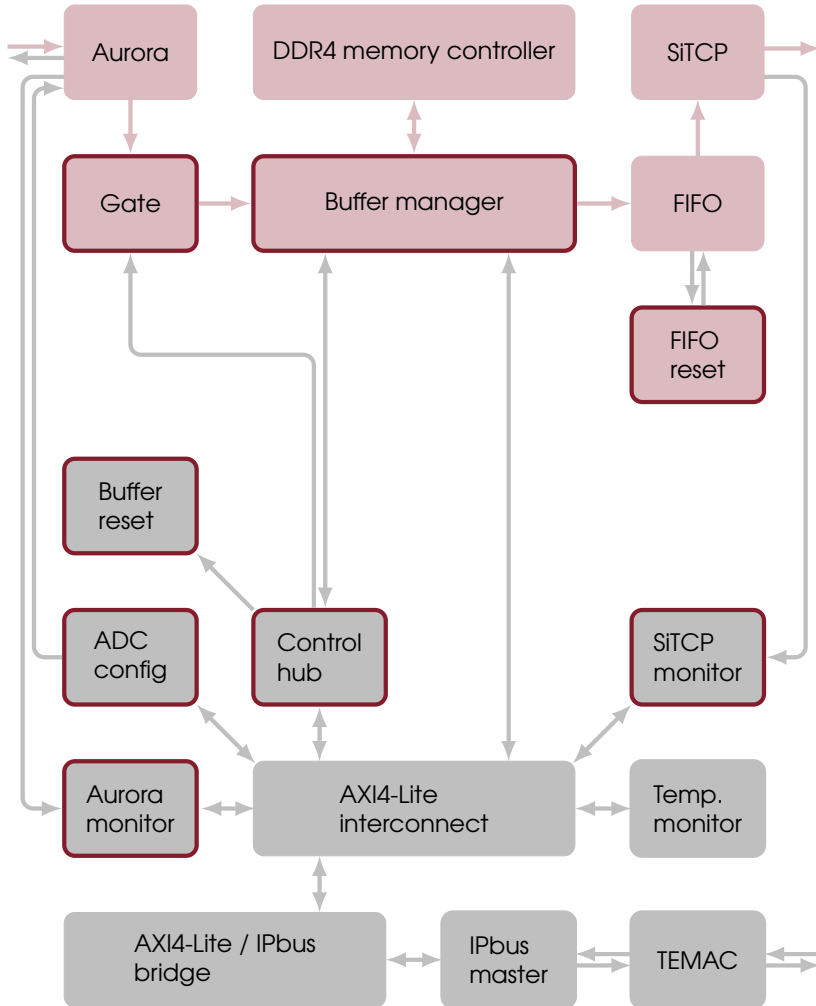
Figure 4.10: Simplified block diagram of the prototype firmware for the event correlator. The IP cores surrounded by a red frame have been developed as part of this thesis. Rose IP cores and arrows represent the path of the ADC data. Slow control connections and IP cores are shown in gray. Arrows with a tip on both sides stand for a memory mapped bus connection (gray: AXI4-Lite, rose: full AXI4). The connection between ADC config and Aurora as well as all internal single-ended arrows in rose depict AXI4-Stream connections. The full block diagram is shown in Appendix A.

Buffer manager   This IP core can redirect the data stream towards the 1 GB DDR4 memory on the correlator board as an alternative buffer. The data is fetched again from the memory and inserted back into the stream towards the PC. However, this feature was deactivated in the beam test and the data was directly sent to the FIFO. The connection between this IP core and the DDR4 memory controller conforms to the full AXI4 standard. Therefore, the Buffer manager IP core has been developed using Vivado HLS.

DDR4 memory controller   This IP core is provided by Xilinx [281]. It represents an AXI4 slave and serves as a bridge to the physical DDR4 memory on board the correlator.

SiTCP   The connection for the outgoing data to the PC is established via Gigabit Ethernet and the TCP/IP standard. The correlator board is assigned an IP address. When connected to a network, the correlator can establish a connection to any other endpoint of the network with an associated IP address. The data is packed in TCP segments. When segment loss is detected, a retransmission is initiated resulting in a lossless data transfer even in complex network topologies.[5] The TCP/IP endpoint is realized by SiTCP (silicon TCP), an available implementation on FPGA logic with slightly reduced functionality [282, 283]. The adaptation of SiTCP to the specific FPGA on the correlator board was performed by Adrian Weber.

FIFO   **FIFO reset**   On the one hand, the data rate between the correlator and the PC is bound by the Gigabit Ethernet limit of 1 Gb/s. On the other hand, the correlator receives the ADC

---

[5]Almost all of the world wide web applications rely on the TCP/IP standard. When not used in the combination "IP core", IP stands for Internet Protocol.

data with 4 Gb/s. This obvious mismatch results in unavoidable data loss. It is handled in the following way: the received data is written with the full data rate into a large FIFO-like buffer[6] and the SiTCP sender reads with a low data rate. As a result, the buffer fills up with time. When full, a reset logic clears the buffer completely and the buffer starts to fill again. This procedure ensures that the data loss does not occur at random positions. Instead, large batches of continuous ADC samples are sent to the PC.

The FIFO is provided by Xilinx [284], while the reset logic has been written specifically for the prototype DAQ.

Firmware for Slow Control on the Correlator

In contrast to the path of the ADC data, the slow control units are organized in a hierarchy. Again, the blocks with red frames represent IP cores, that have been developed as part of this thesis:

IPbus master

Slow control is provided by the open source IPbus protocol [285, 286]. It is based on a UDP/IP via Gigabit Ethernet connection between a notebook PC and the correlator board. UDP is similar to TCP, but without recovery from data loss. It is simpler and hence easier to implement on FPGAs. However, the IPbus protocol provides a method to retransmit lost packets, i.e. data loss is not detected at the UDP level, but at the IPbus level. Hence, IPbus transactions are lossless and reliable. With IPbus, a client on the PC can send read and/or write requests to specific registers on the correlator FPGA. On the FPGA, the IPbus commands are accepted by a piece of logic that acts as a bus master. This master distributes the IPbus transactions to the corresponding slave registers and forwards the reply back to the PC client.

TEMAC

TEMAC stands for Tri-Mode-Ethernet Medium Access Controller and represents an Ethernet implementation. One of

---

[6]FIFO stands for first in - first out.

the three modes correspond to Gigabit Ethernet providing the data link for the UDP/IP protocol of IPbus. The TEMAC IP core has been developed by Xilinx [287].

AXI4-Lite / IPbus bridge   IPbus is designed for a Wishbone bus [288], an alternative standard to AXI4-Lite. In order to benefit from the AXI4 support of the Vivado IP Integrator, this IP core bridges the Wishbone bus to an AXI4-Lite bus. An open-source implementation in VHDL has been used [289].

AXI4-Lite interconnect   The AXI4-Lite interconnect can be viewed as the actual bus structure between the IPbus master and all the slave interfaces. This IP core is provided as part of the Vivado software [290].

Aurora monitor **SiTCP monitor**   Both the Aurora core and the SiTCP core provide status signals. The Aurora monitor and SiTCP monitor IP cores implement read access from the AXI4-Lite bus to those signals. They were developed within Vivado HLS.

Temp. monitor   This IP core monitors not only the on-chip temperature, but also a series of on-chip voltages. The IP core is connected to the bus and hence can be accessed via IPbus. Xilinx provides this IP core [291].

Control hub   This IP core is the control center for taking data. The start and stop of a data taking run is achieved by writing to the corresponding registers of this IP core via IPbus. Furthermore, the command to reset the buffers is issued here.

Buffer reset   All the different IP cores require different types of reset signals. The resets have to be synchronous to different clocks

and need to be asserted for different periods. This IP core generates the required reset signals for the IP cores involved in the processing of ADC data. All buffers are cleared and no data from a previous run can corrupt the data of a new run.

ADC config The only way to access the ADC board is the serial Aurora link to the event correlator. All slow control commands to the ADC board are sent to the event correlator via IPbus, serialized, and sent to the ADC via Aurora. The ADC config IP core stores the commands in registers and generates a data packet to be sent to the Aurora core via the AXI4-Stream protocol. From the Aurora core, the data is sent to the ADC board.

On the PC side, slow control is realized via python scripts using the μHAL library which are part of the full IPbus suite [286].

ADC Firmware

The ADC firmware has been developed on top of a base design by Johannes Müllers (Bonn University) [265] providing a boot sequence for the correct generation of all necessary clock signals and the programming of the ADC chips. Many parts of the firmware were not packed into IP cores and neither was the IP Integrator used. Nevertheless, Figure 4.11 illustrates the interconnections between the different firmware components.

As in the above sections, the blocks with red frames have been developed within the framework of this thesis:

Sync. FIFO For each channel, the ADC chips present a new 14 bit sample at each beat of a 125 MHz clock. However, these ADC clocks are not in phase with the clock of the Aurora core. The data is synchronized by small FIFOs with independent clocks for reading and writing. Since each of the two FPGAs on the board handles 32 channels, this synchronization stage is instantiated 32 times, once for each channel.
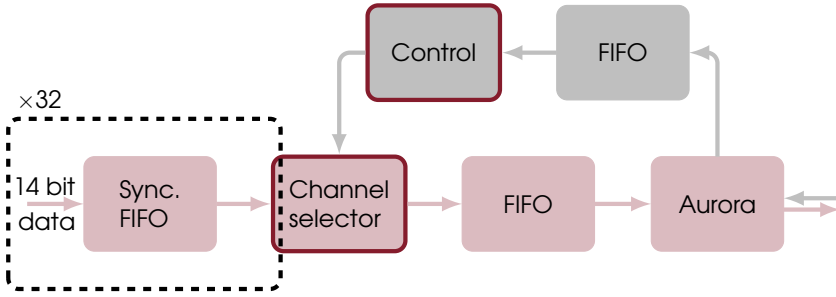
Figure 4.11: Simplified block diagram representing the ADC data path of the prototype firmware for the ADC board. The IP cores surrounded by a red frame have been developed as part of this thesis. Rose IP cores and arrows represent the path of the ADC data. Slow control connections and IP cores are shown in gray.

Channel selector This part acts as a multiplexer: It selects the data of two channels which are sent to the correlator. At this point, the data stream is formatted into 32 bit words.

FIFO FIFO The Aurora core itself does not buffer the data, neither in the transmit nor in the receive path. The insertion of FIFOs compensates for this.

Aurora This is the Aurora core sending the ADC data off-board to the event correlator. In addition, the IP core receives the slow control commands from the event correlator.

Control The slow control commands for the ADC are received by the Aurora core and is formatted according to the AXI4-Stream specification. The Control block receives this data stream. The data is parsed and written into corresponding registers. Two kinds of control signals are handled: the first one specifies the polarity of the SiPM signals and the second one indicates which channel(s) to pipeline to the correlator.
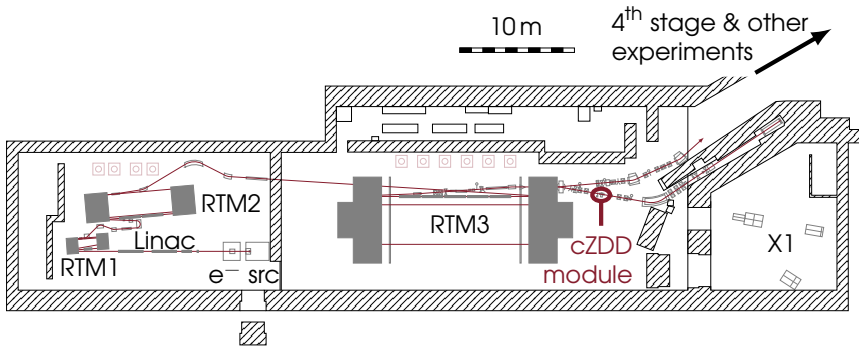
Figure 4.12: First section of the MAMI accelerator. The electrons are transferred from the source via the injector linac to the first RTM. Two more RTMs follow and the beam can either be directed to the fourth acceleration stage or towards the X1 experiment. The cZDD prototype module was positioned at the latter beamline directly after RTM3. Figure based on reference [271].

An earlier version of the prototype DAQ was already running successfully in a test of the prototype module with radioactive ^{60}Co and ^{137}Cs sources. The results were reported in reference [292]. However, both the energy and the rate were far from a realistic emulation of the designated cZDD environment at BESIII. This can only be achieved in a beam test.

4.4.3 Setup and Conduction of the Beam Test

The beam test was carried out at the MAMI (Mainzer Mikrotron) facility [293] at the Institute of Nuclear Physics of the Johannes Gutenberg University (JGU) Mainz in November 2017. MAMI is an accelerator complex providing a continuous beam of (polarized) electrons with energies up to 1.5 GeV and beam currents up to 100 μA. The acceleration proceeds via three consecutive racetrack microtrons (RTMs) and another fourth stage. The prototype module was positioned at the X1 beamline behind the third RTM (see Figure 4.12). At this location, the maximum available beam energy is 855 MeV.

Figure 4.13 shows the cZDD prototype module at the beamline. The module can be positioned in and out of the beam by a remotely

Figure 4.13: Setup of the prototype beam test. The electron beam enters from the right-hand side. Before it hits the module head on, it passes through a thin plastic scintillator paddle. The module was clamped to a remotely controllable table allowing movements in x (horizontal) and y (vertical) directions. The large green structure in the background is one of the two 450 t heavy dipole magnets of RTM3.

controllable x/y table. The detector was positioned in such a way that the crystal front was centrally hit. Thanks to the small beam diameter below 1 mm, no fraction of the beam missed. A plastic scintillator paddle was placed in front of the module for an independent measurement of the event rate. The paddle was sufficiently thin for not triggering an electromagnetic shower. As a result of the fast response of the plastic, the measurement is robust against pile-up. The rate information was available in real time during data taking.

Data of only one channel was recorded: the fast output of the one SiPM being fully covered by the LYSO crystal. The whole data taking was controlled remotely. In order to have an independent DAQ as a benchmark, the pulses were also recorded by an integrating ADC[7]

---

[7]Or charge-to-digital converter (QDC).

operated by Peter Drexler (JGU Mainz). Additionally, the signal was monitored with a digital oscilloscope.

Since the purpose of the cZDD is the detection of ISR photons in the region around 1 GeV, the energy for the beam test was chosen to be 855 MeV. However, the primary goal of the beam test was to study the behavior when exposed to high rates in the MHz region. Therefore, data was taken at several rates around 1 MHz. The beam current was increased stepwise until no individual pulses were recognizable by eye on the oscilloscope and the ADC output. This happened slightly below a rate of 14 MHz. As mentioned in Section 4.3, this is far above the expected rate, in particular for high energy depositions. Additionally, a data sample was recorded at roughly 3 kHz, at which rate the probability for pile-up was very low. This sample can be regarded as pile-up free. It is very important for the development of pile-up detection algorithms being presented in the next Section. In total, the waveforms at 15 different rates were recorded.

4.5 *Waveform Analysis*

The algorithms presented in this Section were developed on a PC using C++ and the ROOT framework [294]. Nevertheless, they meet the strict requirement of being easily implementable on FP-GAs. They were optimized based on the data recorded in the beam test.

4.5.1 *Pulse Detection*

Figure 4.14 shows the recorded waveforms at 718 kHz and 1.5 MHz. Waveforms corresponding to other rates are listed in Appendix B.1. The pulses start with a very sharp rise and reach the peak already at the first or second sample (rise time between 8 and 16 ns). A striking feature of the pulses are the undershoots. They are caused by capacitive coupling in the fast output of the SiPMs [263]. The pulses of the slow output are much longer, but do not have such undershoots. The energy information is encoded in the integral of the positive part. In the following, only this positive part is referred to as a pulse and the part below the baseline is termed undershoot. The duration of a pulse is approximately 100 ns and the undershoot takes about 750 ns until the signal returns to the baseline.
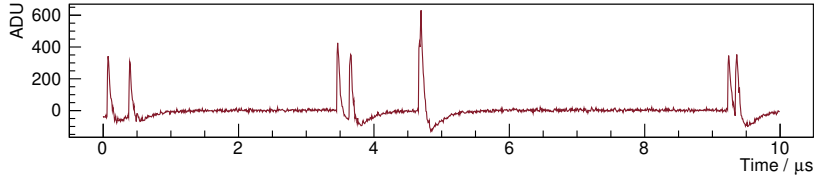
(a)
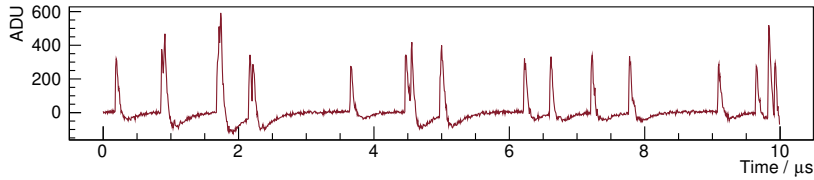
(b)

Figure 4.14: Recorded waveforms at rates of ***(a)*** 718 kHz and ***(b)*** 1.5 MHz.

When comparing the waveforms at increasing rates, not only a more abundant pile-up, but also a decrease of the pulse height is noticeable. Figure 4.15 shows the average pulse integrals as a function of the rate.[8] Data from both the sampling ADC and the QDC is shown. The degradation with increasing rates is apparent in both independent measurements. The QDC observes a slightly stronger effect. Overall, a decrease of more than 60 % percent is observed by the ADC (QDC) for 6 MHz (3 MHz). However, the pulse height will go further down at higher rates. This behavior is likely caused by a long recharging time of capacitors in the preamplifier circuitry. In fact, at the very beginning of the beam test, the effect was much stronger pronounced. As a counter measure, the resistors in the RC circuits were replaced. All data was recorded after the replacement. Unfortunately, the pulse height degradation could not be prevented completely.

The data points line up to a smooth trend with the exception of the data recorded at 50 kHz. Both the QDC and the sampling ADC consistently observe a significant lower pulse integral than expected from the other points. This behavior can be explained by the order in which the data was taken: the deviating data point at 50 kHz

---

[8]The heights and integrals of the pulses are proportional.
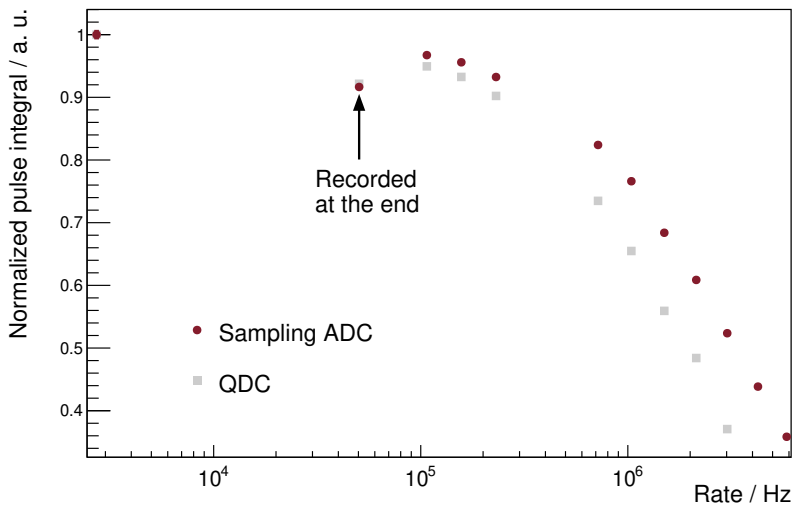
Figure 4.15: Pulse integral degradation as seen by both the sampling ADC and the QDC. The error bars are smaller than the marker size. The second data point (at 50 kHz) was recorded after all the other points. The deviation of this point from the overall trend is explained in the text. The data at the highest rates is not included because the large amount of pile-up does not allow the extraction of a meaningful pulse integral.

was recorded at the very end of the beam test, while the other ones were recorded in the order of increasing rates. In particular, for the higher rates, the crystal was exposed to a non-negligible amount of UV light, which is part of LYSO's scintillation emission spectrum. When illuminated with UV light, however, scintillators exhibit a decrease of light output [295, 296]. The recovery takes several hours to days until the full light output is restored. Only an extreme exposure (direct sun light for several minutes to hours) causes permanent damage. However, the final cZDD probably will not suffer from this UV effect because both the rate and the average energy deposition will be much smaller.

The first step towards a pulse shape analysis is the identification of pulses. The quickly rising edge is a clear indicator for a pulse. As the individual samples are coming in, the algorithm continuously calculates the difference of two consecutive samples. Whenever this difference surpasses a threshold, the algorithm marks the corre-

sponding sample as the beginning of a pulse. For the test beam data, a threshold of 100 ADU has proven to be a good value.[9] The pulses are recognized without any contamination from baseline noise. The pulse is defined to end at the last sample above the baseline. Basically, all consecutive samples above the baseline are defined to be part of the pulse. Therefore, a proper determination of the baseline is necessary. In order to minimize the impact of fluctuations, the baseline is estimated from the average of eight samples before the pulse.

As an effect, the baseline is only estimated correctly, when the baseline has no slope. When the pulse starts during the undershoot of a previous pulse, the baseline is evaluated incorrectly. In the first part of the undershoot, when the signal is falling, the baseline is overestimated. In the second part, when the signal rises, the baseline is underestimated. An underestimated baseline leads to an overestimated pulse integral and vice versa. This effect is proportional to the slope of the signal, i.e. the effect is strongest, when a second pulse arrives in the first part of an undershoot. Figure 4.16 shows for various event rates the average pulse integral as a function of the passed time since the previous pulse. The diagram starts at 240 ns, which is already in the rising part of the undershoot. As expected, the pulse integral is overestimated. The deviation reaches about 6 %. In addition, the diagram implies that the deviation is independent from the total rate. As a consequence, a correction factor can be determined from the time since the last pulse. The correction does not have to be applied on the FPGAs in realtime, but can be performed offline.

4.5.2 Pile-Up Detection

With the previous pulse detection algorithm, the pulse(s) in Figure 4.14(a) at a time of 12.5 μs are interpreted as one single pulse. However, there are actually two pulses shortly after another.

Ratio of Pulse Height to Pulse Integral

Candidates for these pile-up events can easily be identified by comparing the height and the integral of the pulses. For a single event without pile-up, the two quantities are proportional to another. A

---

[9]The unit ADU is commonly used for ADC outputs.
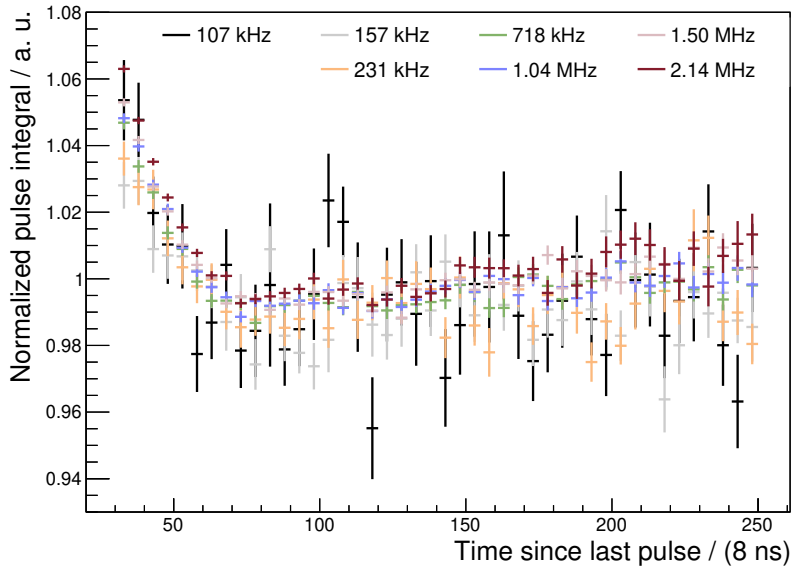
Figure 4.16: Pulse integral variation with the passed time since the previous pulse. The normalized pulse integrals from seven different rates between about 100 kHz and 2 MHz are superimposed. The time axis is plotted in units of the ADC's sampling interval (8 ns).

second pulse, which appears shortly after the first one, increases the total integral, but not the pulse height. Figure 4.17(a) plots the abundance distribution of the detected pulses as a function of both the pulse integral and height for a rate of 1.5 MHz. In Figure 4.17(b), this distribution is projected on the pulse integral axis. The effect of pile-up is visible as a second peak at integral values approximately twice as high as the ones of the main peak. The main peak itself has a tail on the left side, arising from the previously described underestimation of the pulse integral, when the pulse emerges during the start of a previous undershoot. The main peak, its tail, and the pile-up peak can also be seen in the 2D distribution. The main peak corresponds to the dense accumulation marked as A. The tail (B) is visible to the left bending down towards the origin. Pile-up actually corresponds to the two accumulations C and D in the 2D plot. Most of the pile-up events are located at C.

A cut on the ratio of pulse height to pulse integral (illustrated by the gray lines) eliminates the tail as well as a bit more than half of the pile-up as shown in Figure 4.17(b). The pile-up accumulation
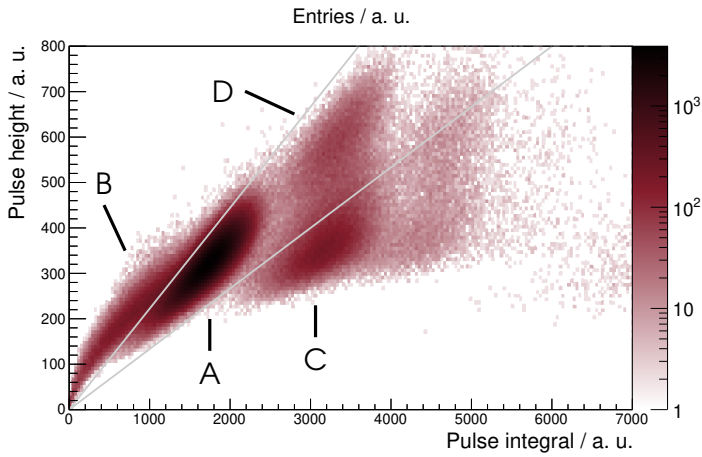
(a)
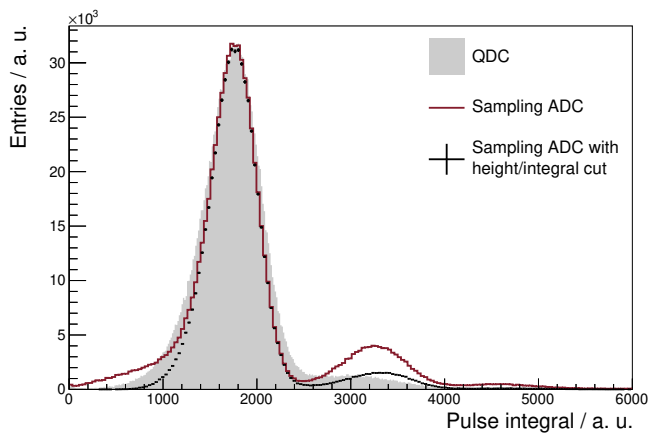
(b)

Figure 4.17: Pile-up detection via the ratio of pulse integral to height. *(a)* Two-dimensional abundance distribution of pulses in the plane spanned by the pulse integral and height. The gray lines indicate the cuts described in the text. *(b)* Distribution of pulse integrals (red line). The same distribution after the cut is plotted with black crosses. For comparison, the gray area depicts the distribution recorded by the QDC. In both plots, data of the 1.5 MHz run is shown.

labeled D cannot be removed by this cut. A significant fraction of pile-up events survive.

More Features

In order to improve the pile-up rejection, an alternative method makes use of additional features of the pulses. In total, it considers the following nine parameters.

Integral / height ratio. The simple method for pile-up detection (presented above) only relies on a cut on this ratio. Here, the ratio is one of many variables.

Pulse length. The width of a pulse is also an indicator for pile-up. Overlapping pulses will extend the duration until the signal crosses the baseline again. As a result, the detected pulse has a larger width. Pulses consisting of more than 20 samples are considered as pile-up and not subjected to any further online analysis.

Secondary peak height. A pile-up event occurring during the falling edge of a previous pulse is visible as a second rise of the signal. The difference between the highest point of the second pulse and the lowest point before that rise is called secondary peak height. Electronic noise from the electronics can also produce such a secondary peak, however, with much smaller height. This variable is not normalized to the integral or the pulse height because noise as well as the height of an overlapping pile-up pulse is independent of the height of the first pulse.

Legendre moments. The shape of a function $f(x)$ can be characterized by moments. The nth order moment is given by (provided the integral converges):

$$\mu_n = \int x^n f(x) \, dx \quad .$$ (4.1)

Applied to functions with a discrete argument, the integral is converted into a sum:

$$\mu_n = \sum_i x_i^n f(x_i) \quad .$$ (4.2)

For the pulse shape analysis, the powers of x are replaced by Legendre polynomials (cf. reference [297]), which are given by

$$P_0(x) = 1 \tag{4.3}$$

$$P_1(x) = x \tag{4.4}$$

$$P_2(x) = \frac{1}{2}\left(3x^2 - 1\right) \tag{4.5}$$

$$P_3(x) = \frac{1}{2}\left(5x^3 - 3x\right) \tag{4.6}$$

$$P_4(x) = \frac{1}{8}\left(35x^4 - 30x^2 + 3\right) \tag{4.7}$$

$$P_5(x) = \frac{1}{8}\left(63x^5 - 70x^3 + 15x\right) \tag{4.8}$$

$$P_6(x) = \frac{1}{16}\left(231x^6 - 315x^4 + 105x^2 - 5\right) \tag{4.9}$$

up to 6th order.

Legendre polynomials are advantageous in that they form an orthonormal basis on a compact interval. For the above representation, the interval is $[-1, 1]$. However, the polynomials can be transformed to any compact interval including $[0, 20]$, the perfect choice for the pulses with a maximum allowed length of 20. For a pulse, the x_i are always just $0, 1, 2, \ldots, 20$. As a consequence, the polynomials $P_n(x_i)$ can be precomputed and do not need to be calculated on the FPGA.

Prior to computing the moments, the pulse samples are normalized to the pulse height. Otherwise, large pulses would always have larger (absolute) moments. The Legendre moments of orders one to six are used. The zeroth order is identical to the pulse integral and corresponds after normalization to the integral to height ratio. This ratio is already the first variable to be used for the pile-up detection (cf. page 81).

The distributions of the first three variables and the first Legendre moment are shown in Figure 4.18 for event rates of 2.72, 718, and 1500 kHz. The data with the lowest rate can be considered as a control sample without pile-up. The distributions of all nine variables are listed for all different rates in Appendix B.2.
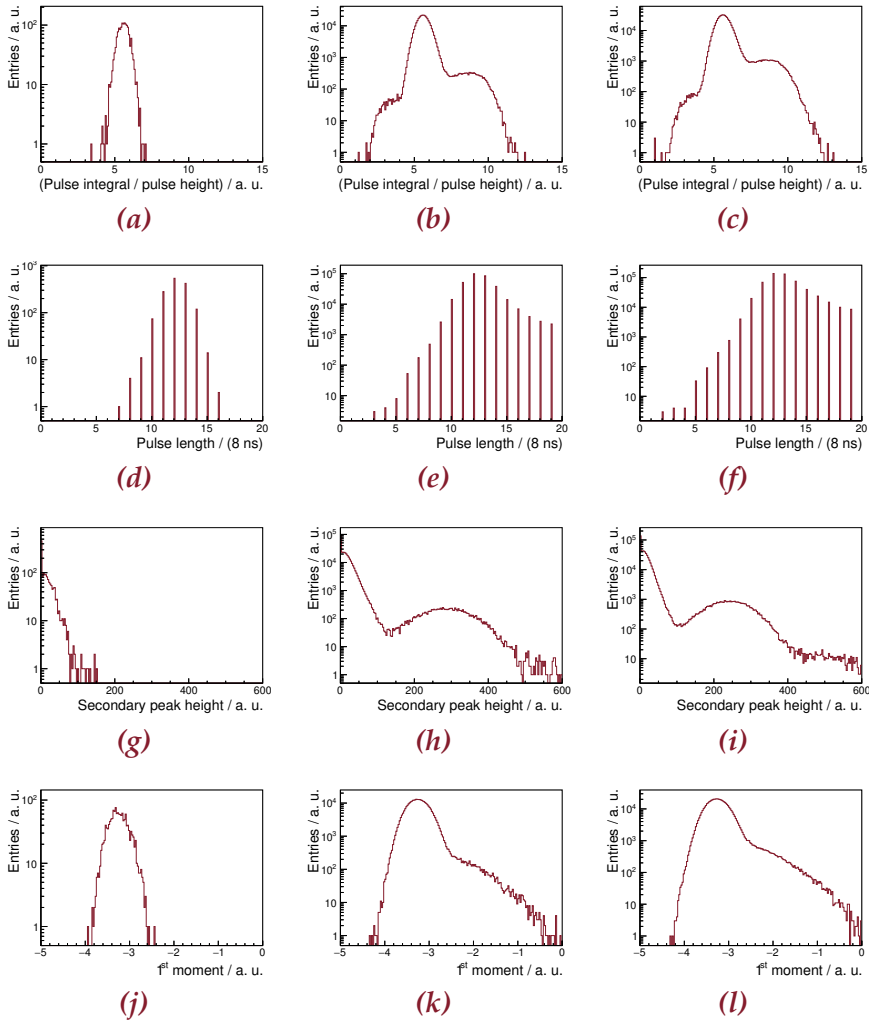
Figure 4.18: Distributions of pulse features used for pile-up detection. The first column shows the data taken at 2.72 kHz. The second (third) column corresponds to 718 kHz (1.5 MHz). *(a)* - *(c)* The first row shows the distributions of the integral / height ratio. *(d)* - *(f)* The second row shows the pulse length distributions. *(g)* - *(i)* The third row shows the secondary peak height distributions. *(j)* - *(l)* The fourth row shows the distributions of the first Legendre moment.

Principal Component Analysis

In an offline algorithm running on a CPU, the aforementioned features could be fed to a neural network or any other machine learning method. Such a design, however, is too complex to be implemented with the available FPGA resources. Nevertheless, directly cutting on the features is not the best alternative because of unknown correlations among them.

By means of a principal component analysis (PCA), the features are converted into decorrelated variables. Formally, this is done by diagonalizing the (symmetric) covariance matrix via the principal axis theorem (cf. reference [298]). If Σ is the covariance matrix, the transformation

$$\Lambda = \Gamma^{\mathrm{T}} \Sigma \Gamma \qquad (4.10)$$

will yield the diagonal matrix Λ. The matrix Γ is constructed from the eigenvectors of Σ. The corresponding eigenvalues appear on the diagonal of Λ. The vector of features f is transformed by

$$p = \Gamma^{\mathrm{T}} f \quad , \qquad (4.11)$$

resulting in p being the vector of principal components (PCs). The PCs are linear combinations of the original features. The new covariance matrix is Λ, hence the PCs are uncorrelated and the variances are on the diagonal. The PC can be ordered by their variance. The larger the variance, the more information is carried. In the pile-up detection algorithm, cuts are applied to the six different PCs with the highest variances. The overall performance does not benefit from a cut on the other PCs. On one hand, the covariance matrix of the features is different for different rates. On the other hand, the transformation must be universally applied to all data independent of the rate. The transformation diagonalizing the covariance matrix of the 1 MHz data is chosen as the universal one.

Prior to the actual PCA, the input features are normalized to have the same variance. This is required to keep the features at a comparable scale. Otherwise, the eigenvalues would be distorted and no longer reflect the information content of the PCs.

Figure 4.19 shows the distributions of the first three PCs at 2.72, 718, and 1500 kHz. Also, the cut values are indicated. They are optimized to enclose the distribution of the 2.72 kHz control sample. Pulses outside these intervals are considered as pile-up. Again, the distributions of all PCs can be found in Appendix B.2 for all rates.
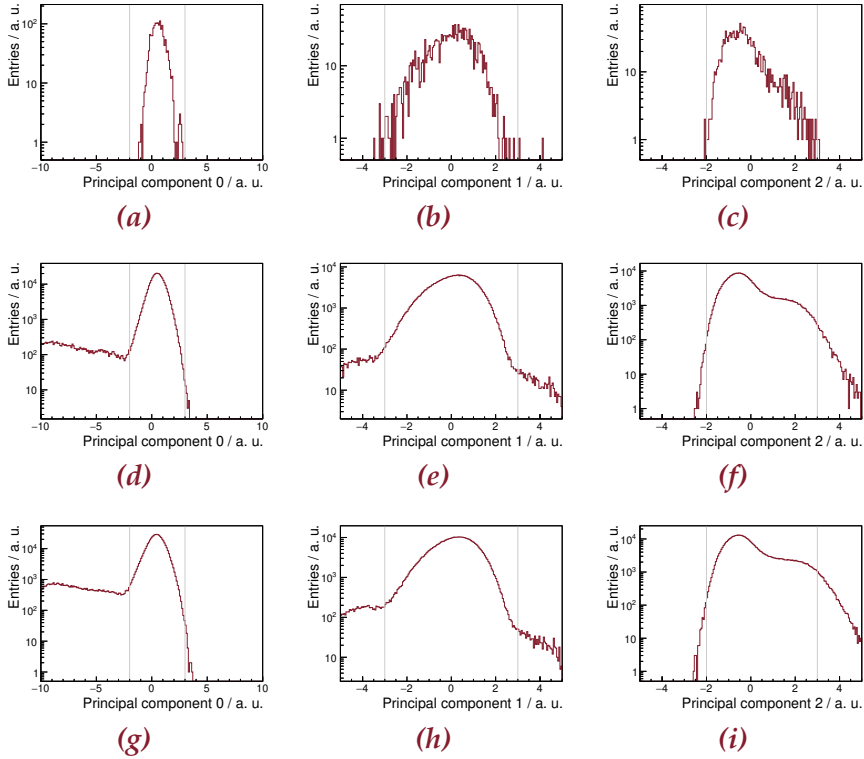
Figure 4.19: Distributions of pulse PCs used for pile-up detection. The first column shows the data taken at 2.72 kHz and the second (third) column corresponds to 718 kHz (1.5 MHz). *(a)* - *(c)* The first row shows the distributions of the integral / height ratio. *(d)* - *(f)* The second row shows the pulse length distributions. *(g)* - *(i)* The third row shows the secondary peak height distributions. The gray lines indicate the cut values, i.e. only data within the two lines is accepted.
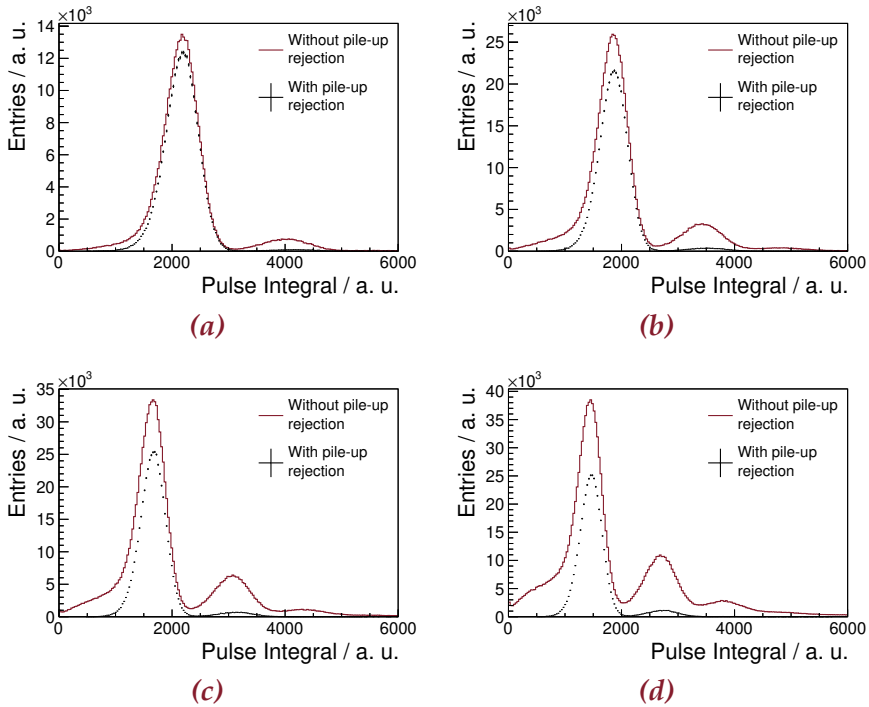
Figure 4.20: Pulse integral spectra with and without pile-up rejection at event rates of *(a)* 718 kHz, *(b)* 1.5 MHz, *(c)* 2.14 MHz, and *(d)* 3.02 MHz.

Result

Figure 4.20 shows the pulse integral spectra of data taken at rates between about 0.7 and 3 MHz. The spectra corresponding to all rates can be found in Appendix B.2. Both the raw spectrum without any cuts as well as the spectrum after pile-up rejection cuts are shown. The cuts not only include the previously discussed PCs, but also two more variables. As mentioned before, maximum pulse length is restricted to 20 sample points. The other cut rejects pulses occurring earlier than 160 ns (20 sampling intervals) after the previous pulse. These pulses start during the falling part of the previous undershoot and the integral is strongly underestimated.

Even at 3 MHz, most of the pile-up can be rejected. However, pile-up can never be reduced to zero. There is always a certain amount of irreducible pile-up, originating from two pulses occur-
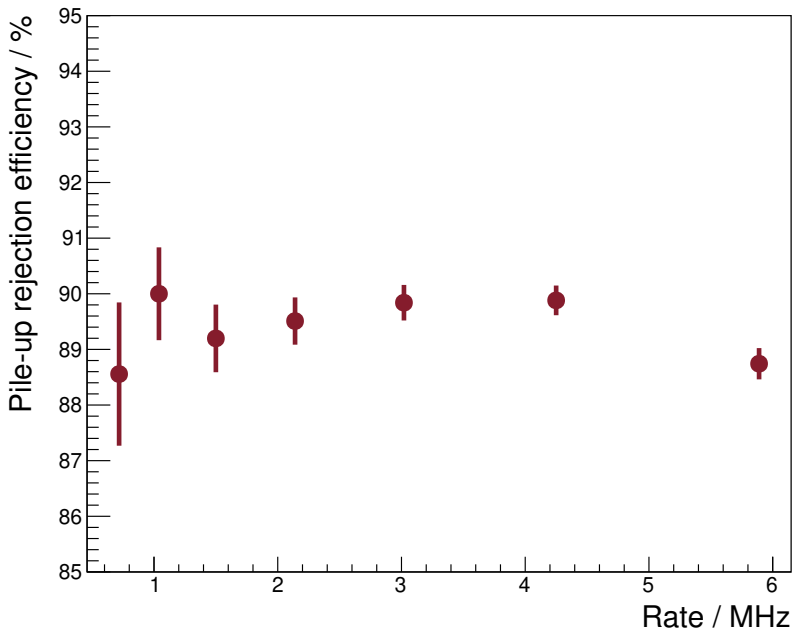
Figure 4.21: Pile-up rejection efficiency for rates between 718 kHz and 5.89 MHz. It is defined by the percentage, by which the pile-up peak in the spectrum of pulse integrals is reduced.

ring within a time window of less than the sampling interval of the ADC (8 ns). Such events cannot be distinguished from a single pulse. With increasing event rates, the probability for this effect increases and so does the amount of irreducible pile-up.

The ratio of the pile-up peak heights before and after the cuts in the spectra can be used to quantify the efficiency of the pile-up rejection. This efficiency is shown in Figure 4.21 for rates between 718 kHz and 5.89 MHz. In this region, the efficiency is slightly below 90 %. In other words, the algorithm reduces the pile-up contamination by almost 90 % for rates up to 6 MHz. However, this value is only an order of magnitude estimate. The efficiency can always be increased by tightening the cuts. A more interesting quantity would be the efficiency of the pile-up recovery in a later stage of the development.

When compared to the simple pile-up detection based only on one cut (Figure 4.17), the analysis based on multiple features rejects much more pile-up. However, it also causes a decrease of the main

peak, which is not the case in the simple method. Here, it is important to emphasize that the terms pile-up detection and pile-up rejection only imply that the corresponding pulse is marked as pile-up. As a consequence, the whole pulse is sent to the event builder instead of just the important features. The pulse is not discarded at all. A more sophisticated offline algorithm will disentangle the overlapping pulses and recover the pile-up. The pulses that were falsely marked as pile-up will be recovered as well. The pulses occurring too soon after a previous pulse will be analyzed with a more accurate modeling of the baseline in the undershoot. From this point of view, the above decrease in the main peak is no complication. The most important objective is to detect as many pile-up events as possible as shown by the strong reduction of the pile-up peak in the spectra above.

Chapter 5

SEARCH FOR $e^+e^- \to X(3872)$
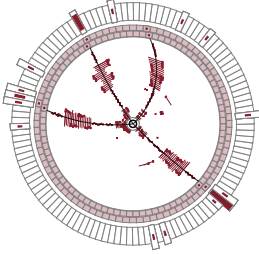
This Chapter describes the analysis of $e^+e^- \to \pi^+\pi^- J/\psi$ at four center-of-mass energies in the vicinity of the $X(3872)$ mass. The respective cross sections are extracted. Based on the data, a Bayesian likelihood analysis determines a new upper limit on the product of the $X(3873)$'s electronic width and the branching ratio $\mathcal{B}(X(3872) \to \pi^+\pi^- J/\psi)$.

THE electronic width Γ_{ee} is an interesting quantity which might shed light on the inner structure of the $X(3872)$ resonance. For an extended object like a $D^0\bar{D}^{*0}$ molecule the naive expectation yields a less likely production in non-hadronic annihilations than for the conventional χ'_{c1} charmonium state. This would be reflected in a smaller electronic width. Overall, Γ_{ee} of the $X(3872)$ state is expected to be very small compared to Γ_{ee} of vector charmonia. Due to the $J^{PC} = 1^{++}$ quantum numbers, at least two virtual photons are required in the Feynman diagram leading to a suppression of $\alpha^2 \approx 1/137^2$. A theoretical consideration using Vector Meson Dominance yields an estimate of $\Gamma_{ee} \gtrsim 30\,\text{meV}$ [299].[1] However, the high luminosity of BEPCII might be sufficient to observe the $e^+e^- \to X(3872)$ formation.

Furthermore, the observation of a large electronic width would motivate a scan measuring the cross section in e^+e^- collisions at tightly spaced points around the $X(3872)$ mass. In such an experiment, the total width might be measured.

This Chapter presents the analysis steps of the search for $X(3872)$ formation in e^+e^- annihilations and the subsequent methods to obtain information about the electronic width.

---

[1]The unit meV does not represent incorrect spelling of MeV. It is really 10^{-3} eV. Throughout this thesis, the values for Γ_{ee} or the product $\Gamma_{ee} \times \mathcal{B}(X(3872) \to \pi^+\pi^- J/\psi)$ are given in meV.

5.1 Analysis Strategy

The X(3872) state is best accessible via the decay to $\pi^+\pi^- J/\psi$, which is also the discovery channel [21]. The J/ψ resonance is easily reconstructed in the decay to either an e^+e^- or a $\mu^+\mu^-$ pair. The overall decay chain of $X(3872) \to \pi^+\pi^- J/\psi \to \pi^+\pi^-\ell^+\ell^-$ with $\ell = e, \mu$ leaves a clear signature in the detector with little background.

The reconstruction of $\pi^+\pi^- J/\psi$ alone does not imply the formation of the X(3872) resonance. Instead, this final state could originate from non-resonant production via a single virtual photon. In the remainder of this thesis, this process is called continuum reaction. The Feynman diagrams of both the continuum process and the X(3872) formation via two virtual photons are depicted in Figure 5.1. Based on an earlier measurement, the non-resonant cross section is expected to be around 17 pb [247]. The X(3872) formation presumably contributes only a small fraction to the overall cross section. It would be visible as an enhancement on top of the continuum. Figure 5.2 shows the expected cross section of $e^+e^- \to \pi^+\pi^- J/\psi$ for center-of-mass energies around the X(3872) mass.

In order to disentangle the continuum from resonant X(3872) formation, the cross section of $e^+e^- \to \pi^+\pi^- J/\psi$ needs to be scanned around the X(3872) mass. From the lineshape of the cross section, the electronic width can be inferred. For this purpose, BESIII recorded two data sets in 2017: one directly at the X(3872) mass and the other one about 4 MeV below. In addition, two older data sets were used for the scan. The collision energies of the four data sets is indicated by the black markers in Figure 5.2. The data sets are described in detail in the next Section.

Because the X(3872) is reconstructed in the $\pi^+\pi^- J/\psi$ decay, the measurement is not directly sensitive to the bare electronic width Γ_{ee} but to the product with the corresponding branching ratio $\Gamma_{ee} \times \mathcal{B}(X(3872) \to \pi^+\pi^- J/\psi)$.[2] The branching ratio is not measured yet. Only a lower limit of 3.2 % at a confidence level of 90 % is known [30]. The current upper limit on the product was determined in an earlier analysis by BESIII using the ISR technique and reads 130 meV at 90 % confidence level [30, 32].

With the current upper limit on the total width of 1.2 MeV at 90 % confidence level, the X(3872) state is very narrow [30, 31]. Therefore,

---

[2]In the following, $\mathcal{B}(X(3872) \to \pi^+\pi^- J/\psi)$ can also be found abbreviated as $\mathcal{B}$.
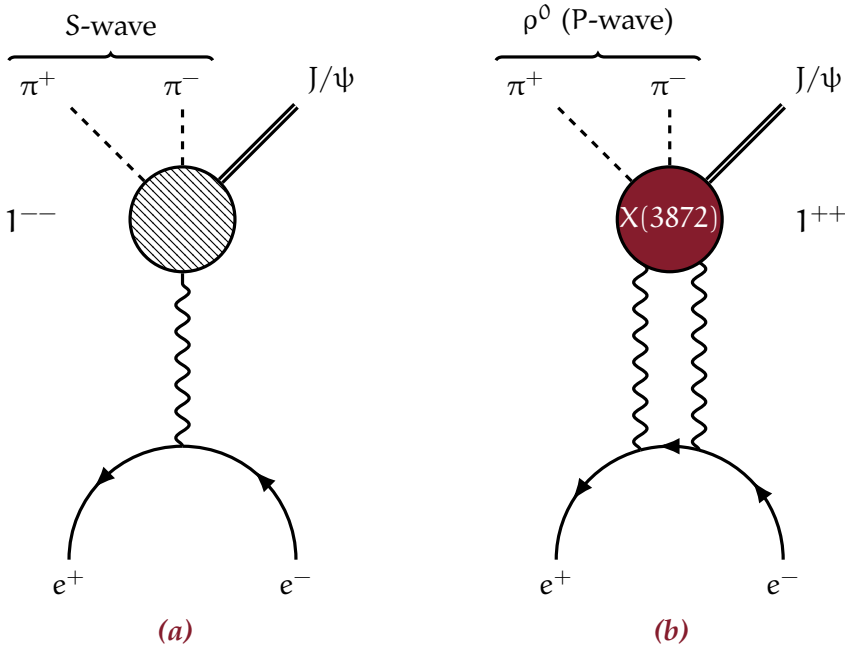
Figure 5.1: Feynman diagrams of *(a)* the non-resonant continuum process $e^+e^- \to \pi^+\pi^- J/\psi$ and *(b)* the resonant signal process $e^+e^- \to X(3872) \to \pi^+\pi^- J/\psi$, of which it is known that the $\pi^+\pi^-$ pair forms a ρ^0 meson [31, 114, 123].

the measurement of the collision energy with highest precision is crucial. Furthermore, the narrow width makes the observed cross section lineshape susceptible to effects of the beam energy spread.[3] In order to model the impact on the measurement of $\Gamma_{ee} \times \mathcal{B}$, accurate measurements of the beam energy spreads are required. The BEMS (cf. Section 3.3) provides a measurement of both the center-of-mass energy as well as the corresponding spread with the required accuracy. It operated during the 2017 data taking.

The road map of this Chapter is as follows: the next Section describes the data sets used for this analysis including the precise determination of the collision energy. Afterwards, Section 5.3 details

---

[3]The electrons and positrons in the accelerator beams do not have unique energies. Instead, their energies follow a certain distribution. The standard deviation of this distribution is called beam energy spread.
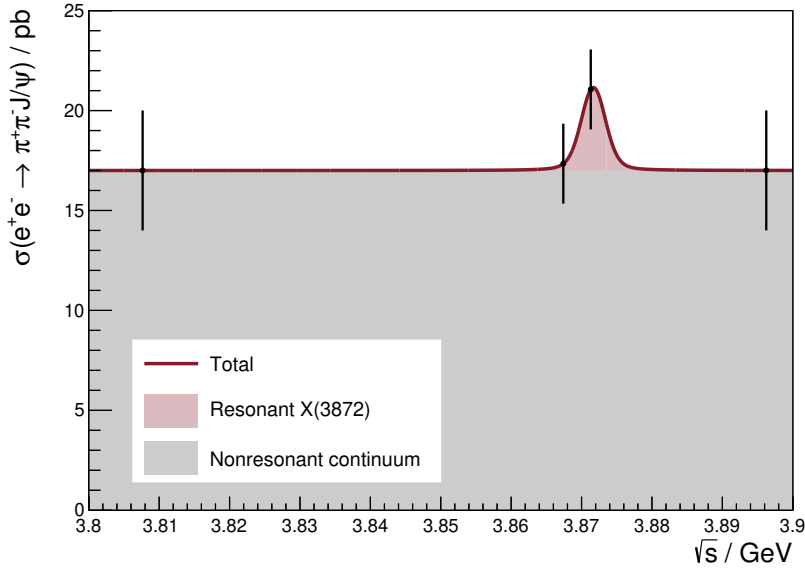
Figure 5.2: Expected cross section of $e^+e^- \to \pi^+\pi^- J/\psi$ assuming an X(3872) signal with the parameters $\Gamma_{ee} \times \mathcal{B} = 13\,\text{meV}$ and a a total width of $\Gamma_{\text{tot}}^{X(3872)} = 1.0\,\text{MeV}$ sitting on top of a constant continuum of 17 pb. The resonance shape is blurred by an assumed $\sqrt{s}$ spread of 1.5 MeV. The black markers indicate the center-of-mass energies of the used data sets. The error bars reflect an estimation of the expected uncertainty based on the integrated luminosity.

the event selection criteria based on MC simulations. A background study is performed in Section 5.4 which impose some additional background rejection criteria. In Section 5.5, the cross section of $e^+e^- \to \pi^+\pi^- J/\psi$ is extracted from a fit to the invariant $\ell^+\ell^-$ mass. All relevant systematic uncertainties are included in the result. Finally in Section 5.6, the measurements are combined into a global likelihood function. This function is subjected to a Bayesian analysis to obtain information on $\Gamma_{ee} \times \mathcal{B}$.

5.2 *Data Sets*

For this analysis, two dedicated data sets were recorded in the vicinity of the X(3872) mass in June 2017. The intended center-of-mass energy for one data set was the X(3872) mass (referred to as on-

Table 5.1: Overview of the data sets. The center-of-mass energy $\sqrt{s}$ and its spread $\delta\sqrt{s}$ are listed. In addition, the integrated luminosity $\int \mathcal{L}\, dt$ and the year of data taking are stated. The superior $\sqrt{s}$ resolution of the 2017 data thanks to the BESMS is evident. Only about $2\,\mathrm{pb}^{-1}$ of the off-resonance data sample is recorded at 3866.32 MeV. The vast majority of the off-resonance data was collected at 3867.41 MeV.

$\sqrt{s}\,/\,\mathrm{MeV}$	$\delta\sqrt{s}\,/\,\mathrm{MeV}$	$\int \mathcal{L}\, dt\,/\,\mathrm{pb}^{-1}$	Year
3807.7 ± 0.6	—	50.5 ± 0.5	2013
3866.32 ± 0.10	1.45 ± 0.20	108.9 ± 1.3	2017
3867.410 ± 0.031	1.406 ± 0.20		
3871.31 ± 0.06	1.73 ± 0.09	110.3 ± 0.8	2017
3896.2 ± 0.8	—	52.6 ± 0.5	2013

resonance sample) and 4 MeV below that value for the other data set (referred to as off-resonance sample). The determination of the center-of-mass energy and the spread of it by means of the BEMS is described in the following Sections. The corresponding integrated luminosities were determined by Yutie Liang [300]. His procedure is described in Appendix C.1.

Additionally, the analysis uses two data sets from 2013 in the wider neighborhood of the X(3872) mass. As they have already been used in many other analyses, their corresponding collision energy and integrated luminosity have been determined via the analysis of Bhabha and dimuon events in previous work by the BESIII collaboration [301, 302]. An overview of the data sets is given in Table 5.1.

In the beginning of data taking, the beam energies were slightly lower than anticipated. After the first two runs (approximately $2\,\mathrm{pb}^{-1}$), they were increased to match the intended collision energy. As a result, the off-resonance sample contains a small fraction (less than 2 %) of data with $\sqrt{s}$ approximately 1 MeV lower.

5.2.1 *Center-of-Mass Energy Determination of the 2017 Data*

In order to have precise $\sqrt{s}$ values around the X(3872) mass, the beam energies were monitored by the BEMS during data taking for the two data sets of 2017. The BEMS measures the beam energy and the beam energy spread of both beams independently. Each

measurement point is the analysis result of the energy spectrum of Compton back scattered photons collected over a certain time period. The BEMS measurements are associated to the BESIII data via a time stamp.

The BEMS result for the beam energies is shown in Figure 5.3. The three different beam energy configurations are clearly noticeable. Although the BEMS recorded data for ca. 17 hours at the first beam energy, there were almost no collisions in this period, and only $2\,\mathrm{pb}^{-1}$ were recorded by BESIII. The step in the beam energies on June 2$^{\mathrm{nd}}$ visualizes the adjustment to the intended energies.

For the on-resonance data set, the BEMS was able to measure the positron beam only at the beginning of data taking. However, Yutie Liang performed a cross check via the analysis of $e^+e^- \to \mu^+\mu^-$ events and found out that the center-of-mass energies agree with the BEMS result and stay constant for the full period of on-resonance data taking (cf. Appendix C.2). Hence, the energy inferred from the limited BEMS data is used for the whole data sample.

For each of the three different beam configurations, the values of the beam energies and beam energy spreads are averaged. The center-of-mass energy is obtained from the average values, taking into account the finite beam crossing angle of $\theta = 22\,\mathrm{mrad}$:

$$\sqrt{s} = 2\cos(\theta/2)\,\sqrt{E_{e^+}E_{e^-}} \quad . \tag{5.1}$$

The corresponding error of this quantity is:

$$\Delta\sqrt{s} = \cos(\theta/2)\,\sqrt{\frac{E_{e^-}}{E_{e^+}}(\Delta E_{e^+})^2 + \frac{E_{e^+}}{E_{e^-}}(\Delta E_{e^-})^2} \quad . \tag{5.2}$$

The results are summarized in Table 5.2.

5.2.2 *Beam Energy Spread*

The BEMS measurement of the beam energy spreads is shown in Figure 5.4. Both the uncertainty of the beam energies and the beam energy spread measure Gaussian deviations from the central beam energy. Therefore, the same relation as in equation (5.2) is used to propagate the energy spreads from the individual beams to the collision energy:

$$\delta\sqrt{s} = \cos(\theta/2)\,\sqrt{\frac{E_{e^-}}{E_{e^+}}(\delta E_{e^+})^2 + \frac{E_{e^+}}{E_{e^-}}(\delta E_{e^-})^2} \quad . \tag{5.3}$$
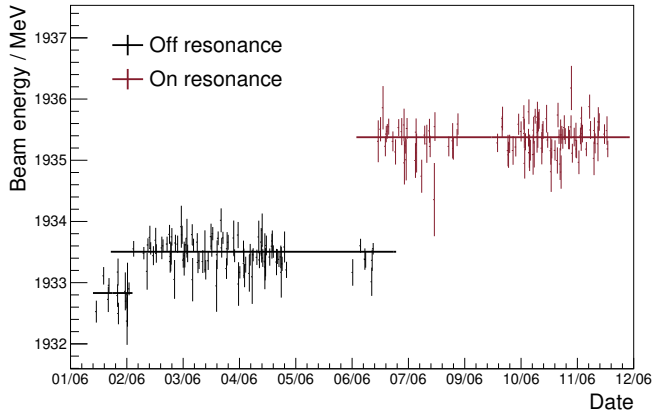
(a) Electron beam.
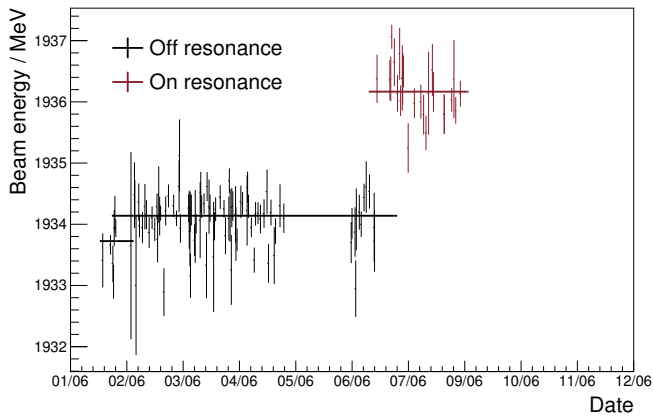
(b) Positron beam.

Figure 5.3: BEMS result of the beam energies. For each of the three different beam configurations, the average values are indicated by the horizontal lines. During the second half of the on-resonance data taking, the BEMS was no longer able to find the positron beam. For this time, there is no BEMS result avaialbe.
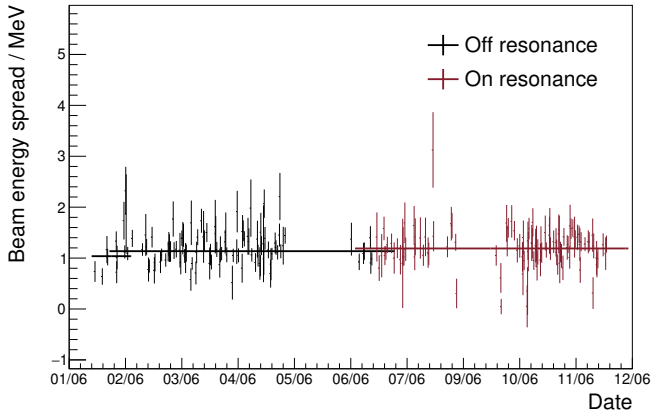
(a) Electron beam.
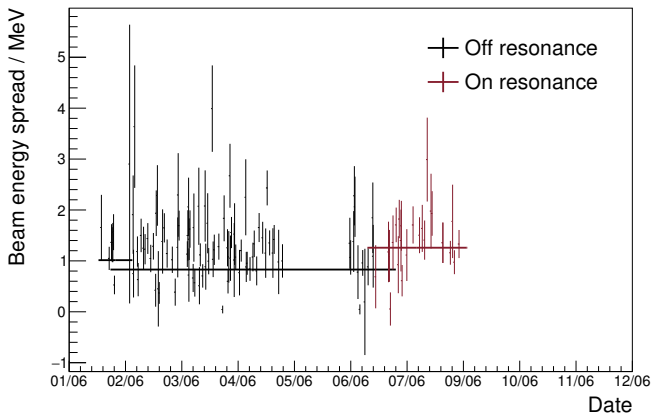
(b) Positron beam.

Figure 5.4: BEMS result of the beam energy spread. For each of the three different beam configurations, the average values are indicated by the horizontal lines. During the second half of the on-resonance data taking, the BEMS was no longer able to find the positron beam. For this time, there is no BEMS result avaialbe.

Table 5.2: BEMS result for the energies as well as their spread. All values are in MeV and the uncertainties are statistical only.

	Off-resonance		On-resonance
E_{e^-}	1932.83 ± 0.05	1933.505 ± 0.016	1935.376 ± 0.018
E_{e^+}	1933.72 ± 0.09	1934.139 ± 0.027	1936.17 ± 0.06
$\sqrt{s}$	3866.32 ± 0.10	3867.410 ± 0.031	3871.31 ± 0.06
δE_{e^-}	1.04 ± 0.06	1.136 ± 0.020	1.189 ± 0.024
δE_{e^+}	1.01 ± 0.11	0.830 ± 0.032	1.26 ± 0.08
$\delta\sqrt{s}$	1.45 ± 0.09	1.406 ± 0.025	1.73 ± 0.06

The ratios $E_{e^\pm}/E_{e^\mp}$ are almost unity and the beam energy spreads are basically added in quadrature. The uncertainty of $\delta\sqrt{s}$ is calculated via Gaussian error propagation:

$$\Delta(\delta\sqrt{s}) = \frac{\cos^2(\theta/2)}{\delta\sqrt{s}} \sqrt{(\delta E_{e^+} \cdot \Delta(\delta E_{e^+}))^2 + (\delta E_{e^-} \cdot \Delta(\delta E_{e^-}))^2} \quad .$$

(5.4)

The result of this calculation is also included in Table 5.2.

5.2.3 *Systematic Uncertainty of the BEMS Result*

Although the systematic uncertainty of the BEMS results are considered negligible [236], an attempt is made to estimate a systematic uncertainty. Strictly speaking, systematics of each measurement point such as detector effects are not covered, but the systematics of the averaging process of the BEMS measurements is estimated. Therefore, an alternative method to obtain the center-of-mass energies and the corresponding spreads is investigated in the following MC toy procedure. All steps are performed for both off- and on-resonance configurations.

1. A BEMS measurement point of the electron beam is randomly selected. The data taking period of the points are used as a weight.

2. This measurement provides a beam energy with a corresponding uncertainty. A Gaussian probability density function (pdf)

is constructed with the beam energy as mean and the uncertainty as standard deviation. A random beam energy is sampled from this Gaussian.

3. The same measurement point provides a beam energy spread with a corresponding uncertainty as well. A random value for the beam energy spread is generated in the same fashion as for the (central) beam energy.

4. At this point, we have a randomly sampled beam energy and a randomly sampled beam energy spread. Together, they constitute a Gaussian energy distribution describing a possible energy profile of the electron beam.

5. Now, one fixed energy is sampled from this profile. We have the energy of a single electron of the beam.

6. The above steps are also performed for the positron beam, resulting in an energy value of a single positron.

7. The two particles collide at a specific center-of-mass energy determined from the individual energies of the electron and positron.

8. Steps 1-7 are repeated several times ($\mathcal{O}(10^7)$) resulting in a distribution of $\sqrt{s}$. The mean and standard deviation are the center-of-mass energy and the spread, respectively.

The $\sqrt{s}$ distributions (cf. Figure 5.5) are not perfect Gaussians, but they have the same central values as the nominal center-of-mass energy values. The standard deviation ($\widehat{=}$ spread of $\sqrt{s}$) is increased compared to the nominal values obtained in the previous Section. The difference between the nominal beam energy spread and the one obtained by this method is taken as a systematic uncertainty on the spread. It is 0.20 MeV and 0.07 MeV for the off- and on- resonance sample, respectively. Combined with the almost negligible statistical error (cf. Table 5.2), the total uncertainty is 0.20 MeV and 0.09 MeV.
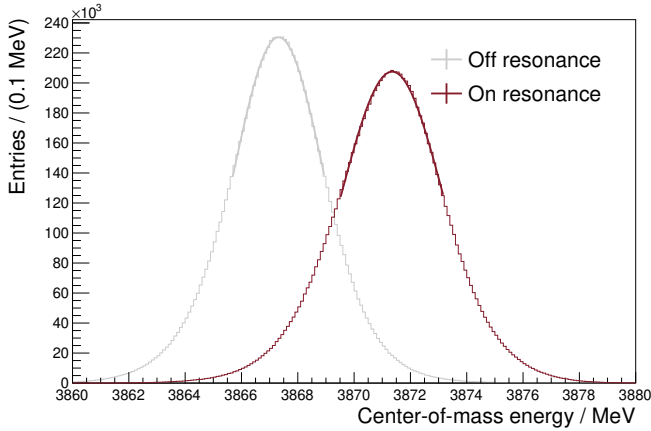
Figure 5.5: Distribution of $\sqrt{s}$ as determined by the MC technique described in the text.

5.3 *Monte Carlo Sets and Event Selection*

The event selection is optimized and the backgrounds are estimated by the use of MC simulations as implemented in the BOSS framework (cf. Section 3.4). In addition, the analysis relies on a lot of programs written using the software toolkit ROOT [294].

The event generation of both the resonant signal process as well as the continuum reaction are performed by a combination of the KKMC [303, 304] and EvtGen [305, 306] event generators and the PHOTOS package [307, 308]. The total reaction of $e^+e^- \rightarrow \pi^+\pi^-\ell^+\ell^-$ is split into the first part $e^+e^- \rightarrow f\bar{f}$ and the second part $f\bar{f} \rightarrow \pi^+\pi^-\ell^+\ell^-$.

KKMC is responsible for the first one, where $f\bar{f}$ stands for a fermion anti-fermion pair. It includes the emission of up to two ISR photons and takes the beam energy spread into account. For ISR, the a priori unknown lineshape of the cross section is required as an input. After all, the lineshape is measured in this analysis. As a first starting point, the cross section is assumed to be flat across the relevant energy region, i.e. constant.

The second part is handled by EvtGen, performing the hadronization and the decay to the final state. The whole decay chain is defined and for each individual (intermediate) decay, a specific model needs to be specified. For example, a certain decay could

be modeled purely by phase space, i.e. neglecting all involved spins and angular momenta. Some models are very specific and can only be used for a few decays. In addition, some models have parameters to be set, e.g. which partial waves should contribute. Furthermore, FSR is modeled by PHOTOS.

In the following the decay chains for the different MC samples are described. The used EVTGEN models are also mentioned. For all the different energies and reactions (resonant and continuum), 5×10^5 events are simulated for each of the two J/ψ decay modes.

5.3.1 *Signal Monte Carlo*

The X(3872) decay into $\pi^+\pi^-$ J/ψ is known to proceed via the intermediate ρ^0 J/ψ state [31, 114, 123]. The signal process is simulated according to

$$
\begin{array}{lll}
e^+e^- \longrightarrow \rho^0\ \text{J}/\psi & & \text{(PARTWAVE)} \\[2mm]
\quad\quad\quad\quad\ \ \hookrightarrow e^+e^- & & \text{(VLL)} \\
\quad\quad\quad\quad\ \ \hookrightarrow \mu^+\mu^- & & \text{(VLL)} \\[2mm]
\quad\quad\quad \hookrightarrow \pi^+\pi^- & & \text{(VSS)}
\end{array}
$$

The decay X(3872) $\to \rho^0$ J/ψ is modeled with PARTWAVE. As the name suggests, it uses the partial wave formalism. Its parameters are set to proceed only via S-wave being consistent with LHCb results [124]. The J/ψ decay is modeled with VLL describing the decay of a vector particle into a $\ell^+\ell^-$ pair. The model VSS for the ρ^0 decay describes the decay of a vector particle into a pair of (pseudo-)scalars.

5.3.2 *Continuum Monte Carlo*

The non-resonant $e^+e^- \to \pi^+\pi^-$ J/ψ reaction proceeds via a single virtual photon and the final state is therefore constrained to the 1^{--} quantum numbers. The relative small phase space available for the $\pi^+\pi^-$ pair suggests that it exists in an S-wave. The different possibilities to model this within EVTGEN are presented in the following. All options model the J/ψ $\to \ell^+\ell^-$ decays with VLL like in the X(3872) signal MC.

- BOSS provides the JPIPI model for the decay of a 1^{--} state to $\pi^+\pi^- J/\psi$ and is tuned to reproduce the kinematics of the $\psi' \to \pi^+\pi^- J/\psi$ decay observed in real data. The mass of the ψ' is $120 - 210\,\text{MeV}$ below the collision energies of the data sets making this model a good candidate for the continuum process. The corresponding decay chain is:

$$e^+e^- \longrightarrow \pi^+\pi^- J/\psi \qquad \text{(JPIPI)}$$
$$\quad\ \hookrightarrow e^+e^- \qquad \text{(VLL)}$$
$$\quad\ \hookrightarrow \mu^+\mu^- \qquad \text{(VLL)}$$
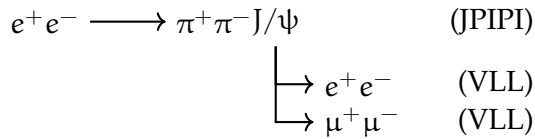
- Very similar to the JPIPI model, there is the VVPIPI for the decay of a 1^{--} state to $\pi^+\pi^-$ and a 1^{--} state, where the $\pi^+\pi^-$ system is dominated by an S-wave. This is a natural choice for the continuum process, since the J/ψ quantum numbers are 1^{--}. The full chain is:

$$e^+e^- \longrightarrow \pi^+\pi^- J/\psi \qquad \text{(VVPIPI)}$$
$$\quad\ \hookrightarrow e^+e^- \qquad \text{(VLL)}$$
$$\quad\ \hookrightarrow \mu^+\mu^- \qquad \text{(VLL)}$$
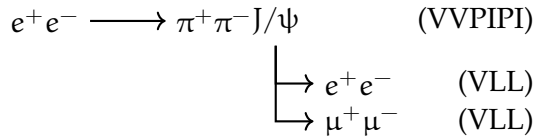
- In the above descriptions, the $\pi^+\pi^-$ system accumulates at high invariant masses, just like a contribution from the $f_0(980)$ resonance. A different $\pi^+\pi^-$ S-wave resonance is the $f_0(500)$, also known as σ meson. Here, the possibility of an intermediate σ meson is considered.

  There is no angular momentum involved in the σ decay to the pion pair (all particles have $J = 0$). Furthermore, it is a two-body decay and no intermediate resonances could occur. Therefore, it is save to use the phase space model (PHSP). Similarly, there is no (relative) angular momentum in the first part of the chain.[4] For the same reason, PHSP is used here.

---

[4] In principle, $L = 2$ (D-wave) could contribute, which is expected to be negligible.

This corresponds to:

$$e^+e^- \longrightarrow \sigma \quad J/\psi \qquad\qquad \text{(PHSP)}$$
$$\hookrightarrow e^+e^- \qquad \text{(VLL)}$$
$$\hookrightarrow \mu^+\mu^- \qquad \text{(VLL)}$$
$$\hookrightarrow \pi^+\pi^- \qquad\qquad \text{(PHSP)}$$
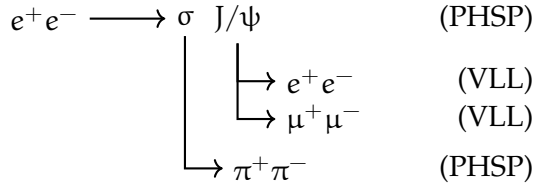
- The VVS_PWAVE model is another possibility to incorporate the σ meson. Here, the decay of a 1^{--} state to another 1^{--} state and a (pseudo-) scalar meson is modeled. The model is configured to only include S-wave. The decay chain is:

$$e^+e^- \longrightarrow \sigma \quad J/\psi \qquad \text{(VVS\_PWAVE)}$$
$$\hookrightarrow e^+e^- \qquad \text{(VLL)}$$
$$\hookrightarrow \mu^+\mu^- \qquad \text{(VLL)}$$
$$\hookrightarrow \pi^+\pi^- \qquad\qquad \text{(PHSP)}$$
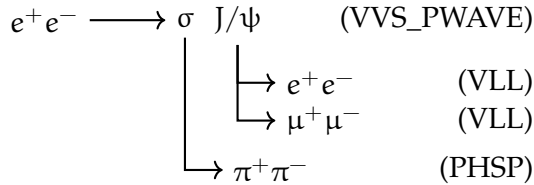
- The simplest (and probably the least realistic) way to simulate the reaction is the PHSP model for the three-body decay:

$$e^+e^- \longrightarrow \pi^+\pi^- J/\psi \qquad\qquad \text{(PHSP)}$$
$$\hookrightarrow e^+e^- \qquad \text{(VLL)}$$
$$\hookrightarrow \mu^+\mu^- \qquad \text{(VLL)}$$
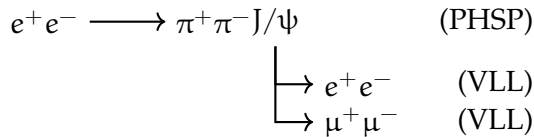
The difference between all models is best visualized in the distributions of the invariant $\pi^+\pi^-$ mass in Figure 5.6.

The limited statistics of the data sets does not allow for a reliable judgment about which of the models reflects reality best. Therefore, another data set of BESIII taken at $\sqrt{s} = 4007.6\,\text{MeV}$ in 2011 is analyzed. This set has $482\,\text{pb}^{-1}$ (compared to the total integrated luminosity of $322.3\,\text{pb}^{-1}$ of the four sets used in the actual analysis) and is only $110\,\text{MeV}$ above the highest energy point of the actual analysis. The $m(\pi^+\pi^-)$ distribution of this data set is shown in Figure 5.7. The majority of events is clustered towards higher dipion
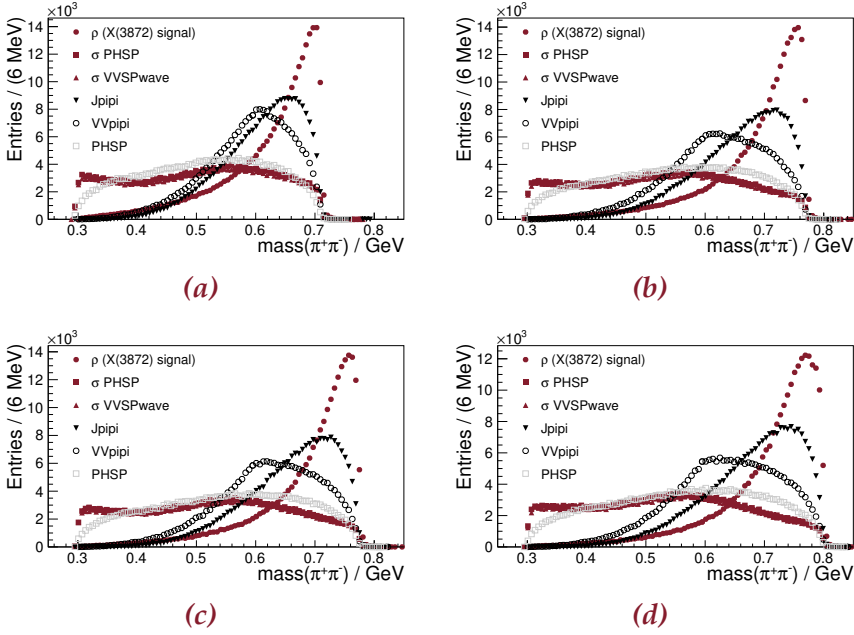
Figure 5.6: Simulated distribution of $m(\pi^+\pi^-)$ for the different data sets and models. The sharp drop between 700 and 800 MeV is caused by the phase space limit. Only the $J/\psi \to \mu^+\mu^-$ mode is shown.

masses. This favors the VVPIPI and JPIPI model over the models with the σ resonance and the PHSP model. Based on this behavior, the VVPIPI model is used for the continuum, but the σ model with PHSP decay is considered in the estimation of the systematic uncertainty (cf. Section 5.5.2).

5.3.3 *Event Selection*

The final state $\pi^+\pi^-\ell^+\ell^-$ ($\ell = e, \mu$) consists of four charged tracks with zero net charge. Events with the following criteria are selected:

- Each charged track is required to fulfill the standard tracking cuts of BESIII: they need to originate from a confined volume around the interaction point and lie within the detectors acceptance:

    - $|z_{poca}| < 10$ cm

(a) $J/\psi \to e^+e^-$ mode.

(b) $J/\psi \to \mu^+\mu^-$ mode.
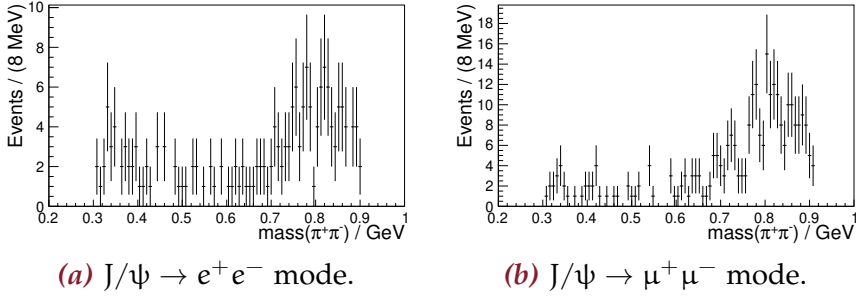
Figure 5.7: Invariant dipion mass distribution for the data at $\sqrt{s} =$ 4007.6 MeV. The shown events correspond to the J/ψ peak region as defined in Section 5.4.2 and Figure 5.9. The accumulation of events in the low $m(\pi^+\pi^-)$ region in the e^+e^- mode is background from $e^+e^- \to \gamma e^+e^-$ as discussed in Section 5.4.

- $r_{poca} < 1$ cm
- $|\cos\theta| < 0.93$

Here, z_{poca} is the z-component of the point of closest approach of the track with respect to the IP. The exact position of the IP in turn is determined for each run independently. The radial component of the point of closest approach is $r_{poca} = \sqrt{x_{poca}^2 + y_{poca}^2}$. For the third requirement, θ is the polar angle of the momentum vector of the track at the point of closest approach. Charged tracks fulfilling these requirements are labeled "good tracks".

- Each candidate event is required to have a total number of four good tracks with net zero charge.

- The lepton tracks arising from the J/ψ decay have large momenta (in the lab frame), while the pion tracks have relatively low momenta (cf. Figure 5.8(a)). Tracks with lower momentum than 600 MeV are identified as pion candidates and lepton candidates are required to have larger momentum than 1.0 GeV. Each candidate event is required to have two oppositely charged pion candidates and two lepton candidates with opposite charge as well.

(a)

(b)
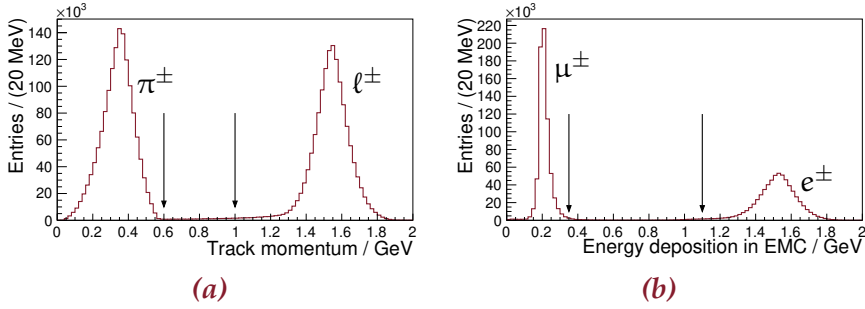
Figure 5.8: Selection of pion and lepton candidates based on a MC simulation of the signal process at $\sqrt{s} = 3871.31\,\text{MeV}$. The arrows indicate the cut values. *(a)* Pion / lepton discrimination by a cut on the lab momentum in the laboratory frame. Pion candidates are required to have a lower momentum than 600 MeV and lepton momenta need to be larger than 1 GeV. *(b)* Electron / muon discrimination by a cut on the energy deposit in the EMC. Charged tracks with an associated energy deposition of less than 350 MeV are identified as muons and electron candidates need to deposit more than 1.1 GeV.

- The two J/ψ decay modes can be distinguished by the energy deposition in the EMC associated to the lepton tracks. Electrons deposit a large fraction of their energy, while the muons pass the EMC almost undisturbed leaving only a small energy deposition (cf. Figure 5.8(b)). To be identified as a muon, a deposition of less than 350 MeV is needed. Electron candidates are required to deposit more than 1.1 GeV.

5.4 *Background Study*

There are many non-$\pi^+\pi^-$ J/ψ processes with the same signature of four charged tracks. In order to reduce the impact of these sources, the event selection criteria are further refined and additional cuts are applied.

5.4.1 *Monte Carlo Simulations of Backgrounds*

The following backgrounds are considered:

Gamma Conversion

The radiative processes of $e^+e^- \to \gamma \ell^+ \ell^-$ by itself is not picked up in the event selection. However, the radiated photon might react with the detector material. Typically, it converts into an e^+e^- pair and a total of four charged tracks are reconstructed.

- The most dominant background for the events of the $J/\psi \to e^+e^-$ mode is the radiative Bhabha process $e^+e^- \to \gamma e^+e^-$ with subsequent conversion of the photon. This background is simulated with the BABAYAGA3.5 event generator [309, 310].

- The equivalent of the $J/\psi \to \mu^+\mu^-$ mode is the $e^+e^- \to \gamma \mu^+\mu^-$ process with the following conversion. Compared to the radiative Bhabha process, this reaction has a much lower cross section. It is simulated with the PHOKHARA event generator [274–276].

Two Photon Processes

The reaction of $e^+e^- \to e^+e^- X$, where X can be anything, involves two virtual photons.[5] When X results in two charged tracks, it easily can be (mis-) identified as the $\pi^+\pi^- e^+e^-$ final state. The following reactions are simulated with BESTWOGAM, an implementation of an event generator developed for the DELPHI experiment [311, 312].

- A pure QED process[6] with four charged tracks in the final state is the reaction $e^+e^- \to e^+e^- e^+e^-$.

- The reaction $e^+e^- \to e^+e^- \mu^+\mu^-$ has a lower cross section than the previous one, but the $\mu^+\mu^-$ pair is much easier misidentified as a $\pi^+\pi^-$ pair.

- Similar to the previous two processes, the reaction $e^+e^- \to e^+e^- q\bar{q}$ may contribute to the overall background. The $q\bar{q}$ stands for an $u\bar{u}$ or a $d\bar{d}$ quark pair. Among others, they can hadronize into a $\pi^+\pi^-$ pair. This final state is identical to the one in the signal process.

---

[5]The photon fusion process described in Section 2.3.3 and Figure 2.7(a) is only one of the contributing Feynman diagrams.

[6]At lowest order.

Exclusive Hadron Production

In the following reactions, four charged pions and/or kaons are produced. They are simulated with the CONEXC event generator [313] including ISR. They all might be misidentified as $\pi^+\pi^-\mu^+\mu^-$ events.

- The most dominant background for the $J/\psi \to \mu^+\mu^-$ reconstruction mode is the reaction $e^+e^- \to \pi^+\pi^-\pi^+\pi^-$. Pions have a similar mass as muons and deposit a similar amount of energy in the EMC.

- Another hadronic background with four charged tracks is the reaction $e^+e^- \to K_S^0 K^{\pm}\pi^{\mp}$ with the subsequent K_S^0 decaying into two charged pions.

- A further hadronic background with the same track multiplicity and a non negligible cross section is the reaction $e^+e^- \to K^+K^-\pi^+\pi^-$.

Radiative Return to the ψ′ Resonance

- The ψ' vector state is only $120 - 210\,\mathrm{MeV}$ below the $\sqrt{s}$ of the analyzed data sets. This implies a non-negligible cross section for ψ' production in ISR. The ψ' state dominantly decays to $\pi^+\pi^- J/\psi$. Without the detection of the ISR photon, this process has the same signature as the signal process. This background is simulated in EVTGEN using the model VECTORISR for the emission of the ISR photon, the model JPIPI for the ψ' decay, and the VLL model for the $J/\psi \to \ell^+\ell^-$ decay.

Complete Background Monte Carlo Cocktail

An overview of the background MC samples is given in Table 5.3. For each process and center-of-mass energy, the cross section σ as calculated by the event generator is shown as well as the number of simulated events N_{sim}. The expected numbers of events within the J/ψ peak region after all background rejection cuts are listed in the $N_{exp}^{\ell\ell}$ columns, each standing for one J/ψ reconstruction mode. The J/ψ peak region as well as the background rejection cuts is defined in the following Section. Based on the MC study, most of the considered background sources are negligible. The strongest contribution is expected from the $e^+e^- \to \pi^+\pi^-\pi^+\pi^-$ process. For this reaction,

ConExc gives a cross section which is approximately a factor five too low compared to the measurement by BABAR [314]. To compensate for this, the ConExc output is rescaled to match the BABAR values.

In the following, the background MC samples are scaled to the integrated luminosity of the data and added up to one cocktail MC sample per energy point.

5.4.2   *Background Rejection Cuts*

The background contamination is reduced by the following cuts:

- As already mentioned, radiative Bhabha scattering followed by the conversion of the photon is the most dominant background in the $J/\psi \rightarrow e^+e^-$ mode. In the $J/\psi \rightarrow \mu^+\mu^-$ mode, the background is also present. The electron (positron) from the conversion is identified as a pion and carries the boost of the photon. Therefore, the two particles are almost collinear. The distribution of the cosine of the opening angle between the pion candidates $\cos\theta_{\pi^+\pi^-}$ has a large peak at 1 (cf. Figures 5.10(a) and (b)). A requirement of $\cos\theta_{\pi^+\pi^-} < 0.95$ greatly reduces the background from gamma conversion.

- The electrons from gamma conversion can also be identified as a $\pi^\pm \ell^\mp$ pair. Due to the much larger abundance of γe^+e^- events compared to $\gamma\mu^+\mu^-$, the cut $\cos\theta_{\pi^\pm e^\mp} < 0.98$ is only applied for the electron mode (cf. Figures 5.10(c) and (d)).

- A very important step in the analysis is the kinematic fit, to which each event is subjected to. The kinematic constraints are the conservation of total four momentum, i.e. the four momenta of all tracks are constrained to add up to $(\sqrt{s}, 0, 0, 0)$ in the center-of-mass frame. Additionally, the tracks are required to originate from a common vertex. The measured beam energy spread is included in the fit. For the 2017 data, the result of the BEMS measurement is used. For the 2013 data, an estimation of 1.5 MeV based on the 2017 values is used.

  During the fit, the track parameters are altered until the constraints are fulfilled. A χ^2 value is determined to quantify the level of agreement between the parameters before and after the fit. Unfortunately, there are inconsistencies between the estimated error of the track parameters in data and in MC. As

Table 5.3: Overview of the generated background MC samples. See text for description.

$e^+e^- \rightarrow$	$\sqrt{s}\,/\,\mathrm{MeV}$	$\sigma\,/\,\mathrm{nb}$	N_{sim}	N_{exp}^{ee}	$N_{exp}^{\mu\mu}$
γe^+e^-	3807.7	35.447	14.9 M	0.84 ± 0.32	0.00 ± 0.12
γe^+e^-	3867.4	35.447	30 M	1.16 ± 0.39	0.00 ± 0.13
γe^+e^-	3871.3	35.447	30 M	1.17 ± 0.39	0.00 ± 0.13
γe^+e^-	3896.2	35.447	15 M	0.50 ± 0.25	0.00 ± 0.12
$\gamma \mu^+\mu^-$	3807.7	0.0501	485 k	0.00 ± 0.01	0.00 ± 0.01
$\gamma \mu^+\mu^-$	3867.4	0.0460	485 k	0.00 ± 0.03	0.03 ± 0.03
$\gamma \mu^+\mu^-$	3871.3	0.0457	480 k	0.00 ± 0.03	0.06 ± 0.04
$\gamma \mu^+\mu^-$	3896.2	0.0441	495 k	0.00 ± 0.01	0.00 ± 0.01
$e^+e^-e^+e^-$	3807.7	16.94	11 M	0.31 ± 0.16	0.00 ± 0.08
$e^+e^-e^+e^-$	3867.4	17.28	11 M	1.37 ± 0.48	0.00 ± 0.17
$e^+e^-e^+e^-$	3871.3	17.30	11 M	1.21 ± 0.46	0.00 ± 0.17
$e^+e^-e^+e^-$	3896.2	17.44	11 M	1.00 ± 0.29	0.00 ± 0.08
$e^+e^-\mu^+\mu^-$	3807.7	7.997	11 M	0.11 ± 0.06	0.04 ± 0.04
$e^+e^-\mu^+\mu^-$	3867.4	8.144	11 M	0.00 ± 0.08	0.16 ± 0.11
$e^+e^-\mu^+\mu^-$	3871.3	8.153	11 M	0.00 ± 0.08	0.16 ± 0.12
$e^+e^-\mu^+\mu^-$	3896.2	8.213	11 M	0.12 ± 0.07	0.12 ± 0.07
$e^+e^-q\bar{q}$	3807.7	1.358	1 M	0.00 ± 0.07	0.00 ± 0.07
$e^+e^-q\bar{q}$	3867.4	1.398	990 k	0.00 ± 0.15	0.00 ± 0.15
$e^+e^-q\bar{q}$	3871.3	1.400	1 M	0.00 ± 0.15	0.00 ± 0.15
$e^+e^-q\bar{q}$	3896.2	1.427	1 M	0.00 ± 0.08	0.00 ± 0.08
$\pi^+\pi^-\pi^+\pi^-$	3807.7	0.845	1 M	0.00 ± 0.04	5.98 ± 0.04
$\pi^+\pi^-\pi^+\pi^-$	3867.4	0.785	1 M	0.09 ± 0.09	12.98 ± 0.09
$\pi^+\pi^-\pi^+\pi^-$	3871.3	0.781	1 M	0.00 ± 0.09	11.29 ± 0.10
$\pi^+\pi^-\pi^+\pi^-$	3896.2	0.758	1 M	0.00 ± 0.04	6.78 ± 0.04
$K_S^0 K^\pm \pi^\mp$	3807.7	0.0269	1 M	$0.00 \pm 0,00$	0.04 ± 0.01
$K_S^0 K^\pm \pi^\mp$	3867.4	0.0254	1 M	$0.00 \pm 0,00$	0.07 ± 0.01
$K_S^0 K^\pm \pi^\mp$	3871.3	0.0253	1 M	$0.00 \pm 0,00$	0.04 ± 0.01
$K_S^0 K^\pm \pi^\mp$	3896.2	0.0247	1 M	$0.00 \pm 0,00$	0.03 ± 0.01
$K^+K^-\pi^+\pi^-$	3807.7	0.2044	500 k	0.00 ± 0.02	0.00 ± 0.02
$K^+K^-\pi^+\pi^-$	3867.4	0.1932	500 k	0.00 ± 0.04	0.00 ± 0.04
$K^+K^-\pi^+\pi^-$	3871.3	0.1925	500 k	0.00 ± 0.04	0.00 ± 0.04
$K^+K^-\pi^+\pi^-$	3896.2	0.1882	500 k	0.00 ± 0.02	0.00 ± 0.02
$\gamma_{ISR}\psi'$	3807.7	0.0892	1 M	0.01 ± 0.01	0.00 ± 0.00
$\gamma_{ISR}\psi'$	3867.4	0.0577	1 M	0.07 ± 0.02	0.09 ± 0.02
$\gamma_{ISR}\psi'$	3871.3	0.0564	1 M	0.09 ± 0.02	0.11 ± 0.03
$\gamma_{ISR}\psi'$	3896.2	0.0490	1 M	0.04 ± 0.01	0.06 ± 0.01

a consequence, the χ^2 distributions of the kinematic fit differ between data and MC too. However, this is a known effect and the consistency can be restored by a correction of the MC track parameter errors, as described in reference [315].

A χ^2 value below 60 is required for all events. The corresponding distributions are shown in Figures 5.10(e) and (f). The value of 60 is the result of figure-of-merit optimization shown in Figures D.1 and D.2 in the Appendix. This cut is important for the rejection of all non-$\pi^+\pi^-\ell^+\ell^-$ backgrounds, where the total four-momentum balance is non-zero. In particular, it is crucial for the rejection of the $\gamma_{ISR}\psi' \to \gamma_{ISR}\pi^+\pi^- J/\psi$ background.

The invariant mass distributions of the dilepton pairs after all cuts are shown in Figure 5.9. The J/ψ peak is clearly noticeable and the peak region $3.08\,\text{GeV} < m(\ell^+\ell^-) < 3.12\,\text{GeV}$ is indicated by black arrows as well as the sideband region $m(\ell^+\ell^-)/\text{GeV} \in [3.02, 3.06] \cup [3.14, 3.18]$ (gray arrows). In the electron mode, the background MC fails to describe the data.

The reason for this is suspected to be a certain setting in the event generator for the radiative Bhabha scattering. For a realistic estimation of the background, the number of simulated events should be proportional to the very large cross section of $e^+e^- \to \gamma e^+e^-$. In order to keep this number at a reasonable level, the cross section can be reduced artificially in the generator by requiring a minimum energy for the ISR photons. Naively, a relatively high value for this threshold can be applied and the remaining e^+e^- system still covers the J/ψ mass region.

However, the situation is more complicated because the event generator simulates the emission of not only one but up to two ISR photons. Furthermore, the e^+e^- pairs from the conversions can also be misidentified as $\pi^\pm e^\mp$ pairs. Here, the correlation between the energy of the radiated photon and the reconstructed e^+e^- mass is no longer straightforward. As a matter of fact, the background contribution in the J/ψ region increases, when the photon energy threshold is reduced, even at medium values. In the end, a rather low threshold should be used for a realistic estimation. Unfortunately, this would require an extreme amount of events to be simulated, too many to be practicable.

(a) $J/\psi \rightarrow e^+e^-$ mode.

(b) $J/\psi \rightarrow \mu^+\mu^-$ mode.
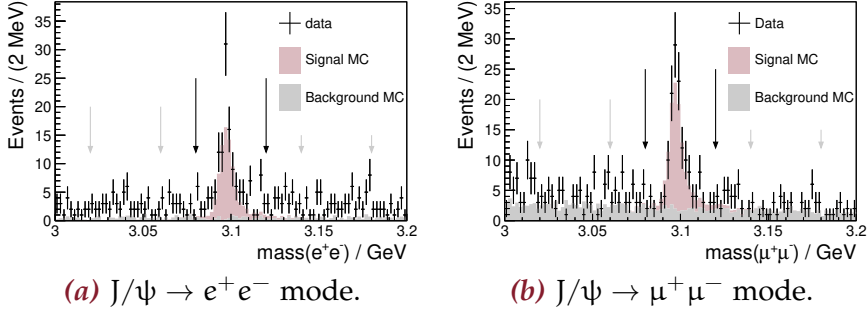
Figure 5.9: Comparison between data, signal MC, and background MC distributions of $m(\ell^+\ell^-)$. All four data sets are combined and all cuts are applied. The MC distributions are scaled to match the integrated luminosity of the data. The black (gray) arrows indicate the peak (sideband) region.

As an alternative, the background contamination is estimated by real events in the J/ψ sidebands. Figure 5.10 shows the corresponding distributions of all observables subjected to a cut and Figure 5.11 shows the distributions of the invariant dipion mass. The normalized distributions of signal MC and sidebands add up to the data distributions observed in the signal region. The fact that this holds true not only for the absolute number of events[7] but also the shape of the distributions indicate the absence of peaking J/ψ backgrounds.

The comparisons of all these observables with the background MC are shown in the Appendix in Figures D.3-D.5. In the muon mode, the background MC describes the data well. In the electron mode, the disagreement is manifested in the scale, not the shape of the distributions. In addition to the issue with the configuration of the $e^+e^- \rightarrow \gamma e^+e^-$ event generator, this supports the hypothesis of no peaking background too.

---

[7]This is automatically fulfilled because the scaling of the sigal MC is determined by the fit to data.

(a) $J/\psi \to e^+e^-$ mode.

(b) $J/\psi \to \mu^+\mu^-$ mode.

(c) $J/\psi \to e^+e^-$ mode.

(d) $J/\psi \to \mu^+\mu^-$ mode.

(e) $J/\psi \to e^+e^-$ mode.

(f) $J/\psi \to \mu^+\mu^-$ mode.
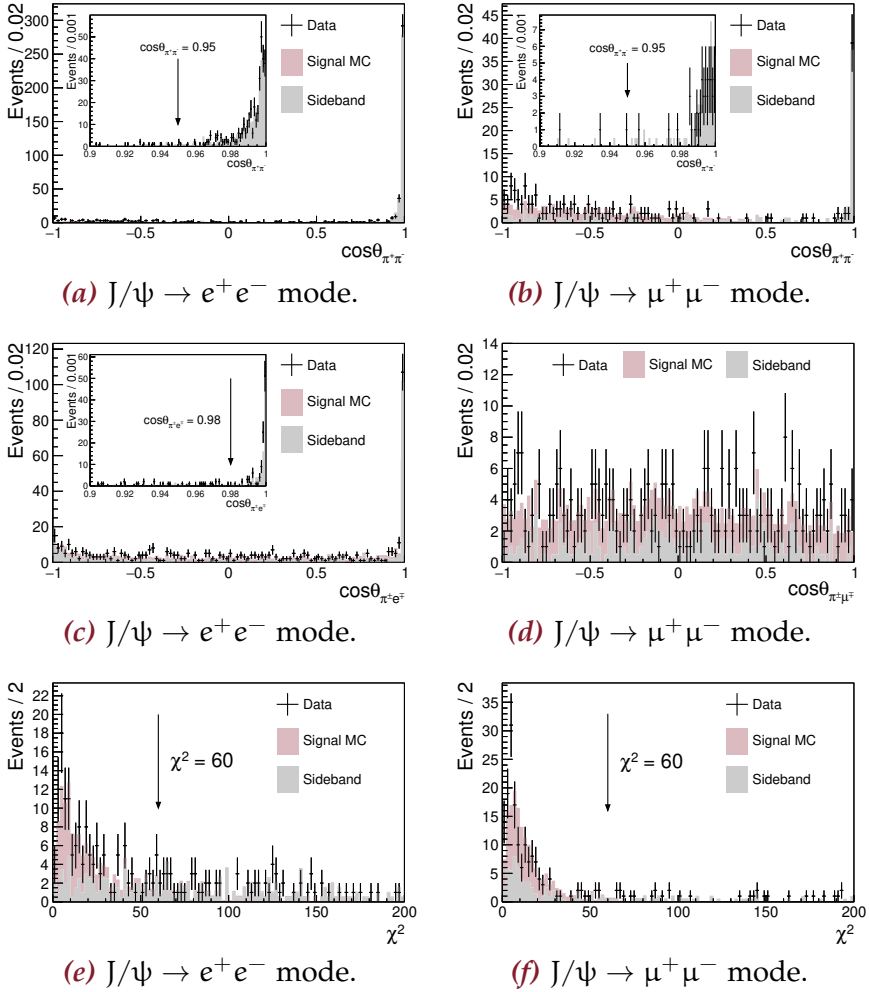
Figure 5.10: Distributions of the variables used for background rejection. Data in the signal region is compared to the sum of signal MC and data in the sidebands. All four data sets are combined and the MC distributions are scaled to match the integrated luminosity of the data. The left column shows the events in the $J/\psi \to e^+e^-$ reconstruction mode and the right column corresponds to $J/\psi \to \mu^+\mu^-$. The cut values are indicated by arrows, while all other cuts are applied. *(a)* and *(b)* distributions of $\cos\theta_{\pi^+\pi^-}$. *(c)* and *(d)* distributions of $\cos\theta_{\pi^\pm\ell^\mp}$. *(e)* and *(f)* distributions of χ^2.

(a) $J/\psi \to e^+e^-$ mode.   *(b)* $J/\psi \to \mu^+\mu^-$ mode.
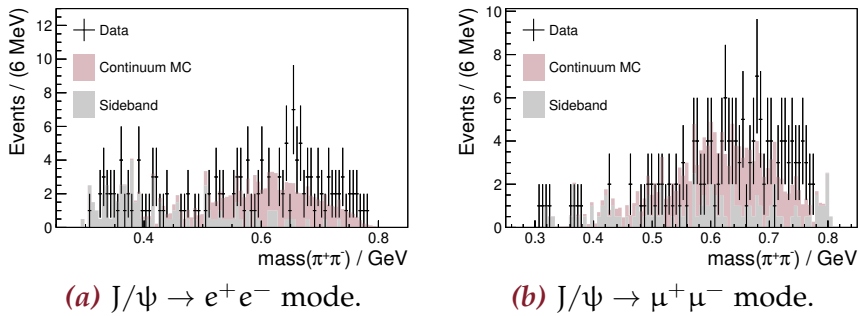
Figure 5.11: Distributions of the invariant dipion mass. Data in the signal region is compared to the sum of signal MC and data in the sidebands. All four data sets are combined and the MC distributions are scaled to match the integrated luminosity of the data.

5.5   Cross Section of $e^+e^- \to \pi^+\pi^- J/\psi$

For each of the four collision energies, the cross section of the process $e^+e^- \to \pi^+\pi^- J/\psi$ is determined using

$$\sigma^{\ell^+\ell^-}(e^+e^- \to \pi^+\pi^- J/\psi) = \frac{N_{obs}}{\int \mathcal{L}\, dt \cdot \epsilon \cdot (1+\delta) \cdot \mathcal{B}(J/\psi \to \ell^+\ell^-)} ,$$
(5.5)

in the $J/\psi \to \ell^+\ell^-$ reconstruction mode with:

- N_{obs} is the number of observed signal events, extracted from a fit to the $\ell^+\ell^-$ mass spectrum (cf. next Section). The number of events in the J/ψ peak is equal to N_{obs}.

- $\int \mathcal{L}\, dt$ is the integrated luminosity (cf. Table 5.1).

- The efficiency ϵ is determined from the analysis of the generated MC samples. Since the continuum model and the signal model yield different efficiencies, they need to be averaged with the actual $X(3872)$ fraction as a weight. In the beginning, this contribution is unknown and as a starting point, the efficiency is solely determined from the continuum MC. After the measurement of the $X(3872)$ contribution, the efficiency is adjusted and a new value for the signal fraction is obtained. This procedure is reiterated until the final result does not change anymore.

- $(1+\delta)$ is the radiative correction factor to account for ISR (cf. equation (2.11)). It is calculated from the KKMC event generator which in the beginning assumes a constant lineshape of the cross section. After the measurement of the lineshape, the new one is fed to KKMC determining a new value of $(1+\delta)$. This alternation of simulation and measurement is integrated in the aforementioned iterative procedure for the efficiency determination. This is particularly important because the radiative corrections have a direct impact on the efficiency.

- Finally, the reconstruction of the J/ψ in the exclusive dilepton channels needs to be incorporated by the corresponding branching fraction $\mathcal{B}(J/\psi \to \ell^+\ell^-)$. The values are taken from the PDG [30]. In the following, $\mathcal{B}(J/\psi \to \ell^+\ell^-)$ is abbreviated as $\mathcal{B}_{\ell\ell}$.

5.5.1 *Fit to the* $m(\ell^+\ell^-)$ *Distribution*

As mentioned above, the number of signal events is extracted from a maximum likelihood fit to the invariant dilepton mass spectrum. This is done independently for both J/ψ decay modes in the range of $3.0\,\mathrm{GeV} < m(\ell^+\ell^-) < 3.2\,\mathrm{GeV}$.

Because the recoil mass of the two pions before the fit has a better resolution (2.8 MeV) than the invariant $\ell^+\ell^-$ mass after the kinematic fit (3.3 MeV), the fit is applied to the spectrum of the recoil mass.[8] Figure 5.12 compares the resolutions of both methods. The reason for the better recoil mass resolution is the better momentum resolution for tracks with lower (transverse) momentum. The transverse momentum resolution of a multiwire drift chamber in a magnetic field, such as the MDC, gets worse when transverse momentum increases [316]. As a result, the pion tracks are reconstructed with a much better momentum resolution than the lepton tracks. Before the kinematic fit, the dipion recoil mass has a far better resolution than the invariant dilepton mass. In the fit, the four-momenta are forced to exactly add up to the four-momentum of the center-of-mass system. During this process, the resolution of the lepton momenta improve, however, at the expense of a deteriorated pion momentum resolution. After the fit, the invariant dilepton mass and the dipion recoil mass have identical values. In the end, the best resolution is obtained by using the recoil mass of the two pions before the fit. In the remainder of the chapter, $m_{\mathrm{rec}}(\pi^+\pi^-)$ is sometimes written with the superscript $\ell^+\ell^-$ to indicate which of the two dilepton channels is referred to.

The signal pdf $\mathrm{sig}(m)$ is modeled according to the MC distribution and has no parameters. The background pdf $\mathrm{bkg}(m|a)$ is described by a linear function with one parameter a.[9] With the signal fraction f, the model pdf $p(m|a,f)$ and the likelihood function

---

[8]The four momentum of the dipion system $p^\mu_{\pi^+\pi^-}$ and the dilepton system $p^\mu_{\ell^+\ell^-}$ add up to the four momentum of the center-of-mass system p^μ_{CMS}. Now, the invariant mass of the $\ell^+\ell^-$ system can be inferred by either squaring $p^\mu_{\ell^+\ell^-}$ or $(p^\mu_{\mathrm{CMS}} - p^\mu_{\pi^+\pi^-})$. The latter is called the recoil mass of the dipion system. Its resolution is determined by the resolution of the pion momenta. The CMS four momentum is given by the accelerator with negligible resolution.

[9]The normalization of the pdf eliminates one of the two parameters required for a linear function.

(a) $J/\psi \to e^+e^-$ mode.

(b) $J/\psi \to \mu^+\mu^-$ mode.
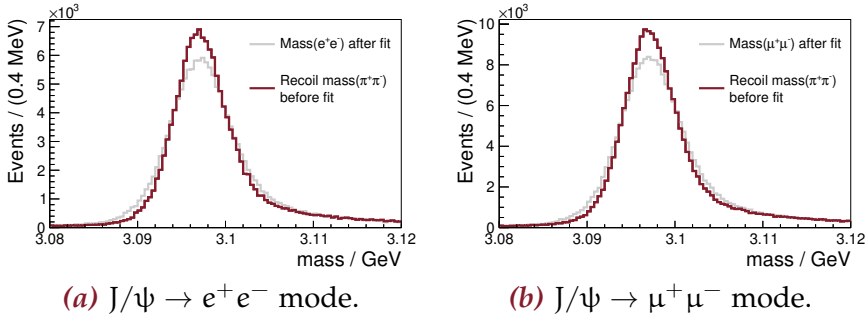
Figure 5.12: Comparison between the invariant $\ell^+\ell^-$ mass after the kinematic fit and the recoil mass of the two pions before the fit. The distributions correspond to the signal MC at $\sqrt{s} = 3871.3\,\text{MeV}$.

$L(a, f)$ (cf. reference [317]) are given by

$$p(m|a, f) = f \cdot sig(m) + (1 - f) \cdot bkg(m, a) \quad , \tag{5.6}$$

$$L(a, f) = \prod_{i=1}^{N} p(m_i|a, f) \quad , \tag{5.7}$$

where N is the total number of events included in the fit and the recoil dipion mass of event i is m_i.

Instead of maximizing the likelihood function directly, the negative log-likelihood function $NLL = -\log N$ is minimized, which is equivalent but numerically much more stable. The fit is performed in the ROOT framework [294] using the RooFit [318] library and the Minuit minimizer [319]. The number of signal events is $N_{obs} = \hat{f} \cdot N$ where $\hat{f}$ is the fitted value of f at the global minimum of NLL. The error of $\hat{f}$ is estimated from the second derivative of $NLL|_{min}$ with respect to the fit parameters.

Alternatively, an extended maximum likelihood fit can be performed. Here, the expected number of events ν is included and directly substituted by the expected number of signal (background) events $\nu_s = \nu f$ ($\nu_b = \nu(1 - f)$).

Table 5.4: Result of the fit to the recoil dipion mass distribution. The results of the two independent J/ψ modes and a combined value are shown. Only statistical uncertainties are listed and rounded to the PDG rounding convention [30]. They come from the number of observed events $N_{obs}^{\ell^+\ell^-}$. The uncertainties of all other quantities are of systematic nature and are listed in the next two Tables 5.5 and 5.6.

$\sqrt{s}$ / MeV	3807.7	3867.4	3871.3	3896.2
$\mathcal{L}_{int}$ / pb^{-1}	50.5	108.9	110.3	52.6
$(1+\delta)$	0.895	0.895	0.895	0.895
$\mathcal{B}_{ee}$ / %	5.971	5.971	5.971	5.971
$N_{obs}^{e^+e^-}$	19 ± 5	30 ± 7	24 ± 6	16 ± 5
$\epsilon^{e^+e^-}$ / %	31.78	31.34	31.29	31.68
$\sigma^{e^+e^-}$ / pb	22 ± 6	16 ± 4	12.7 ± 3.3	17 ± 5
$\mathcal{B}_{\mu\mu}$ / %	5.961	5.961	5.961	5.961
$N_{obs}^{\mu^+\mu^-}$	18 ± 5	40 ± 8	29 ± 6	17 ± 5
$\epsilon^{\mu^+\mu^-}$ / %	45.38	44.90	44.72	45.14
$\sigma^{\mu^+\mu^-}$ / pb	15 ± 4	15.3 ± 2.9	10.9 ± 2.4	13 ± 4
$\sigma^{\ell^+\ell^-}$ / pb	16.9 ± 3.4	15.7 ± 2.3	11.6 ± 1.9	15.0 ± 3.2

The extended likelihood function contains an additional Poissonian term:

$$L(a, \nu_s, \nu_b) = e^{-\nu} \frac{\nu^N}{N!} \prod_{i=1}^{N} p(m_i|a, \nu_s, \nu_b) \qquad (5.8)$$

$$\propto e^{-\nu_s-\nu_b} \prod_{i=1}^{N} [\nu_s \operatorname{sig}(m) + \nu_b \operatorname{bkg}(m|a)] \qquad (5.9)$$

As long as the model has no explicit dependency on ν, the minimization of the corresponding NLL will yield the same result as the standard maximum likelihood fit [317].

Figures 5.13 and 5.14 show the $m_{rec}(\pi^+\pi^-)$ distribution with the fit pdf overlaid. The result of the fit is summarized in Table 5.4.

(a) $\sqrt{s} = 3807.7\,\text{MeV}.$

(b) $\sqrt{s} = 3867.4\,\text{MeV}.$

(c) $\sqrt{s} = 3871.3\,\text{MeV}.$

(d) $\sqrt{s} = 3896.2\,\text{MeV}.$
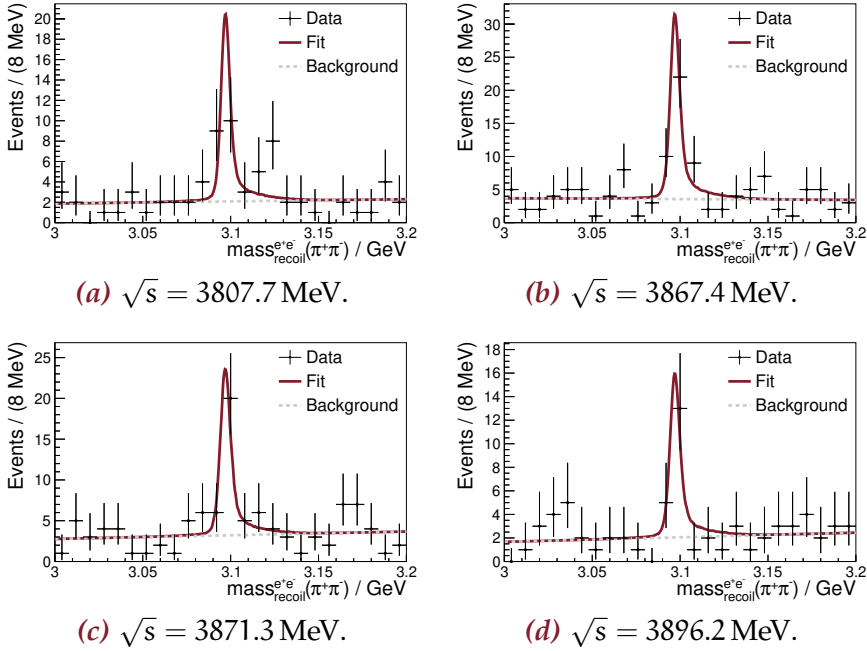
Figure 5.13: Fits to the $m_{\text{rec}}^{e^+e^-}(\pi^+\pi^-)$ distributions. The markers with error bars stand for the data distribution. The red line represents the fit pdf, while the dashed gray line is the background contribution to the pdf.

5.5.2 *Systematic Uncertainties*

All the quantities entering the cross section formula in equation (5.5) have associated systematic uncertainties, which are discussed in the following.

Number of Observed Events

The systematic uncertainty of the number of observed J/ψ events is closely connected to the fit procedure, as discussed below:

- In the fit to the $m_{\text{rec}}(\pi^+\pi^-)$ distribution, the background is modeled as a linear function. This choice has a certain ambiguity and its impact on the extracted cross section is accompanied by a systematic uncertainty which can be estimated by

(a) $\sqrt{s} = 3807.7\,\text{MeV}$.

(b) $\sqrt{s} = 3867.4\,\text{MeV}$.

(c) $\sqrt{s} = 3871.3\,\text{MeV}$.

(d) $\sqrt{s} = 3896.2\,\text{MeV}$.
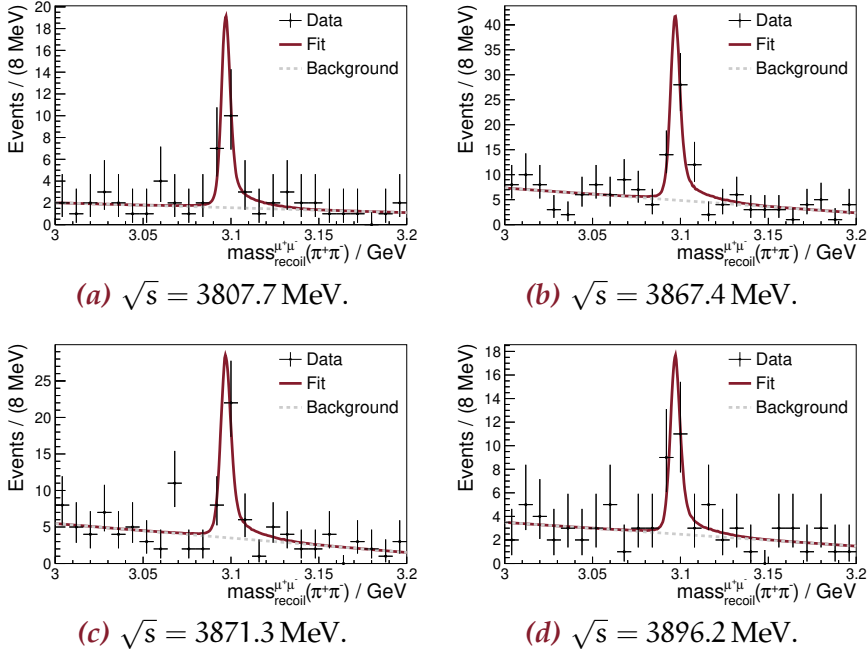
Figure 5.14: Fits to the $m_{rec}^{\mu^+\mu^-}(\pi^+\pi^-)$ distributions. The markers with error bars is the data distribution. The markers with error bars stand for the data distribution. The red line represents the fit pdf, while the dashed gray line is the background contribution to the pdf.

the difference in N_{obs} when the fit is performed with a different background parameterization. However, this method is susceptible to statistical fluctuations, which are already taken into account in the statistical uncertainty. In order to minimize the influence of statistics, a bootstrap method is applied: the fit is performed with a quadratic function as background to 1000 pseudo data sets. These pseudo data sets are sampled from the real data set, but events are allowed to be selected multiple times. In other words, some events are selected more than once and other events are not selected at all. The results of 1000 fits are averaged and the difference to the nominal fit is taken as systematic uncertainty.

- In order to account for the difference of the $m_{rec}(\pi^+\pi^-)$ resolution in data and simulation, an alternative fit to the $m_{rec}(\pi^+\pi^-)$

distribution is performed. The signal pdf is convolved with a Gaussian and the variance is allowed to float freely. The resulting difference to the nominal fit in N_{obs} is taken as a systematic uncertainty. In all instances, the uncertainty is found to be less than 0.1 % and can be neglected.

Integrated Luminosity

The uncertainties of the integrated luminosities are listed in Table 5.1.

Efficency Estimation

The various sources contributing to the systematic uncertainties associated with the efficiency are described in the following:

- For the measurement, four charged tracks are analyzed. At BESIII, the uncertainty of the tracking efficiency is 1 % per charged track yielding a total uncertainty of 4 % [86, 320].

- The ambiguity of modeling the continuum process $e^+e^- \rightarrow \pi^+\pi^- J/\psi$ was already mentioned in Section 5.3.2 and is indicated in Figure 5.6. For the continuum model, the systematic uncertainty associated to this ambiguity is estimated by the efficiency difference when using the σ PHSP model instead of the VVPIPI model. For the resonant X(3872) MC, the PARTWAVE model for the decay to $\rho^0 J/\psi$ is exchanged by a simple PHSP model. The efficiency difference is taken as the systematic uncertainty.

- The efficiency ϵ is determined by the analysis of MC events. The statistically limited MC sets attach an uncertainty on the efficiency. The relatively large size of each signal and continuum MC set of 500 k events implies a relatively small error. It is less than 0.1 % and can be neglected.

- Reference [315] shows that the uncertainty associated with the kinematic fit can be estimated by half the efficiency difference of the MC analysis with and without the helix parameter correction (cf. Section 5.4.2).

Table 5.5: Relative systematic uncertainties (in %) affecting the measured cross section $\sigma(e^+e^- \to \pi^+\pi^- J/\psi)$ via the $J/\psi \to e^+e^-$ mode. The total uncertainty is the quadratic sum of the individual errors.

Source	3807.7 MeV	3867.4 MeV	3871.3 MeV	3896.2 MeV
$\int \mathcal{L} \, dt$	1.0	1.2	0.7	1.0
Tracking	4.0	4.0	4.0	4.0
$\mathcal{B}_{ee}$	0.5	0.5	0.5	0.5
Line shape	0.8	1.2	1.3	0.7
Kinematic fit	0.9	0.8	0.9	0.9
Decay model	2.1	2.7	2.2	2.4
$m_{rec}(\pi^+\pi^-)$ fit	4.9	2.2	4.2	11.8
Total	6.8	5.7	6.5	12.8

Radiative Correction Factor

The uncertainty of the cross section lineshape of $e^+e^- \to \pi^+\pi^- J/\psi$ affects both the radiative correction factor $(1+\delta)$ and the efficiency. Hence, the systematic uncertainty of the product $\epsilon \times (1+\delta)$ is considered. It is determined from the difference between using the lineshape obtained in this analysis and the one from an earlier measurement [247]

J/ψ Branching Fractions

The values for $\mathcal{B}_{\ell\ell}$ together with their uncertainties are taken from the PDG [30].

Total Systematic Uncertainties

The contributions of each source of systematic uncertainty are listed in Tables 5.5 and 5.6. The uncertainty associated with the fit to the $m_{rec}(\pi^+\pi^-)$ distribution varies strongly between the different center-of-mass energies and J/ψ decay channels. The bootstrap method could not mitigate the statistical effect completely and the systematics are overestimated. However, the total uncertainties are still dominated by the statistical error and the systematics play only a subordinate role. The overall precision would not benefit from further efforts to reduce the systematics uncertainties.

Table 5.6: Relative systematic uncertainties (in %) affecting the measured cross section $\sigma(e^+e^- \to \pi^+\pi^-J/\psi)$ via the $J/\psi \to \mu^+\mu^-$ mode. The total uncertainty is the quadratic sum of the individual errors.

Source	3807.7 MeV	3867.4 MeV	3871.3 MeV	3896.2 MeV
$\int \mathcal{L}\,\mathrm{dt}$	1.0	1.2	0.7	1.0
Tracking	4.0	4.0	4.0	4.0
$\mathcal{B}_{\ell\ell}$	0.6	0.6	0.6	0.6
Line shape	0.8	1.7	1.3	0.6
Kinematic fit	0.7	0.7	0.7	0.7
Decay model	3.6	4.0	3.7	4.0
$m_{rec}(\pi^+\pi^-)$ fit	1.2	1.7	7.7	4.2
Total	5.7	6.3	9.6	7.2

Table 5.7: Cross section of $e^+e^- \to \pi^+\pi^-J/\psi$ as determined in this analysis. The first error is the statistical and the second one is the systematic uncertainty.

	$\sigma(e^+e^- \to \pi^+\pi^-J/\psi)\,/\,\mathrm{pb}$		
$\sqrt{s}\,/\,\mathrm{MeV}$	e^+e^- mode	$\mu^+\mu^-$ mode	combined
3907.7	$22.0 \pm 6.4 \pm 1.5$	$14.8 \pm 4.0 \pm 0.8$	$16.9 \pm 3.4 \pm 0.7$
3867.4	$16.4 \pm 3.6 \pm 0.9$	$15.3 \pm 2.9 \pm 1.0$	$15.7 \pm 2.3 \pm 0.7$
3871.3	$12.7 \pm 3.3 \pm 0.8$	$10.9 \pm 2.4 \pm 1.0$	$11.6 \pm 1.9 \pm 0.6$
3896.2	$17.5 \pm 5.1 \pm 2.2$	$13.4 \pm 4.1 \pm 1.0$	$15.0 \pm 3.2 \pm 0.9$

5.5.3 Result

The final result of the cross section measurement is listed in Table 5.7 and shown in Figure 5.15. The values for the two 2013 data sets (lowest and highest $\sqrt{s}$) agree well with a previous analysis [247]. As already mentioned, the statistical uncertainty clearly dominates the overall uncertainty. There is no enhancement at the X(3872) mass visible. In fact, there is a small dip in the cross section. However, the deviation between the on-resonance and the off-resonance data sets is only at the level of 1.3 standard deviations.

The measured cross section is in good agreement with a constant.[10] The initial values for the efficiency ϵ and the radiative cor-

---

[10]A simple fit of a constant to the measured values gives $\chi^2/\mathrm{NDF} = 2.71/3$ or alternatively a p-value of 0.44.
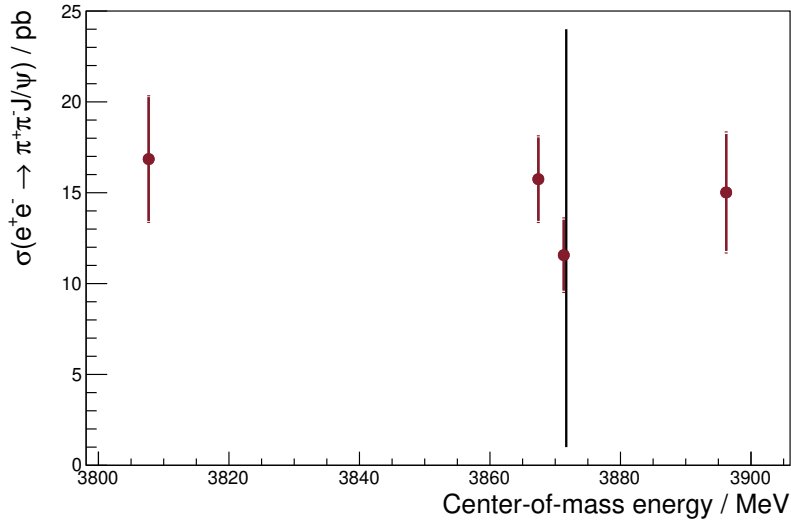
Figure 5.15: Cross section of $e^+e^- \to \pi^+\pi^- J/\psi$. The results of both J/ψ decay modes are combined. The nominal mass of the X(3872) as listed in the PDG [30] is indicated by the vertical line. The error bars represent the statistical errors and the small horizontal lines above and below the error bars represent the total uncertainties, i.e. the quadratic sum of the statistical and systematic errors. The precision is fully determined by statistics.

rection factor $(1 + \delta)$ were based on the assumption of a flat cross section with no X(3872) contribution. Since this coincides with the outcome of the measurement, the iterative procedure for the determination of $\epsilon \times (1 + \delta)$ described in Section 5.5.1 does not have to be carried out. Since there is no sign of direct X(3872) formation, an upper limit on $\Gamma_{ee} \times \mathcal{B}$ is determined in the next Section.

5.6   Upper Limit on $\Gamma_{ee} \times \mathcal{B}(X(3872) \to \pi^+\pi^- J/\psi)$

5.6.1   Improved Sensitivity to the $X(3872)$ Signal

In order to increase the sensitivity to the $X(3872) \to \rho^0 J/\psi$ signal, an additional cut is applied. By requiring $m(\pi^+\pi^-) > 0.6\,\text{GeV}$, the ratio of the ρ^0 contribution compared to the $\pi^+\pi^-$ S-wave of the continuum process is enhanced. The same fitting procedure as in Section 5.5.1 is applied with the exception that the efficiency is estimated from the $X(3872)$ MC model. As one can imagine, this results in an incorrect value for the reconstructed cross section because there is no evidence for an $X(3872)$ signal. The $e^+e^- \to \pi^+\pi^- J/\psi$ process is fully governed by continuum, which is reconstructed with a different efficiency, in particular after the cut on $m(\pi^+\pi^-)$. Nevertheless, Appendices E.2 and E.3 verify that this incorrect cross section leads to the correct estimation of $\Gamma_{ee} \times \mathcal{B}$. To underline that this cross section yields an incorrect value, it is called pseudo cross section and labeled as $\tilde{\sigma}$ from now on.

The $m_{\text{rec}}(\pi^+\pi^-)$ distributions after the $m(\pi^+\pi^-)$ cut are shown in Appendix D.3, Figures D.6 and D.7 with the fit result overlaid. The fit result is summarized in Table D.1. The systematic uncertainties are determined in the same way as in Section 5.5.2, but with the following differences:

- The systematic uncertainty associated with the choice of the MC model is estimated by the efficiency difference between the nominal model ($X(3872) \to \rho^0 J/\psi$ PARTWAVE) and the one, where the is modeled with PHSP.

- In contrast to the systematic uncertainties in Section 5.5.2, the impact of the $m_{\text{rec}}(\pi^+\pi^-)$ resolution is not negligible, but still small.

The systematic uncertainties are summarized in Tables D.2 and D.3.

The result of the pseudo cross section measurement is shown in Figure 5.16 and Table 5.8. Again, there is no enhancement at the $X(3872)$ mass and the pseudo cross section is fully populated by the one photon exchange continuum $e^+e^- \to \pi^+\pi^- J/\psi$. In fact, the deviation between the on-resonance and the off-resonance values is larger than in the previous Section, but the significance is only at 2.4 standard deviations.
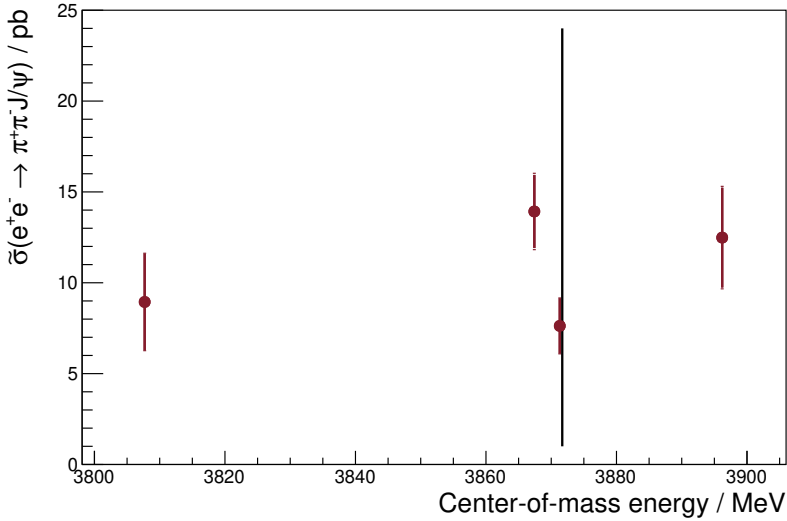
Figure 5.16: Pseudo cross section of $e^+e^- \to \pi^+\pi^- J/\psi$. The results of both J/ψ decay modes are combined. The nominal mass of the $X(3872)$ as listed in the PDG [30] is indicated by the vertical line. The error bars represent the statistical errors and the small horizontal lines above and below the error bars represent the total uncertainties, i.e. the quadratic sum of the statistical and systematic errors. The precision is fully determined by statistics.

Table 5.8: Pseudo Cross section of $e^+e^- \to \pi^+\pi^- J/\psi$. The first error is the statistical and the second one is the systematic uncertainty.

	$\tilde{\sigma}(e^+e^- \to \pi^+\pi^- J/\psi) / \mathrm{pb}$		
$\sqrt{s} / \mathrm{MeV}$	e^+e^- mode	$\mu^+\mu^-$ mode	combined
3907.7	$9.7 \pm 4.4 \pm 0.7$	$8.5 \pm 3.3 \pm 0.5$	$8.9 \pm 2.7 \pm 0.4$
3867.4	$15.2 \pm 3.1 \pm 0.8$	$13.0 \pm 2.7 \pm 0.9$	$13.9 \pm 2.0 \pm 0.6$
3871.3	$7.5 \pm 2.3 \pm 0.4$	$7.7 \pm 2.0 \pm 0.4$	$7.6 \pm 1.5 \pm 0.3$
3896.2	$14.8 \pm 4.2 \pm 1.1$	$10.8 \pm 3.6 \pm 0.8$	$12.5 \pm 2.7 \pm 0.6$

Instead of these values, which are the results of maximum likelihood fits, the likelihood functions itself are used in the further analysis. The systematic uncertainties in Table 5.8, however, are used.

5.6.2 *Lineshape and Likelihood Function*

Due to the different quantum numbers of the continuum process and the resonant X(3872) formation, their amplitudes cannot interfere.[11] The total lineshape of $\tilde{\sigma}(e^+e^- \to \pi^+\pi^- J/\psi)$ is modeled as an incoherent sum. The continuum contribution is assumed to be flat, i.e. constant, and the X(3872) is described by a relativistic Breit-Wigner resonance [321]. Only the $\pi^+\pi^- J/\psi$ decay mode is taken into account, so the corresponding branching fraction needs to be included in the lineshape parameterization:

$$\tilde{\sigma}(\sqrt{s}) = \tilde{\sigma}_{\text{cont}} + 12\pi \frac{\Gamma_{\text{tot}}\Gamma_{ee} \times \mathcal{B}}{\left(s - m_0^2\right)^2 + m_0^2\Gamma_{\text{tot}}^2} \quad , \qquad (5.10)$$

where $\tilde{\sigma}_{\text{cont}}$, Γ_{tot}, and Γ_{ee} are the constant continuum, the total width, and the electronic width of the X(3872), respectively. Here, m_0 is the X(3872) mass and s is the Mandelstam variable (squared center-of-mass energy). Of the X(3872) parameters, only the mass is known ($m(X(3872)) = (3871.69 \pm 0.17)\,\text{MeV}$ [30]). Since the branching ratio $\mathcal{B}(X(3872) \to \pi^+\pi^- J/\psi)$ has not been determined yet,[12] the product $\Gamma_{ee} \times \mathcal{B}$ is treated as one parameter and an upper limit on this product is set instead of a limit on Γ_{ee} alone. In total, there are three unknown parameters: $\tilde{\sigma}_{\text{cont}}$, Γ_{tot}, and $\Gamma_{ee} \times \mathcal{B}$.

The spread of $\sqrt{s}$ is taken into account by a convolution of the lineshape with a Gaussian of the corresponding standard deviation:

$$\tilde{\sigma}_i = \left[\tilde{\sigma}(\sqrt{s}) \otimes N(\sqrt{s}|0, \delta\sqrt{s_i})\right]_{\sqrt{s}=\sqrt{s_i}} \quad , \qquad (5.11)$$

where $N(x|\mu, \sigma)$ is a Gaussian with mean μ and standard deviation σ. Since the spread is different for the different data sets (cf. Table 5.1), the convolution has to be carried out for each data set individually. For the 2017 data, the BEMS information is available.

---

[11]Nevertheless, Appendix E.1 discusses the possibility of interference with $e^+e^- \to \gamma^*\gamma^* \to \rho^0 J/\psi$ via double vector meson dominance.

[12]In fact, there is no definite value for any of the branching fractions. Only lower limits are available [30].

The two 2013 data points are far away from the X(3872) mass. As a result, they are only sensitive to the constant term σ_{cont} in the lineshape and a convolution with a moderate energy spread will not alter the cross section value. Nevertheless, a $\sqrt{s}$ spread of 1.5 MeV is assumed for these data points. The pseudo cross section for the data set i is predicted by the aforementioned three parameters to be $\tilde{\sigma}_i$ given by equation (5.11).

The global likelihood function is obtained by connecting the above lineshape parameterization with the likelihood functions defined in Section 5.5.1. With the lineshape parameterization, the model acquires an explicit dependence on the total number of events. The extended likelihood functions as defined in equation (5.9) is used. Equation (5.5) is used to substitute the expected number of signal events ν_s with a function of the pseudo cross section $\tilde{\sigma}$. As a result, the likelihood function for each data set i and J/ψ mode j is now depending on the cross section:

$$L_i^j(\nu_{s,i}^j, \nu_{b,i}^j, a_i^j) \longrightarrow L_i^j(\tilde{\sigma}, \nu_{b,i}^j, a_i^j) \quad . \tag{5.12}$$

Now, the global likelihood function is the product of eight individual likelihood functions L_i^j (four data sets and two J/ψ decay modes):

$$L = \prod_{i=1}^{4} \prod_{j=ee,\mu\mu} L_i^j(\tilde{\sigma} = \tilde{\sigma}_i, a_i^j, \nu_{b,i}^j) \quad . \tag{5.13}$$

Here, $\tilde{\sigma}$ is the variable of interest in the likelihood function L_i^j and $\tilde{\sigma}_i \equiv \tilde{\sigma}_i(\tilde{\sigma}_{\text{cont}}, \Gamma_{\text{tot}}, \Gamma_{ee} \times \mathcal{B})$ is the pseudo cross section predicted by the three lineshape parameters. In the global likelihood function, the variable of interest is substituted by $\tilde{\sigma}_i$. By doing so, the global likelihood function is now a function of the three lineshape parameters in addition to the background parameters a_i^j and the number of background events $\nu_{b,i}^j$. With the likelihood function depending on $\Gamma_{ee} \times \mathcal{B}$, a corresponding upper limit is determined by means of Bayesian inference.

5.6.3 *Bayesian Formalism*

In the Bayesian formalism, the likelihood function $L(x, \theta)$ with data $x \in \mathbb{R}^m$ and parameters is interpreted as the conditional pdf $f(x|\theta)$,

i.e. the likelihood of observing data $x \in \mathbb{R}^n$ given the parameter $\theta \in \mathbb{R}^m$ [317]. Using Bayes' Theorem [322], this pdf can be turned into a conditional pdf of the parameters θ given the data x:

$$f(\theta|x) = \frac{f(x|\theta)\pi(\theta)}{\int f(x|\theta)\pi(\theta)\,d\theta} \quad , \tag{5.14}$$

$$\propto f(x|\theta)\pi(\theta) \quad . \tag{5.15}$$

The prior pdf $\pi(\theta)$ gives the likelihood of the parameters before the measurement x was obtained. In (5.14) the denominator is independent of θ and can be viewed as a normalization constant. In most cases, the prior pdf is unknown and very often assumed to be constant. On one hand, a constant is strictly speaking not a pdf and not in all cases the optimal choice.[13] On the other hand, it has the advantage that the mode of the resulting posterior pdf $(\theta|x)$ coincides with the maximum likelihood fit result. In this analysis, the priors are set to zero in the unphysical region of negative widths. In the physical region ($\Gamma_{tot} > 0$ and $\Gamma_{ee} \times \mathcal{B} > 0$), the prior pdf of $\Gamma_{ee} \times \mathcal{B}$ is assumed to be flat. The prior pdf of the total width is taken from the Belle publication in which the current upper limit of $\Gamma_{tot} < 1.2\,\text{MeV}$ at $90\,\%$ confidence level was determined [31]. Its shape is approximated by Gaussian with a mean at zero. Both the Belle result and the approximation are shown in Figure 5.17.

Often, a model depends also on parameters that are not of interest, e.g. the coefficients of a polynomial describing a background. Consider the parameter set $\theta = (\vartheta, \theta_n)$ where ϑ is the interesting parameter set and θ_n are the others, so-called nuisance parameters. The posterior pdf of only the parameters of interest is obtained by the marginalization of the nuissance parameters[317]:

$$f(\vartheta|x) = \int f((\vartheta, \theta_n)|x)\,d\theta_n \tag{5.16}$$

In the analysis, the two parameters of interest are $\Gamma_{ee} \times \mathcal{B}$ and Γ_{tot}. The marginalization needs to be carried out over the background parameters a_i^j, the numbers of background events $\nu_{b,i}^j$, and

---

[13]A constant cannot be normalized and is therefore no pdf. Nevertheless, it can result in a proper, i.e. normalizable, posterior pdf $(\theta|x)$. There are different approaches to construct so-called non-informative or objective priors, which are favorable, but very difficult to obtain in multi-parameter models [323, 324].
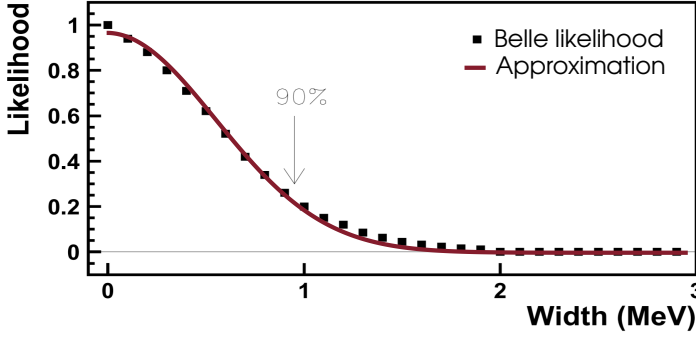
Figure 5.17: Prior pdf of the total width of the X(3872) state, the posterior pdf or likelihood function of Γ_{tot} of a measurement by the Belle collaboration [31]. The current upper limit is based on this likelihood function. The final value of 1.2 MeV at 90 % confidence level, however, is obtained after a bias correction. The curve is approximated by a Gaussian with a mean at zero. For the further analysis, a standard deviation of 0.73 MeV is used, which ensures the 90 % limit to be at 1.2 MeV. Figure adapted from reference [31].

the pseudo cross section of the continuum $\tilde{\sigma}_{cont}$. Fortunately, the marginalization over a_i^j and $\nu_{b,i}^j$ can be performed before the product in equation (5.13) is built. The marginalized likelihood functions of the $m_{rec}(\pi^+\pi^-)$ fits are given by

$$\hat{\mathfrak{L}}_i^j(\tilde{\sigma}) = \int L_i^j(\tilde{\sigma}, a_i^j, \nu_{b,i}^j) \, da_i^j \, d\nu_{b,i}^j \quad . \tag{5.17}$$

They only depend on the parameter $\tilde{\sigma}$. After the substitution with the pseudo cross section $\tilde{\sigma}_i$ from equation (5.11), the product is formed again. All that is left, is the marginalization over $\tilde{\sigma}_{cont}$:

$$\hat{\mathfrak{L}}(\Gamma_{ee} \times \mathcal{B}, \Gamma_{tot}) = \int \prod_{i=1}^{4} \prod_{j=ee,\mu\mu} \hat{\mathfrak{L}}_i^j(\tilde{\sigma} = \tilde{\sigma}_i) \, d\tilde{\sigma}_{cont} \tag{5.18}$$

This is the marginalized global likelihood function. After the integration, the likelihood function only depends on the parameters of interest $\Gamma_{ee} \times \mathcal{B}$ and Γ_{tot}. All the integrations are performed numerically within software based on ROOT [294].

A 90 % credible interval[14] in Bayesian inference can be defined by the following two properties [317]:

- The integral of the normalized posterior pdf (marginalized likelihood) over the interval must be 90 %.

- For each point in the interval, the posterior pdf is larger than for every other point outside the interval.

The definition can be extended to the multi-parameter case, where the interval becomes a multi-dimensional region. Usually, when the lower interval boundary coincides with the border to the unphysical region, only the upper limit is reported.

5.6.4   *Incorporation of Systematic Uncertainties*

Before the upper limit can be obtained, systematic uncertainties need to be incorporated into the global likelihood function. The input likelihoods from the $m_{rec}(\pi^+\pi^-)$ fits $\hat{\mathfrak{L}}_i^j$ reflect only statistical effects.

There are two different kinds of systematic uncertainties which have to be treated differently. The first kind affects the cross section measurement and is described in Section 5.5.2. The second kind affects the lineshape parameterization and includes the uncertainties associated with the X(3872) mass, $\sqrt{s}$, and the beam spread.

Uncertainty of the Cross Section

The systematic uncertainties of the cross section are described in Section 5.6.1 and listed in Tables D.2, D.3, and 5.8. They are incorporated by convolving the marginalized likelihoods $\hat{\mathfrak{L}}_i^j$ given by equation (5.17) with a Gaussian of the corresponding variance:

$$\mathfrak{L}_i^j(\tilde{\sigma}) = \hat{\mathfrak{L}}_i^j(\tilde{\sigma}) \otimes N(\tilde{\sigma}|0, \Delta\tilde{\sigma}_i^j) \qquad (5.19)$$

The marginalized likelihoods $\hat{\mathfrak{L}}_i^j(\tilde{\sigma})$ and $\mathfrak{L}_i^j(\tilde{\sigma})$ as well as the product $\mathfrak{L}_i(\tilde{\sigma}) := \mathfrak{L}_i^{ee}(\tilde{\sigma}) \times \mathfrak{L}_i^{\mu\mu}(\tilde{\sigma})$ are shown in Figure 5.18.

This method lacks the possibility to include the correlations of the systematic uncertainties among the different data points and

---

[14]The more commonly used name "confidence interval" is a term used in frequantists stochastic. In the Bayesian paradigm however, the term "credible interval" is established.
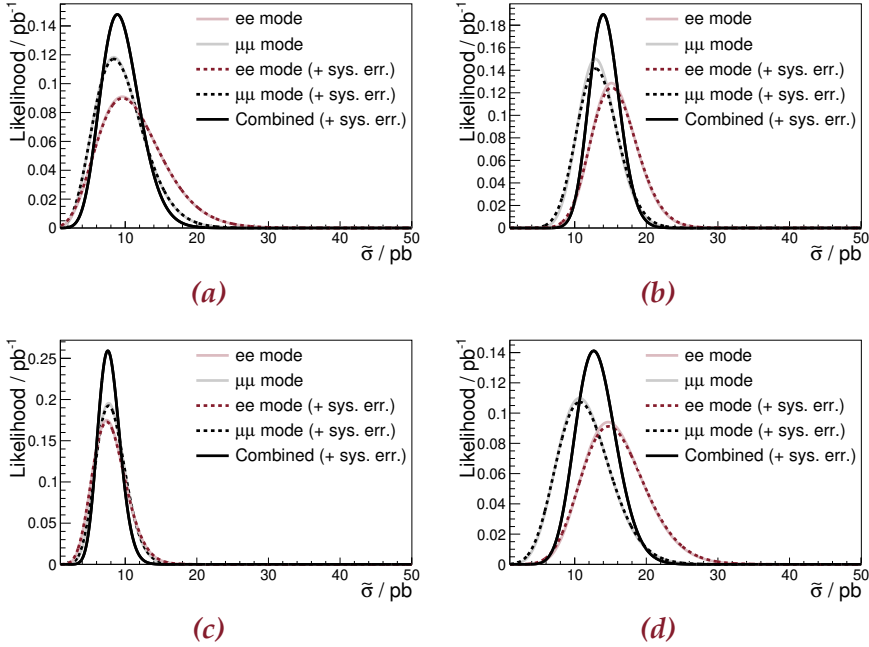
Figure 5.18: The marginalized likelihoods before and after the con-
volution with the systematic uncertainties $\hat{\mathcal{L}}_i^j$ and $\mathcal{L}_i^j$ as functions of
the pseudo cross section $\tilde{\sigma}$. In addition, the normalized product of
both modes are overlaid. As expected from the previous discussions,
the systematic uncertainties have only little effect.

J/ψ decay modes. However, a study in Appendix E.4 shows that
the improvement of the upper limit due to the incorporation of cor-
relations is smaller than the rounding precision. Consequently, the
correlation of the systematic uncertainties are neglected.

Uncertainty of the Lineshape Parameterization

The uncertainties affecting the lineshape are the following:

- The uncertainty of the X(3872) mass of 0.17 MeV is taken from
  the PDG [30].

- The measured center-of-mass energies have uncertainties
  which have to be taken into account (cf. Table 5.1).

- Due to the convolution of the pseudo cross section lineshape with a Gaussian representing the spread of $\sqrt{s}$ (cf. equation 5.11), the overall result is sensitive to the corresponding uncertainty. The BEMS provided the uncertainties of the energy spread for the 2017 data (cf. Table 5.1). For the 2013 data, there is no such information, but Section 5.6.2 discussed the negligible impact of the energy spread for those data points. Nevertheless, uncertainties of 0.2 MeV are assumed, identical to the off-resonance data set.

A common approach to include these systematic uncertainties is the extension of the likelihood function. The affected quantities are treated as nuisance parameters with corresponding Gaussian prior pdfs. After the marginalization, the likelihood function depends only on Γ_{tot} and $\Gamma_{ee} \times \mathcal{B}$ again. However, this turns the one-dimensional integral of (5.18) into a ten-dimensional integral making it computationally very expensive. This issue is resolved by the application of a MC integration technique [325, 326]. The following two steps are repeated several times ($\mathcal{O}(10^4)$).

1. The values for the parameters with systematic uncertainty are sampled from the corresponding normal distributions.

2. The marginalized likelihood $\hat{\mathcal{L}}(\Gamma_{ee} \times \mathcal{B}, \Gamma_{tot})$ as defined in equation (5.18) but already including the systematics of the cross section is calculated. Only a one-dimensional integral is involved.

Finally, the likelihoods of each repetition are summed up. This is equivalent to the average because the likelihoods are not normalized. Effectively, a nine-dimensional integral is converted into a sum:

$$\mathcal{L}(\Gamma_{ee} \times \mathcal{B}, \Gamma_{tot}) = \sum_i \hat{\mathcal{L}}(\Gamma_{ee} \times \mathcal{B}, \Gamma_{tot}, \theta)|_{\theta=\theta_i} \qquad (5.20)$$

where θ stands for the parameters with uncertainties and θ_i are the sampled values in iteration i. $\mathcal{L}(\Gamma_{ee} \times \mathcal{B}, \Gamma_{tot})$ is now the global likelihood function including all systematic uncertainties.

In Figure 5.19 a fixed value of $\Gamma_{tot} = 1.2$ MeV is assumed and the obtained upper limit of $\Gamma_{ee} \times \mathcal{B}$ at 90 % confidence level is plotted
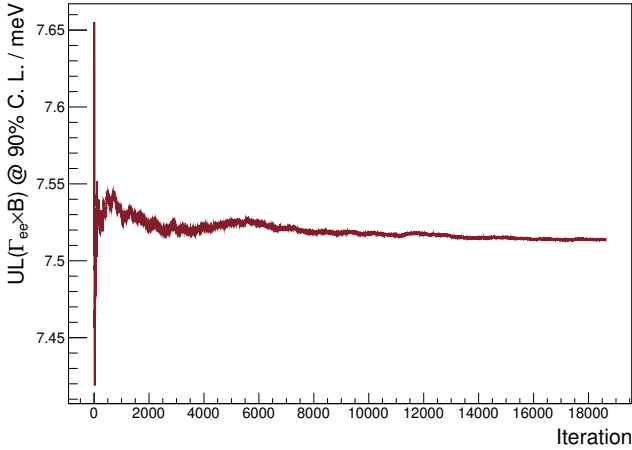
Figure 5.19: Development of the obtained upper limit on $\Gamma_{ee} \times \mathcal{B}$ at 90 % C.L. depending on the number of iterations in the MC integration. A total width of $\Gamma_{\text{tot}} \approx 1.2\,\text{MeV}$ is assumed, the current upper limit.

as a function of the number of iterations in the MC integration. It is noteworthy that all values in the range of the y-axis are rounded to 8 meV when following the PDG convention [30]. The values must be rounded up because it is an upper limit. Again, the systematic uncertainties play a negligible role. The number of approximately 18 000 iterations is by far sufficient.

5.6.5   *Result*

The likelihood function of equation (5.20) is shown in Figure 5.20. The largest fraction of the likelihood is concentrated towards the origin. This is expected because the non-observation of any X(3872) enhancement in the measured cross section favors small values of $\Gamma_{ee} \times \mathcal{B}$. After all, an electronic width of zero describes the data best. The measurement provides no sensitivity to the total width, but the prior pdf for Γ_{tot}, which describes the current knowledge about the width, attracts the likelihood to small values.

An upper limit on $\Gamma_{ee} \times \mathcal{B}$ can be obtained in two different ways. The first one assumes a fixed total width. The likelihood function is then integrated along the $\Gamma_{ee} \times \mathcal{B}$ axis until the integral reaches 90 %. The corresponding value for $\Gamma_{ee} \times \mathcal{B}$ is the upper limit. Figure 5.21(a) shows the determination of the limit for an assumed total
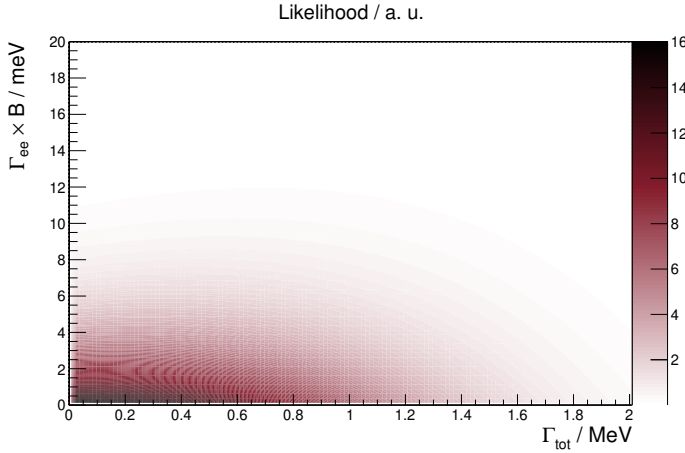
Figure 5.20: Likelihood function of $\Gamma_{ee} \times \mathcal{B}$ and Γ_{tot}.

width of 1.2 MeV. Figure 5.21(b) shows the obtained upper limits as a function of the Γ_{tot} assumption. For $\Gamma_{\text{tot}} = 1.2$ MeV, the 90 % limit is 8 meV after rounding.

The second way to obtain an upper limit on $\Gamma_{ee} \times \mathcal{B}$ is the marginalization of the likelihood function over Γ_{tot} and the subsequent integration until the 90 % mark. Figure 5.22(a) shows the likelihood function after this marginalization. After rounding, the resulting limit reads 7 meV at 90 % confidence level. Compared to the limit currently listed by the PDG, an improvement of a factor of about 20 is achieved [30, 32].

The two-dimensional likelihood function (cf. Figure 5.20) can also be used for the construction of a two-dimensional credible region in the $\Gamma_{\text{tot}} \times (\Gamma_{ee} \times \mathcal{B})$ plane. It is shown in Figure 5.22(b).
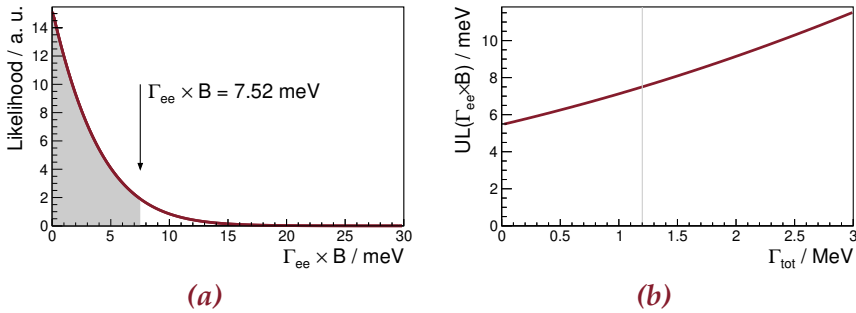
Figure 5.21: Determination of the upper limit on $\Gamma_{ee} \times \mathcal{B}$ for fixed Γ_{tot} assumptions. *(a)* Γ_{tot} is assumed to be 1.2 MeV, the current upper limit. The curve is basically a slice along the $\Gamma_{ee} \times \mathcal{B}$ axis through the two-dimensional likelihood function of Figure 5.20 at $\Gamma_{tot} = 1.2$ MeV. The gray area indicates the 90 % integral below the curve. The upper limit is the value at the right edge of that area. *(b)* The 90 % upper limit as a function of the total width assumption. The gray line indicates the current upper limit on Γ_{tot}.
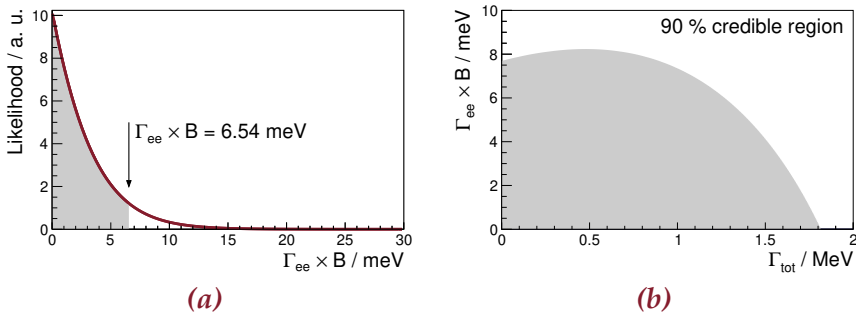
Figure 5.22: *(a)* Likelihood function of $\Gamma_{ee} \times \mathcal{B}$ after the marginalization over Γ_{tot}. The 90 % integral is indicated as the gray area. The right edge corresponds to the upper limit. *(b)* Two-dimensional credible region at 90 % in the $\Gamma_{tot} \times (\Gamma_{ee} \times \mathcal{B})$ plane.

———

CONCLUSION

I N this thesis, two different topics in in the framework of the BE-SIII experiment are addressed: firstly, the developments in the context of the cZDD. Secondly the analysis of $e^+e^- \to \pi^+\pi^- J/\psi$ in the vicinity of the $X(3872)$ mass with the subsequent determination of a new upper limit on its electronic width times the corresponding branching ratio. Both subjects are summarized and discussed separately.

Developments Regarding the cZDD

In order to improve the capabilities of BESIII to detect photons from ISR, a new detector called cZDD is foreseen to be placed in the very forward and backward region of BESIII [292]. This close to the beam axis, the detector will experience an extremely high background rate in the order of 1 MHz. Together with the limited available space, the high background demands strict design requirements. The design is based on a previous work by Marcel Werner [260]. The detector is made from the inorganic scintillator LYSO with SiPMs converting the scintillation light in electric signals. These signals in turn get digitized by sampling ADCs and correlated with the BESIII L1 trigger on FPGA based hardware. The work presented in Chapter 4 is an important step towards the completion and commissioning of the cZDD at BESIII.

One contribution worked out in the context of this thesis is the implementation of the geometry of the accelerator structure in front of the detector into a GEANT4 simulation. The simulations show the dramatic effect of the introduced material budget. The detector is still able to register the events, but cannot provide an energy information. The cZDD can be instrumented as a tagger, but not as a calorimeter.

Another contribution of this thesis is the development of a prototype DAQ for the cZDD. It already utilizes the designated hardware for the final cZDD DAQ. The analog signals are digitized by a sampling ADC originally developed for the electromagnetic calorimeter

of the $\overline{P}$ANDA experiment [262, 264, 265]. The ADC samples up to 64 channels with a resolution of 14 bit at a sampling frequency of 125 MHz. The centerpiece of the DAQ builds the interconnection between the ADC, slow control, and mass storage. It is realized on a commercially available FPGA based development board [267]. The digitized waveforms stream freely from the ADC to this platform via optical fibers and the Xilinx® Aurora 8b/10b protocol [280] running at 5 Gb/s. Due to the missing trigger in the prototype setup, the data is directly sent to a PC writing to disk. The connection is established via Gigabit Ethernet and the SiTCP solution of the TCP/IP standard [282, 283]. Slow control is provided by the IPbus protocol, also running via Gigabit Ethernet [285, 286]. In November 2017, this DAQ reading out the single channel of a prototype cZDD module was tested in a high rate beam test. The test was carried out at the MAMI facility in Mainz providing an electron beam with 855 MeV. The detector and the DAQ were operated successfully at 15 different rates of up to 13.9 MHz, which is far beyond the requirements.

The recorded data was analyzed offline and algorithms for the detection of pile-up were developed. As an intermediate result, a degradation of the pulse height with increasing event rates was observed. This can be mitigated by modifying the preamplifier circuitry, which is independent from the DAQ.

Algorithms for the extraction of different characteristics of the pulses were designed. Based on these characteristics, two pile-up strategies with different complexity were developed. The simple method considers only one of the features and meets a decision, whether a pulse is marked as pile-up or not. The achieved efficiency of pile-up detection is slightly higher than 50 %. The second method uses all available features and performs a multivariate analysis by the means of a PCA. The additional effort is rewarded by a superior identification of pile-up compared to the simple method. The performance is illustrated in Figure 4.20 for rates of 718 kHz, 1.5 MHz, 2.14 MHz, and 3.02 MHz. Figure B.20 demonstrates the effect of the pile-up detection for all 15 rates. For rates of up to 6 MHz, pile-up events are identified with an efficiency of about 90 %. Both methods were developed with the intention in mind to be implementable on FPGAs. In the final cZDD, the algorithms need to be run in realtime. The algorithms only consist of algebra that can easily be implemented in FPGA logic.

However, the achieved pile-up detection is only a qualitative demonstration in a well defined situation of a monoenergetic beam. The next step will be the actual implementation of the pile-up detection on the FPGA hardware and its test in a beam with a realistic energy profile. In the final setup at BESIII, the detector will be exposed to an energy spectrum dominated by low energetic photons. The shape of this distribution is currently estimated from MC simulations. A realistic spectrum will be obtained, when the prototype module is placed at or close to the designated position at BESIII.

Search for $e^+e^- \to X(3872)$

The electronic width of the exotic $X(3872)$ state is an important quantity for solving the riddle about its inner structure. Therefore, BESIII recorded about $220 \, \mathrm{pb}^{-1}$ of collision data at and slightly below the $X(3872)$ mass in June 2017. Since the $X(3872)$ state is very narrow, both the center-of-mass energy $\sqrt{s}$ and the spread of $\sqrt{s}$ need to be known with highest possible precision. For that reason, the BEMS, a laser Compton back-scattering apparatus, was operating during data taking. It provides measurements for the beam energy and the corresponding spreads with the best achievable accuracy at BESIII.

In the framework of this thesis, a search for the resonant $X(3872)$ formation has been performed via the $X(3872) \to \pi^+\pi^- J/\psi$ decay and the subsequent $J/\psi \to \ell^+\ell^-$ decays with $\ell = e, \mu$. Based on two older data sets with each approximately $50 \, \mathrm{pb}^{-1}$ of integrated luminosity as well as the newly recorded data, the cross section of $e^+e^- \to \pi^+\pi^- J/\psi$ has been determined in the vicinity of the $X(3872)$ mass. Based on these values, an upper limit on the product of the electronic width and the branching fraction $\mathcal{B}$ of the $X(3872) \to \pi^+\pi^- J/\psi$ decay has been obtained.

As a preparing step, the collision energy and the corresponding spread have been determined from the BEMS result. The actual analysis starts with the event selection, which has been optimized based on MC simulations of various $e^+e^- \to \pi^+\pi^- J/\psi$ models. Background sources have been identified by a study of nine exclusive background channels in MC and real data in the J/ψ sidebands. The overall background contamination has been reduced by appropriate cuts. The dominant background in the $J/\psi \to e^+e^-$ reconstruction mode is radiative Bhabha scattering ($e^+e^- \to \gamma e^+e^-$) with the following conversion of the radiated photon. In the $J/\psi \to \mu^+\mu^-$

mode, the reaction of $e^+e^- \to \pi^+\pi^-\pi^+\pi^-$ is the dominating background.

The cross section has been determined from the number of J/ψ events observed in fits to distributions of the recoil $\pi^+\pi^-$ masses. The systematic uncertainties including effects from radiative corrections, MC model ambiguities, etc., have been estimated and found to be more than a factor of three smaller than the statistical uncertainty. The result of the cross section measurement is listed in Table 5.7 and shown in Figure 5.15. It is compatible with a constant cross section.

Because there is no enhancement at the X(3872) mass, an upper limit for the product $\Gamma_{ee} \times \mathcal{B}$ has been determined by a Bayesian likelihood analysis. The limit has been determined as a function of the unknown total width (cf. Figure 5.21(b)) and in an independent way. For an assumed total width of 1.2 MeV, the upper limit on $\Gamma_{ee} \times \mathcal{B}$ is 8 meV at the 90 % confidence level. When the current upper limit on the total width of 1.2 MeV is incorporated by means of a Bayesian prior likelihood, the independent upper limit is 7 meV at the 90 % confidence level, which is an improvement by a factor of approximately 20 compared to the previous limit [32]. However, it is still an order of magnitude above the theoretical lower limit of $\Gamma_{ee} \times \mathcal{B} \gtrsim 0.96$ meV [30, 299]. Since only limits for both the electronic and the total width exist, a two-dimensional credible region (at 90 %) in the $\Gamma_{tot} \times (\Gamma_{ee} \times \mathcal{B})$ plane has been constructed as well. It is shown in Figure 5.22(b). Remarkably, the scales of the x- and y-axis are MeV and meV, respectively. The sensitivity to Γ_{tot} and $\Gamma_{ee} \times \mathcal{B}$ is nine orders of magnitude apart!

Since the precision of the results is totally dominated by statistics, the result can easily be improved by recording more data. The implementation of the new top-up injection scheme at BEPCII and the resulting increase of average luminosity by approximately 30 % makes it more cost-effective than the 2017 beam time. Ultimately, a future super τ-charm factory [327, 328] with a hundredfold larger luminosity than BEPCII will be in an excellent position to observe $e^+e^- \to$ X(3872).

In the end, this study could push the upper limit approximately a factor 20 further down. Hopefully, this finding will trigger efforts in the theory community to link the new results to the internal structure of the X(3872) state. The non-observation of an X(3872) signal, however, implies that no new information about the total width could be obtained.

In addition, this analysis is not the only application of the collected data. Although the observation of the reaction $e^+e^- \rightarrow$ X(3872) in the other decay channels is not expected, these additional measurements in combination with the results of this analysis could still be able to improve the limit on Γ_{ee}. As the X(3872) mass coincides with the $D^0\bar{D}^{*0}$ threshold, the behavior of open-charm cross sections at the recorded data points are of interest and might provide insight in open-charm dynamics as well.

Appendices

Appendix A

FIRMWARE OF THE PROTOTYPE DAQ

This Appendix shows the full block diagram of the firmware running on the event correlator in the prototype DAQ.
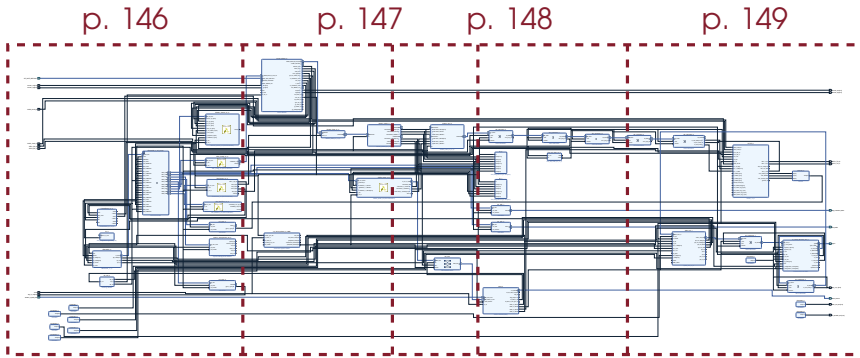
Figure A.1: Block diagram of the prototype firmware of the event correlator. The following four pages show magnified views of the diagram as indicated by the dashed rectangles.

The firmware for the event correlator FPGA in the beam test setup has been developed using the IP Integrator of the Xilinx Vivado design suite. The individual IP cores are represented as boxes in a block diagram. The interconnections between the IP cores are drawn as lines. Figure A.1 shows the block diagram as a whole and Figure A.2 shows detailed views of the diagram on the next four pages.
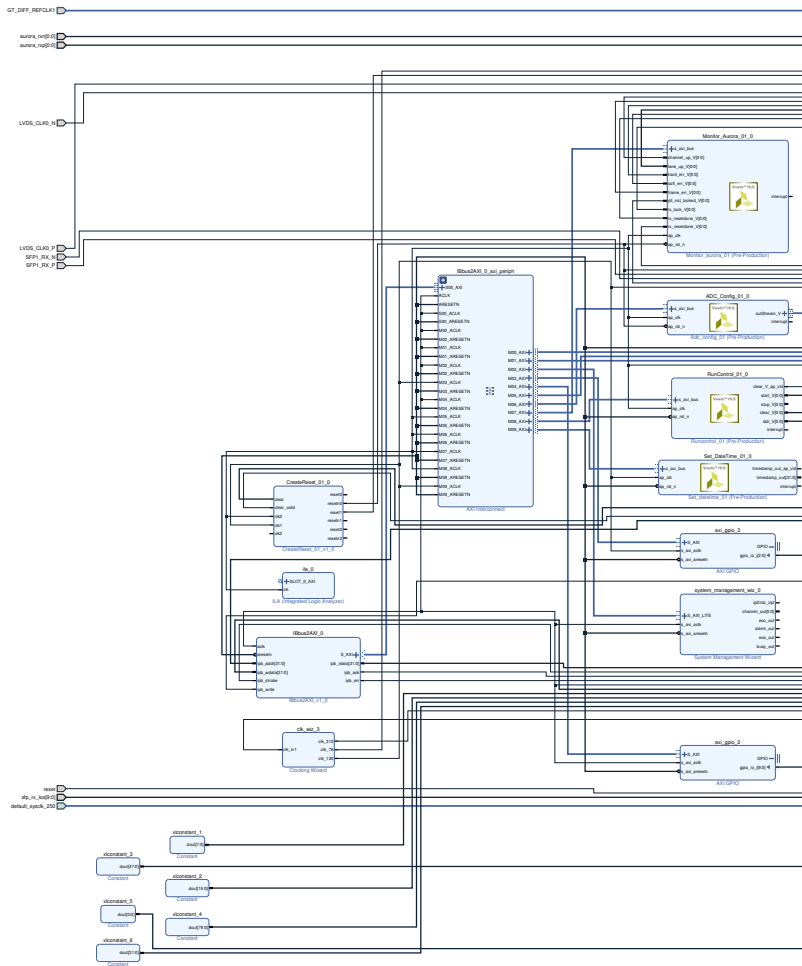
(a)

Figure A.2: Magnified view of the block diagram.
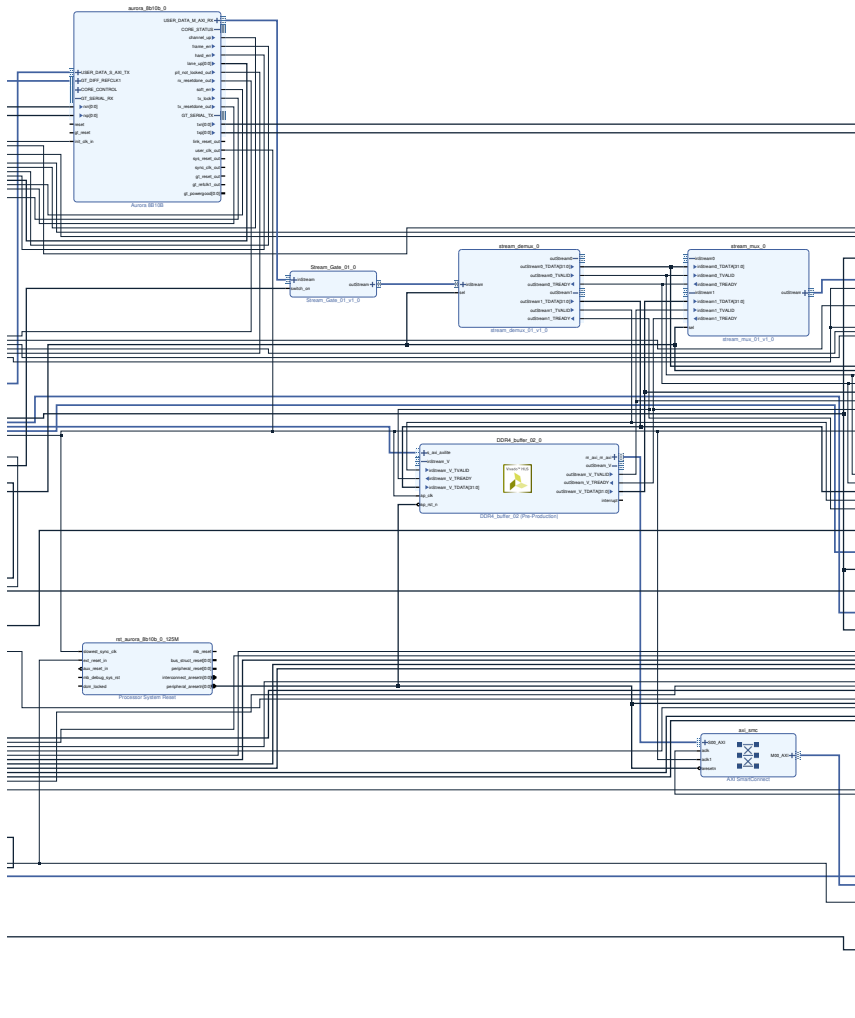
(b)

Figure A.2: continued.
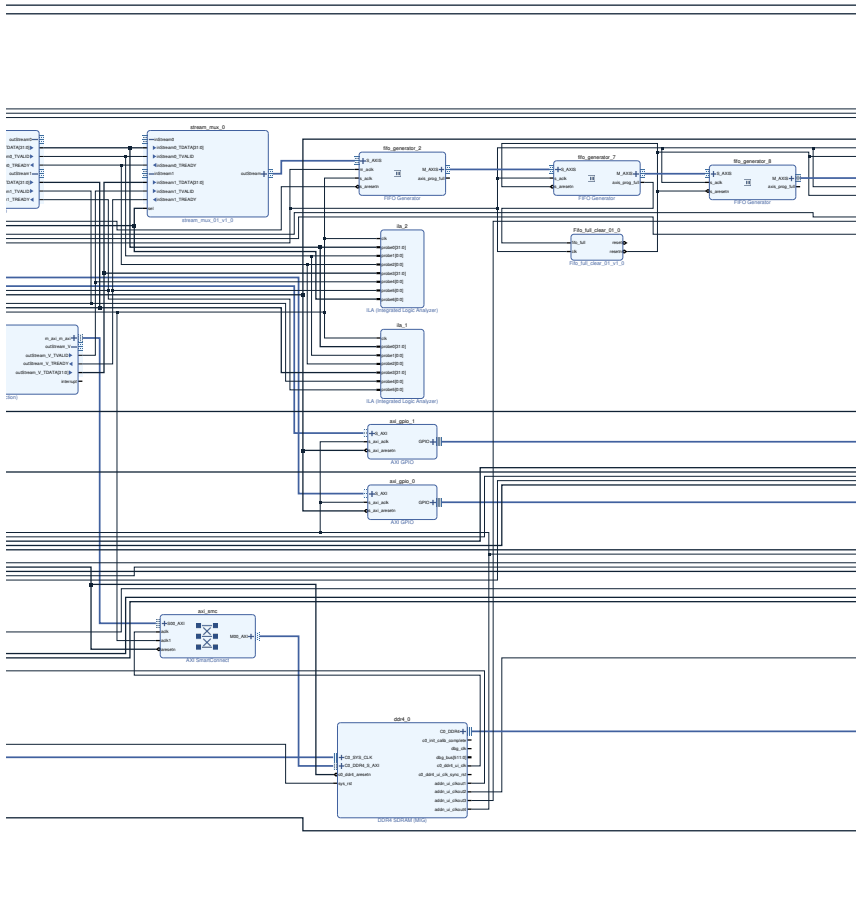
(c)

Figure A.2: continued.
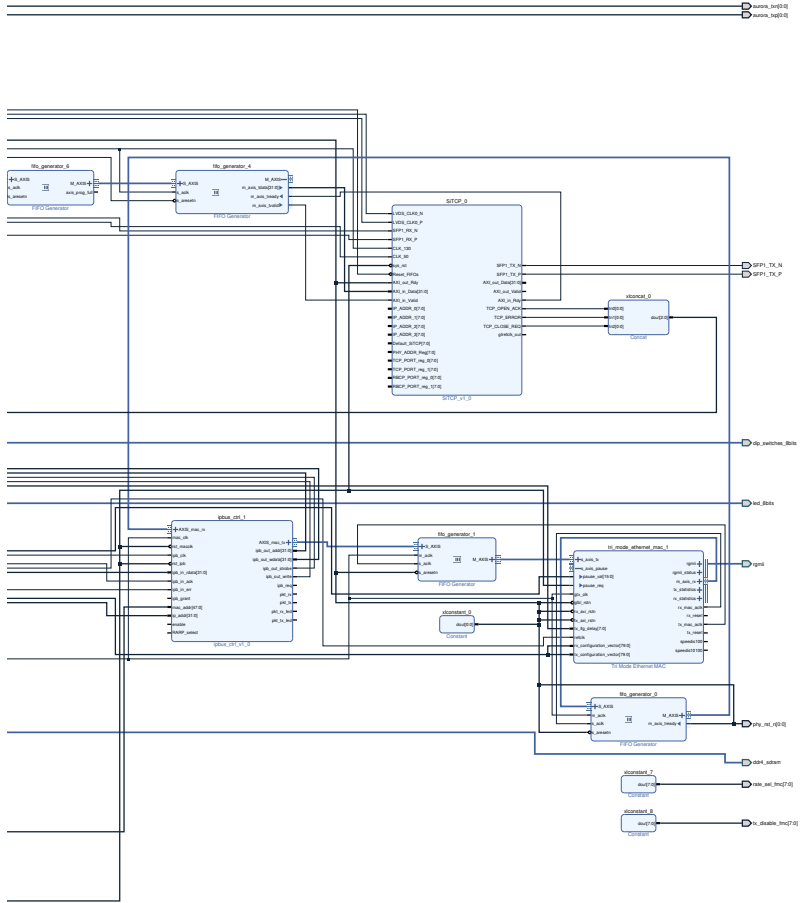
(d)

Figure A.2: concluded.

Appendix B

PLOTS OF THE BEAM TEST DATA

This Appendix lists a lot of graphs and distributions of data that was recorded during the beam test.

B.1 Waveforms

In the beam test, data at 15 different event rates has been recorded. The following Figures show the baseline subtracted raw data, i.e. the digitized waveforms, for a duration of $10\,\mu s$. The pulses with the respective undershoots are clearly noticeable. With increasing event rates, the pulse height decreases and the increasing amount of pile-up becomes apparent. The event rate is indicated underneath each graph.
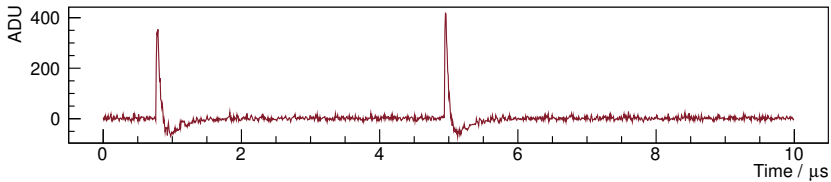
(a) 2.72 kHz.
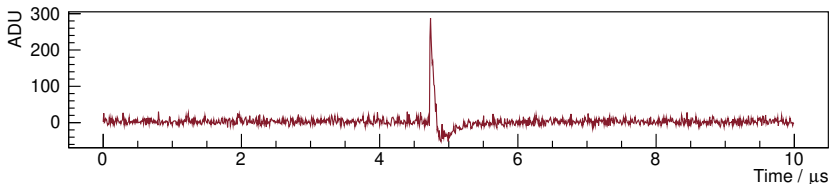
(b) 50.4 kHz.

Figure B.1: Recorded waveforms for all 15 different event rates.
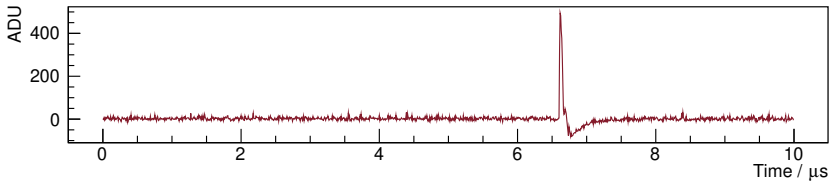
(c) 107 kHz.
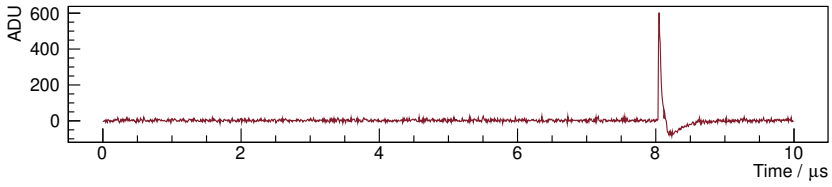
(d) 157 kHz.
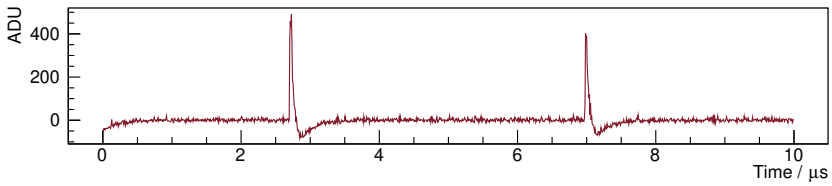
(e) 231 kHz.
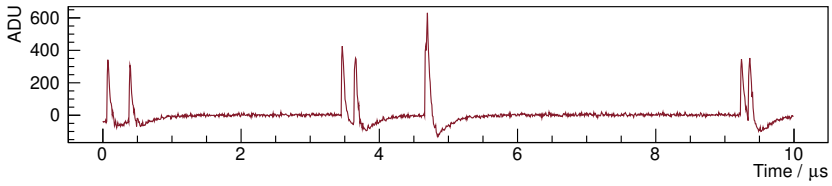
(f) 718 kHz.
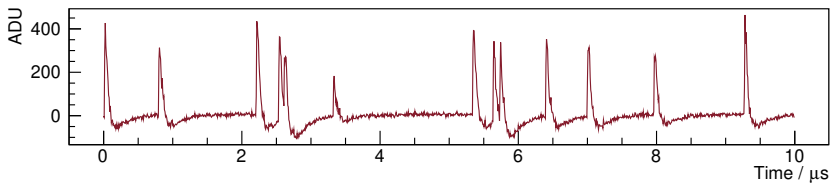
(g) 1.04 MHz.

Figure B.1: continued.
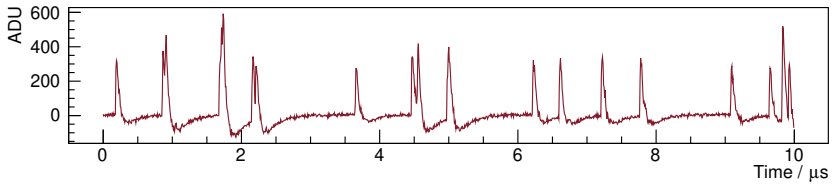
(h) 1.50 MHz.
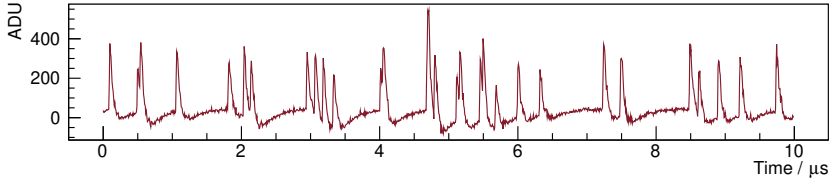
(i) 2.14 MHz.
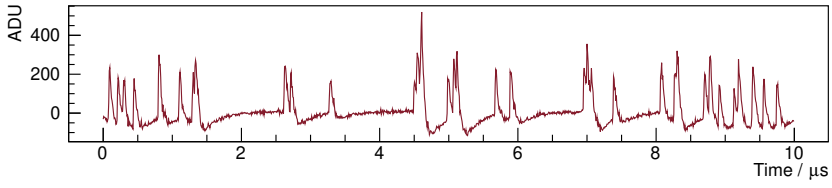
(j) 3.02 MHz.
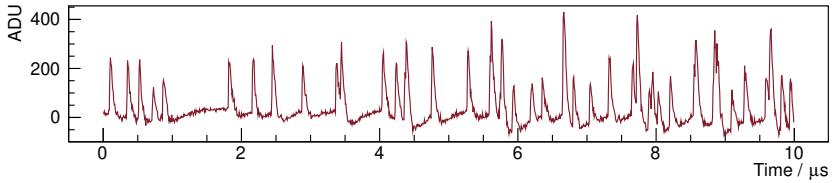
(k) 4.25 MHz.
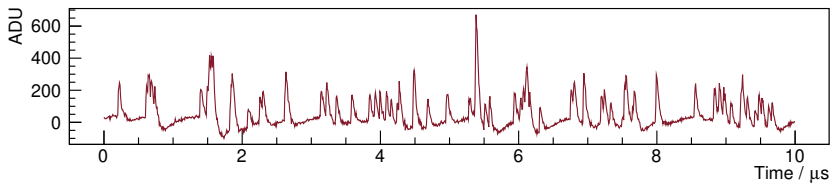
(l) 5.89 MHz.

Figure B.1: continued.
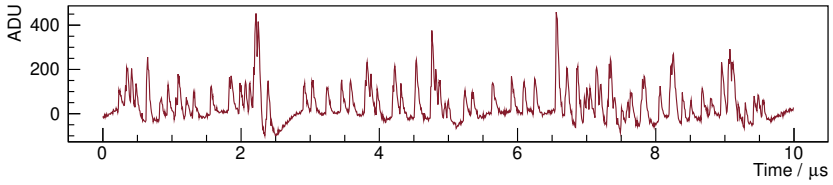
(m) 8.04 MHz.
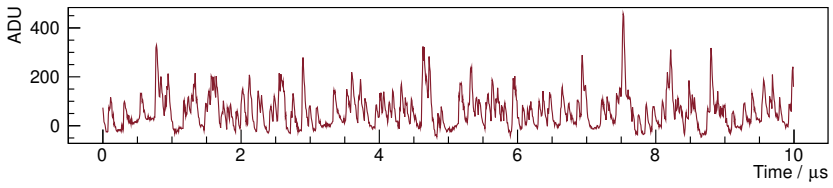
(n) 10.75 MHz.
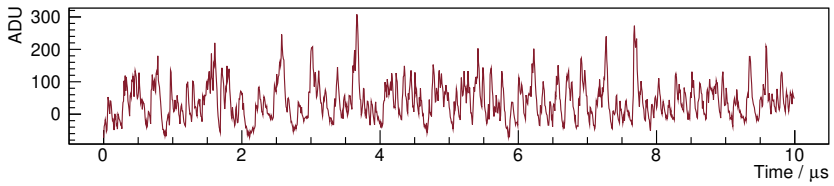
(o) 13.90 MHz.

Figure B.1: concluded.

B.2 Feature Distributions

On the next pages, various feature distributions of the data recorded during the beam test are shown. From each detected pulse, the features are extracted and filled into the histograms. Each Figure shows the distributions of one variable for all 15 event rates. The corresponding event rates are printed below each distribution. The association of Figure number to the variable is given below:

Figure	Distributions of...
B.2	Ratio of pulse integral to pulse height
B.3	Pulse length
B.4	Secondary peak height
B.5	1st normalized Legendre moment
B.6	2nd normalized Legendre moment
B.7	3rd normalized Legendre moment
B.8	4th normalized Legendre moment
B.9	5th normalized Legendre moment
B.10	6th normalized Legendre moment
B.11	0th principal component
B.12	1st principal component
B.13	2nd principal component
B.14	3rd principal component
B.15	4th principal component
B.16	5th principal component
B.17	6th principal component
B.18	7th principal component
B.19	8th principal component
B.20	Pulse integral with and without pile-up rejection

(a) 2.72 kHz.

(b) 50.4 kHz.

(c) 107 kHz.

(d) 157 kHz.

(e) 231 kHz.

(f) 718 kHz.

(g) 1.04 MHz.

(h) 1.50 MHz.

(i) 2.14 MHz.

(j) 3.02 MHz.

(k) 4.25 MHz.

(l) 5.89 MHz.

(m) 8.04 MHz.

(n) 10.75 MHz.

(o) 13.90 MHz.
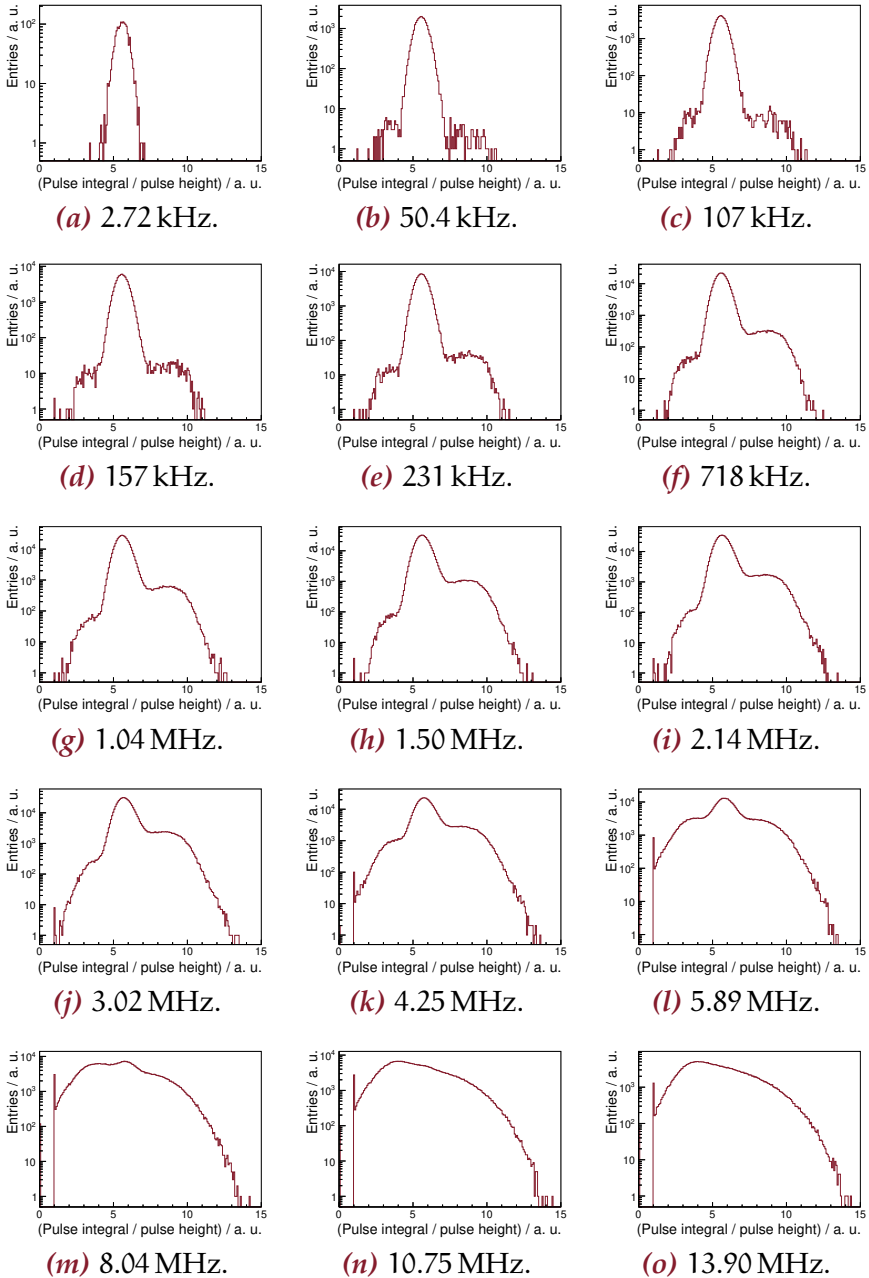
Figure B.2: Distributions of the ratio of pulse integral to pulse height.

(a) 2.72 kHz.

(b) 50.4 kHz.

(c) 107 kHz.

(d) 157 kHz.

(e) 231 kHz.

(f) 718 kHz.

(g) 1.04 MHz.

(h) 1.50 MHz.

(i) 2.14 MHz.

(j) 3.02 MHz.

(k) 4.25 MHz.

(l) 5.89 MHz.

(m) 8.04 MHz.

(n) 10.75 MHz.

(o) 13.90 MHz.
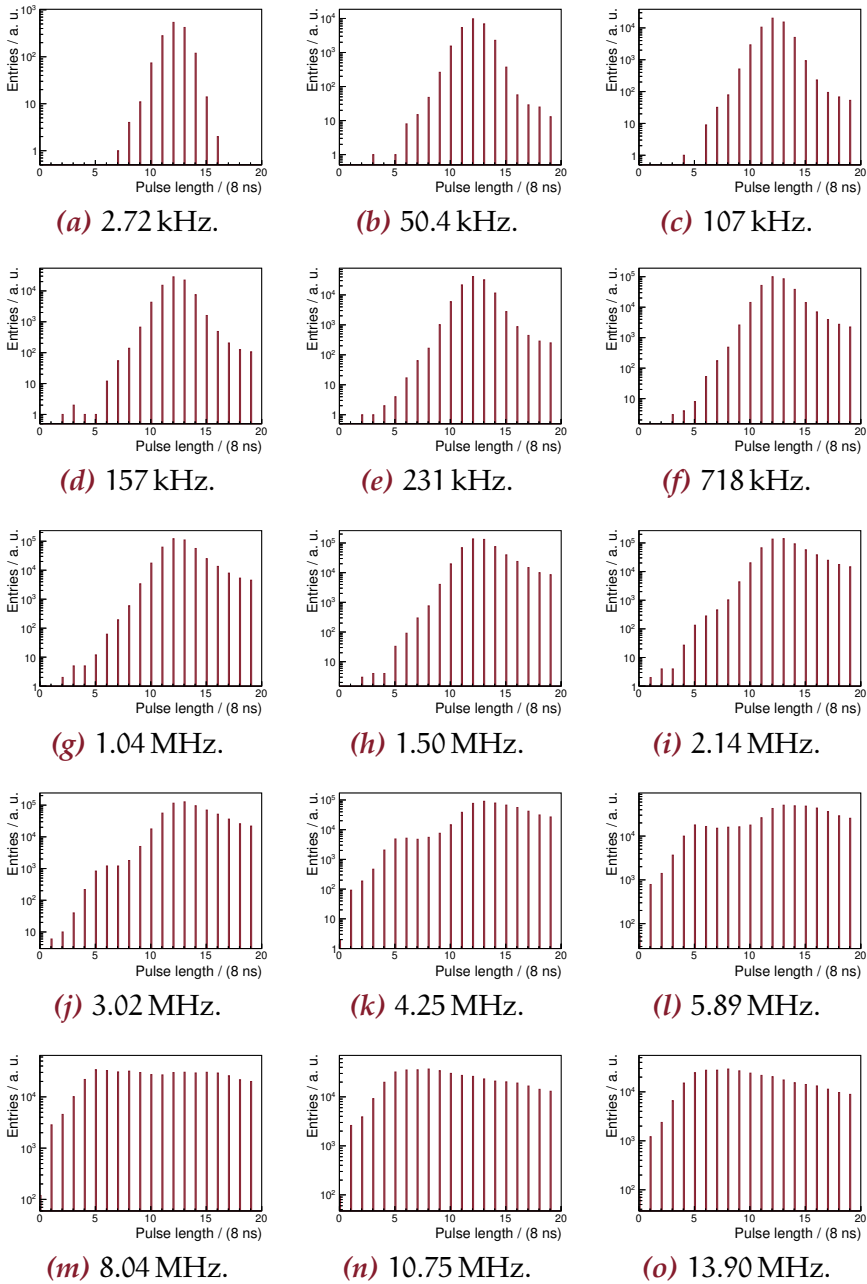
Figure B.3: Distributions of the pulse length.

(a) 2.72 kHz.

(b) 50.4 kHz.

(c) 107 kHz.

(d) 157 kHz.

(e) 231 kHz.

(f) 718 kHz.

(g) 1.04 MHz.

(h) 1.50 MHz.

(i) 2.14 MHz.

(j) 3.02 MHz.

(k) 4.25 MHz.

(l) 5.89 MHz.

(m) 8.04 MHz.

(n) 10.75 MHz.

(o) 13.90 MHz.
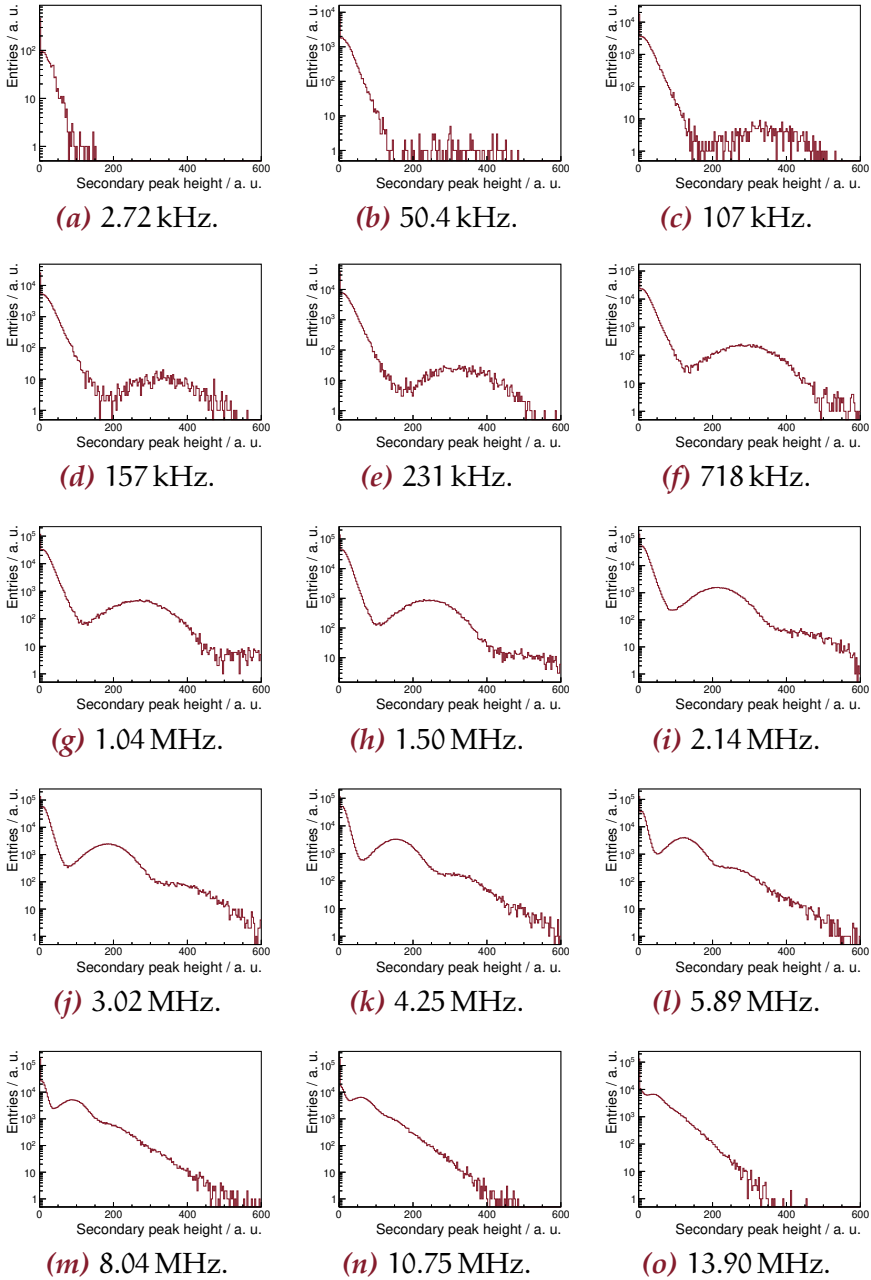
Figure B.4: Distributions of the secondary peak height.

(a) 2.72 kHz.   *(b)* 50.4 kHz.   *(c)* 107 kHz.

(d) 157 kHz.   *(e)* 231 kHz.   *(f)* 718 kHz.

(g) 1.04 MHz.   *(h)* 1.50 MHz.   *(i)* 2.14 MHz.

(j) 3.02 MHz.   *(k)* 4.25 MHz.   *(l)* 5.89 MHz.

(m) 8.04 MHz.   *(n)* 10.75 MHz.   *(o)* 13.90 MHz.
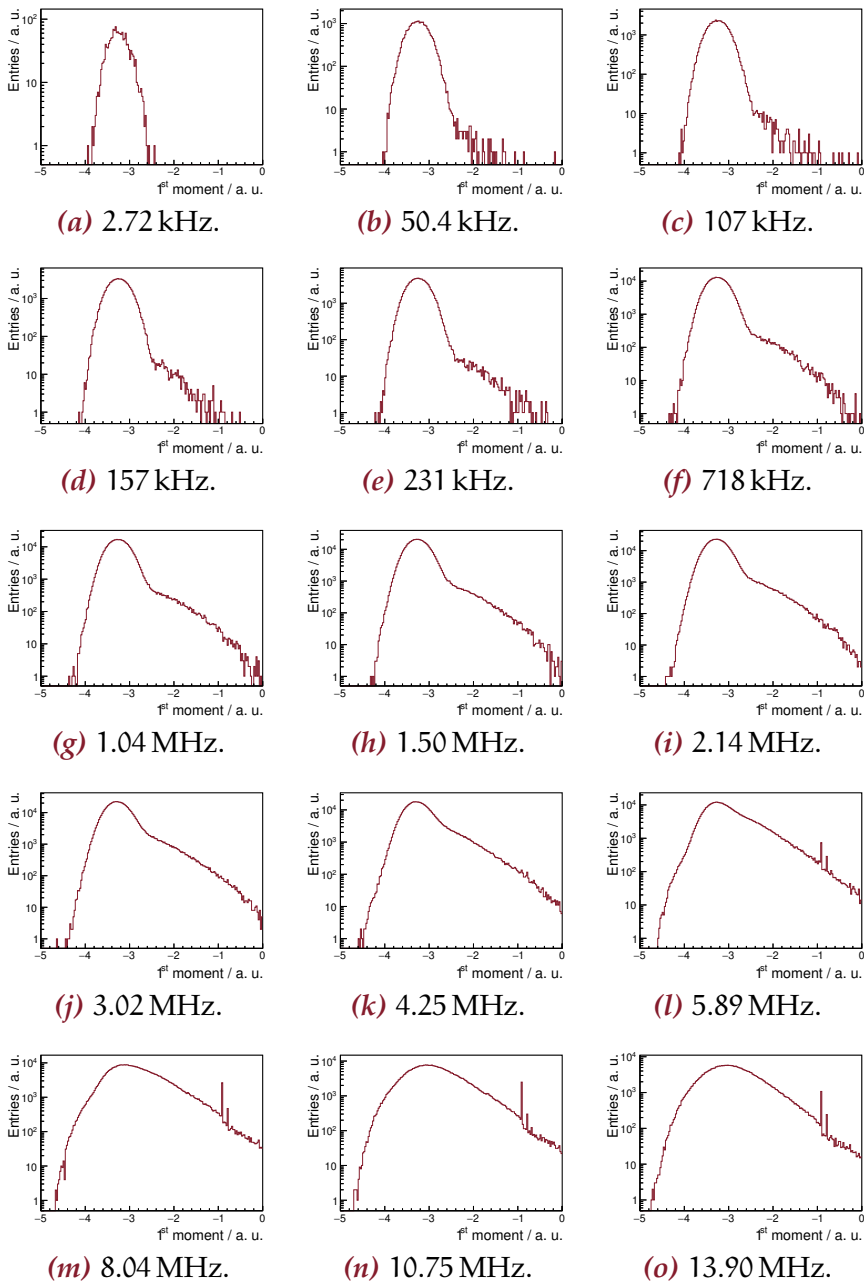
Figure B.5: Distributions of the 1st normalized Legendre moment.

(a) 2.72 kHz.

(b) 50.4 kHz.

(c) 107 kHz.

(d) 157 kHz.

(e) 231 kHz.

(f) 718 kHz.

(g) 1.04 MHz.

(h) 1.50 MHz.

(i) 2.14 MHz.

(j) 3.02 MHz.

(k) 4.25 MHz.

(l) 5.89 MHz.

(m) 8.04 MHz.

(n) 10.75 MHz.

(o) 13.90 MHz.
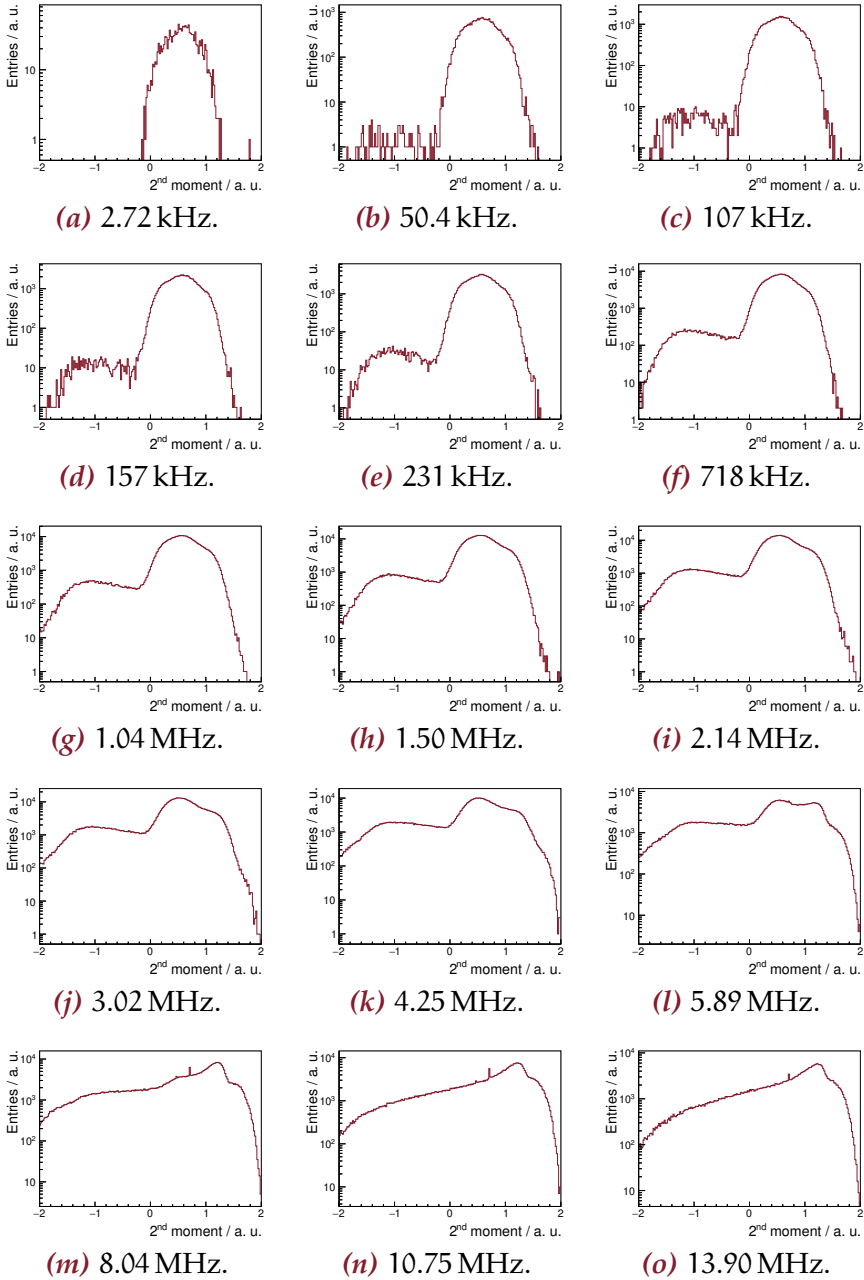
Figure B.6: Distributions of the 2nd normalized Legendre moment.

(a) 2.72 kHz.   *(b)* 50.4 kHz.   *(c)* 107 kHz.

(d) 157 kHz.   *(e)* 231 kHz.   *(f)* 718 kHz.

(g) 1.04 MHz.   *(h)* 1.50 MHz.   *(i)* 2.14 MHz.

(j) 3.02 MHz.   *(k)* 4.25 MHz.   *(l)* 5.89 MHz.

(m) 8.04 MHz.   *(n)* 10.75 MHz.   *(o)* 13.90 MHz.
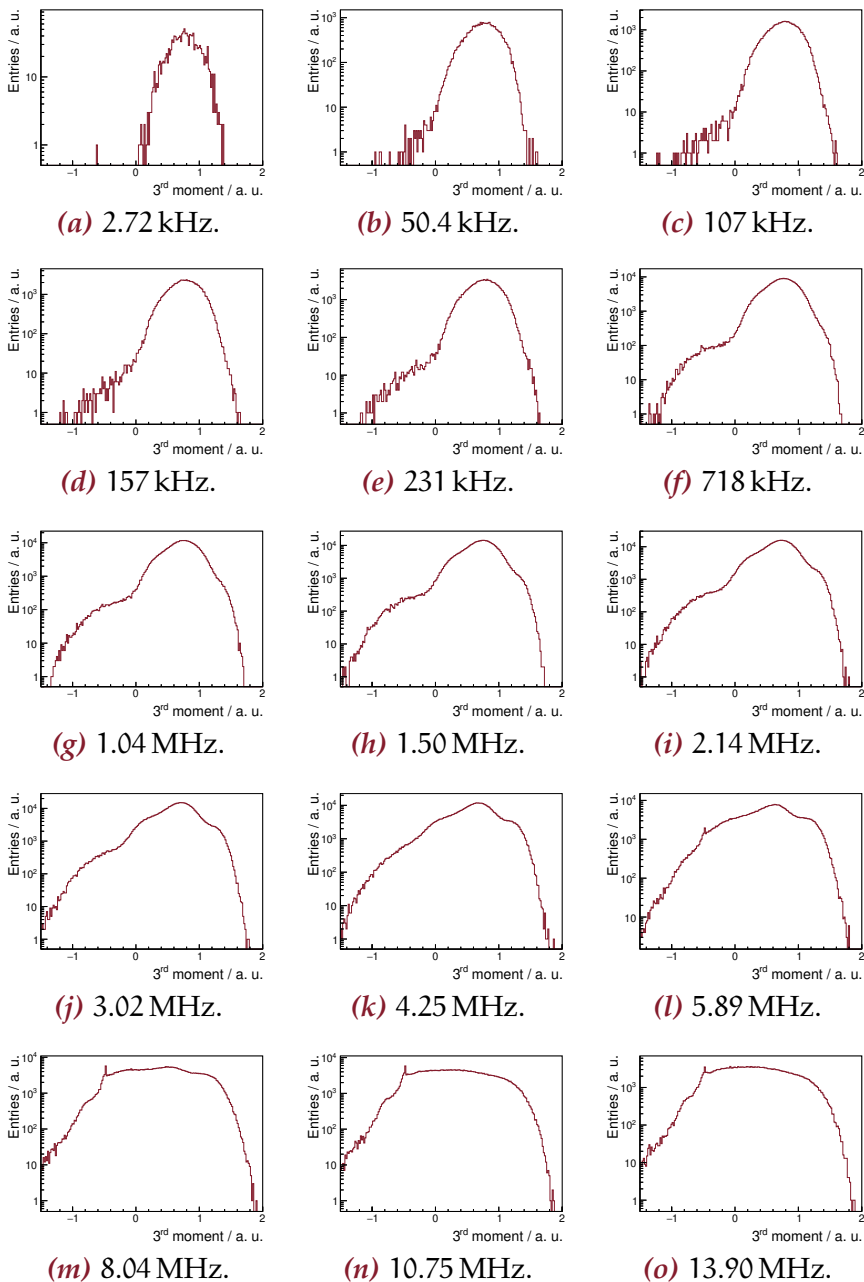
Figure B.7: Distributions of the 3rd normalized Legendre moment.

(a) 2.72 kHz.

(b) 50.4 kHz.

(c) 107 kHz.

(d) 157 kHz.

(e) 231 kHz.

(f) 718 kHz.

(g) 1.04 MHz.

(h) 1.50 MHz.

(i) 2.14 MHz.

(j) 3.02 MHz.

(k) 4.25 MHz.

(l) 5.89 MHz.

(m) 8.04 MHz.

(n) 10.75 MHz.

(o) 13.90 MHz.
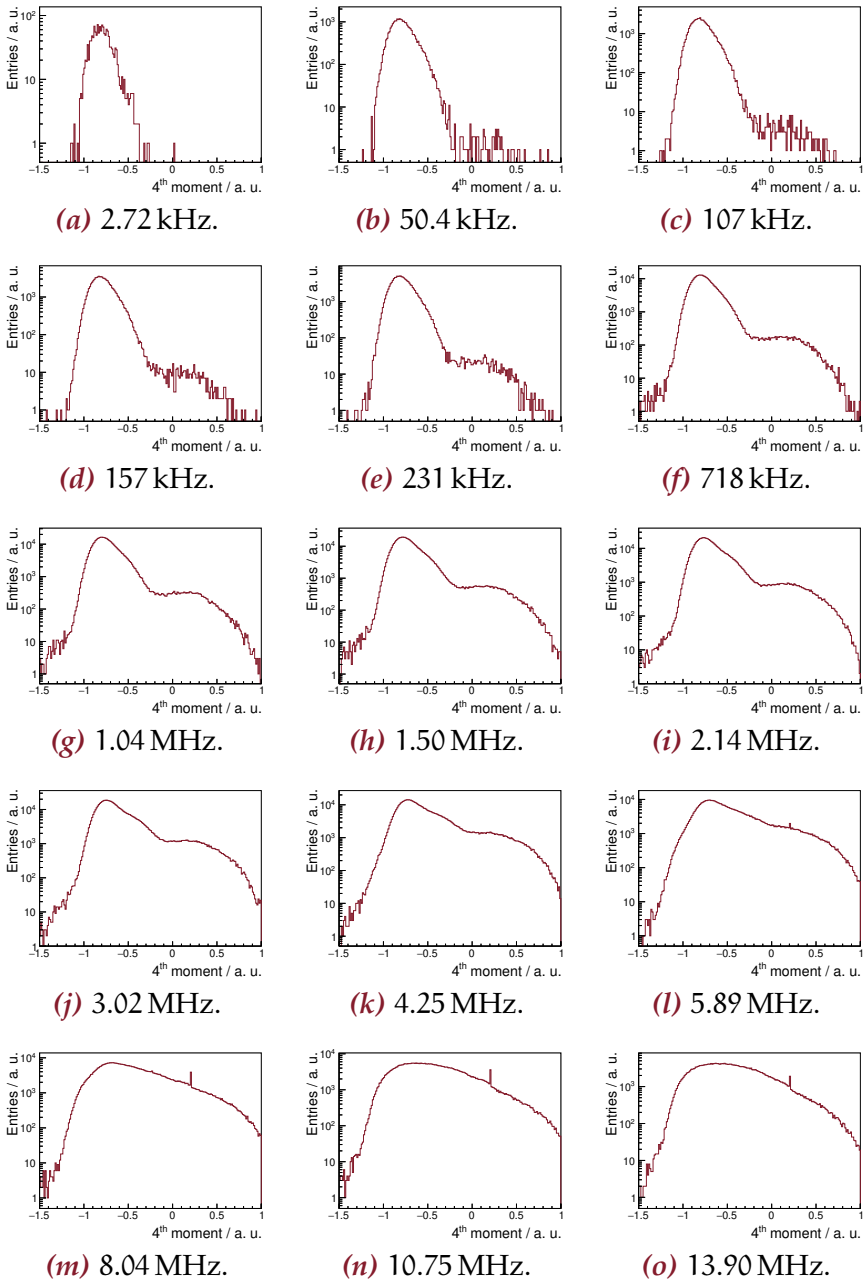
Figure B.8: Distributions of the 4th normalized Legendre moment.
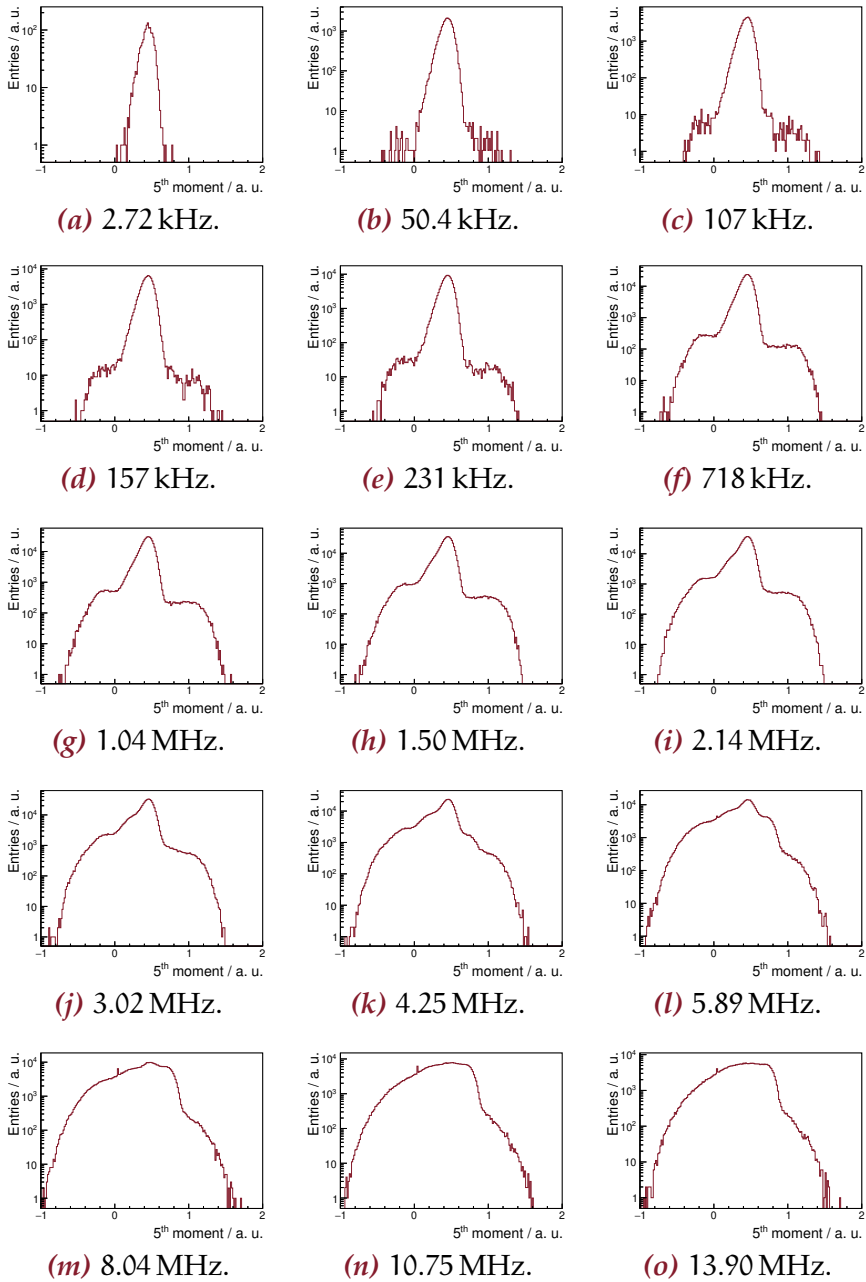
Figure B.9: Distributions of the 5th normalized Legendre moment.

(a) 2.72 kHz.   *(b)* 50.4 kHz.   *(c)* 107 kHz.

(d) 157 kHz.   *(e)* 231 kHz.   *(f)* 718 kHz.

(g) 1.04 MHz.   *(h)* 1.50 MHz.   *(i)* 2.14 MHz.

(j) 3.02 MHz.   *(k)* 4.25 MHz.   *(l)* 5.89 MHz.

(m) 8.04 MHz.   *(n)* 10.75 MHz.   *(o)* 13.90 MHz.
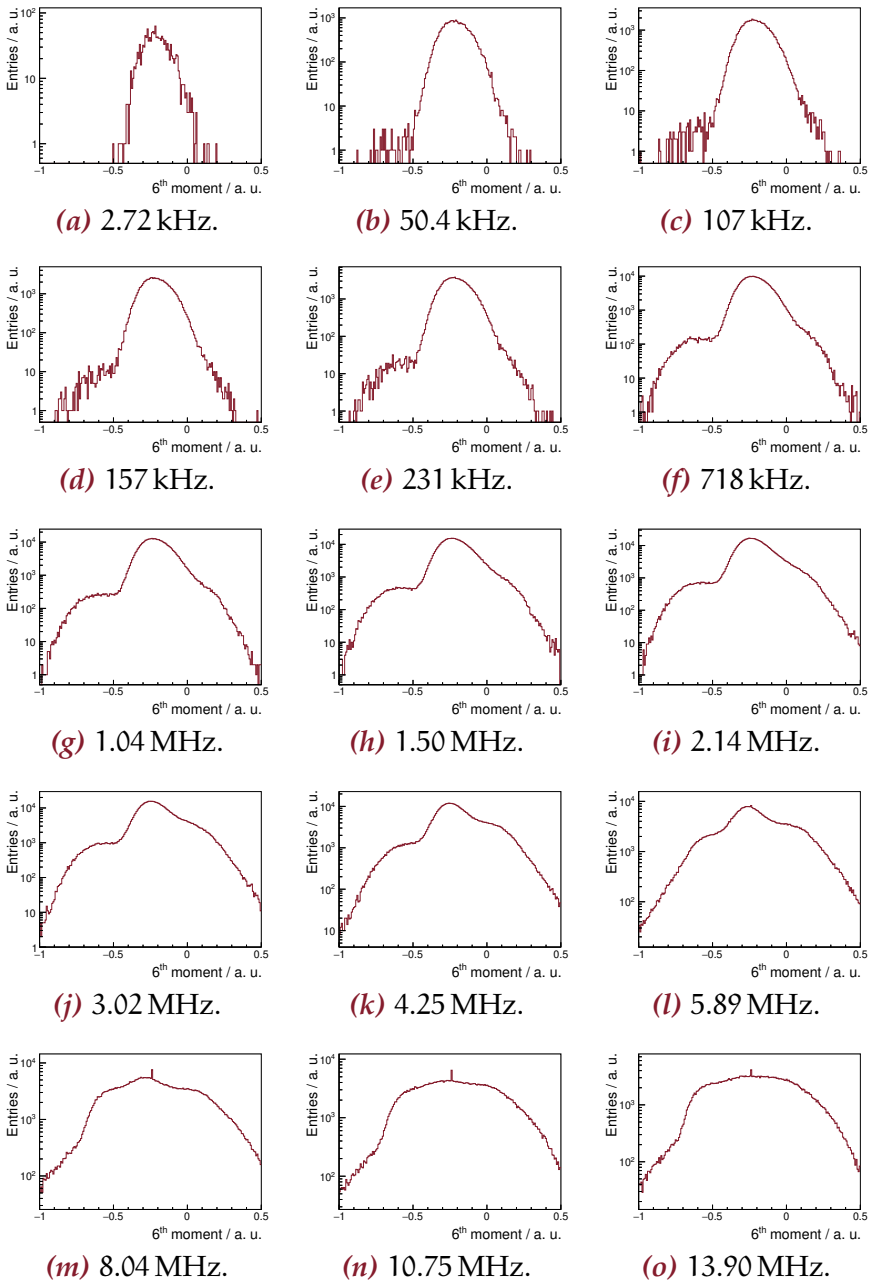
Figure B.10: Distributions of the 6th normalized Legendre moment.

(a) 2.72 kHz.

(b) 50.4 kHz.

(c) 107 kHz.

(d) 157 kHz.

(e) 231 kHz.

(f) 718 kHz.

(g) 1.04 MHz.

(h) 1.50 MHz.

(i) 2.14 MHz.

(j) 3.02 MHz.

(k) 4.25 MHz.

(l) 5.89 MHz.

(m) 8.04 MHz.

(n) 10.75 MHz.

(o) 13.90 MHz.
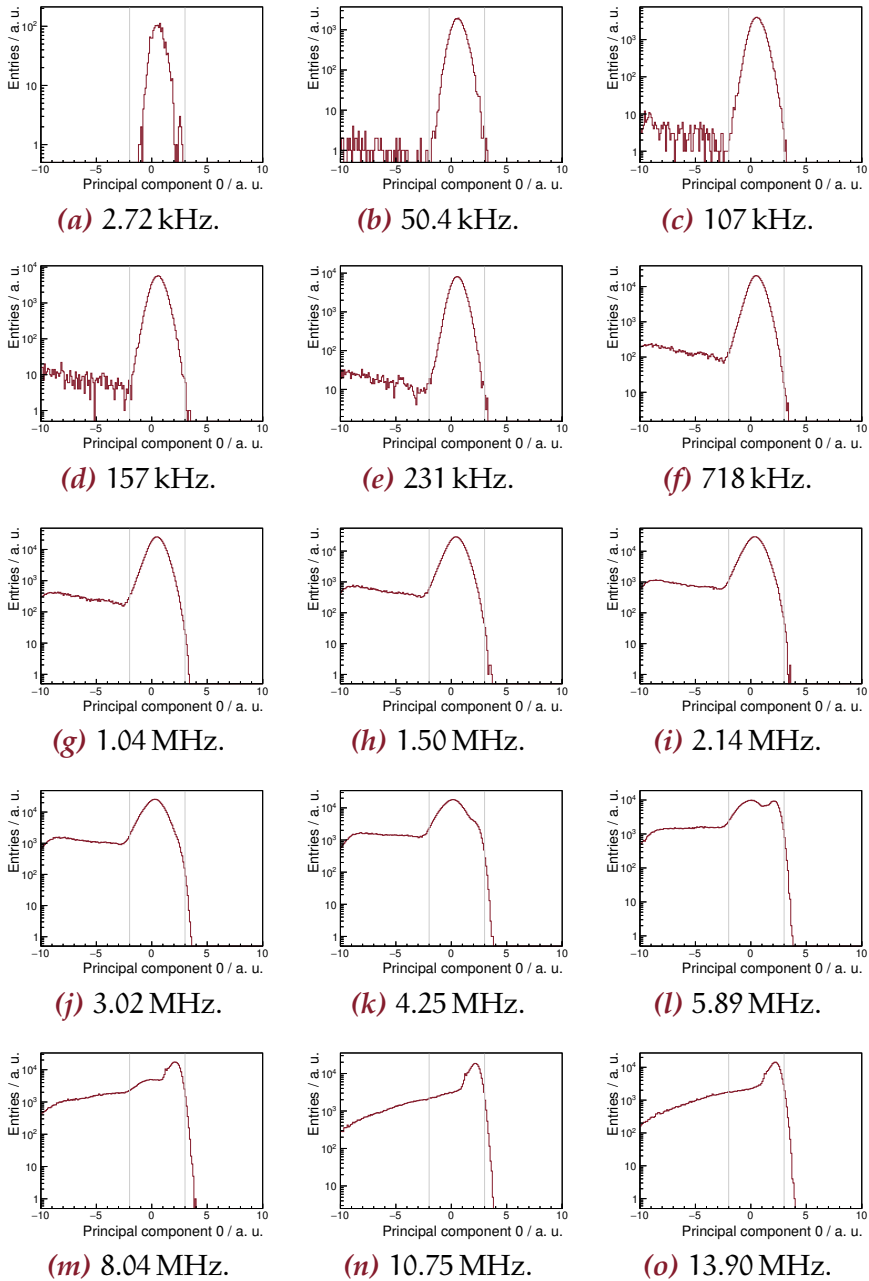
Figure B.11: Distributions of the 0th principal component.
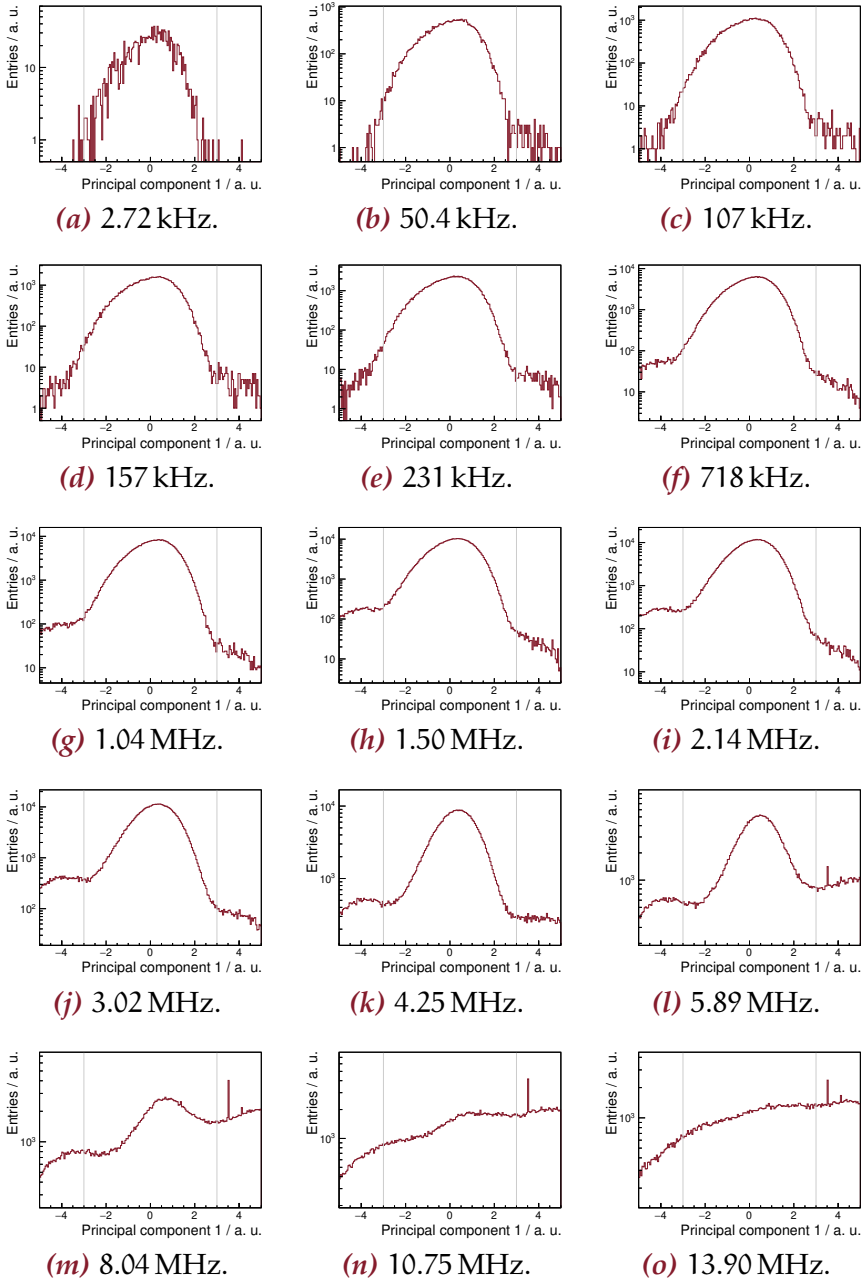
Figure B.12: Distributions of the 1st principal component.

(a) 2.72 kHz. *(b)* 50.4 kHz. *(c)* 107 kHz.

(d) 157 kHz. *(e)* 231 kHz. *(f)* 718 kHz.

(g) 1.04 MHz. *(h)* 1.50 MHz. *(i)* 2.14 MHz.

(j) 3.02 MHz. *(k)* 4.25 MHz. *(l)* 5.89 MHz.

(m) 8.04 MHz. *(n)* 10.75 MHz. *(o)* 13.90 MHz.
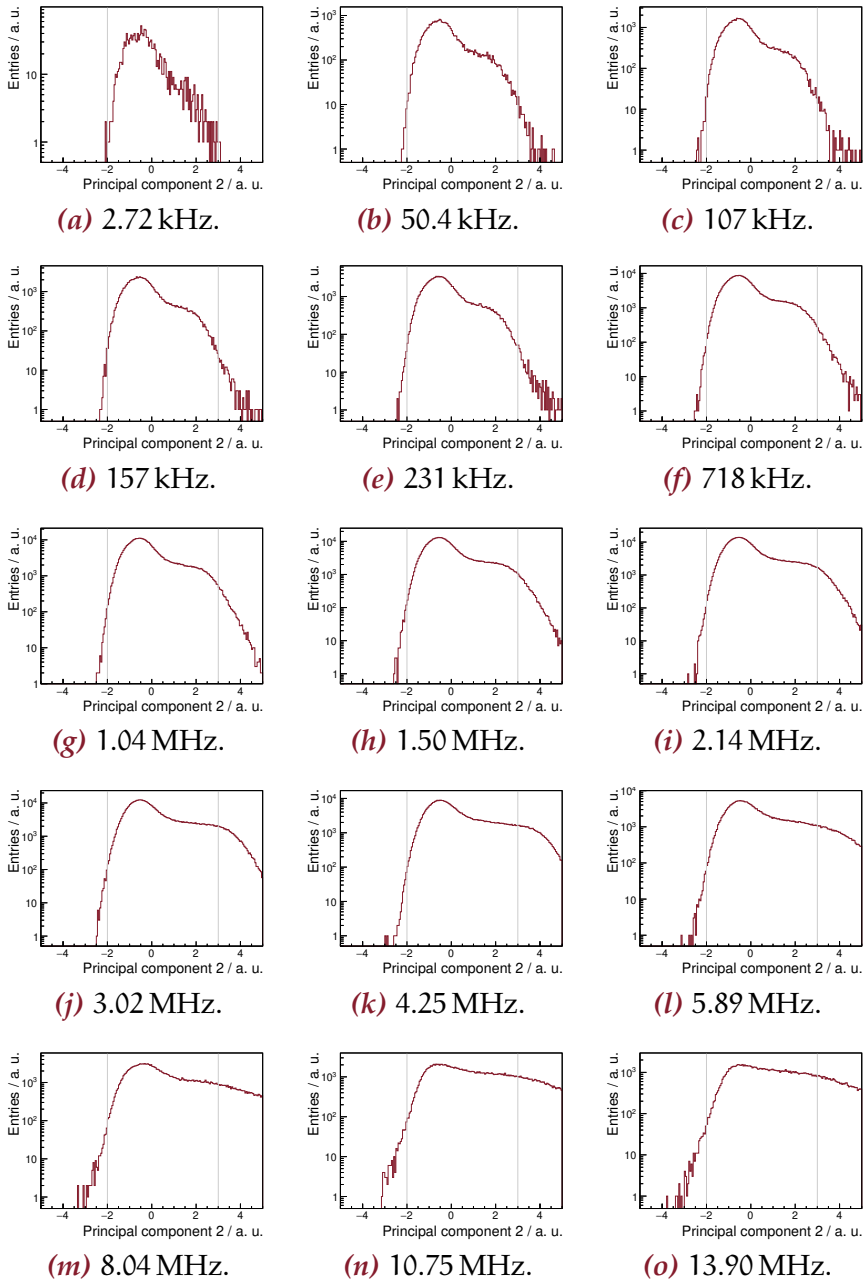
Figure B.13: Distributions of the 2nd principal component.

(a) 2.72 kHz.

(b) 50.4 kHz.

(c) 107 kHz.

(d) 157 kHz.

(e) 231 kHz.

(f) 718 kHz.

(g) 1.04 MHz.

(h) 1.50 MHz.

(i) 2.14 MHz.

(j) 3.02 MHz.

(k) 4.25 MHz.

(l) 5.89 MHz.

(m) 8.04 MHz.

(n) 10.75 MHz.

(o) 13.90 MHz.
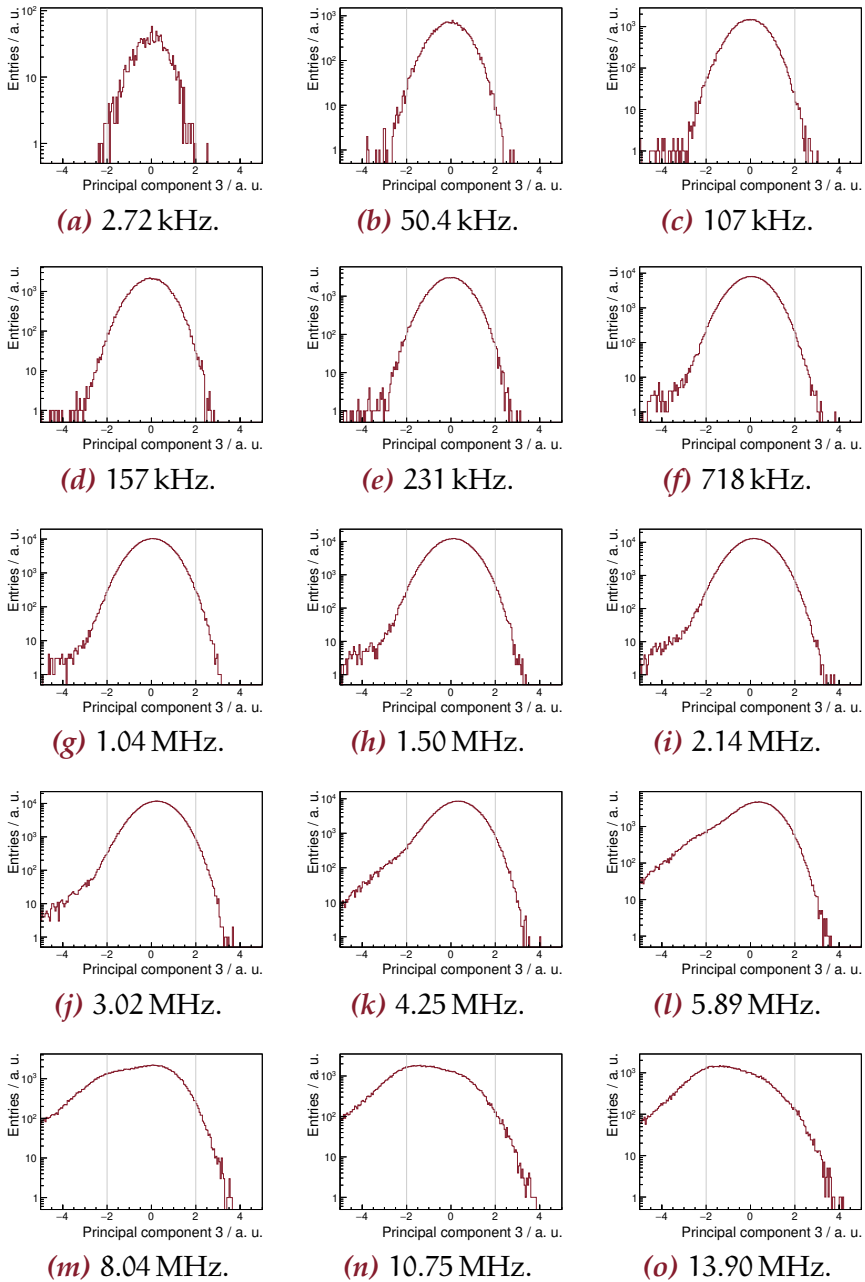
Figure B.14: Distributions of the 3rd principal component.

(a) 2.72 kHz.

(b) 50.4 kHz.

(c) 107 kHz.

(d) 157 kHz.

(e) 231 kHz.

(f) 718 kHz.

(g) 1.04 MHz.

(h) 1.50 MHz.

(i) 2.14 MHz.

(j) 3.02 MHz.

(k) 4.25 MHz.

(l) 5.89 MHz.

(m) 8.04 MHz.

(n) 10.75 MHz.

(o) 13.90 MHz.
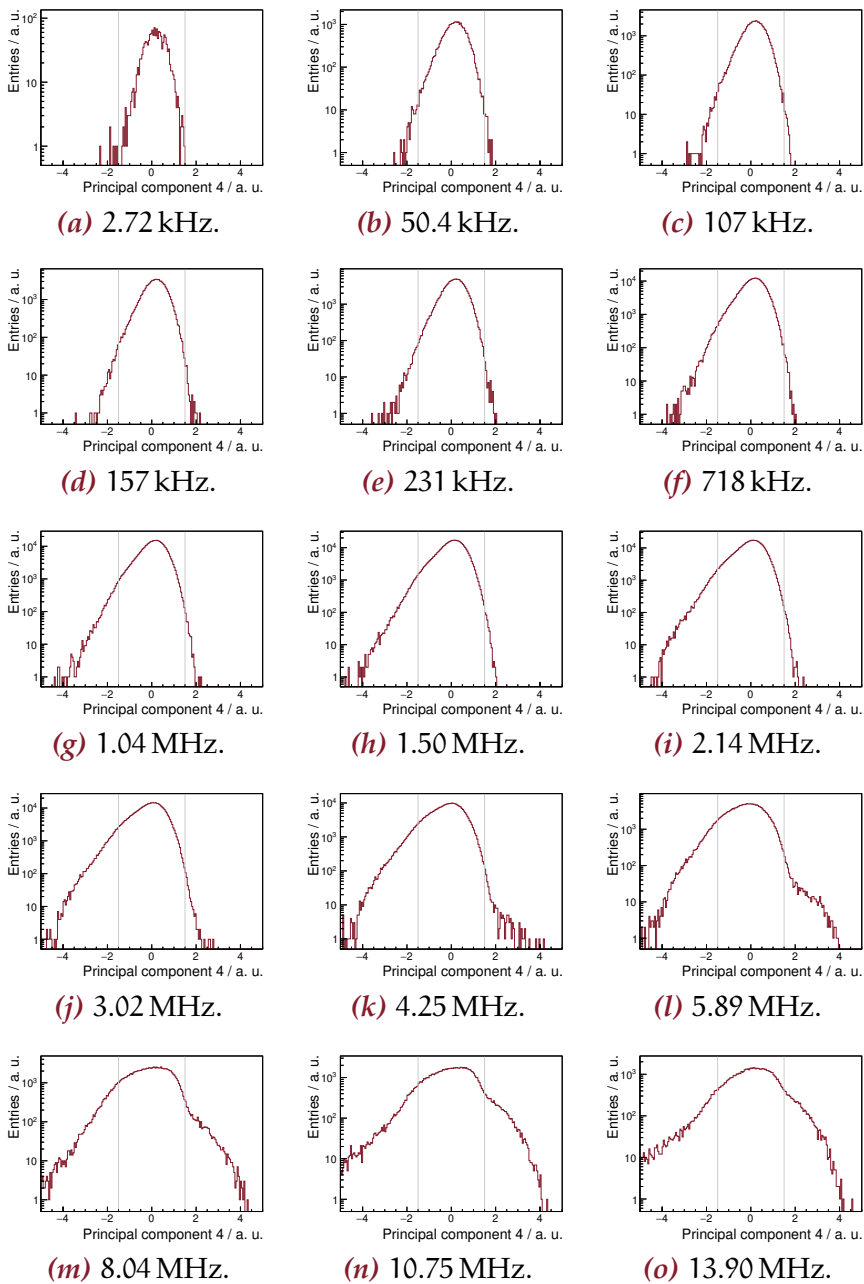
Figure B.15: Distributions of the 4$^{\text{th}}$ principal component.

(a) 2.72 kHz.   *(b)* 50.4 kHz.   *(c)* 107 kHz.

(d) 157 kHz.   *(e)* 231 kHz.   *(f)* 718 kHz.

(g) 1.04 MHz.   *(h)* 1.50 MHz.   *(i)* 2.14 MHz.

(j) 3.02 MHz.   *(k)* 4.25 MHz.   *(l)* 5.89 MHz.

(m) 8.04 MHz.   *(n)* 10.75 MHz.   *(o)* 13.90 MHz.
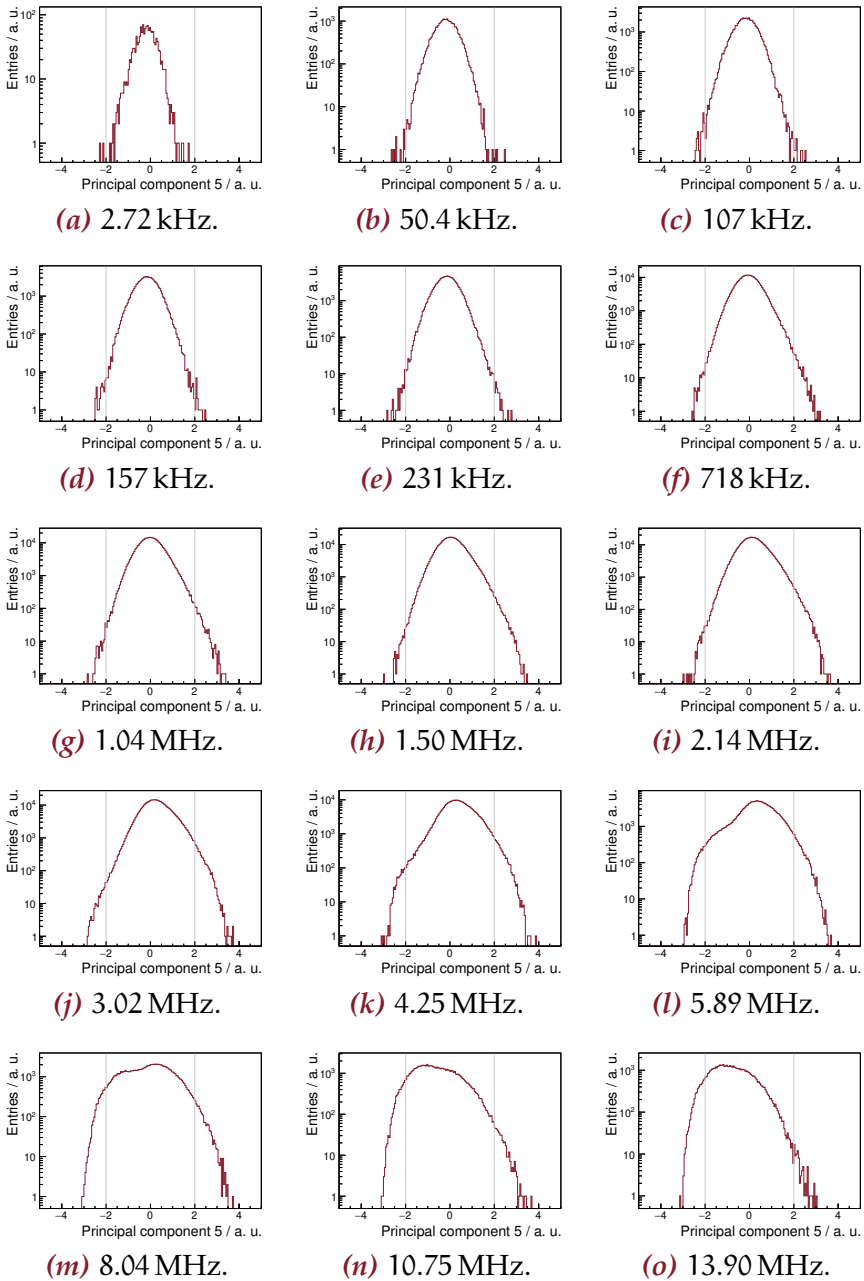
Figure B.16: Distributions of the 5$^{\text{th}}$ principal component.

(a) 2.72 kHz. *(b)* 50.4 kHz. *(c)* 107 kHz.

(d) 157 kHz. *(e)* 231 kHz. *(f)* 718 kHz.

(g) 1.04 MHz. *(h)* 1.50 MHz. *(i)* 2.14 MHz.

(j) 3.02 MHz. *(k)* 4.25 MHz. *(l)* 5.89 MHz.

(m) 8.04 MHz. *(n)* 10.75 MHz. *(o)* 13.90 MHz.
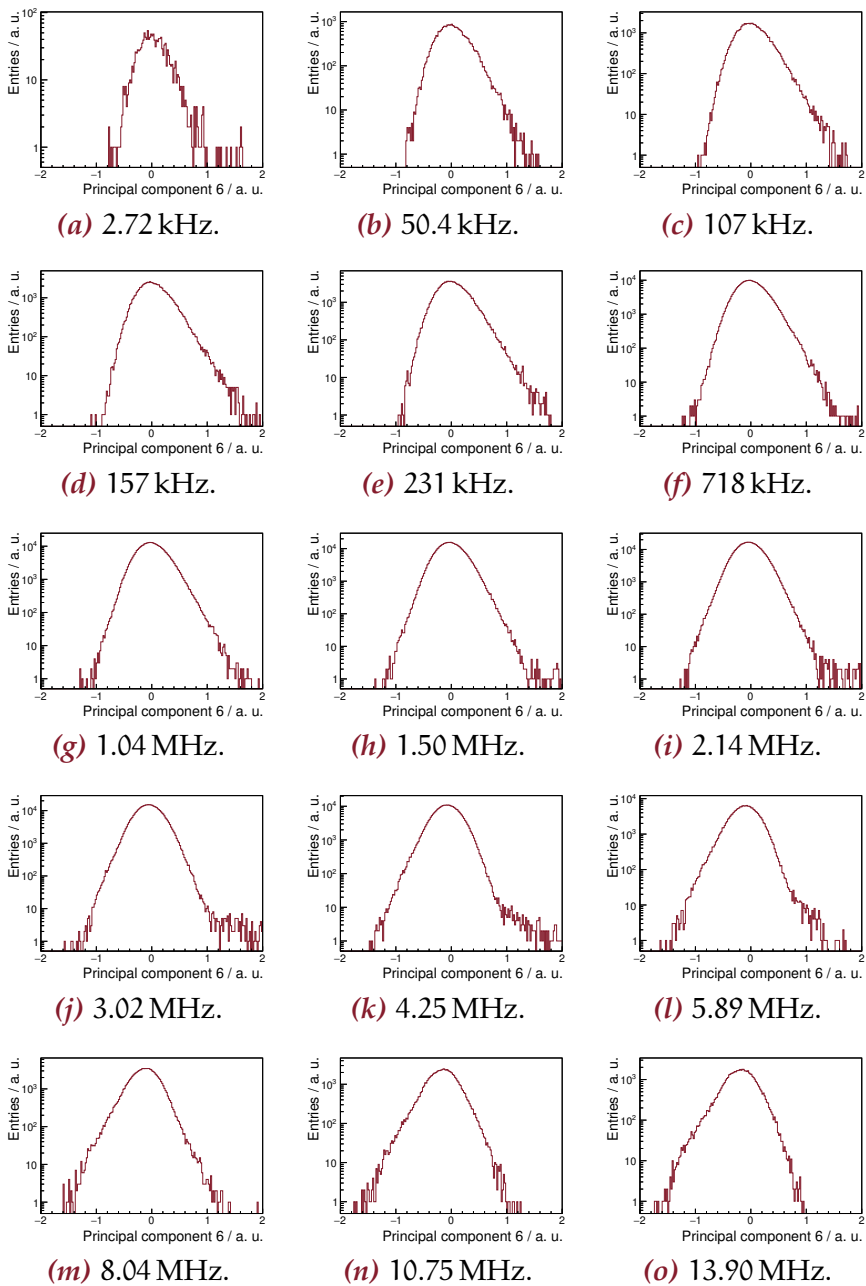
Figure B.17: Distributions of the 6th principal component.

(a) 2.72 kHz.　　*(b)* 50.4 kHz.　　*(c)* 107 kHz.

(d) 157 kHz.　　*(e)* 231 kHz.　　*(f)* 718 kHz.

(g) 1.04 MHz.　　*(h)* 1.50 MHz.　　*(i)* 2.14 MHz.

(j) 3.02 MHz.　　*(k)* 4.25 MHz.　　*(l)* 5.89 MHz.

(m) 8.04 MHz.　　*(n)* 10.75 MHz.　　*(o)* 13.90 MHz.
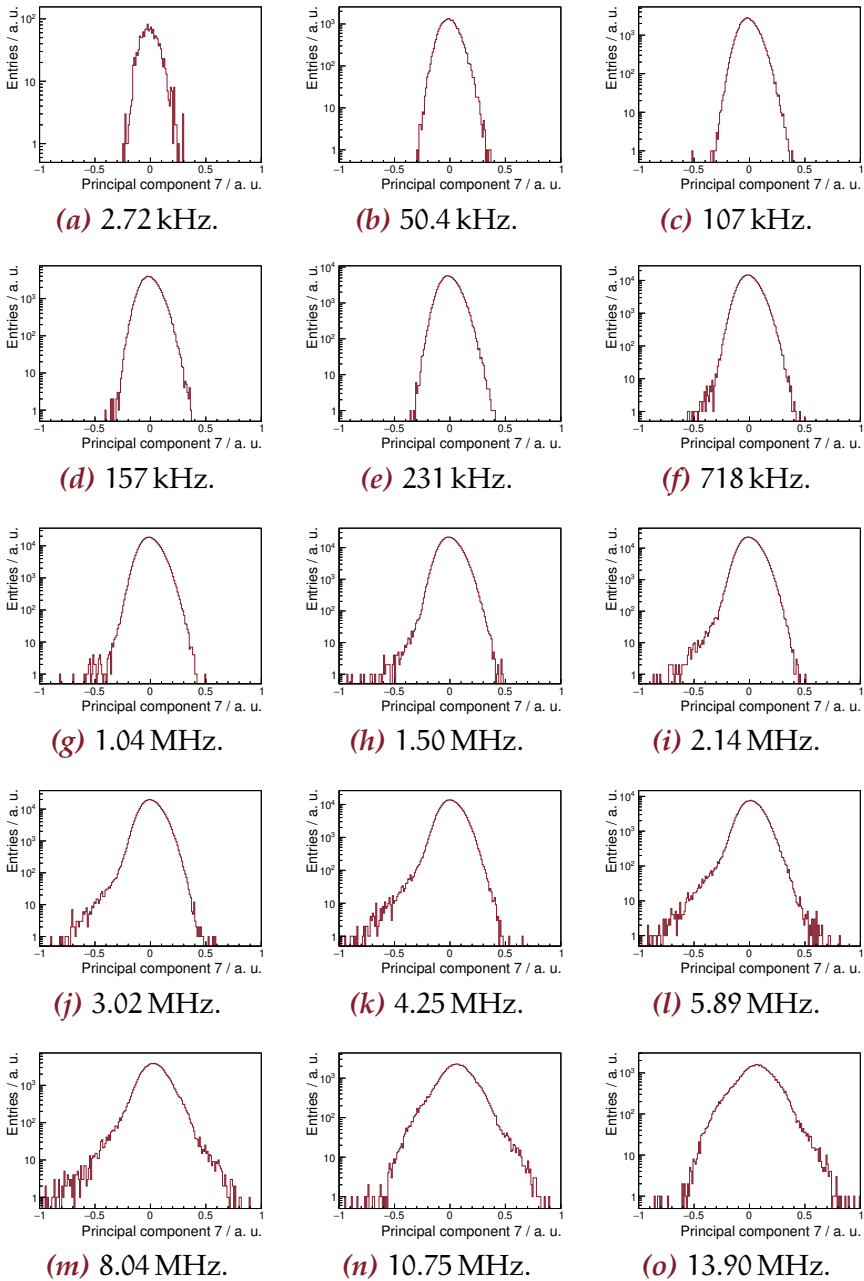
Figure B.18: Distributions of the 7th principal component.

(a) 2.72 kHz.

(b) 50.4 kHz.

(c) 107 kHz.

(d) 157 kHz.

(e) 231 kHz.

(f) 718 kHz.

(g) 1.04 MHz.

(h) 1.50 MHz.

(i) 2.14 MHz.

(j) 3.02 MHz.

(k) 4.25 MHz.

(l) 5.89 MHz.

(m) 8.04 MHz.

(n) 10.75 MHz.

(o) 13.90 MHz.
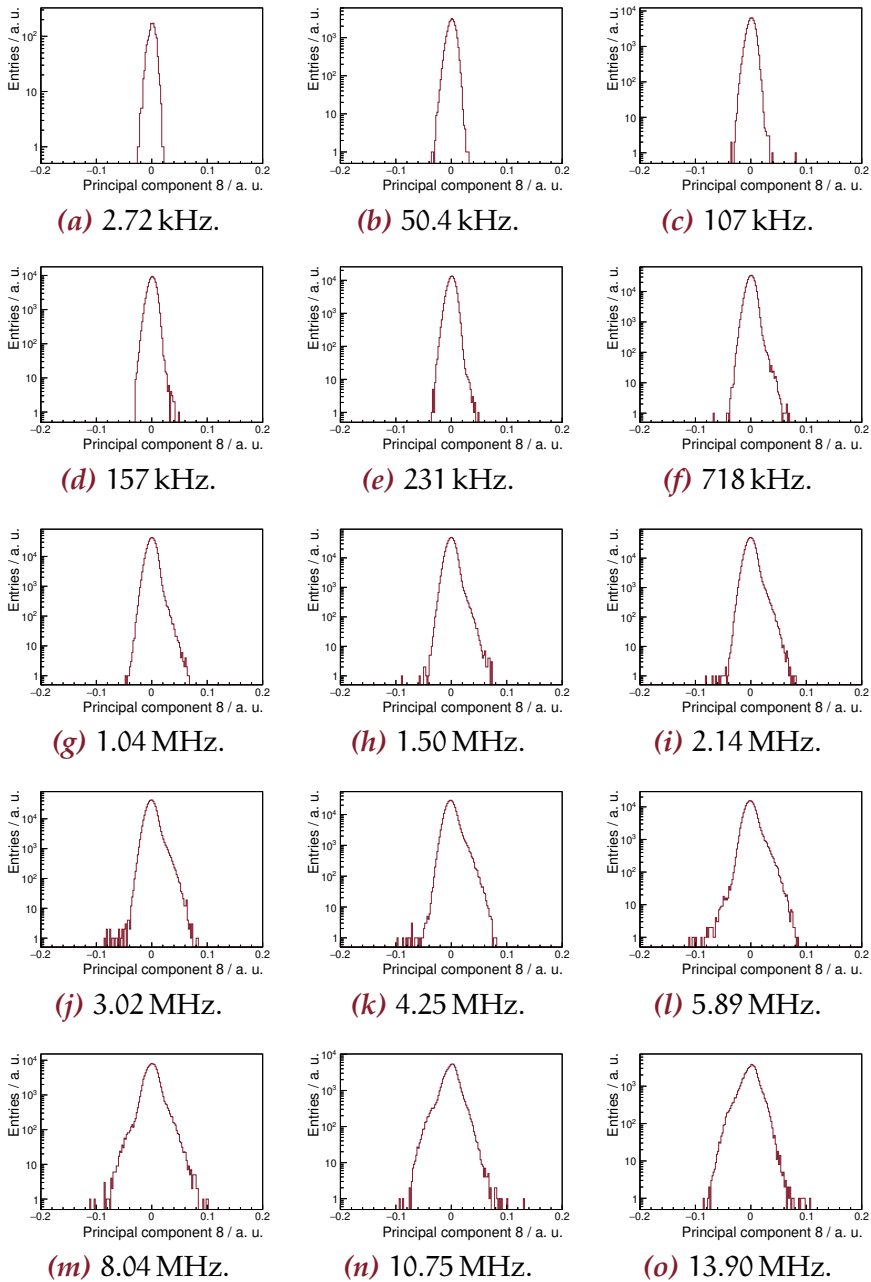
Figure B.19: Distributions of the 8th principal component.

(a) 2.72 kHz.

(b) 50.4 kHz.

(c) 107 kHz.

(d) 157 kHz.

(e) 231 kHz.

(f) 718 kHz.

(g) 1.04 MHz.

(h) 1.50 MHz.

(i) 2.14 MHz.

(j) 3.02 MHz.

(k) 4.25 MHz.

(l) 5.89 MHz.

(m) 8.04 MHz.

(n) 10.75 MHz.

(o) 13.90 MHz.
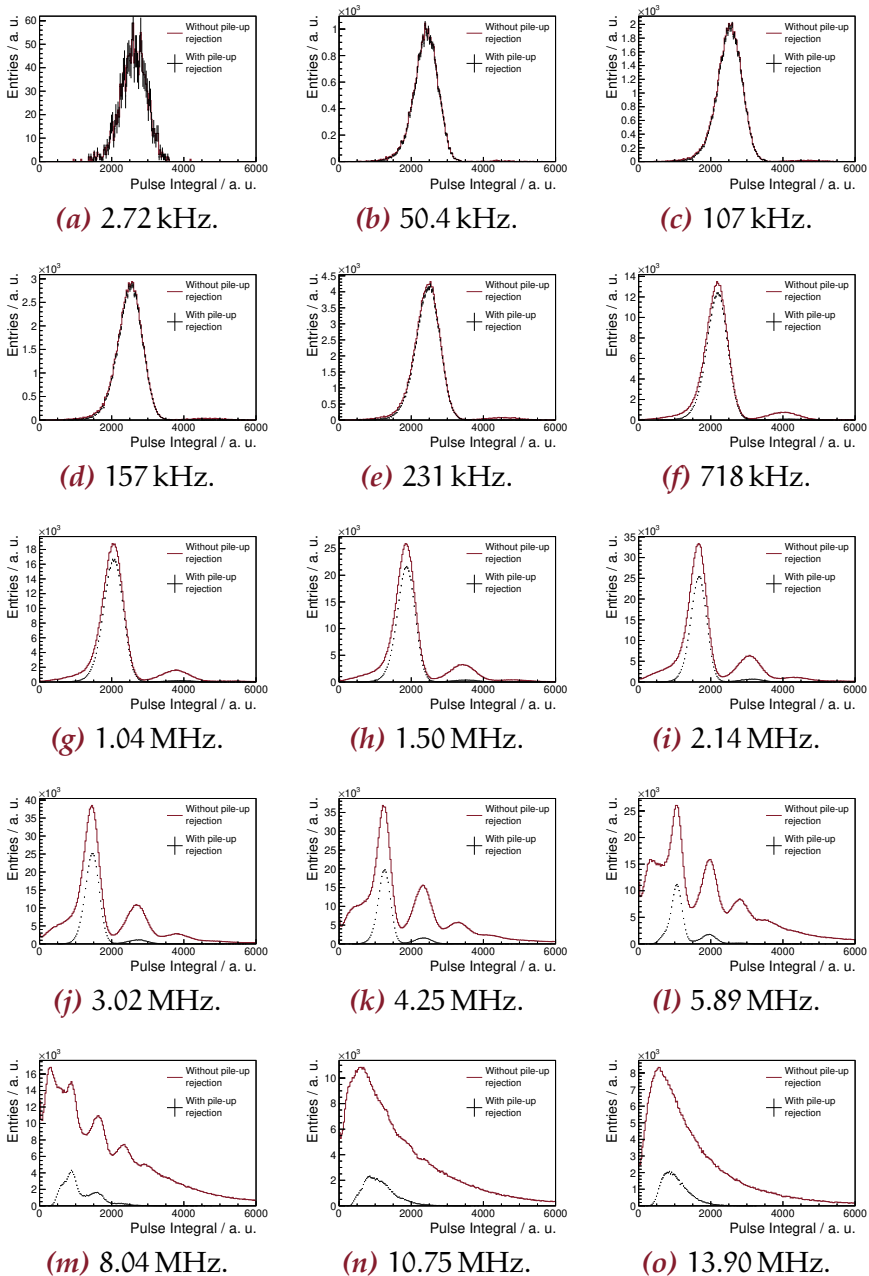
Figure B.20: Pulse integral distribution with and without pile-up rejection.

PROPERTIES OF THE 2017 DATA SETS

This Appendix describes the work of Yutie Liang which is relevant for the analysis described in Chapter 5. The first part is the determination of the integrated luminosity of the newly recorded data. The second part is a cross check of the BEMS result. The collision energy is determined using $e^+e^- \to (\gamma)\mu^+\mu^-$ events in a run dependent way to verify the stability of $\sqrt{s}$ over time.

C.1 Determination of the Integrated Luminosity of the 2017 Data

Since the work in this thesis is the first analysis of the two 2017 data sets, its integrated luminosities need to be determined. This is done by the analysis of (radiative) Bhabha events. The reaction $e^+e^- \to (\gamma)e^+e^-$ has a large cross section, which can be calculated by theory with an accuracy at the sub-percent level. The integrated luminosity is then given by the relation

$$\int \mathcal{L} \, dt = \frac{N_{obs}}{\sigma \cdot \epsilon} \quad , \tag{C.1}$$

where σ is calculated by the event generator, N_{obs} is the number of observed Bhabha events and the efficiency ϵ is determined by the analysis of MC events.

The analysis strategy follows the one from the luminosity determination of the 2013 data published in Reference [302].

C.1.1 Monte Carlo Data Set

The MC events are generated with Babayaga 3.5 [309, 310]. For both energy points, a MC data set of each 2×10^5 events is generated.

C.1.2 Event Selection

The $e^+e^- \to (\gamma)e^+e^-$ events are selected by the following criteria:

Table C.1: Determination of the integrated luminosity. For both center-of-mass energies, the Bhabha cross section as calculated by the event generator, the efficiency, the number of observed events as well as the integrated luminosity are listed. The shown error is statistical only.

$\sqrt{s}$ / MeV	σ / nb	ϵ / %	N_{obs}	$\int \mathcal{L} \, dt$ / pb^{-1}
3867.4	490.22 ± 0.35	14.4 ± 0.1	7681324	108.87 ± 0.04
3871.3	489.54 ± 0.35	14.4 ± 0.1	7768498	110.31 ± 0.04

- Exactly one positively and one negatively charged track are required.

- They have to fulfill the standard vertex requirements: $|z_{poca}| < 10\,cm$ and $r_{poca} < 1\,cm$.

- The tracks are constrained to the barrel region: $|\cos\theta| < 0.8$.

- The tracks have to have a minimum momentum: $p > p_{cut}$. The cut value is proportional to $\sqrt{s}$:

$$p_{cut} = \frac{\sqrt{s}}{4.26\,GeV} \times 2.0\,GeV \qquad (C.2)$$

This relation as well as the following was optimized in Reference [302] to the data set at $\sqrt{s} = 4.26\,GeV$

- The eletrons are identified by minimum energy deposition in the EMC, which is also $\sqrt{s}$ dependend:

$$E_{EMC} > \frac{\sqrt{s}}{4.26\,GeV} \times 1.55\,GeV \qquad (C.3)$$

Figures C.1-C.4 show the good agreement between various distributions of the data and MC samples. The determined luminosity is summarized in Table C.1.

C.1.3 Systematic Uncertainties

The systematic uncertainties affecting the luminosity are the following. They are determined using the same strategy as in Reference [302], where the justification for the specific values of the cut variations can be found as well.

(a) $\sqrt{s} = 3867.4\,\text{MeV}$.

(b) $\sqrt{s} = 3871.3\,\text{MeV}$.

(c) $\sqrt{s} = 3867.4\,\text{MeV}$.

(d) $\sqrt{s} = 3871.3\,\text{MeV}$.
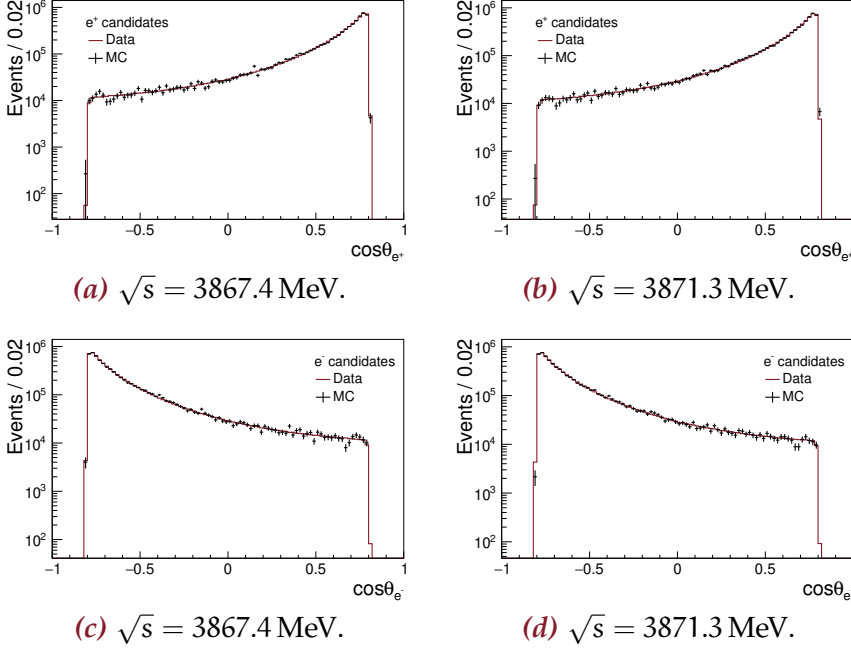
Figure C.1: Comparison of the track $\cos\theta$ distributions of data and MC. The MC histograms are normalized to the data histograms. The top (bottom) row shows the positively (negatively) charged track and the left (right) hand column shows the off-resonance (on-resonance) data set. The cut on the barrel region is already applied.

- The tracking uncertainty is determined by the reconstruction of Bhabha events with MDC and EMC and the reconstruction with the EMC only. Some event selection criteria are changed or added:

  - $p_{e^{\pm}} > \frac{2}{4.26} \cdot \sqrt{s}$. This cut is only applied for the method using the MDC and the EMC.
  - $E_{e^{\pm}}^{EMC} > \frac{1.8}{4.26} \cdot \sqrt{s}$
  - $5° < |\Delta\phi| < 40°$, with $\Delta\phi = |\phi_{e^+}^{EMC} - \phi_{e^-}^{EMC}| - 180°$ and $\phi_{e^{\pm}}^{EMC}$ being the azimuthal angle of the $e^{\pm}$ cluster in the EMC.
  - The constraint to the barrel region is applied to the EMC clusters instead of the momenum vectors: $|\cos\theta_{e^{\pm}}^{EMC}| < 0.8$.

(a) $\sqrt{s} = 3867.4\,\text{MeV}$.   *(b)* $\sqrt{s} = 3871.3\,\text{MeV}$.

(c) $\sqrt{s} = 3867.4\,\text{MeV}$.   *(d)* $\sqrt{s} = 3871.3\,\text{MeV}$.
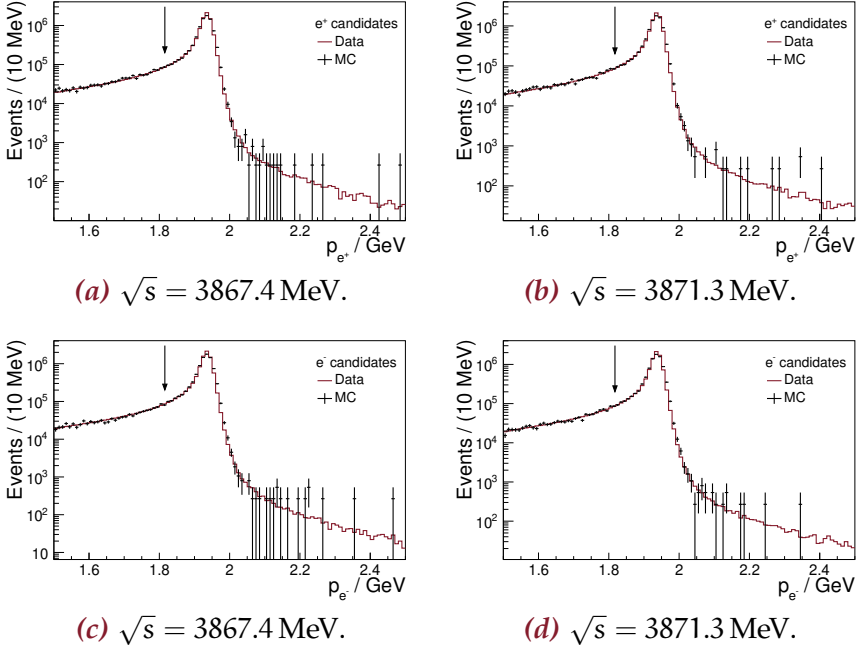
Figure C.2: Comparison of the track momentum distributions of data and MC. The MC histograms are normalized to the data histograms. The top (bottom) row shows the positively (negatively) charged track and the left (right) hand column shows the off-resonance (on-resonance) data set. The arrows indicate the cut values.

The change of integrated luminosity is taken as systematic uncertainty.

- The cut on $\cos(\theta_{e\pm})$ has been varied from 0.8 to 0.7 and the difference in the resulting luminosity is taken as the systematic uncertainty of this cut.

- The cut value of $E_{e\pm}^{EMC}$ is increased by 10 % and the change in luminosity is taken as the uncertainty.

- The cut value of $p_{e\pm}$ is increased by 3 % and the change in luminosity is taken as the uncertainty.

- To be conservative, the $\sqrt{s}$ uncertainty is estimated by a 2 MeV shift of the MC sample. As a result, the selection efficiency and

(a) $\sqrt{s} = 3867.4\,\text{MeV}$.

(b) $\sqrt{s} = 3871.3\,\text{MeV}$.

(c) $\sqrt{s} = 3867.4\,\text{MeV}$.

(d) $\sqrt{s} = 3871.3\,\text{MeV}$.
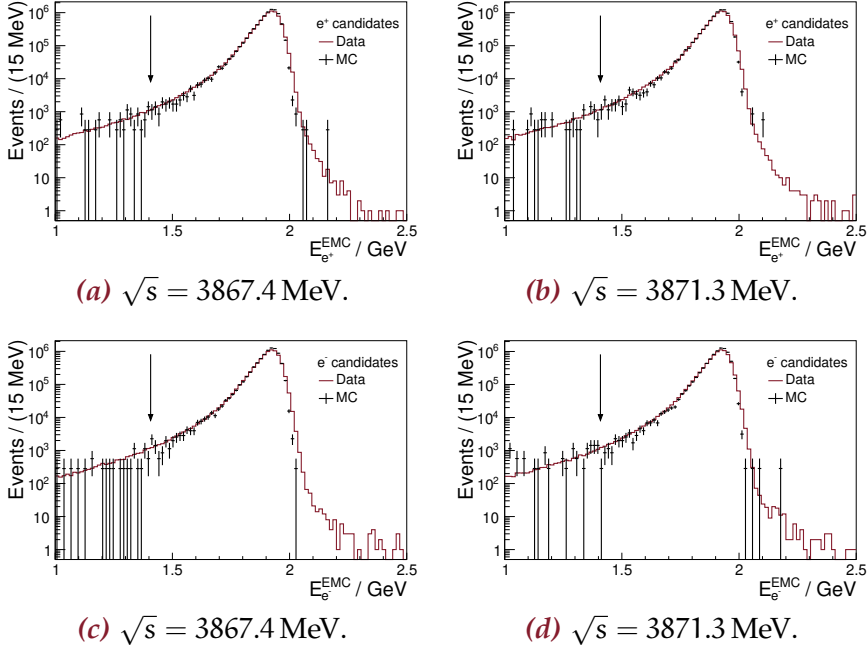
Figure C.3: Comparison of the energy deposition distributions of data and MC. The MC histograms are normalized to the data histograms. The top (bottom) row shows the positively (negatively) charged track and the left (right) hand column shows the off-resonance (on-resonance) data set. The arrows indicate the cut values.

the calculated cross section are altered and the change in luminosity is taken as the systematic uncertainty. This variation is larger than the difference to the $\sqrt{s}$ of the first two runs of the off-resonance data set.

- The uncertainty of the cross section calculation is quoted from Babayaga 3.5 [309, 310].

- The trigger efficiency uncertainty has been determined in reference [228].

Their values and the total systematic uncertainties are listed in Table C.2.

(a) $\sqrt{s} = 3867.4\,\text{MeV}$.

(b) $\sqrt{s} = 3871.3\,\text{MeV}$.

(c) $\sqrt{s} = 3867.4\,\text{MeV}$.

(d) $\sqrt{s} = 3871.3\,\text{MeV}$.
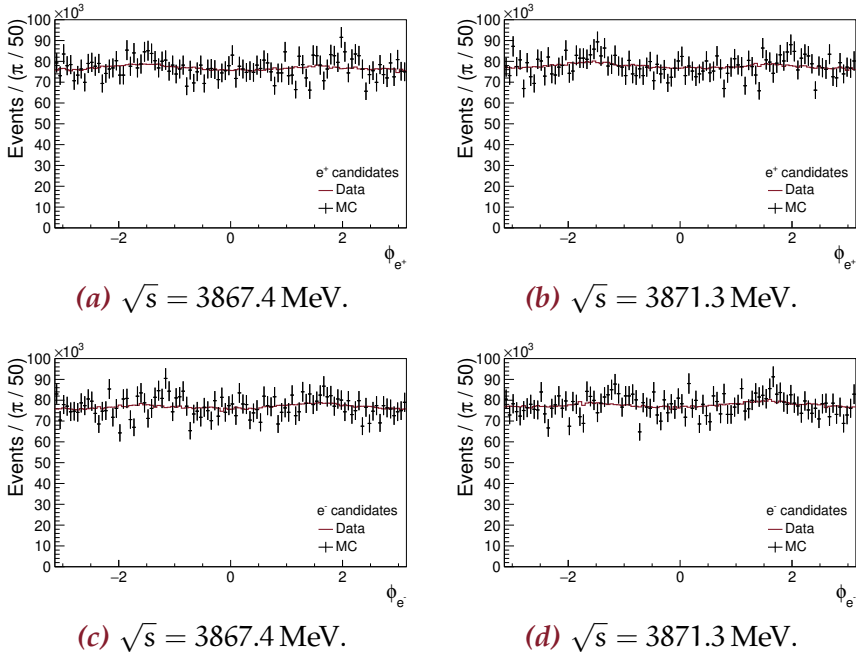
Figure C.4: Comparison of the track azimuthal angle distributions of data and MC. The MC histograms are normalized to the data histograms. The top (bottom) row shows the positively (negatively) charged track and the left (right) hand column shows the off-resonance (on-resonance) data set.

Table C.2: Relative systematic uncertainties (in %) of the integrated luminosity. The total error is the quadratic sum.

Source	3867.4 MeV	3871.3 MeV
Tracking	0.80	0.48
$\cos(\theta_{e^\pm})$ cut	0.09	0.12
$E^{EMC}_{e^\pm}$ cut	0.09	0.06
$p_{e^\pm}$ cut	0.09	0.16
$\sqrt{s}$	0.65	0.02
σ	0.50	0.50
Trigger	0.10	0.10
Total	1.16	0.71

Table C.3: Integrated luminosity of th two 2017 data sets. The first error is statistical and the second one is systematic.

$\sqrt{s}\,/\,\mathrm{MeV}$	$\int \mathcal{L}\,\mathrm{dt}\,/\,\mathrm{pb}^{-1}$
3867.4	$108.87 \pm 0.04 \pm 1.26$
3871.3	$110.31 \pm 0.04 \pm 0.78$

Table C.4: Integrated luminosity of the two 2013 data sets. The errors of the values obtained in this analysis are statistical, while the errors of the published values are the quadratic sums of statistical and systematic uncertainties.

$\sqrt{s}\,/\,\mathrm{MeV}$	$\int \mathcal{L}\,\mathrm{dt}\,/\,\mathrm{pb}^{-1}$	
	this analysis	published value
3807.7	50.584 ± 0.026	50.5 ± 0.5
3896.2	52.775 ± 0.027	52.6 ± 0.5

C.1.4 Result

The result is summarized in Table C.3.

C.1.5 Cross Check: Luminosity Determination of the 2013 Data

As a cross check, the same method was applied to the 2013 data samples. Table C.4 compares the luminosity obtained by this analysis to the published values. Although the systematic uncertainties are missing in this analysis, the result is in very good agreement to the published values.

C.2 Center-of-Mass Energy Determination via the Dimuon process

To verify the BEMS result and in particular to check the stability of the center-of-mass energy after the BEMS could no longer provide information on the positron beam, the center-of-mass energy is determined by the analysis of the reaction $e^+e^- \rightarrow (\gamma_{\mathrm{ISR/FSR}})\mu^+\mu^-$. This study is guided by the already published $\sqrt{s}$ determination of

the 2013 data [301]. The center-of-mass energy is given by

$$\sqrt{s}_{\mu^+\mu^-} = m(\mu^+\mu^-) + \Delta m_{rad} + \Delta m_{calib} \quad, \qquad (C.4)$$

where $m(\mu^+\mu^-)$ is the invariant dimuon mass, Δm_{rad} is the correction due to ISR/FSR, and Δm_{calib} is the correction due to momentum calibration.

C.2.1 MC Samples

For the center-of-mass determination with the dimuon process, several MC samples of each 200 k events have been generated:

- For both data samples (on/off-resonance), the process $e^+e^- \to (\gamma_{ISR/FSR})\mu^+\mu^-$ is simulated with Babayaga 3.5 [309, 310] including ISR and FSR.

- In order to study the effect of radiative corrections, the $e^+e^- \to \mu^+\mu^-$ reaction is simulated with Babayaga 3.5 without ISR and FSR. Again, MC samples for both center-of-mass energies are generated.

- For the momentum calibration, the process $e^+e^- \to \gamma_{ISR}(\gamma_{FSR})J/\psi(\to \mu^+\mu^-)$ is simulated with EvtGen and the VECTORISR model [305, 306]. For the on-resonance $\sqrt{s}$, two MC sets are generated: one with FSR and one without FSR.

C.2.2 Invariant Dimuon Mass

The $e^+e^- \to (\gamma)\mu^+\mu^-$ events are selected by the following criteria:

- Exactly one positively and one negatively charged track are required.

- These have to fulfill the standard vertex requirements: $|z_{poca}| < 10\,cm$ and $r_{poca} < 1\,cm$.

- The tracks are constrained to the barrel region: $|\cos\theta| < 0.8$.

- The tracks have to be back-to-back, i.e. the cosine of the opening angle between the two tracks needs to less than -0.9997. This corresponds to a minimum opnening angle of $178.6°$.

(a) Off-resonance.

(b) On-resonance.

(c) Off-resonance.

(d) On-resonance.
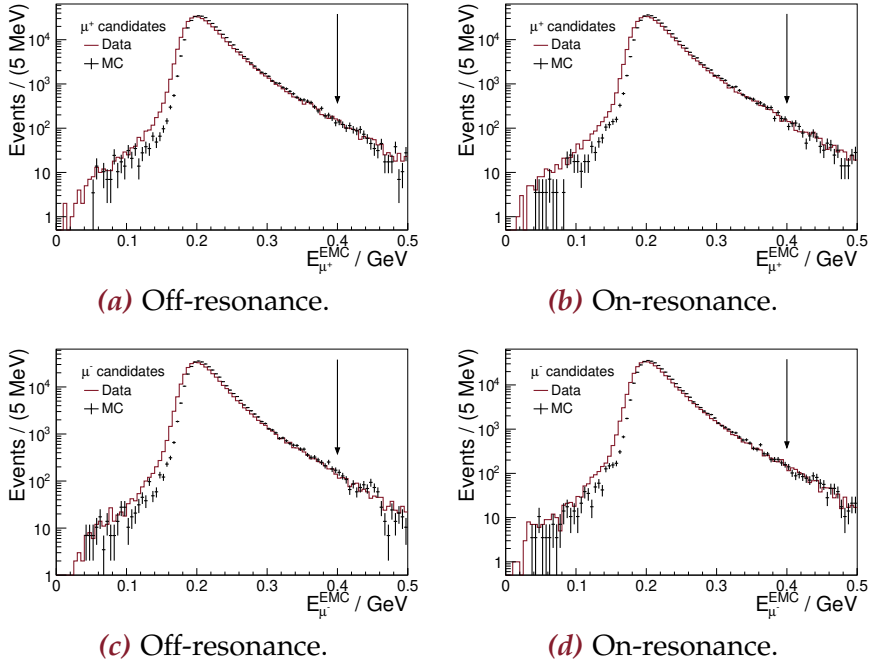
Figure C.5: Comparison of the energy deposition distributions of data and MC. The MC histograms are normalized to the data histograms. The top (bottom) row shows the positively (negatively) charged track and the left (right) hand column shows the off-resonance (on-resonance) data set. The arrows indicate the cut value. A slight shift between data and MC is noticable.

- The muons are identified by a maximum energy deposition in the EMC: $E_{EMC} < 0.4\,\text{GeV}$

- Background from cosmic muons is suppressed by requiring the difference of the timing signals in the TOF associated with the two tracks to be less than $2\,\text{ns}$.

Figures C.5- C.9 show the comparisson between data and MC in various distributions. In general, there is good agreement between data and MC. However, there is a slight shift in the distributions of the energy deposition in the EMC and the opening angle between the two tracks.

(a) Off-resonance.

(b) On-resonance.

(c) Off-resonance.
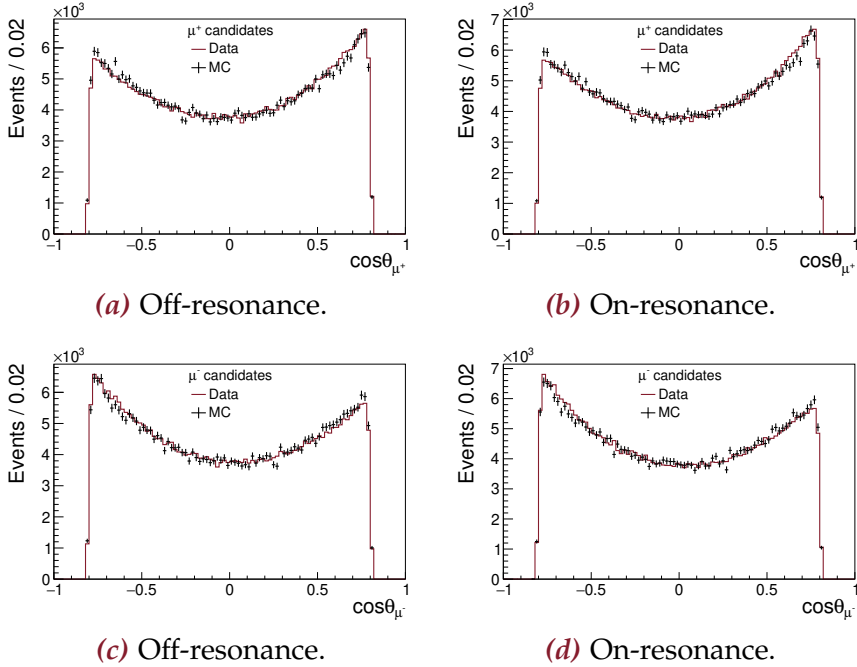
(d) On-resonance.

Figure C.6: Comparison of the track $\cos\theta$ distributions of data and MC. The MC histograms are normalized to the data histograms. The top (bottom) row shows the positively (negatively) charged track and the left (right) hand column shows the off-resonance (on-resonance) data set. The cut on the barrel region is already applied.

Figure C.10 shows the invariant dimuon mass distributions for the on- and off-resonance data sets. A fit with a Gaussian is superimposed. The fit range is defined by $[\mu - \sigma, \mu + 1.5\sigma]$. The results are $(3865.52 \pm 0.08)\,\mathrm{MeV}$ and $(3869.48 \pm 0.08)\,\mathrm{MeV}$ for the off- and on-resonance data sets respectively.

C.2.3   *Radiative Correction*

The effect of ISR and FSR is determined by the analysis of MC events with and without ISR/FSR. Therefore, the event selection criteria are the same as above. Figure C.11 shows the fits to the corresponding dimuon mass distributions. The correction due to ISR/FSR Δm_{rad}

(a) Off-resonance.
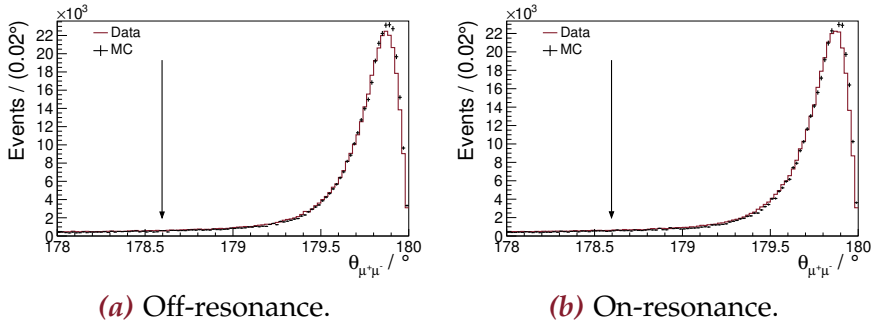
(b) On-resonance.

Figure C.7: Comparison of the distributions of the opening angle between the two tracks of data and MC. The MC histograms are normalized to the data histograms. The left (right) hand histogram shows the off-resonance (on-resonance) data set. The arrows indicate the cut value.

(a) Off-resonance.
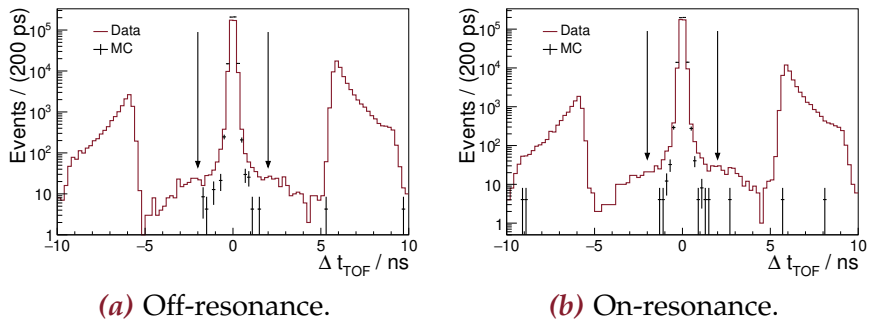
(b) On-resonance.

Figure C.8: Comparison of the time difference of both tracks in the TOF of data and MC. The MC histograms are normalized to the data histograms. The left (right) hand histogram shows the off-resonance (on-resonance) data set. The arrows indicate the cut values. The accumulations in data at $|\Delta t_{TOF}| > 5\,\text{ns}$ are due to cosmic muons.

(a) Off-resonance.   *(b)* On-resonance.
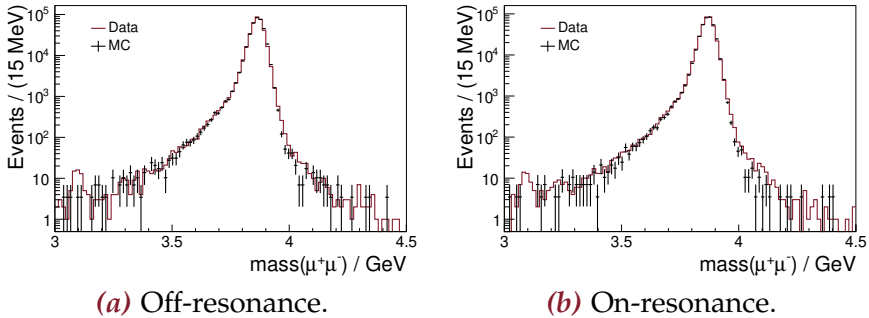
Figure C.9: Comparison of the invariant $\mu^+\mu^-$ mass distributions of data and MC. The MC histograms are normalized to the data histograms. The left (right) hand histogram shows the off-resonance (on-resonance) data set.

(a) Off-resonance.   *(b)* On-resonance.
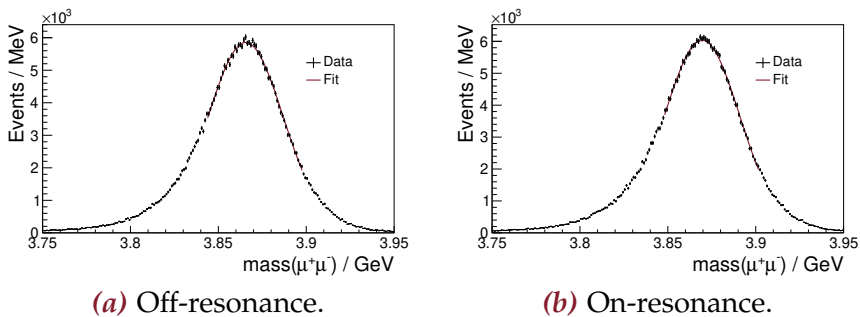
Figure C.10: Fit to the observed invariant $\mu^+\mu^-$ mass distribution. The left (right) hand plot shows the off-resonance (on-resonance) data set. The obtained values are $(3865.52 \pm 0.08)\,\text{MeV}$ and $(3869.48 \pm 0.08)\,\text{MeV}$ for the off- and on-resonance data sets respectively.

(a) Off-resonance.

(b) On-resonance.

(c) Off-resonance.
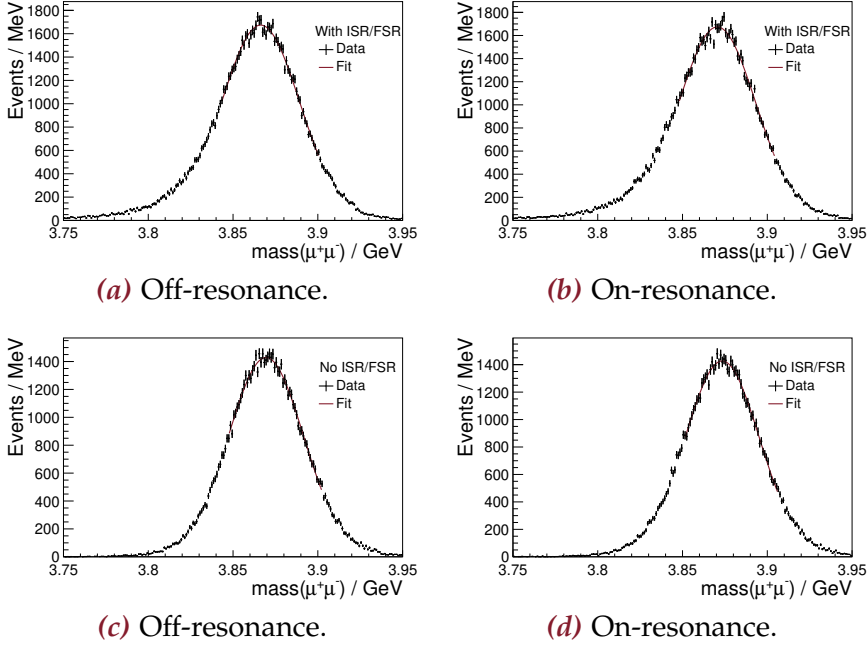
(d) On-resonance.

Figure C.11: Fit to the invariant $\mu^+\mu^-$ mass distribution of the MC set with and without ISR/FSR. The top (bottom) row shows the radiative corrections switched on (off) and the left (right) hand column shows the off-resonance (on-resonance) MC set.

from (C.4) is given by

$$\Delta m_{\mathrm{rad}} = m_0^{\mathrm{MC}}(\mu^+\mu^-) - m_{\mathrm{ISR/FSR}}^{\mathrm{MC}}(\mu^+\mu^-) \quad , \qquad (C.5)$$

when $m_0^{\mathrm{MC}}(\mu^+\mu^-)$ is the fitted mass of the MC set without ISR/FSR and $m_{\mathrm{ISR/FSR}}^{\mathrm{MC}}(\mu^+\mu^-)$ is the fitted mass of the MC set with ISR/FSR. The resulting values are summarized in Table C.5. Since both center-of-mass energies are very close together, the effect of radiative corrections are expected to be the same for both data sets. This is taken into account by avergaing both values and apply it to both data sets. The final value is $\Delta m_{\mathrm{rad}} = (3.03 \pm 0.16)\,\mathrm{MeV}$.

C.2.4 *Momentum Calibration*

The momentum calibration is checked with the determination of the J/ψ mass in the reaction $e^+e^- \rightarrow \gamma_{\mathrm{ISR}}(\gamma_{\mathrm{FSR}})J/\psi(\rightarrow \mu^+\mu^-)$. There-

Table C.5: Correction to the invariant dimuon mass due to radiative effects.

	Off-resonance	On-resonance
$m_0^{MC}(\mu^+\mu^-)\,/\,\mathrm{MeV}$	3869.44 ± 0.16	3873.39 ± 0.16
$m_{ISR/FSR}^{MC}(\mu^+\mu^-)\,/\,\mathrm{MeV}$	3866.28 ± 0.15	3870.50 ± 0.15
$\Delta m_{rad}\,/\,\mathrm{MeV}$	3.16 ± 0.22	2.89 ± 0.22

fore, the event selection criteria are the same as above with the exception that the requirement of the opening angle between the two tracks is dropped. Figure C.12(a) shows the fit to data (both data samples combined) in the J/ψ region. The signal is modeled by a Crystal Ball function and the background is modeled as a quadratic function. The obtained mass $m_{FSR}^{data}(J/\psi)$ needs to be corrected for FSR effects, which are determined using MC with and without FSR. The fits with the same fit models are shown in Figures C.12(b) and C.12(c). The resulting value for the $/J/\psi$ mass and its deviation from the PDG value are listed in Table C.6. For a center-of-mass energy corresponding to the J/ψ mass, the correction to the dimuon mass due to momentum calibration is $\Delta m_{calib}^{J/\psi} = (-1.1 \pm 0.4)\,\mathrm{MeV}$. However, this correction is not independent from $\sqrt{s}$. In an earlier work of BESIII, it was shown that this correction can be described by a linear function with a slope of $(5.44 \pm 0.33) \times 10^{-4}\,/\,\mathrm{MeV}$ [329]. Using this slope, Δm_{calib} is extrapolated from the J/ψ mass to the X(3872) mass region and yields $\Delta m_{calib} = (-1.5 \pm 0.3)\,\mathrm{MeV}$

C.2.5 *Result*

The combination of the above intermediate results is shown in Table C.7. The final result of the dimuon analysis agrees within the statistical error bars with the BEMS measurement. Since this only serves as a cross check, the systematic uncertainty is not determined.

C.2.6 *Run Dependency of the Center-of-Mass Energy*

The center-of-mass energy has also been determined for each run independently. The result is shown in Figure C.13. In particular, it shows that $\sqrt{s}$ is stable during the on-resonance data taking. This justifies the usage of the BEMS result of this period, which is missing a large part of measurements.

Table C.6: Summary of the Fits to the J/ψ peak in $e^+e^- \to \gamma_{ISR}(\gamma_{FSR})J/\psi(\to \mu^+\mu^-)$ and the resulting corrections. $m^{data}_{FSR}(J/\psi)$ is the fitted mass in data. $m^{MC}_{FSR}(J/\psi)$ and $m^{MC}_{noFSR}(J/\psi)$ are the fitted masses in MC with and without FSR. The difference, of the two, i.e. the effect of FSR at the J/ψ mass, is $\Delta m^{J/\psi}_{FSR}$. The fitted data mass after the FSR correction is $m^{data}_0(J/\psi)$ and its difference to the PDG value is $\Delta m^{J/\psi}_{calib}$, which is then also the mass correction due to momentum calibration for $\sqrt{s} = m(J/\psi)c^2$.

$m^{data}_{FSR}(J/\psi)$	$(3097.48 \pm 0.28)\,\mathrm{MeV}$
$m^{MC}_{FSR}(J/\psi)$	$(3098.35 \pm 0.05)\,\mathrm{MeV}$
$m^{MC}_{noFSR}(J/\psi)$	$(3098.83 \pm 0.05)\,\mathrm{MeV}$
$\Delta m^{J/\psi}_{FSR}$	$(0.48 \pm 0.07)\,\mathrm{MeV}$
$m^{data}_0(J/\psi)$	$(3098.0 \pm 0.3)\,\mathrm{MeV}$
$\Delta m^{J/\psi}_{calib}$	$(-1.1 \pm 0.3)\,\mathrm{MeV}$

Table C.7: Result of the center-of-mass determination via the analysis of dimuon events. $m(\mu^+\mu^-)$ is the invariant dimuon mass, Δm_{rad} is the correction due to ISR/FSR, and Δm_{calib} is the correction due to the momentum calibration. The result $\sqrt{s}_{\mu^+\mu^-}$ is compared to the BEMS result $\sqrt{s}_{BEMS}$. Both results agree within the error bars. All masses are given in MeV and the energies in MeV.

Data Set	Off-resonance	On-resonance
$m(\mu^+\mu^-)$	3865.52 ± 0.08	3869.48 ± 0.08
Δm_{rad}	3.03 ± 0.16	3.03 ± 0.16
Δm_{calib}	-1.5 ± 0.3	-1.5 ± 0.3
$\sqrt{s}_{\mu^+\mu^-}$	3867.05 ± 0.35	3871.01 ± 0.35
$\sqrt{s}_{BEMS}$	3867.410 ± 0.031	3871.31 ± 0.06
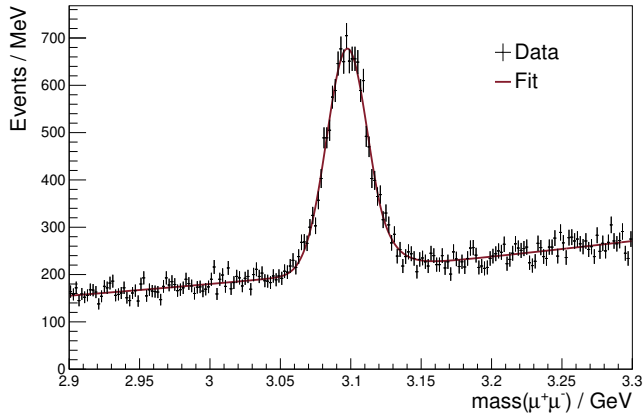
(a) Data.
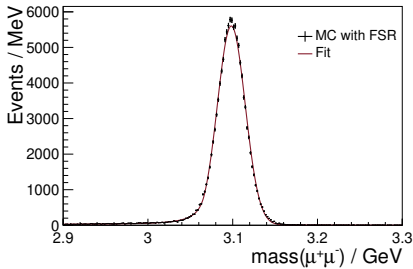
(b) MC with FSR.
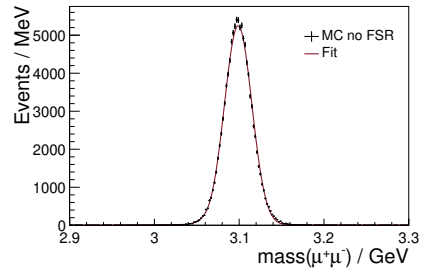
(c) MC without FSR.

Figure C.12: Fit to the J/ψ peak in $e^+e^- \rightarrow \gamma_{ISR}(\gamma_{FSR})J/\psi(\rightarrow \mu^+\mu^-)$.
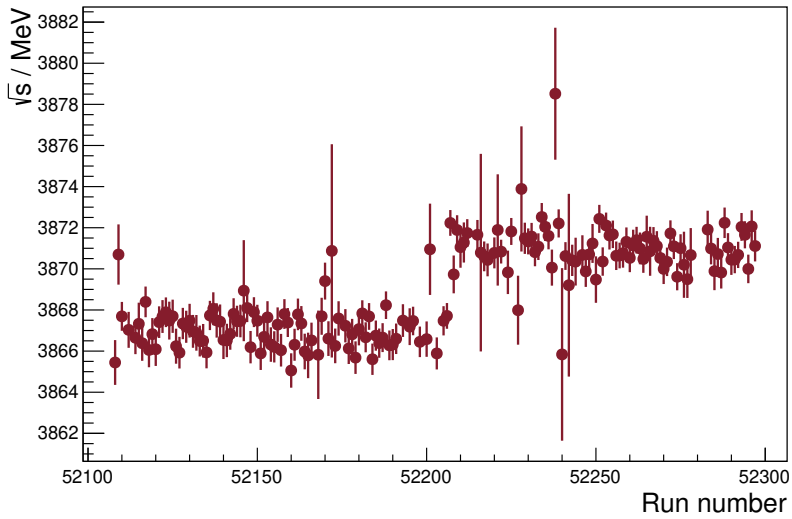
Figure C.13: The center-of-mass energy as determined for each run via the analysis of dimuon events. The two different energies for the on- and off-resonance data samples are clearly visible. The energy does not show large fluctuations within the two separate samples.

PLOTS AND TABLES ON $e^+e^- \to \pi^+\pi^- J/\psi$

This Appendix lists a lot of plots and tables relating to intermediate steps of the cross section determination of $e^+e^- \to \pi^+\pi^- J/\psi$.

D.1 χ^2 Cut Optimization and Comparison Plots

In Section 5.4.2, the background rejection cuts for the $e^+e^- \to \pi^+\pi^- J/\psi \to \pi^+\pi^-\ell^+\ell^-$ event selection are described. The cut on the χ^2 value of the kinematic fit is optimized by a figure-of-merit analysis. Figures D.1 and D.2 show $N_{sig}/\sqrt{N_{sig} + N_{bkg}}$ as a function of the χ^2 cut. In order to be less sensitive to statistical fluctuations, the cut value is chosen to be slightly larger than the one at the maximum.

D.2 Data and Monte Carlo Comparison

In Figures D.3 to D.5, data and MC distributions are compared. The MC sets are combinations of the signal MC and the background MC cocktail. In total, the distributions of the four variables $\cos\theta_{\pi^+\pi^-}$, $\cos\theta_{\pi^\pm\ell^\mp}$, χ^2, and $m(\pi^+\pi^-)$ are drawn.

(a)   *(b)*

(c)   *(d)*
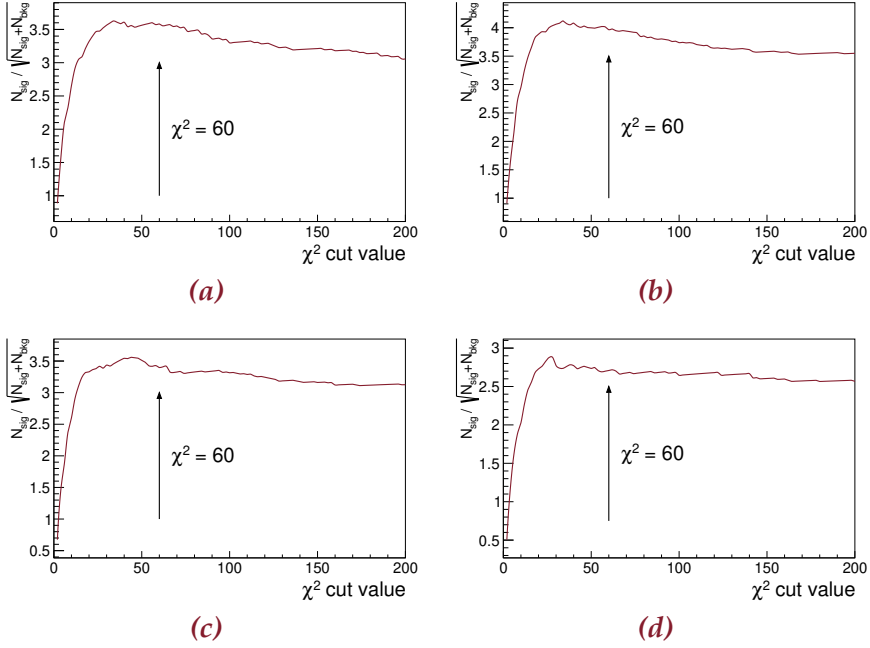
Figure D.1: Optimization of the χ^2 cut of the electron mode. N_{sig} and N_{bkg} are estimated from the signal MC and data sidebands, respectively. The statistical fluctuations originate in the limited size of the sideband. In order to be less sensitive to these fluctuations, the cut value (black arrow) is chosen to be further away from the edge at low χ^2 than the value maximizing the figure-of-merit. The value at the cut position is only slightly smaller than at the maximum.
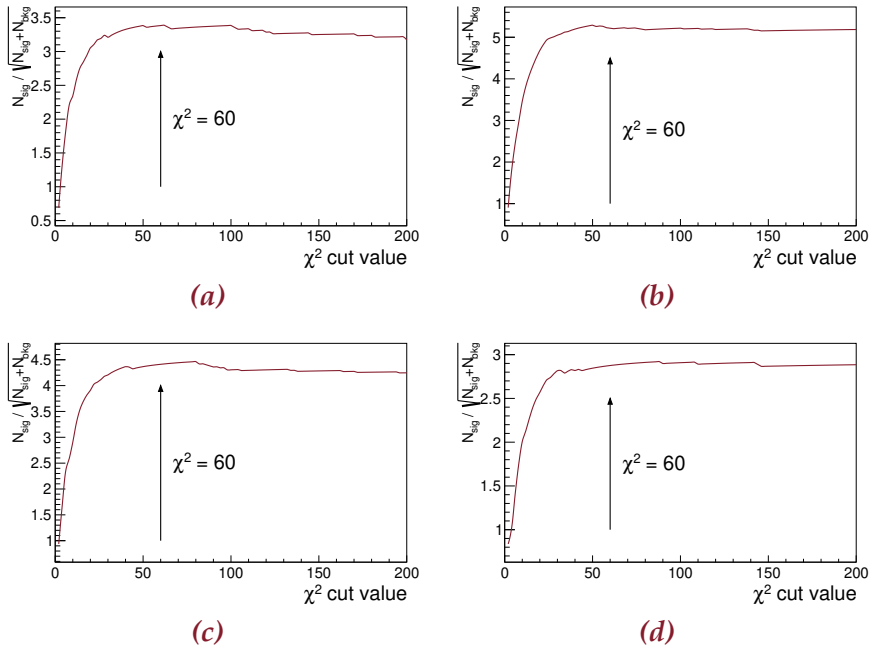
Figure D.2: Optimization of the χ^2 cut of the muon mode. N_{sig} and N_{bkg} are estimated from the signal MC and data sidebands, respectively. The cut value is indicated by the black arrow.
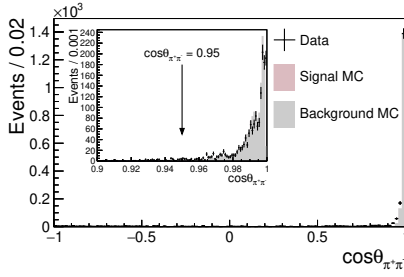
(a) $J/\psi \to e^+e^-$ mode.
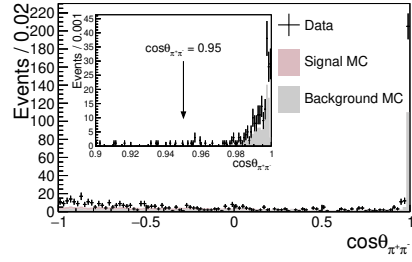
(b) $J/\psi \to \mu^+\mu^-$ mode.
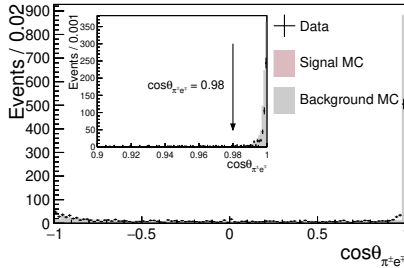
(c) $J/\psi \to e^+e^-$ mode.
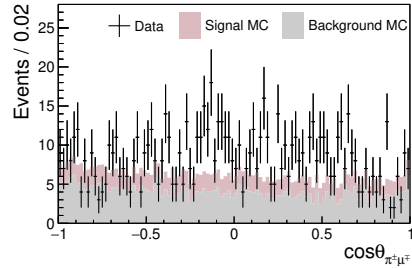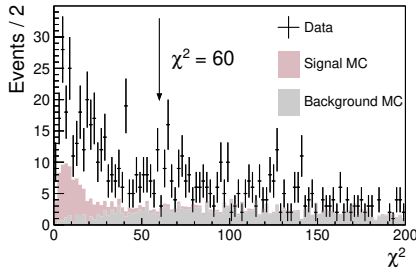
(d) $J/\psi \to \mu^+\mu^-$ mode.

(e) $J/\psi \to e^+e^-$ mode.
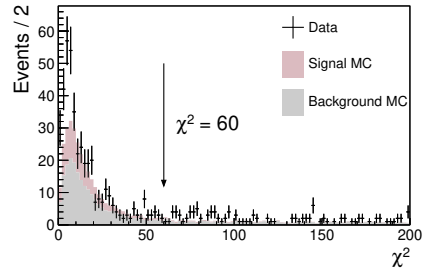
(f) $J/\psi \to \mu^+\mu^-$ mode.

Figure D.3: Distributions of the variables used for background rejection. Data in the fit region is compared to the sum of signal MC and background MC. All four data sets are combined and the MC distributions are scaled to match the integrated luminosity of the data. The left column shows the events in the $J/\psi \to e^+e^-$ reconstruction mode and the right column corresponds to $J/\psi \to \mu^+\mu^-$. The cut values are indicated by arrows, while all other cuts are applied. *(a)* and *(b)* distributions of $\cos\theta_{\pi^+\pi^-}$. *(c)* and *(d)* distributions of $\cos\theta_{\pi^\pm\ell^\mp}$. *(e)* and *(f)* distributions of χ^2.
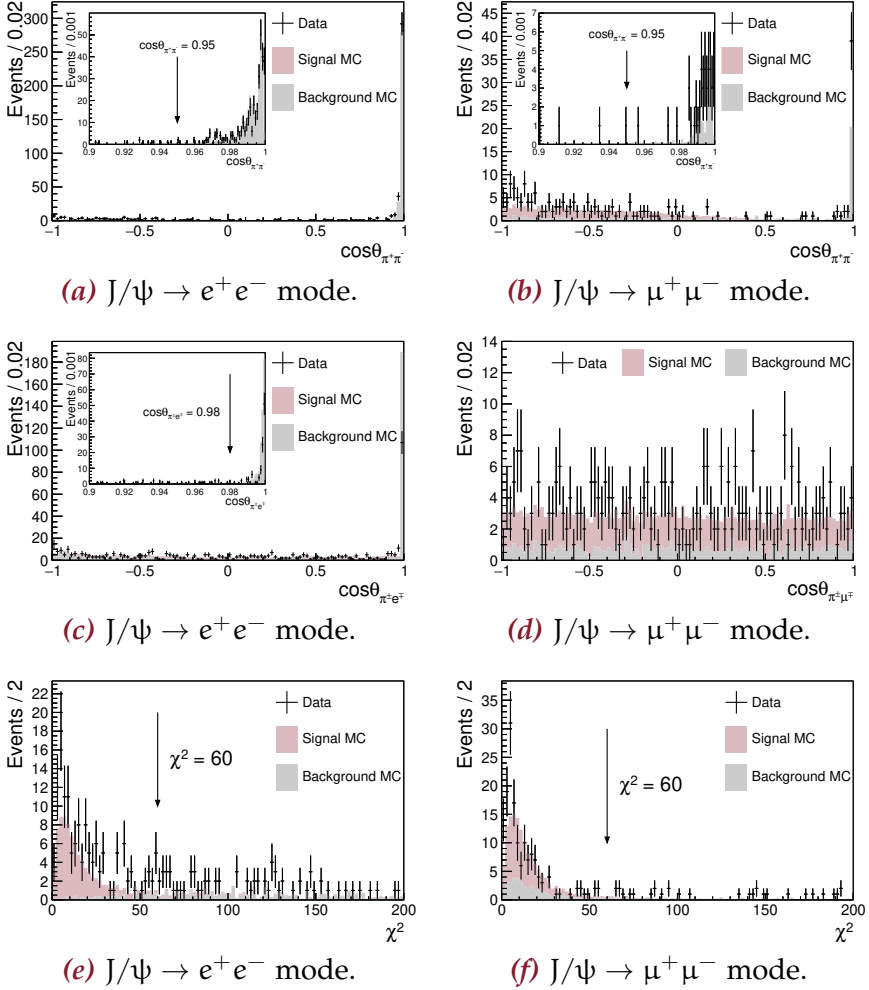
Figure D.4: Distributions of the variables used for background rejection. Data in the J/ψ peak region is compared to the sum of signal MC and background MC. All four data sets are combined and the MC distributions are scaled to match the integrated luminosity of the data. The left column shows the events in the J/ψ → e^+e^- reconstruction mode and the right column corresponds to J/ψ → $\mu^+\mu^-$. The cut values are indicated by arrows, while all other cuts are applied. *(a)* and *(b)* distributions of $\cos\theta_{\pi^+\pi^-}$. *(c)* and *(d)* distributions of $\cos\theta_{\pi^\pm\ell^\mp}$. *(e)* and *(f)* distributions of χ^2.

(a) $J/\psi \to e^+e^-$ mode.

(b) $J/\psi \to \mu^+\mu^-$ mode.

(c) $J/\psi \to e^+e^-$ mode.

(d) $J/\psi \to \mu^+\mu^-$ mode.
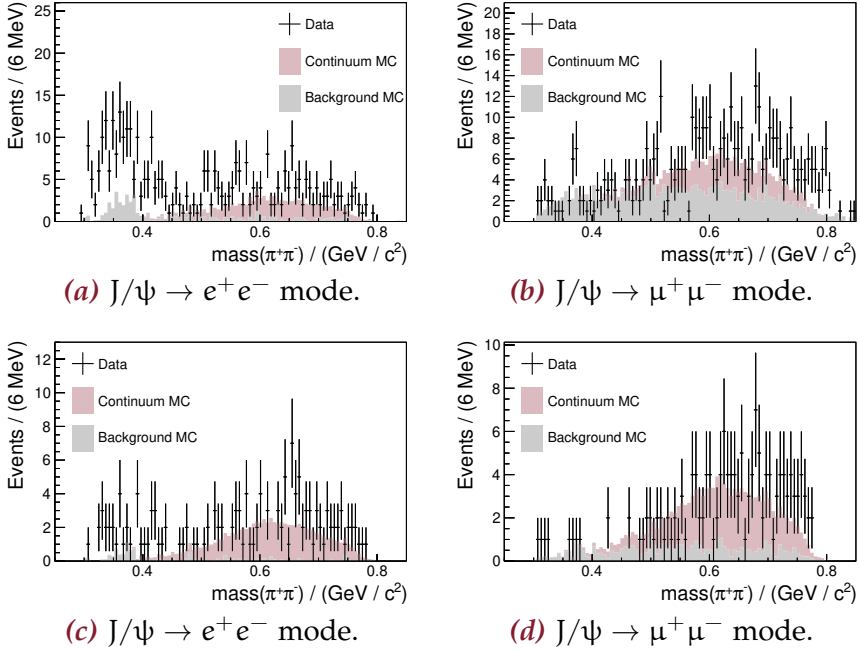
Figure D.5: Comparison between data, continuum MC, and background MC distributions of $m(\pi^+\pi^-)$. All four data sets are combined. All cuts are applied. The MC distributions are scaled to match the integrated luminosity of the data. The top row shows all events in the fit range and the bottom row shows all events in the J/ψ peak region.

(a) $\sqrt{s} = 3807.7\,\text{MeV}$.

(b) $\sqrt{s} = 3867.4\,\text{MeV}$.

(c) $\sqrt{s} = 3871.3\,\text{MeV}$.

(d) $\sqrt{s} = 3896.2\,\text{MeV}$.
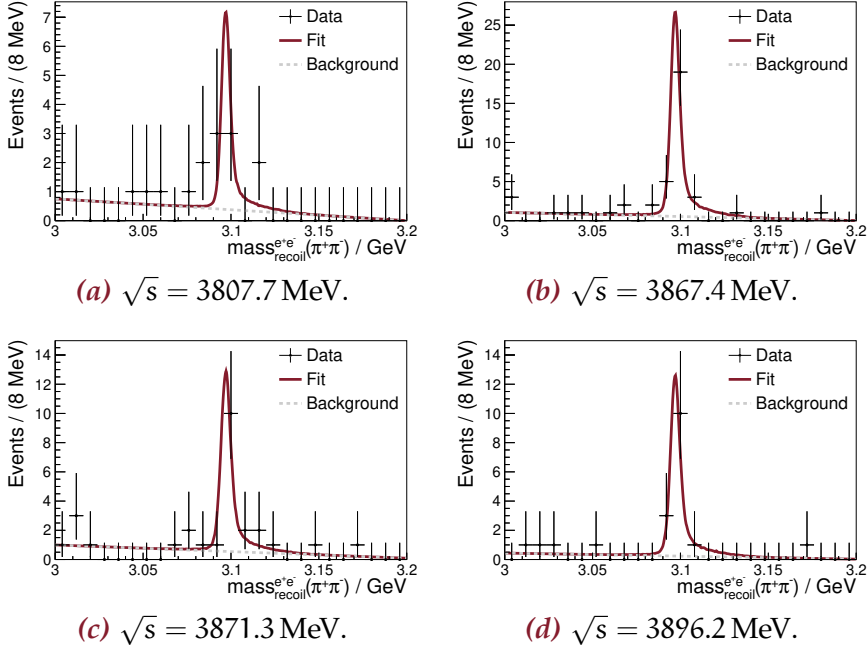
Figure D.6: Fit of the $m_{\text{rec}}^{e^+e^-}(\pi^+\pi^-)$ distribution for each data set with the $m(\pi^+\pi^-) > 0.6\,\text{GeV}$ cut. The markers with error bars is the data distribution. The red line represents the fit pdf, while the dashed gray line is the non-J/ψ background contribution to the pdf.

D.3 Analysis with the m($\pi^+\pi^-$) Cut

The $m_{\text{rec}}(\pi^+\pi^-)$ distributions with the overlaid fit are shown in Figures D.6 and D.7. The fit results are listed in Table D.1 and the systematic uncertainties are listed in Tables D.2 and D.3.

Table D.1: Result of the fit to the recoil dipion mass distribution with the $m(\pi^+\pi^-) > 0.6\,\text{GeV}$ cut. Shown are the results of the two independent J/ψ modes and a combined value. Although the values presented here are rounded according to the PDG rounding convention [30], all available digits are used in further calculations.

$\sqrt{s}$ / MeV	3807.7	3867.4	3871.3	3896.2
$\int \mathcal{L}\,dt$ / pb^{-1}	50.5	108.9	110.3	52.6
$(1+\delta)$	0.895	0.895	0.895	0.895
$\mathcal{B}_{ee}$ / %	5.971	5.971	5.971	5.971
$N_{\text{obs}}^{e^+e^-}$	6.6 ± 3.0	27 ± 5	13 ± 4	13 ± 4
$\epsilon^{e^+e^-}$ / %	25.10	30.20	30.41	31.70
$\sigma^{e^+e^-}$ / pb	10 ± 4	15.2 ± 3.1	7.5 ± 2.3	15 ± 4
$\mathcal{B}_{\mu\mu}$ / %	5.961	5.961	5.961	5.961
$N_{\text{obs}}^{\mu^+\mu^-}$	8.1 ± 3.2	32 ± 7	19 ± 5	13 ± 5
$\epsilon^{\mu^+\mu^-}$ / %	35.37	42.54	42.79	44.56
$\sigma^{\mu^+\mu^-}$ / pb	8.5 ± 3.3	13.0 ± 2.7	7.7 ± 2.0	11 ± 4
$\sigma^{\ell^+\ell^-}$ / pb	8.9 ± 2.7	13.9 ± 2.0	7.6 ± 1.5	12.5 ± 2.7

Table D.2: Relative systematic uncertainties (in %) affecting the measured cross section assuming the ρ^0 resonance in the $\pi^+\pi^-$ subsystem via the $J/\psi \to e^+e^-$ mode. The total uncertainty is the quadratic sum of the individual errors.

Source	3807.7 MeV	3867.4 MeV	3871.3 MeV	3896.2 MeV
$\int \mathcal{L}\,dt$	1.0	1.2	0.7	1.0
Tracking	4.0	4.0	4.0	4.0
$\mathcal{B}_{ee}$	0.5	0.5	0.5	0.5
Line shape	0.4	1.8	1.6	0.7
Kinematic fit	0.8	0.8	0.8	0.8
Decay model	1.1	1.5	1.7	1.4
$m_{\text{rec}}(\pi^+\pi^-)$ fit	5.1	1.8	0.9	5.5
$m_{\text{rec}}(\pi^+\pi^-)$ res	0.2	< 0.1	< 0.1	< 0.1
Total	6.7	5.2	4.8	7.1
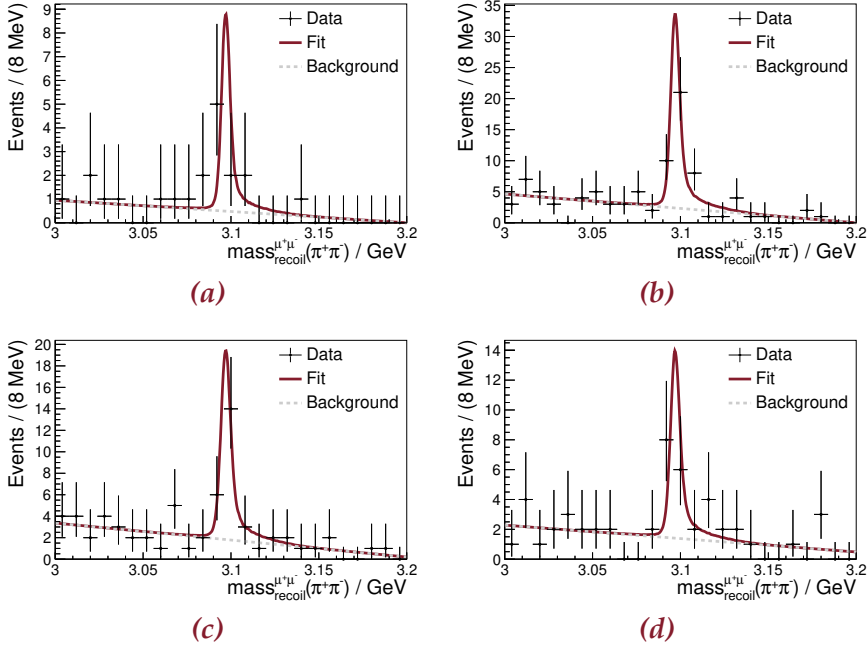
Figure D.7: Fit of the $m_{rec}^{\mu^+\mu^-}(\pi^+\pi^-)$ distribution for each data set with the $m(\pi^+\pi^-) > 0.6\,\text{GeV}$ cut. The markers with error bars is the data distribution. The red line represents the fit pdf, while the dashed gray line is the non-J/ψ background contribution to the pdf.

Table D.3: Relative systematic uncertainties (in %) affecting the measured cross section assuming the ρ^0 resonance in the $\pi^+\pi^-$ subsystem via the $J/\psi \to \mu^+\mu^-$ mode. The total uncertainty is the quadratic sum of the individual errors.

Source	3807.7 MeV	3867.4 MeV	3871.3 MeV	3896.2 MeV
$\int \mathcal{L}\,dt$	1.0	1.2	0.7	1.0
Tracking	4.0	4.0	4.0	4.0
$\mathcal{B}_{\mu\mu}$	0.6	0.6	0.6	0.6
Line shape	0.2	1.6	1.4	0.6
Kinematic fit	0.6	0.7	0.7	0.6
Decay model	1.3	1.6	1.2	1.6
$m_{rec}(\pi^+\pi^-)$ fit	3.6	5.4	1.0	5.7
$m_{rec}(\pi^+\pi^-)$ res	0.6	0.8	0.8	1.1
Total	5.7	7.3	4.7	7.4

CROSS CHECKS OF THE X(3872) ANALYSIS

This Appendix describes cross checks of the applied methods in search for the $e^+e^- \to X(3872)$ reaction.

E.1 Possibility of Interference Between X(3872) Formation and Continuum

Within QED and QCD, only processes with $J^{PC} = 1^{++}$ quantum numbers can interfere with the X(3872) formation. One might argue that the process $e^+e^- \to \gamma^*\gamma^* \to \rho^0 J/\psi$ with 1^{++} quantum numbers could take place via double vector meson dominance. It is noteworthy that the threshold for this reaction is very close to the X(3872) mass. Nonetheless, a simplified calculation according to reference [170] yields a global maximum of the $e^+e^- \to \rho^0 J/\psi$ cross section of less than $0.24\,\mathrm{pb}$ ($\approx 2\,\%$ of the measured cross section), which in addition is dominated by the 0^{++} and 2^{++} states. Furthermore, the cross section is strongly peaked towards $\cos\theta = \pm 1$, which is outside the detectors acceptance. In total, there is little room for a 1^{++} amplitude interfering with the formation of the X(3872) state.

E.2 Estimation of the Resonant X(3872) Cross Section

The contribution of the X(3872) formation is essentially given by the difference of the (pseudo) cross section between the on-resonance point and the off-resonance point. Starting at the true continuum and X(3872) cross sections, this difference is evaluated in the following. At the off-resonance data point, only the continuum process contributes to the reaction $e^+e^- \to \pi^+\pi^- J/\psi$ and the number of

events is given by

$$N_{obs}^{off} = \int_{off} \mathcal{L} \, dt \cdot (1+\delta)^{off} \cdot \mathcal{B}_{\ell\ell} \cdot \sigma_{cont}^{true} \cdot \epsilon_{cont} \quad , \tag{E.1}$$

where the cross section and the efficiency are the true values. At the on-resonance point, there is the additional X(3872) contribution with σ_X^{true}:

$$N_{obs}^{on} = \int_{on} \mathcal{L} \, dt \cdot (1+\delta)^{on} \cdot \mathcal{B}_{\ell\ell} \cdot \left(\sigma_{cont}^{true} \cdot \epsilon_{cont} + \sigma_X^{true} \cdot \epsilon_X \right) \tag{E.2}$$

During the reconstruction and the determination of the pseudo cross section, only the efficiency of the X(3872) model is used. Other than that, the same relation as in equation (5.5) is used:

$$\tilde{\sigma}^{off} = \frac{N_{obs}^{off}}{\int_{off} \mathcal{L} \, dt \cdot \epsilon_X \cdot (1+\delta)^{off} \cdot \mathcal{B}_{\ell\ell}} \quad , \tag{E.3}$$

$$\tilde{\sigma}^{on} = \frac{N_{obs}^{on}}{\int_{on} \mathcal{L} \, dt \cdot \epsilon_X \cdot (1+\delta)^{on} \cdot \mathcal{B}_{\ell\ell}} \quad . \tag{E.4}$$

Inserting equations (E.1) and (E.2) into (E.3) and (E.4) and canceling all the constants results in

$$\tilde{\sigma}^{off} = \frac{\sigma_{cont}^{true} \cdot \epsilon_{cont}}{\epsilon_X} \quad , \tag{E.5}$$

$$\tilde{\sigma}^{on} = \frac{\sigma_{cont}^{true} \cdot \epsilon_{cont} + \sigma_X^{true} \cdot \epsilon_X}{\epsilon_X} \quad . \tag{E.6}$$

The difference of the on-resonance value and the off-resonance value is

$$\begin{aligned} \Delta\tilde{\sigma} &= \tilde{\sigma}^{on} - \tilde{\sigma}^{off} \\ &= \sigma_X^{true} \cdot \frac{\epsilon_X}{\epsilon_X} + \sigma_{cont}^{true} \cdot \frac{\epsilon_{cont}}{\epsilon_X} - \sigma_{cont}^{true} \cdot \frac{\epsilon_{cont}}{\epsilon_X} \\ &= \sigma_X^{true} \quad . \end{aligned} \tag{E.7}$$

Even though the pseudo cross sections itself do not represent the true cross sections, the difference results in the true X(3872) cross section. This argument is reinforced by a MC toy study in the next Section showing that the upper limit on $\Gamma_{ee} \times \mathcal{B}$ is estimated correctly when based on the pseudo cross sections.

E.3 MC Toy Study for the Estimation of the Upper Limit

Section 5.6 describes the determination of the upper limit on $\Gamma_{ee} \times \mathcal{B}$. It is obtained by the integration of a global likelihood function, for which the likelihood functions of the cross sections at each data point and J/ψ decay are an important ingredient. They are shown in Figure 5.18 and include the efficiency which in turn is estimated for all data points purely from the $X(3872)$ MC model. In order to check whether the upper limit from Section 5.6.5 is estimated correctly, a MC toy study has been performed. Each of 5000 pseudo experiments have been simulated in the following procedure:

1. The three parameters describing the lineshape in equation (5.10) are randomly sampled:

    - σ_{cont} is sampled from a Gaussian with mean 14.1 pb and a standard deviation of 1.3 pb which is the result of a fit of a constant to the cross sections measurements in Table 5.7 and Figure 5.15.

    - $\Gamma_{ee} \times \mathcal{B}$ is sampled from a uniform distribution from 0 to 30 meV.

    - Γ_{tot} is sampled from the corresponding prior used in Section 5.6.3, a zero mean Gaussian with a 90 % quantile of 1.2 MeV.

2. The lineshape parameterization is divided into the sum of continuum and $X(3872)$ contribution: $\sigma = \sigma_{cont} + \sigma_{X(3872)}$. The previously sampled parameters result in values for σ_{cont} and $\sigma_{X(3872)}$. For each data point, J/ψ decay mode, and continuum or $X(3872)$ contribution, these values are multiplied by the factor $\int \mathcal{L}dt \cdot (1 + \delta) \cdot \mathcal{B}_{\ell\ell}$ to result in the number of expected events N_{exp}.

3. The number of events to be simulated N_{sim} is sampled from a Poissonian expecting N_{exp} events.

4. N_{sim} events are simulated, reconstructed, and analyzed in BOSS. N_{sim}^{cont} events are generated in the continuum MC model, and $N_{sim}^{X(3872)}$ events are generated with the $X(3872)$ model.

5. The global likelihood function is determined with a pure X(3872) model for the efficiency estimation, like it is done for data. Systematic uncertainties are neglected. Appendix E.4 shows that the systematics have limited influence on the upper limit.

6. The likelihood function is used to construct 90% credible intervals for $\Gamma_{ee} \times \mathcal{B}$ for an assumed total width corresponding to the simulated width.

In total there are 5000 90 % credible intervals, of which 89.1 % cover the simulated value of $\Gamma_{ee} \times \mathcal{B}$. Additionally, the 90 % credible intervals are determined after the likelihood function is marginalized over Γ_{tot}. Here, the coverage is 89.3 %. This very good agreement[1] demonstrates the validity of the method and the obtained upper limit, although the efficiency was estimated from a pure X(3872) MC model.

E.4   *Effects of Correlations of the Systematic Uncertainties*

Equation (5.18) describes the likelihood function that is used to determine the upper limit of $\Gamma_{ee} \times \mathcal{B}$. In Section 5.6.4, the systematic uncertainties of the cross section measurements are included by the convolution of the likelihood functions of the cross sections with a Gaussian with the corresponding variance. In this procedure, the correlations of the systematics between the different data points and J/ψ decay modes cannot be included. Intuitively, the incorporated correlations in the likelihood function leads to an improved upper limit. The limit is determined by the difference of the cross section at the on-resonance and at the off-resonance data points and correlated uncertainties might cancel. Since the total uncertainty is dominated by statistics, the effect is expected to be small. In order to investigate the impact of the correlations on the upper limit, the following study is performed. Instead of performing the convolution, the systematic uncertainties of the cross section are incorporated in

---

[1] If the systematics had been included in the likelihood funtion, the intervals would have been slightly larger, so that they would cover slightly more simulated values. As a result, the coverage would move from 89 % towards 90 %, which is an even better agreement.

the same way as the uncertainties of the lineshape parameters: after multiple ($\mathcal{O}(10^4)$) iterations, the likelihood function is averaged, when in each iteration the following steps are done:

1. For a given set of σ_{cont}, Γ_{tot}, and $\Gamma_{ee} \times \mathcal{B}$, the lineshape parameterization gives a value of the cross section for each datapoint and J/ψ decay mode.

2. These cross section values are multiplied by a correction factor $(1 + \delta\epsilon)$, where $\delta\epsilon$ is a randomly sampled value of the relative systematic uncertainty. Of course, they are sampled from Gaussian distributions with the corresponding variance. Here, the correction factors are constructed to be fully correlated. In reality, the correlation is not 100 %, but for this study the most extreme scenario is assumed.

3. The uncertainties associated with the lineshape parameters are handled as before.

Figure E.1 shows the comparison of the upper limit on $\Gamma_{ee} \times \mathcal{B}$ as a function of Γ_{tot} for the cases, where no correlations are included, full correlations are assumed, and where systematics are neglected completely. As expected, the effect is small. For an assumed total width of 1.2 MeV, the upper limit is reduced from 7.50 meV to 7.33 meV. After rounding, both values are 8 meV. Since it is an upper limit, the value always needs to be rounded up. If the likelihood functions include the prior for Γ_{tot} and are integrated over it, the assumed correlation reduces the value of Γ_{tot}: 6.54 to 6.38 meV. Again, the difference vanishes after rounding. In reality, the correlation is not exactly known, but the extreme case of 100% correlation does not have a significant effect on the upper limit. Thus, they can be neglected and the procedure described in Section 5.6.4 is valid.
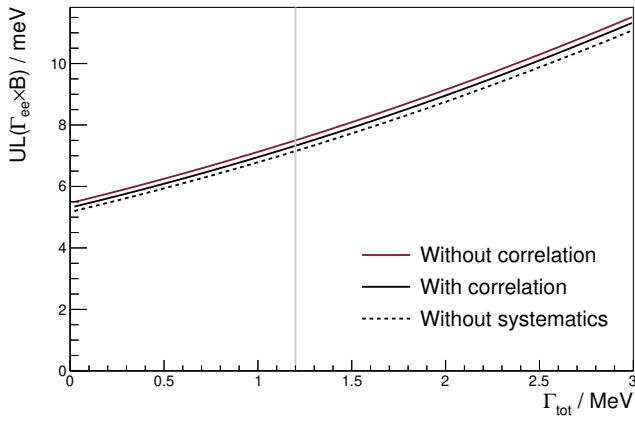
Figure E.1: Comparison of the 90 % confidence level upper limit on $\Gamma_{ee} \times \mathcal{B}$ as a function of Γ_{tot} for the cases, where no correlations are included (red), full correlations are assumed (solid black), and where systematics are neglected completely (dashed black). The grey line indicates the current 90 % upper limit on the total width.

LIST OF FIGURES

LIST OF TABLES

BIBLIOGRAPHY

[1] M. Gell-Mann, Phys. Lett. **8**, 214 (1964).

[2] G. Zweig, CERN-TH-401 (1964).

[3] G. Zweig, in *DEVELOPMENTS IN THE QUARK THEORY OF HADRONS. VOL. 1. 1964 - 1978*, edited by D. Lichtenberg and S. P. Rosen (1964) pp. 22–101.

[4] K. G. Wilson, Phys. Rev. D **10**, 2445 (1974).

[5] S. Dürr *et al.*, Science **322**, 1224 (2008).

[6] Z. Fodor and C. Hoelbling, Rev. Mod. Phys. **84**, 449 (2012).

[7] S. Aoki *et al.*, The European Physical Journal C **77**, 112 (2017).

[8] F. J. Dyson, Phys. Rev. **75**, 1736 (1949).

[9] J. Schwinger, Proceedings of the National Academy of Sciences **37**, 452 (1951).

[10] E. E. Salpeter and H. A. Bethe, Phys. Rev. **84**, 1232 (1951).

[11] R. Alkofer and L. von Smekal, Physics Reports **353**, 281 (2001).

[12] E. S. Swanson, AIP Conference Proceedings **1296**, 75 (2010).

[13] C. S. Fischer, S. Kubrak, and R. Williams, The European Physical Journal A **50**, 126 (2014).

[14] R. Williams, C. S. Fischer, and W. Heupel, Phys. Rev. D **93**, 034026 (2016).

[15] G. Eichmann *et al.*, Progress in Particle and Nuclear Physics **91**, 1 (2016).

[16] G. Eichmann, C. S. Fischer, and H. Sanchis-Alepuz, Phys. Rev. D **94**, 094033 (2016).

[17]   R. Machleidt and D. R. Entem, Physics Reports **503**, 1 (2011), arXiv:1105.2919 [nucl-th] .

[18]   S. Scherer and M. R. Schindler, Arxiv e-prints (2005), arXiv:hep-ph/0505265 [hep-ph] .

[19]   A. Pineda and J. Soto, Nuclear Physics B - Proceedings Supplements **64**, 428 (1998), proceedings of the QCD 97 Euroconference 25th Anniversary of QCD.

[20]   N. Brambilla *et al.*, Rev. Mod. Phys. **77**, 1423 (2005).

[21]   S. K. Choi *et al.* (Belle Collaboration), Phys. Rev. Lett. **91**, 262001 (2003), arXiv:hep-ex/0309032 [hep-ex] .

[22]   B. Aubert *et al.* (BABAR Collaboration), Phys. Rev. D **71**, 071103 (2005).

[23]   B. Aubert *et al.* (BABAR Collaboration), Phys. Rev. Lett. **95**, 142001 (2005).

[24]   Q. He *et al.* (CLEO Collaboration), Phys. Rev. D **74**, 091104 (2006).

[25]   M. Ablikim *et al.* (BESIII Collaboration), Phys. Rev. Lett. **110**, 252001 (2013).

[26]   Z. Q. Liu *et al.* (Belle Collaboration), Phys. Rev. Lett. **110**, 252002 (2013), erratum: Phys. Rev. Lett. **111**, 019901 (2013).

[27]   R. F. Lebed, R. E. Mitchell, and E. S. Swanson, Progress in Particle and Nuclear Physics **93**, 143 (2017).

[28]   A. Ali, J. S. Lange, and S. Stone, Progress in Particle and Nuclear Physics **97**, 123 (2017).

[29]   S. L. Olsen, T. Skwarnicki, and D. Zieminska, Rev. Mod. Phys. **90**, 015003 (2018).

[30]   M. Tanabashi *et al.* (Particle Data Group), Phys. Rev. D **98**, 030001 (2018).

[31]   S. K. Choi *et al.* (Belle Collaboration), Phys. Rev. D **84**, 052004 (2011), arXiv:1107.0163 [hep-ex] .

[32] M. Ablikim *et al.* (BESIII Collaboration), Phys. Lett. B **749**, 414 (2015), arXiv:1505.02559 [hep-ex] .

[33] M. Ablikim *et al.* (BESIII Collaboration), Nucl. Instrum. Meth. **A614**, 345 (2010), arXiv:0911.4960 [physics.ins-det] .

[34] C. Yu *et al.*, in *Proc. of International Particle Accelerator Conference (IPAC'16), Busan, Korea, May 8-13, 2016*, International Particle Accelerator Conference No. 7 (JACoW, Geneva, Switzerland, 2016) pp. 1014–1018.

[35] BESIII, "BESIII Accumulates 10 Billion J/ψ Events," `http://english.ihep.cas.cn/bes/doc/3314.html` (2019), accessed 03/01/2019.

[36] V. P. Druzhinin *et al.*, Rev. Mod. Phys. **83**, 1545 (2011).

[37] V. N. Baier and V. A. Khoze, Sov. Phys. JETP **21**, 1145 (1965).

[38] F. Jegerlehner and A. Nyffeler, Physics Reports **477**, 1 (2009).

[39] J. Prades, E. de Rafael, and A. Vainshtein, Adv. Ser. Direct. High Energy Phys. **20**, 303 (2009), arXiv:0901.0306 [hep-ph] .

[40] G. W. Bennett *et al.* (Muon g-2 Collaboration), Phys. Rev. D **73**, 072003 (2006).

[41] A. Einstein, Annalen der Physik **354**, 769 (1916).

[42] D. Perkins, *Introduction to High Energy Physics*, Addison-Wesley student edition (Addison-Wesley Publishing Company, 1987).

[43] M. Thomson, *Modern particle physics* (Cambridge University Press, New York, 2013).

[44] J. Schwinger, Phys. Rev. **73**, 416 (1948).

[45] R. P. Feynman, Rev. Mod. Phys. **20**, 367 (1948).

[46] J. Schwinger, Phys. Rev. **74**, 1439 (1948).

[47] F. J. Dyson, Phys. Rev. **75**, 486 (1949).

[48] R. P. Feynman, Phys. Rev. **76**, 749 (1949).

[49] R. P. Feynman, Phys. Rev. **76**, 769 (1949).

[50] R. P. Feynman, Phys. Rev. **80**, 440 (1950).

[51] R. P. Feynman, Phys. Rev. **84**, 108 (1951).

[52] N. Cabibbo, Phys. Rev. Lett. **10**, 531 (1963).

[53] M. Kobayashi and T. Maskawa, Progress of Theoretical Physics **49**, 652 (1973).

[54] B. Pontecorvo, Sov. Phys. JETP **6**, 429 (1957), [Zh. Eksp. Teor. Fiz.33,549(1957)].

[55] Z. Maki, M. Nakagawa, and S. Sakata, Prog. Theor. Phys. **28**, 870 (1962).

[56] B. Pontecorvo, Sov. Phys. JETP **26**, 984 (1968), [Zh. Eksp. Teor. Fiz.53,1717(1967)].

[57] S. L. Glashow, Nucl. Phys. **22**, 579 (1961).

[58] A. Salam, *8th Nobel Symposium Lerum, Sweden, May 19-25, 1968*, Conf. Proc. **C680519**, 367 (1968).

[59] S. Weinberg, Phys. Rev. Lett. **19**, 1264 (1967).

[60] S. L. Glashow, J. Iliopoulos, and L. Maiani, Phys. Rev. D **2**, 1285 (1970).

[61] F. Englert and R. Brout, Phys. Rev. Lett. **13**, 321 (1964).

[62] P. W. Higgs, Phys. Lett. **12**, 132 (1964).

[63] P. W. Higgs, Phys. Rev. Lett. **13**, 508 (1964).

[64] G. S. Guralnik, C. R. Hagen, and T. W. B. Kibble, Phys. Rev. Lett. **13**, 585 (1964).

[65] P. W. Higgs, Phys. Rev. **145**, 1156 (1966).

[66] H. Fritzsch, M. Gell-Mann, and H. Leutwyler, Phys. Lett. **47B**, 365 (1973).

[67] H. D. Politzer, Phys. Rev. Lett. **30**, 1346 (1973).

[68] D. J. Gross and F. Wilczek, Phys. Rev. D **8**, 3633 (1973).

[69] D. J. Gross and F. Wilczek, Phys. Rev. D **9**, 980 (1974).

[70] A. Deur, S. J. Brodsky, and G. F. de Téramond, Progress in Particle and Nuclear Physics **90**, 1 (2016).

[71] B. Odom *et al.*, Phys. Rev. Lett. **97**, 030801 (2006), erratum: Phys. Rev. Lett. **97**, 030802 (2006).

[72] M. Cadoret *et al.*, Phys. Rev. Lett. **101**, 230801 (2008).

[73] D. Hanneke, S. Fogwell Hoogerheide, and G. Gabrielse, Phys. Rev. A **83**, 052122 (2011).

[74] G. Sterman *et al.*, Rev. Mod. Phys. **67**, 157 (1995).

[75] U. Mosel, *Path Integrals in Field Theory*, Advanced Texts in Physics (Springer, Berlin, Heidelberg, 2004).

[76] T. Barnes, S. Godfrey, and E. S. Swanson, Phys. Rev. **D72**, 054026 (2005), arXiv:hep-ph/0505002 [hep-ph] .

[77] E. Eichten *et al.*, Phys. Rev. D **17**, 3090 (1978).

[78] E. Eichten *et al.*, Phys. Rev. D **21**, 203 (1980).

[79] Y. Koma, M. Koma, and H. Wittig, Phys. Rev. Lett. **97**, 122003 (2006).

[80] Y. Koma and M. Koma, Nuclear Physics B **769**, 79 (2007).

[81] L. Liu *et al.* (Hadron Spectrum Collaboration), Journal of High Energy Physics **2012**, 126 (2012).

[82] G. K. Cheung *et al.* (Hadron Spectrum Collaboration), Journal of High Energy Physics **2016**, 89 (2016).

[83] T. Hilger *et al.*, Phys. Rev. D **91**, 034013 (2015).

[84] C. S. Fischer, S. Kubrak, and R. Williams, The European Physical Journal A **51**, 10 (2015).

[85] C. Patrignani *et al.* (Particle Data Group), Chin. Phys. **C40**, 100001 (2016).

[86] M. Ablikim *et al.* (BESIII Collaboration), Phys. Rev. Lett. **112**, 092001 (2014).

[87] F.-K. Guo *et al.*, Rev. Mod. Phys. **90**, 015004 (2018).

[88] A. De Rújula, H. Georgi, and S. L. Glashow, Phys. Rev. Lett. **38**, 317 (1977).

[89] N. A. Tornqvist, Z. Phys. **C61**, 525 (1994), arXiv:hep-ph/9310247 [hep-ph] .

[90] Q. Wang, C. Hanhart, and Q. Zhao, Phys. Rev. Lett. **111**, 132003 (2013).

[91] L. Maiani *et al.*, Phys. Rev. Lett. **93**, 212002 (2004).

[92] L. Maiani *et al.*, Phys. Rev. D **71**, 014028 (2005).

[93] S. J. Brodsky, D. S. Hwang, and R. F. Lebed, Phys. Rev. Lett. **113**, 112001 (2014).

[94] G. Eichmann, C. S. Fischer, and W. Heupel, Physics Letters B **753**, 282 (2016).

[95] W. Heupel, *Light tetraquarks and mesons in a DSE/BSE approach*, Ph.D. thesis, Giessen U. (2015).

[96] P. C. Wallbott, G. Eichmann, and C. S. Fischer, Journal of Physics: Conference Series **1024**, 012035 (2018).

[97] S. Dubynskiy and M. Voloshin, Physics Letters B **666**, 344 (2008).

[98] F. E. Close and P. R. Page, Nuclear Physics B **443**, 233 (1995).

[99] F. Close and S. Godfrey, Physics Letters B **574**, 210 (2003).

[100] J. J. Dudek, Phys. Rev. D **84**, 074023 (2011).

[101] E. Gregory *et al.*, Journal of High Energy Physics **2012**, 170 (2012).

[102] W. Sun *et al.*, Chinese Physics C **42**, 093103 (2018).

[103] H. Sanchis-Alepuz *et al.*, Phys. Rev. D **92**, 034001 (2015).

[104] E. P. Wigner, Phys. Rev. **73**, 1002 (1948).

[105] N. A. Törnqvist, Zeitschrift für Physik C Particles and Fields **68**, 647 (1995).

[106] D. V. Bugg, Journal of Physics G: Nuclear and Particle Physics **35**, 075005 (2008).

[107] E. S. Swanson, Phys. Rev. D **91**, 034009 (2015).

[108] E. S. Swanson, International Journal of Modern Physics E **25**, 1642010 (2016).

[109] A. Bondar *et al.* (Belle Collaboration), Phys. Rev. Lett. **108**, 122001 (2012), arXiv:1110.2251 [hep-ex] .

[110] R. Aaij *et al.* (LHCb Collaboration), Phys. Rev. Lett. **115**, 072001 (2015).

[111] D. Acosta *et al.* (CDF II Collaboration), Phys. Rev. Lett. **93**, 072001 (2004).

[112] V. M. Abazov *et al.* (D0 Collaboration), Phys. Rev. Lett. **93**, 162002 (2004).

[113] R. Aaij *et al.* (LHCb Collaboration), The European Physical Journal C **72**, 1972 (2012).

[114] S. Chatrchyan *et al.* (CMS Collaboration), Journal of High Energy Physics **2013**, 154 (2013).

[115] V. Bhardwaj *et al.* (Belle Collaboration), Phys. Rev. Lett. **107**, 091803 (2011).

[116] B. Aubert *et al.* (BABAR Collaboration), Phys. Rev. Lett. **102**, 132001 (2009).

[117] R. Aaij *et al.* (LHCb Collaboration), Nuclear Physics B **886**, 665 (2014).

[118] P. del Amo Sanchez *et al.* (BABAR Collaboration), Phys. Rev. D **82**, 011101 (2010).

[119] T. Aushev *et al.* (Belle Collaboration), Phys. Rev. D **81**, 031103 (2010).

[120] G. Gokhroo *et al.* (Belle Collaboration), Phys. Rev. Lett. **97**, 162002 (2006).

[121] B. Aubert *et al.* (BABAR Collaboration), Phys. Rev. D **77**, 011102 (2008).

[122] M. Ablikim *et al.* (BESIII Collaboration), Arxiv e-prints (2019), arXiv:1901.03992 [hep-ex] .

[123] R. Aaij *et al.* (LHCb Collaboration), Phys. Rev. Lett. **110**, 222001 (2013), arXiv:1302.6269 [hep-ex] .

[124] R. Aaij *et al.* (LHCb Collaboration), Phys. Rev. D **92**, 011102 (2015).

[125] N. A. Törnqvist, Physics Letters B **590**, 209 (2004).

[126] E. Braaten and M. Kusunoki, Phys. Rev. D **69**, 074005 (2004).

[127] N. Li and S.-L. Zhu, Phys. Rev. D **86**, 074022 (2012).

[128] A. Abulencia *et al.* (CDF Collaboration), Phys. Rev. Lett. **98**, 132002 (2007).

[129] M. Aaboud *et al.* (ATLAS Collaboration), Journal of High Energy Physics **2017**, 117 (2017).

[130] C. Bignamini *et al.*, Phys. Rev. Lett. **103**, 162001 (2009).

[131] M. Albaladejo *et al.*, Chinese Physics C **41**, 121001 (2017).

[132] N. N. Achasov and E. V. Rogozina, Mod. Phys. Lett. **A30**, 1550181 (2015), arXiv:1501.03583 [hep-ph] .

[133] M. Nielsen and C. M. Zanetti, Phys. Rev. **D82**, 116002 (2010), arXiv:1006.0467 [hep-ph] .

[134] S. Narison, F. S. Navarra, and M. Nielsen, Phys. Rev. **D83**, 016004 (2011), arXiv:1006.4802 [hep-ph] .

[135] M. Takizawa and S. Takeuchi, PTEP **2013**, 093D01 (2013), arXiv:1206.4877 [hep-ph] .

[136] P. A. M. Dirac, Proc. Roy. Soc. Lond. **A117**, 610 (1928).

[137] P. A. M. Dirac, Proc. Roy. Soc. Lond. **A118**, 351 (1928).

[138] T. Aoyama *et al.*, Phys. Rev. Lett. **109**, 111808 (2012).

[139] B. Chakraborty *et al.* (HPQCD Collaboration), Phys. Rev. D **96**, 034516 (2017).

[140] T. Blum *et al.*, Phys. Rev. D **96**, 034515 (2017).

[141] H. B. Meyer and H. Wittig, Prog. Part. Nucl. Phys. **104**, 46 (2019), arXiv:1807.09370 [hep-lat] .

[142] T. Goecke, C. S. Fischer, and R. Williams, Physics Letters B **704**, 211 (2011).

[143] I. Danilkin, C. F. Redmer, and M. Vanderhaeghen, Arxiv e-prints (2019), arXiv:1901.10346 [hep-ph] .

[144] J. Grange *et al.* (Muon g-2 Collaboration), ArXiv e-prints (2015), arXiv:1501.06858 [physics.ins-det] .

[145] J. L. Holzbauer (Muon g-2 Collaboration), *Proceedings, 2017 International Workshop on Neutrinos from Accelerators (NuFact17): Uppsala University Main Building, Uppsala, Sweden, September 25-30, 2017*, PoS **NuFact2017**, 116 (2018), arXiv:1712.05980 [hep-ex] .

[146] W. Gohn (2017) arXiv:1801.00084 [hep-ex] .

[147] M. F. M. Lutz *et al.* (PANDA Collaboration), Arxiv e-prints (2009), arXiv:0903.3905 [hep-ex] .

[148] M. Ablikim *et al.* (BESIII Collaboration), Phys. Rev. Lett. **118**, 092002 (2017).

[149] M. Ablikim *et al.* (BESIII Collaboration), Phys. Rev. Lett. **114**, 092003 (2015).

[150] M. Ablikim *et al.* (BESIII Collaboration), Phys. Rev. Lett. **104**, 132002 (2010).

[151] W. Tanenbaum *et al.*, Phys. Rev. D **17**, 1731 (1978).

[152] M. Ablikim *et al.* (BESIII Collaboration), Phys. Rev. D **87**, 052005 (2013).

[153] R. E. Mitchell *et al.* (CLEO Collaboration), Phys. Rev. Lett. **102**, 011801 (2009), erratum: Phys. Rev. Lett. **106**, 159903 (2011).

[154] M. Ablikim *et al.* (BESIII Collaboration), Phys. Rev. Lett. **115**, 112003 (2015).

[155] M. Ablikim *et al.* (BESIII Collaboration), Phys. Rev. Lett. **119**, 072001 (2017).

[156] M. Ablikim *et al.* (BESIII Collaboration), Phys. Rev. D **96**, 032004 (2017).

[157] M. Ablikim *et al.* (BESIII Collaboration), Phys. Rev. D **97**, 052001 (2018).

[158] A. Denig and G. Salme, Prog. Part. Nucl. Phys. **68**, 113 (2013), arXiv:1210.4689 [hep-ex] .

[159] S. J. Brodsky *et al.*, Phys. Rev. **D69**, 054022 (2004), arXiv:hep-ph/0310277 [hep-ph] .

[160] R. Baldini *et al.*, *e+ e- physics at intermediate-energies. Proceedings, Workshop, Stanford, USA, April 30 - May 2, 2001*, eConf **C010430**, T20 (2001), [,169(2001)], arXiv:hep-ph/0106006 [hep-ph] .

[161] F. Iachello, *Proceedings, Workshop on e+ e- in the 1-2 GeV Range: Physics and Accelerator Prospects - ICFA Mini-workshp - Working Group on High Luminosity e+ e- Colliders: Alghero, Sardinia, Italy, September 10-13, 2003*, eConf **C0309101**, FRWP003 (2003), arXiv:nucl-th/0312074 [nucl-th] .

[162] A. Antonelli *et al.*, Nuclear Physics B **517**, 3 (1998).

[163] C. Z. Yuan *et al.* (Belle Collaboration), Phys. Rev. Lett. **99**, 182004 (2007).

[164] X. L. Wang *et al.* (Belle Collaboration), Phys. Rev. Lett. **99**, 142002 (2007).

[165] B. Aubert *et al.* (BABAR Collaboration), Phys. Rev. Lett. **98**, 212001 (2007).

[166] Y. Guo, Nuclear and Particle Physics Proceedings **294-296**, 153 (2018), the 20th High-Energy Physics International Conference in Quantum Chromodynamics (QCD 17).

[167] C. F. Redmer (BESIII Collaboration), in *13th Conference on the Intersections of Particle and Nuclear Physics (CIPANP 2018) Palm Springs, California, USA, May 29-June 3, 2018* (2018) arXiv:1810.00654 [hep-ex] .

[168] B. Aubert *et al.* (BABAR Collaboration), Phys. Rev. D **80**, 052002 (2009).

[169] B. Aubert *et al.* (BABAR Collaboration), Phys. Rev. Lett. **97**, 112002 (2006).

[170] M. Davier, M. E. Peskin, and A. Snyder, ArXiv e-prints (2006), arXiv:hep-ph/0606155 [hep-ph] .

[171] M.-H. Ye and Z.-P. Zheng, Int. J. Mod. Phys. **A2**, 1707 (1987).

[172] S.-X. Fang and S.-Y. Chen, *Proceedings, 14th International Conference on High-Energy Accelerators, HEACC 1989, pt.1-5: Tsukuba, Japan, August 22-26, 1989*, Part. Accel. **26**, 51 (1990).

[173] C. Zhang (BEPC & BEPCII Teams), *Proceedings of APAC, Gyeongju, Korea* , 15 (2004).

[174] Y.-F. Wang, International Journal of Modern Physics A **21**, 5371 (2006).

[175] BESIII Collaboration, Nucl. Instrum. Meth. **A598**, 7 (2009), instrumentation for Colliding Beam Physics.

[176] J. Z. Bai *et al.* (BES Collaboration), Nucl. Instrum. Meth. **A344**, 319 (1994).

[177] J. Z. Bai *et al.* (BES Collaboration), Nucl. Instrum. Meth. **A458**, 627 (2001).

[178] X. L. Guo *et al.*, Radiation Detection Technology and Methods **3**, 14 (2019).

[179] C. H. Yu, (2018), private communication.

[180] M. G. Ullrich, *Measurement of $\sigma(\psi(3770) \rightarrow p\bar{p}\pi^0)$ and determination of $\sigma(p\bar{p} \rightarrow \psi(3770)\pi^0)$ for the $\overline{P}ANDA$ experiment*, Ph.D. thesis, Giessen U. (2013).

[181] X. Li *et al.*, Nucl. Instrum. Meth. **A585**, 40 (2008).

[182] J. Liu *et al.*, Nucl. Instrum. Meth. **A557**, 436 (2006).

[183] C. Chen *et al.*, in *2007 IEEE Nuclear Science Symposium Conference Record*, Vol. 3 (2007) pp. 1844–1846.

[184] M. Y. Dong, in *2009 IEEE Nuclear Science Symposium Conference Record (NSS/MIC)* (2009) pp. 699–701.

[185] BESIII Collaboration, "Conceptual Design Report of the BESIII Cylindrical GEM Inner Tracker," (2014).

[186] I. Garzia *et al.*, *Proceedings, 3rd International Conference on Technology and Instrumentation in Particle Physics (TIPP 2014): Amsterdam, Netherlands, June 2-6, 2014*, PoS **TIPP2014**, 292 (2014).

[187] G. Mezzadri, Journal of Physics: Conference Series **742**, 012036 (2016).

[188] L. Lavezzi *et al.* (CGEM-IT Group), *Proceedings, International Conference on Instrumentation for Colliding Beam Physics (INSTR17): Novosibirsk, Russia*, JINST **12**, C07038 (2017), arXiv:1706.02428 [physics.ins-det] .

[189] L. Lavezzi *et al.* (CGEM-IT Group), in *16th Incontri di Fisica delle Alte Energie (IFAE 2017) Trieste, Italia, April 19-21, 2017* (2018) arXiv:1803.07263 [physics.ins-det] .

[190] S. Marcello *et al.*, International Journal of Modern Physics: Conference Series **48**, 1860119 (2018).

[191] Saint-Gobain, "Premium Plastic Scintillators," `https://www.crystals.saint-gobain.com/sites/imdf.crystals.com/files/documents/bc400-404-408-412-416-data-sheet.pdf` (2018), accessed 03/01/2019.

[192] Hamamatsu Photonics K.K., "Photomultiplier Tubes," `https://www.hamamatsu.com/resources/pdf/etd/PMT_TPMZ0002E.pdf` (2016), accessed 03/01/2019.

[193] Hamamatsu Photonics K.K., "Photomultiplier Tubes and Assemblies," `https://www.hamamatsu.com/resources/pdf/etd/High_energy_PMT_TPMZ0003E.pdf` (2017), accessed 03/01/2019.

[194] C. Wu *et al.*, Nucl. Instrum. Meth. **A555**, 142 (2005).

[195] Y. Heng *et al.*, *Proceedings, International Symposium On Detector Development For Particle, Astroparticle And Synchrotron Radiation Experiments (SNIC 2006): Menlo Park, California, April 3-6, 2006*, eConf **C0604032**, 0115 (2006).

[196] Y. Heng, in *Proceedings, 2007 IEEE Nuclear Science Symposium and Medical Imaging Conference (NSS/MIC 2007): Honolulu, Hawaii, October 28-November 3, 2007*, Vol. 1 (2007) pp. 53–56.

[197] Z. Chuan *et al.*, Chinese Physics C **35**, 72 (2011).

[198] S. Shengsen, Journal of Physics: Conference Series **396**, 022051 (2012).

[199] S. H. An *et al.*, Measurement Science and Technology **17**, 2650 (2006).

[200] S. Yong-Jie *et al.*, Chinese Physics C **36**, 429 (2012).

[201] S. Yang *et al.*, Nucl. Instrum. Meth. **A763**, 190 (2014).

[202] R. X. Yang *et al.*, Journal of Instrumentation **9**, C09032 (2014).

[203] X. Wang *et al.*, The European Physical Journal C **76**, 211 (2016).

[204] Z. Wu *et al.*, Journal of Instrumentation **11**, C07005 (2016).

[205] X. Li *et al.*, Radiation Detection Technology and Methods **1**, 13 (2017).

[206] Y.-X. Guo *et al.*, Radiation Detection Technology and Methods **1**, 15 (2017).

[207] F. Anghinolfi *et al.*, Nucl. Instrum. Meth. **A533**, 183 (2004), proceedings of the Seventh International Workshop on Resistive Plate Chambers and Related Detectors.

[208] M. Ullrich *et al.*, Nucl. Instrum. Meth. **A769**, 32 (2015), arXiv:1407.6168 [physics.ins-det] .

[209] C. Liu, Journal of Physics: Conference Series **293**, 012048 (2011).

[210] J. Fang and Z. Wang, Journal of Physics: Conference Series **404**, 012040 (2012).

[211] Hamamatsu Photonics K.K., "Si PIN photodiode," https://www.hamamatsu.com/resources/pdf/ssd/s2744-08_etc_kpin1049e.pdf (2011), accessed 03/01/2019.

[212] D. Ming-Yi *et al.*, Chinese Physics C **32**, 908 (2008).

[213] V. Prasad *et al.*, Arxiv e-prints (2016), arXiv:1606.00248 [hep-ex] .

[214] Z. Zhu *et al.*, in *Proceedings of the Twentieth International Cryogenic Engineering Conference (ICEC20)*, edited by L. Zhang, L. Lin, and G. Chen (Elsevier Science, Oxford, 2005) pp. 593 – 596.

[215] B. Wang *et al.*, IEEE Transactions on Applied Superconductivity **15**, 1263 (2005).

[216] Q. Xu *et al.*, Cryogenics **47**, 292 (2007).

[217] H. Shike *et al.*, Cryogenics **47**, 406 (2007), third Asian Conference on Applied Superconductivity and Cryogenics (ACASC 2005).

[218] J. Zhang *et al.*, Nucl. Instrum. Meth. **A540**, 102 (2005).

[219] J. Han *et al.*, Nucl. Instrum. Meth. **A577**, 552 (2007).

[220] J. Zhang *et al.*, Nucl. Instrum. Meth. **A580**, 1250 (2007).

[221] J. Zhang *et al.*, Nucl. Instrum. Meth. **A614**, 196 (2010).

[222] Z. Liu *et al.*, in *2007 15th IEEE-NPSS Real-Time Conference* (2007) pp. 1–4.

[223] Y. Liu *et al.*, in *2007 15th IEEE-NPSS Real-Time Conference* (2007) pp. 1–4.

[224] F. Cheng-Dong *et al.*, Chinese Physics C **32**, 329 (2008).

[225] S. Liu *et al.*, IEEE Transactions on Nuclear Science **57**, 625 (2010).

[226] S.-J. Wei *et al.*, Nucl. Instrum. Meth. **A598**, 323 (2009), instrumentation for Collding Beam Physics.

[227] J. Zhao *et al.*, in *2016 IEEE-NPSS Real Time Conference (RT)* (2016) pp. 1–3.

[228] N. Berger *et al.*, Chinese Physics C **34**, 1779 (2010).

[229] W. Yong-gang *et al.*, in *2008 IEEE Instrumentation and Measurement Technology Conference* (2008) pp. 1155–1158.

[230] X. Zhen *et al.*, Chinese Physics C **34**, 487 (2010).

[231] X. Zhen *et al.*, Chinese Physics C **35**, 1 (2011).

[232] M. Anelli *et al.*, Nucl. Instrum. Meth. **A718**, 118 (2013), proceedings of the 12th Pisa Meeting on Advanced Detectors.

[233] M. Xiao-Hu *et al.*, Chinese Physics C **32**, 995 (2008).

[234] M. N. Achasov *et al.*, Nuclear Physics B - Proceedings Supplements **189**, 366 (2009), proceedings of the Tenth International Workshop on Tau Lepton Physics.

[235] M. Xiao-Hu *et al.*, Chinese Physics C **34**, 912 (2010).

[236] E. Abakumova *et al.*, Nucl. Instrum. Meth. **A659**, 21 (2011).

[237] J. Zhang *et al.*, Nuclear Physics B - Proceedings Supplements **225-227**, 309 (2012), proceedings of the International Workshop on e+e- collisions from Phi to Psi.

[238] J.-Y. Zhang *et al.*, Chinese Physics C **40**, 076001 (2016).

[239] M. Achasov and N. Muchnoi, Journal of Instrumentation **12**, C08007 (2017).

[240] M. Ablikim *et al.* (BESIII Collaboration), Phys. Rev. D **90**, 012001 (2014).

[241] G. Barrand *et al.*, Computer Physics Communications **140**, 45 (2001).

[242] W. Li *et al.*, in *15th International Conference on Computing in High Energy and Nuclear Physics (CHEP 2006) Mumbai, Maharashtra, India, February 13-17, 2006* (2006).

[243] S. Agostinelli *et al.* (GEANT4 Collaboration), Nucl. Instrum. Meth. **A506**, 250 (2003).

[244] R. E. Kalman, Transactions of the ASME–Journal of Basic Engineering **82**, 35 (1960).

[245] D. M. Asner *et al.*, Int. J. Mod. Phys. **A24**, S1 (2009), arXiv:0809.1869 [hep-ex] .

[246] BESIII, "Data Sets," `http://english.ihep.cas.cn/bes/doc/2250.html` (2019), accessed 03/01/2019.

[247] M. Ablikim *et al.* (BESIII Collaboration), Phys. Rev. Lett. **118**, 092001 (2017).

[248] M. Ablikim *et al.* (BESIII Collaboration), Phys. Rev. D **96**, 012001 (2017).

[249] M. Ablikim *et al.* (BESIII Collaboration), Phys. Rev. D **97**, 071101 (2018).

[250] M. Ablikim *et al.* (BESIII Collaboration), ArXiv e-prints (2018), arXiv:1808.02847 [hep-ex] .

[251] M. Ablikim *et al.* (BESIII Collaboration), Physics Letters B **744**, 339 (2015).

[252] M. Ablikim *et al.* (BESIII Collaboration), Phys. Lett. **B734**, 227 (2014), arXiv:1404.4691 [hep-ex] .

[253] M. Ablikim *et al.*, Phys. Rev. D **89**, 051104 (2014).

[254] M. Ablikim *et al.* (BESIII Collaboration), Phys. Rev. D **94**, 072004 (2016).

[255] M. Ablikim and others. (BESIII Collaboration), Phys. Rev. Lett. **122**, 071802 (2019).

[256] M. Ablikim *et al.* (BESIII Collaboration), Phys. Rev. Lett. **116**, 052001 (2016).

[257] M. Ablikim *et al.* (BESIII Collaboration), Phys. Lett. **B774**, 252 (2017), arXiv:1705.04265 [hep-ex] .

[258] Kuraray, "Plastic scintillating fibers," `http://kuraraypsf.jp/pdf/all.pdf`, accessed: 2018-12-18.

[259] A. Calcaterra, (2015), private communication.

[260] M. Werner, *The Crystal Zero Degree Detector at BESIII as a realistic high rate environment for evaluating PANDA data acquisition modules*, Ph.D. thesis, Giessen U. (2015).

[261] R. Novotny and H.-G. Zaunick, "Lecture notes in MP-28E: Detektorkonzepte der Mittel und Hochenergiephysik Teil 5," (2014), Justus-Liebig-Universität Gießen.

[262] W. Erni *et al.* (PANDA Collaboration), ArXiv e-prints (2008), arXiv:0810.1216 [physics.ins-det] .

[263] Sensl, Inc., "C Series Datasheet," `http://www.sensl.com/downloads/ds/DS-MicroCseries.pdf` (2014), accessed 03/01/2019.

[264] M. Kavatsyuk *et al.*, in *2011 IEEE Nuclear Science Symposium Conference Record* (2011) pp. 43–47.

[265] J. Müllers *et al.*, *Proceedings, Topical Workshop on Electronics for Particle Physics (TWEPP17): Santa Cruz, CA, USA, September 11-15, 2017*, PoS **TWEPP-17**, 052 (2017).

[266] Xilinx, Inc., "7 Series FPGAs Data Sheet: Overview," `https://www.xilinx.com/support/documentation/data_sheets/ds180_7Series_Overview.pdf` (2018), accessed 03/01/2019.

[267] Avnet, Inc., "Kintex UltraScale KU040 Development Board Hardware User Guide," `https://products.avnet.com/opasdata/d120001/medias/docus/13/aes-AES-KU040-DB-G-User-Guide.pdf` (2015), accessed 03/01/2019.

[268] Xilinx, Inc., "Xilinx UtraScale Development Kit," `https://www.xilinx.com/products/boards-and-kits/1-buuhej.html` (2019), accessed 03/01/2019.

[269] Xilinx, Inc., "UltraScale Architecture and Product Data Sheet: Overview," `https://www.xilinx.com/support/documentation/data_sheets/ds890-ultrascale-overview.pdf` (2019), accessed 03/01/2019.

[270] Y. Yang, (2016), private communication.

[271] R. Heine *et al.*, *Proceedings, 1st International Particle Accelerator Conference (IPAC'10): Kyoto, Japan, May 23-28, 2010*, Conf. Proc. **C100523**, THPD025 (2010).

[272] R. Kleiss and H. Burkhardt, Computer Physics Communications **81**, 372 (1994).

[273] B. Garillon, (2017), private communication.

[274] G. Rodrigo *et al.*, The European Physical Journal C - Particles and Fields **24**, 71 (2002).

[275] H. Czyż, J. H. Kühn, and A. Wapienik, Phys. Rev. D **77**, 114005 (2008).

[276] H. Czyż and J. H. Kühn, Phys. Rev. D **80**, 034035 (2009).

[277] Xilinx, Inc., "Vivado Design Suite - HLx Editions," `https://www.xilinx.com/products/design-tools/vivado.html` (2019), accessed 04/01/2019.

[278] Xilinx, Inc., "AMBA AXI4 Interface Protocol," `https://www.xilinx.com/products/intellectual-property/axi.html` (2019), accessed 04/01/2019.

[279] Xilinx, Inc., "Vivado High-Level Synthesis," `https://www.xilinx.com/products/design-tools/vivado/integration/esl-design.html` (2019), accessed 04/01/2019.

[280] Xilinx, Inc., "Aurora 8B/10B," `https://www.xilinx.com/products/intellectual-property/aurora8b10b.html` (2019), accessed 03/01/2019.

[281] Xilinx, Inc., "Memory Interface," `https://www.xilinx.com/products/intellectual-property/mig.html` (2019), accessed 04/01/2019.

[282] T. Uchida, IEEE Transactions on Nuclear Science **55**, 1631 (2008).

[283] Bee Beans Technologies Co.,Ltd., "SiTCP Repository," `https://github.com/BeeBeansTechnologies`, accessed 03/01/2019.

[284] Xilinx, Inc., "FIFO Generator," `https://www.xilinx.com/products/intellectual-property/fifo_generator.html` (2019), accessed 04/01/2019.

[285] C. Ghabrous Larrea *et al.*, Journal of Instrumentation **10**, C02019 (2015).

[286] IPbus, "IPbus Repository," `https://github.com/ipbus`, accessed 03/01/2019.

[287] Xilinx, Inc., "Tri-Mode Ethernet Media Access Controller (TEMAC)," `https://www.xilinx.com/products/intellectual-property/temac.html` (2019), accessed 04/01/2019.

[288] OpenCores, "SoC Interconnection: WISHBONE," `https://opencores.org/howto/wishbone`, accessed 04/01/2019.

[289] P. Miedzik, "WishboneAXI Repository," `https://github.com/qermit/WishboneAXI`, accessed 04/01/2019.

[290] Xilinx, Inc., "AXI Interconnect," `https://www.xilinx.com/products/intellectual-property/axi_interconnect.html` (2019), accessed 04/01/2019.

[291] Xilinx, Inc., "System Management Wizard," `https://www.xilinx.com/products/intellectual-property/system-management-wiz.html` (2019), accessed 04/01/2019.

[292] L. Koch *et al.*, Journal of Instrumentation **12**, C07001 (2017).

[293] JGU Mainz, Institut für Kernphysik, "Mainzer Mikrotron," `https://www.kernphysik.uni-mainz.de/beschleuniger/mainzer-mikrotron/` (2016), accessed 03/01/2019.

[294] R. Brun and F. Rademakers, in *AIHENP'96 Workshop, Lausane*, Vol. 389 (1996) pp. 81–86, see also `http://root.cern.ch/`.

[295] Saint-Gobain, "Effects of Ultraviolet (UV) Light on NaI, CsI and BGO Crystals," `https://www.crystals.saint-gobain.com/sites/imdf.crystals.com/files/documents/effects-of-uv-light-on-nai-csi-bgo_70412.pdf` (2016), accessed 03/01/2019.

[296] W. Lauth, (2019), private communication.

[297] K. Königsberger, *Analysis 1* (Springer, Berlin, Heidelberg, 2004).

[298] K. Königsberger, *Analysis 2* (Springer, Berlin, Heidelberg, 2004).

[299] A. Denig *et al.*, Phys. Lett. B **736**, 221 (2014).

[300] Y. Liang, (2017), private communication.

[301] M. Ablikim *et al.* (BESIII Collaboration), Chinese Physics C **40**, 063001 (2016).

[302] M. Ablikim *et al.* (BESIII Collaboration), Chinese Physics C **39**, 093001 (2015).

[303] S. Jadach, B. F. L. Ward, and Z. Wąs, Computer Physics Communications **130**, 260 (2000).

[304] S. Jadach, B. F. L. Ward, and Z. Wąs, Phys. Rev. D **63**, 113009 (2001).

[305] D. J. Lange, *Proceedings, 7th International Conference on B physics at hadron machines (BEAUTY 2000)*, Nucl. Instrum. Meth. A **462**, 152 (2001).

[306] R.-G. Ping, Chinese Physics C **32**, 599 (2008).

[307] E. Richter-Was, Physics Letters B **303**, 163 (1993).

[308] P. Golonka and Z. Was, The European Physical Journal C - Particles and Fields **45**, 97 (2006).

[309] C. M. Carloni Calame *et al.*, Nucl. Phys. **B584**, 459 (2000), arXiv:hep-ph/0003268 [hep-ph] .

[310] C. M. Carloni Calame *et al.*, *Hadronic cross section at low energy. Proceedings, Workshop, SIGHAD03, Pisa, Italy, October 8-10, 2003*, Nucl. Phys. Proc. Suppl. **131**, 48 (2004), [,48(2003)], arXiv:hep-ph/0312014 [hep-ph] .

[311] P. A. Aarnio *et al.* (DELPHI Collaboration), Nucl. Instrum. Meth. **A303**, 233 (1991).

[312] S. Nova, A. Olchevski, and T. Todorov, DELPHI note 90-35 PROG 152 (1990).

[313] R.-G. Ping, Chin. Phys. **C38**, 083001 (2014), arXiv:1309.3932 [hep-ph] .

[314] J. P. Lees *et al.* (BABAR Collaboration), Phys. Rev. D **85**, 112009 (2012).

[315] M. Ablikim *et al.* (BESIII Collaboration), Phys. Rev. D **87**, 012002 (2013).

[316] R. L. Gluckstern, Nucl. Instrum. Meth. **24**, 381 (1963).

[317] O. Behnke *et al.*, eds., *Data analysis in high energy physics* (Wiley-VCH, Weinheim, Germany, 2013).

[318] W. Verkerke and D. P. Kirkby, *Statistical Problems in Particle Physics, Astrophysics and Cosmology (PHYSTAT 05): Proceedings, Oxford, UK, September 12-15, 2005*, eConf **C0303241**, MOLT007 (2003), [,186(2003)], arXiv:physics/0306116 [physics] .

[319] F. James and M. Roos, Computer Physics Communications **10**, 343 (1975).

[320] M. Ablikim *et al.* (BESIII Collaboration), Phys. Rev. D **94**, 032009 (2016).

[321] G. Breit and E. Wigner, Phys. Rev. **49**, 519 (1936).

[322] T. Bayes, Philosophical Transactions **53**, 370 (1763).

[323] J. O. Berger, J. M. Bernardo, and D. Sun, Ann. Statist. **37**, 905 (2009).

[324] J. O. Berger, J. M. Bernardo, and D. Sun, Bayesian Anal. **10**, 189 (2015).

[325] D. P. K. Reuven Y. Rubinstein, *Simulation and the Monte Carlo Method, 3rd Edition* (Wiley, 2016).

[326] G. P. Lepage, Journal of Computational Physics **27**, 192 (1978).

[327] S. Eidelman, *Proceedings, 13th International Workshop on Tau Lepton Physics (TAU 2014): Aachen, Germany, September 15-19, 2014*, Nucl. Part. Phys. Proc. **260**, 238 (2015).

[328] Z. Zhou *et al.*, in *Proceedings, 7th International Particle Accelerator Conference (IPAC 2016): Busan, Korea, May 8-13, 2016* (2016) p. THPOR047.

[329] L. Longzhou and Y. Changzheng, (2017), private communication.